

# Florida State University Libraries

---

Electronic Theses, Treatises and Dissertations

The Graduate School

---

2019

## Hurricane Boundary Layer Structure during Intensity Change: An Observational and Numerical Analysis

Kyle K. (Kyle Kevin) Ahern

FLORIDA STATE UNIVERSITY  
COLLEGE OF ARTS AND SCIENCES

HURRICANE BOUNDARY LAYER STRUCTURE DURING INTENSITY CHANGE:  
AN OBSERVATIONAL AND NUMERICAL ANALYSIS

By

KYLE K. AHERN

A Dissertation submitted to the  
Department of Earth, Ocean, and Atmospheric Science  
in partial fulfillment of the  
requirements for the degree of  
Doctor of Philosophy

2019

Copyright © 2019 Kyle K. Ahern. All Rights Reserved.

Kyle K. Ahern defended this dissertation on August 8, 2019.

The members of the supervisory committee were:

Mark A. Bourassa  
Professor Co-Directing Thesis

Robert E. Hart  
Professor Co-Directing Thesis

Kristine Harper  
University Representative

Henry E. Fuelberg  
Committee Member

Vasubandhu Misra  
Committee Member

Jeffrey Chagnon  
Committee Member

The Graduate School has verified and approved the above-named committee members, and certifies that the dissertation has been approved in accordance with university requirements.

# ACKNOWLEDGMENTS

I want to acknowledge the resources allotted to me by the Center for Ocean-Atmospheric Prediction Studies (COAPS); and in particular the immense amount of computing resources provided via the High-Performance Computing Cluster at Florida State University, as well as through Dr. Robert Hart's lab cluster. I am grateful for generous financial support from several sources throughout this work: NASA Jet Propulsion Laboratory contract #1419699, Mississippi State University Northern Gulf Institute grant #191001-363405-03 / TO 001 and 007 (NOAA prime award #NA11OAR4320199), James J. O'Brien graduate student presentation grant, and Florida State University Congress of Graduate Students presentation grant.

I thank my committee members for their willingness to oversee and critique this research, providing perspectives to the work that have made it complete. I am deeply thankful for the invaluable opportunity to interact and work with scientists at the Hurricane Research Division and Rosenstiel School of Marine and Atmospheric Science, which culminated in a collaborative publication with Dr. Jun Zhang and Dr. Robert Rogers. I want to extend my deepest gratitude to my advisors, Dr. Mark Bourassa and Dr. Robert Hart, for making it all possible and providing all the guidance, support, and patience I could ask for (and then some).

Lastly, I want to acknowledge the essential support of my family, friends, and teachers at Florida State University and beyond, who have in countless ways helped me get from point A to point B. From the selfless support of public school teachers that actually cared about their students, to the constant camaraderie of my friends at COAPS and the Hart Lab, all of them kept my head up and my feet moving.

# TABLE OF CONTENTS

List of Tables . . . . .	vi
List of Figures . . . . .	vii
Abstract . . . . .	xx
<b>1 Introduction</b>	<b>1</b>
<b>2 Background</b>	<b>6</b>
2.1 Properties of the TCBL . . . . .	6
2.1.1 Agradient Forcing . . . . .	6
2.1.2 Transverse Circulation . . . . .	12
2.1.3 Jets and Supergradient Flow . . . . .	15
2.1.4 Thermodynamics . . . . .	19
2.2 TC Maintenance and Intensification . . . . .	23
2.2.1 Air-sea Interaction . . . . .	23
2.2.2 Convection, Heating, and Vorticity Conversion . . . . .	25
<b>3 Observational Composite of the Hurricane Boundary Layer</b>	<b>28</b>
3.1 Methodology . . . . .	28
3.1.1 Data . . . . .	28
3.1.2 Compositing Technique . . . . .	29
3.2 Data Climatology . . . . .	34
3.3 Axisymmetric Analysis . . . . .	41
3.3.1 Primary Circulation . . . . .	41
3.3.2 Secondary Circulation . . . . .	47
3.3.3 Thermodynamic Structure . . . . .	49
3.4 Summary . . . . .	54
3.5 Discussion . . . . .	57
<b>4 Low-Shear Numerical Analysis: Hurricane Irma (2017)</b>	<b>60</b>
4.1 Methodology . . . . .	60
4.2 General Overview . . . . .	65
4.3 Primary Circulation . . . . .	70
4.3.1 Axisymmetric Structure . . . . .	70
4.3.2 Asymmetric Structure . . . . .	75
4.4 Secondary Circulation . . . . .	84
4.4.1 Axisymmetric Structure . . . . .	84
4.4.2 Asymmetric Structure . . . . .	90
4.5 Thermodynamics . . . . .	99
4.5.1 Axisymmetric Structure . . . . .	99

4.5.2	Asymmetric Structure . . . . .	103
4.6	Summary . . . . .	108
<b>5</b>	<b>Moderate-Shear Numerical Analysis: Hurricane Earl (2010)</b>	<b>114</b>
5.1	Methodology . . . . .	114
5.2	General Overview . . . . .	115
5.3	Primary Circulation . . . . .	121
5.3.1	Axisymmetric Structure . . . . .	121
5.3.2	Asymmetric Structure . . . . .	127
5.4	Secondary Circulation . . . . .	136
5.4.1	Axisymmetric Structure . . . . .	136
5.4.2	Asymmetric Structure . . . . .	143
5.5	Thermodynamics . . . . .	154
5.5.1	Axisymmetric Structure . . . . .	154
5.5.2	Asymmetric Structure . . . . .	158
5.6	Summary . . . . .	165
<b>6</b>	<b>Conclusion</b>	<b>172</b>
<b>Appendix</b>		
<b>A</b>	<b>Data Conversion from Earth-Relative to Vortex-Relative Space</b>	<b>180</b>
A.1	Explanation of the Problem . . . . .	180
A.2	Solution to Position Error . . . . .	183
A.3	Solution to Rotation Error . . . . .	184
	References . . . . .	188
	Biographical Sketch . . . . .	198

# LIST OF TABLES

2.1	Definitions of variables and terms used in Equations 2.2–2.4. . . . .	7
3.1	List of Atlantic hurricanes included in composites. Number of used dropsondes are shown, as well as the amount of dropsondes launched under each intensification identifier. Ranges of best-track storm intensity and SFMR-detected radius of maximum winds at times of observation are disclosed. . . . .	38
3.2	Mean environmental conditions at launch of dropsondes in IN, SS, and WE composites. Standard deviations are given in parentheses. Shear, SST, and low-level relative humidity data are pulled from SHIPS data. . . . .	39
4.1	Summary of details and specifications for the WRF model used to simulate Hurricanes Irma (2017) and Earl (2010). The simulations for Hurricanes Irma and Earl differ only in simulation time and domain specification. . . . .	63

# LIST OF FIGURES

1.1	Schematic of the boundary layer (BL, shaded light blue) beneath the free atmosphere and above a surface layer. The free atmosphere extends upward from about 1–2 km above the surface, and the surface layer is assumed to be about 100 m thick. Associated with a uniform flow in the free atmosphere (diagonal black arrows above the BL), frictional dissipation in the BL leads to a reduction of momentum and turning of the wind with height (shown with leftward black arrows in the BL). Turbulent motions and horizontal vorticity associated with vertical shear (red and black arrows) mix kinematic and thermodynamic properties throughout the BL. . . . .	2
1.2	Annual average errors of (a) National Hurricane Center (NHC) official Atlantic basin TC forecast track for the period 1989–2015 in nautical miles (n mi), and (b) NHC official Atlantic basin TC forecast intensity for the period 1990–2015 in knots (kt). Line color defines the forecast hour. Dotted lines resemble least-squares trends. These images were gathered from the NHC Forecast Verification webpage ( <a href="http://www.nhc.noaa.gov/verification/verify5.shtml">http://www.nhc.noaa.gov/verification/verify5.shtml</a> ), which contains further information and up-to-date figures. . . . .	5
2.1	Schematics for horizontal flow associated with a common cyclone in gradient wind balance (left) and with negative agradient forcing (right) in the Northern Hemisphere, based on Figure 3.5 in Holton (2004). PGF, COR, CEN, and $\vec{V}_{gr}$ represent the pressure gradient force, Coriolis force, centrifugal force, and gradient-balanced flow vector, respectively. Black vectors depict flow in gradient balance, whereas red vectors illustrate the otherwise-gradient flow after introducing frictional dissipation. In the left system, the combined effects of Coriolis deflection and centrifugal forcing balance the pressure gradient force. With friction introduced in the right system, the Coriolis and centrifugal terms are relatively reduced, inducing a net inward agradient forcing. . . . .	8
2.2	Observations of gradient wind balance in (left) rapidly intensifying Hurricane Diana (1984) during a reconnaissance flight from 0228–0903 UTC 11 September at 850 hPa, and (right) weakening Hurricane Gloria (1985) from 1422–2132 UTC 26 September at 700 hPa. Solid curves depict axisymmetrized tangential wind averaged over mission time, and individual marks are calculations of gradient wind. Figures are modified from Willoughby (1990). . . . .	9
2.3	Schematic of the secondary circulation (on the $r$ - $z$ plane) based on radar returns typically observed in the TC core. Heavy-shaded regions indicate rainshafts, situated radially outward of the inner and outer eyewall updrafts. The radar brightband demarcates frozen and liquid hydrometeors (i.e., the melting layer). Original figure in Willoughby (1988). . . . .	10

2.4	Simplified volumetric schematic depicting the low-level structure of an axisymmetric hurricane in the Northern Hemisphere. Horizontal flow (white arrows, magnitudes scaled by thickness) is gradient-balanced in the free atmosphere, and subgradient in the BL outside of the inner eyewall (purple wall). Vertical motions are drawn with bold, colored arrows (red/orange for ascent, blue for descent). Fluxes of latent and sensible heat (red wavy arrows) occur in a surface layer. Heights used to demarcate the free atmosphere, BL, and surface layer are used as reasonable examples, and they do not reflect strict definitions of the boundaries of those layers. . . . .	11
2.5	Azimuthally averaged dropsonde composite radial velocity fields, normalized by peak radial inflow values for (left) all hurricanes (peak inflow of $20 \text{ m s}^{-1}$ ), (center) category 1–3 storms (peak inflow of $17 \text{ m s}^{-1}$ ), and (right) category 4–5 storms (peak inflow of $25.5 \text{ m s}^{-1}$ ). Negative values indicate inflow, and the contour interval is 10%. The thick black line is the “inflow layer height,” defined here as where inflow is 10% of the peak inflow. The $\times$ symbol is the location of maximum tangential wind. Figure adapted from Zhang et al. (2011). . . . .	13
2.6	Normalized $r$ - $z$ cross sections of GPS dropsonde composite radial velocity (shaded in $\text{m s}^{-1}$ ), azimuthally averaged by deep-layer shear-relative quadrant (downshear-left, top-left panel; downshear-right, top-right panel; upshear-left, bottom-left panel; upshear-right, bottom-right panel). Radial distances are normalized by the radius of maximum winds (RMW). Negative values indicate inflow, and the white line represents the height of 10% peak inflow. Composite results using Doppler radar are shown in black contours (interval $0.5 \text{ m s}^{-1}$ ), where solid and dotted lines indicate outflow and inflow, respectively. Figure adapted from Zhang et al. (2013). . . . .	14
2.7	(left) Mean GPS dropwindsonde soundings of hurricane wind speed for eyewall (solid line) and outer-vortex (dashed line) regions, and (right) mean dropsonde profiles of eyewall mean wind speed profiles for seven individual hurricanes in 1998 and 1999. All wind speeds are normalized by the 700-hPa wind speed. The minimum number of soundings that represent data throughout each average profile is indicated in parentheses (a “minimum” number is used as the sampling frequency can vary with height). Figure adapted from Franklin et al. (2003). . . . .	16
2.8	Radial profiles of observed tangential wind speeds from GPS dropwindsondes (open circles) and calculated gradient wind speed profiles (solid curves) in (left) Hurricane Georges (1998) and (right) Hurricane Mitch (1998). The top panels are use data at $z = 2000 \text{ m}$ , while the middle and bottom panels represent data at $z = 1000 \text{ m}$ and $z = 500 \text{ m}$ , respectively. Open circles placed above the solid curve indicate supergradient wind speed measurements. Near an apparent radius of maximum winds, Hurricane Mitch is clearly associated with more supergradient winds than Hurricane Georges, which is arguably due to the radial profile of tangential wind speed and associated advection of absolute angular momentum. These figures are scaled together from Kepert (2006a,b). . . . .	17

2.9	(top) Radius-height cross sections of axisymmetrized storm-relative (top) tangential velocity (shaded, $\text{m s}^{-1}$ ) and radial velocity (contour, $\text{m s}^{-1}$ ) from observations in Hurricane Isabel. (bottom) Axisymmetrized equivalent potential temperature $\theta_e$ (shaded, K) and absolute angular momentum $M_a$ (contour, $\text{m}^2 \text{s}^{-1} \times 10^6$ ) from the same case. Both panels depict the transverse secondary circulation with vectors ( $\text{m s}^{-1}$ ; see legend at bottom-right of figure). All data are derived from a blend of GPS dropwindsonde and flight-level data on 13 September 2003 in Hurricane Isabel. Figure adapted from Bell and Montgomery (2008). . . . .	20
2.10	Three GPS dropwindsonde vertical profiles of equivalent potential temperature $\theta_e$ (in K, left-side profile in each panel) and storm-relative radial velocity (in $\text{m s}^{-1}$ , right-side profile in each panel) from Hurricane Bonnie (1998). Negative radial velocities indicate inflow. Horizontal lines between dual-sounding plots delineate distinct layers where $\theta_e$ increases with height. Figure adapted from Barnes (2008). . . . .	20
3.1	Schematic depiction of determining the RMW for a storm using Hurricane Katrina for example [lower fuselage radar reflectivity (dBZ) shaded]. The black line is the aircraft flight path, and the barb represents flight level wind speed (kt) and direction. White ovals ( $R_{out}$ and $R_{in}$ ) are borders of the area where RMW searches occur. (top) Scanning for $r_i$ begins after the aircraft enters the area via $R_{out}$ . (center) $r_i$ is recorded after plane exits the area through $R_{in}$ ; searching for $r_f$ starts when the plane reenters the area. (bottom) Searching for $r_f$ ends, and RMW is calculated. . . . .	32
3.2	Time series of 60-second averaged surface wind speed (black, left axis) and great circle distance from interpolated 2-minute track position (blue, right axis), taken from the stepped frequency microwave radiometer (SFMR) onboard NOAA aircraft 43RF during its mission into Hurricane Katrina on 28 August 2005 (same flight in Figure 3.1). Times of recorded $r_i$ and $r_f$ values are marked with red lines. . . . .	33
3.3	Launch positions of all composited dropsondes for Atlantic hurricanes from 1998 to 2015. Each dot is colored, representing the intensity change identifier associated with a dropsonde at launch time (summarized in the legend). The amount of dropsondes utilized in each composite is contained in brackets next to each descriptor in the legend. Landmask for determining whether dropsonde data or storm centers were over land (and thus discarded) is colored in gray. . . . .	36
3.4	Composited dropsonde launch positions on the horizontal plane for (left) intensifying, (center) steady-state, and (right) weakening Atlantic storms. The $x$ and $y$ distances from the storm center are expressed in multiples of detected RMW. Concentric dividers represent contours of $r_*$ with an interval of 1. The bold gray vector represents the environmental wind shear as determined from SHIPS. The number in the corner of each shear-relative quadrant represents the number of sondes launched in that quadrant. . . . .	37

3.5	Relative frequency of at-dropsonde-launch (hereafter “at-launch”) estimated storm intensity (5-kt bin width) for each radial bin. The value of a shaded cell at $(r_*, V_{max})$ represents the ratio of dropsondes launched at $r_*$ with storm intensity $V_{max}$ to the total number of launches at $r_*$ . Thus, the sum of all values in a column is unity. Variability across $r_*$ signifies radial heterogeneity in sampling for given $V_{max}$ , whereas variability across $V_{max}$ implies diverse sampling of storm intensity for given $r_*$ . . . .	40
3.6	Similar to Figure 3.5, except the y-axis represents the at-launch environmental vertical wind shear magnitude (as estimated with SHIPS data). The bin width used for shear data is 3 kt. . . . .	40
3.7	Normalized radius-height cross sections of azimuthally averaged, storm-relative tangential velocity $v$ (in $\text{m s}^{-1}$ ) for all composites. The solid, white contour highlights the radial inflow layer adjacent to the surface. For defining the inflow layer, storm-relative radial velocity is smoothed 5 times with a 1-2-1 filter and then normalized by peak inflow. The inflow layer is where the normalized radial velocity is at least 10% of the peak inflow (omitted above $z = 1500$ m). . . . .	42
3.8	Axisymmetrized, normalized radius-height cross sections of estimated storm intensity $V_{max}$ (in $\text{m s}^{-1}$ ) at the time of sampling, interpolated from HURDAT2 data. Values of $V_{max}$ associated with all samples in a given $r_*$ - $z$ bin are averaged to yield this figure. . . . .	43
3.9	Azimuthally averaged, normalized radius-height cross sections of the difference between estimated storm intensity and storm-relative tangential velocity, defined as $\delta v \equiv V_{max} - v$ (in $\text{m s}^{-1}$ ). The white contour marks the inflow layer height as defined in Figure 3.7. . . . .	45
3.10	Vertical profiles of (top) $\partial(\delta v)/\partial r$ (in $10^{-4} \text{ s}^{-1}$ ) and (bottom) inertial stability $I^2$ (in $10^{-7} \text{ kg}^{-2} \text{ s}^{-2}$ ) using azimuthally averaged dropsonde data from Hurricane Earl (2010) during intensification (red profiles) and weakening (blue profiles). The top of each plot is labeled with the interval of $r_*$ displayed. Both calculations used bin-averaged values for $r$ , $v$ , and $M_a$ , with a 0.5 RMW radial resolution. . . . .	46
3.11	Normalized radius-height cross sections of azimuthally averaged, storm-relative radial velocity divided by the magnitude of peak inflow in each group (listed at the top of each panel). Negative values indicate inflow. Black lines connect black circles representing the height at which $v$ (smoothed with a 1-2-1 filter 5 times) is maximized at each radial bin outside of $r_* = 0.5$ . . . . .	48
3.12	Similar to Figure 3.7, except virtual potential temperature $\theta_v$ (in K) is shaded. Differences between IN and WE with statistical significance (to 95% confidence) are depicted with diagonal lines (where $\theta_v$ is greater in WE) or cross hatching (where $\theta_v$ is greater in IN) in the WE panel. . . . .	50

3.13	Axisymmetric, normalized radius-height cross sections of static stability $N^2$ plotted between 100 m and 2400 m AGL (shaded in $10^{-5} \text{ s}^{-2}$ ). The data in this figure were composited into lower resolution vertical bins with 100 m thickness to reduce noise. The vertical derivative of $\theta_v$ is calculated using a centered finite difference. The white line is defined identically as in Figure 3.7. . . . .	51
3.14	Similar to Figure 3.7, except equivalent potential temperature $\theta_e$ (in K) is shaded. Statistically significant differences between IN and WE are plotted the same as in Figure 3.12 (using a darker color for clarity). . . . .	52
3.15	Radius-height conceptual diagrams of the azimuthal-mean tropospheric structure in (left) IN hurricanes and (right) non-IN hurricanes, based on the composite analysis. Circles with crosses indicate tangential flow (into the page), and their sizes are proportional to their magnitude. Regions of differing inertial stability are marked along the radial axis. Vectors in the BL are shaded by MSE using the scale at the bottom of the figure. Radial vectors in the BL have lengths proportional to radial wind speed. Red wavy vectors at the surface indicate upward heat fluxes at the air-sea interface. Above the BL, dashed vectors indicate possible convective motions, and solid vectors represent the secondary circulation in the free atmosphere with boldness proportional to circulation strength. . . . .	58
4.1	Map illustration of the four domains set at initialization (0000 UTC 03 September 2017) for this WRF-ARW simulation of Hurricane Irma. Contours of mean sea-level pressure (from eta reduction) at initialization time from NCEP FNL Operational Global Analysis data (NCEP 2000) are drawn in blue (hPa, 4 hPa interval). The outermost domain (region containing “D1”) is static with a horizontal resolution of 36 km. Domains labeled “D2,” “D3,” and “D4” are vortex-following with horizontal resolutions of 12 km, 4 km, and 1.333 km, respectively. . . . .	62
4.2	Simulated outgoing longwave radiation at the top of the atmosphere (shaded using the right-side color bar, $\text{W m}^{-2}$ ) at various times (labeled at the top of each panel). A storm-motion vector is drawn at the diagnosed center of Hurricane Irma (shaded based on magnitude in knots using the left-side color bar), along with a wind barb denoting the deep-layer shear. Gray hatched areas represent land used in the model. . . . .	66
4.3	Vertical velocity ( $\text{m s}^{-1}$ ) at the model levels closest to 850 hPa ( $z \approx 1.4 \text{ km}$ , left panels) and 200 hPa ( $z \approx 12.2 \text{ km}$ , right panels) in Hurricane Irma, shaded using the right-side color bar. The snapshots are taken from 0000 UTC 06 September (top panels) and 07 September (bottom panels). The storm-motion vector is drawn at the center of the hurricane (shaded using the left-side color bar). A wind barb representing the deep-layer shear is drawn in black at the center. Gray hatched areas represent land used in the model. . . . .	67

4.4	Hurricane Irma’s simulated center track (red) and HURDAT2 best-track center (black) as it generally moved westward between 04 September and 10 September. Circles mark Hurricane Irma’s position at 0000 UTC for a given day. . . . .	68
4.5	Time series of Hurricane Irma’s modeled intensity ( $\text{m s}^{-1}$ ) throughout the simulation, shaded by intensity change identifiers (red, intensifying; gray, steady-state; blue, weakening). The 6-hourly HURDAT2 best-track intensity is plotted in black. . . . .	69
4.6	Radius-height plots of Hurricane Irma’s azimuthally averaged primary circulation using storm-relative tangential wind $v$ , absolute angular momentum $M_a$ , inertial stability $I^2$ , and agradient wind $v_{ag} \equiv v - V_{gr}$ on 1200 UTC 05 September (left, during IN) and 2100 UTC 05 September (right, during WE). Each row of figures uses the color bar to its right; units are given above each plot. The dashed, black line marks the RMW. The bold, black line indicates the radial inflow layer (10% of the maximum inflow). The scale used for $I^2$ is geometric (0, 0.05, 0.1, 0.2, 0.4, ...). . . . .	71
4.7	Time-radius Hovmöller diagrams of Hurricane Irma’s storm-relative tangential flow $v$ (top), absolute angular momentum $M_a$ (middle), and inertial stability $I^2$ (bottom). All fields are taken at the model height where the tangential wind jet occurs ( $z \approx 710$ m). A timeline shaded by intensity change (red for IN, gray for SS, blue for WE) is drawn at the bottom of each panel. The bold, black line represents the RMW. Each plot uses the color bar to its right, and units are displayed above each plot. . . . .	73
4.8	Similar to Figure 4.7, except using agradient wind $v_{ag}$ near the top of the inflow layer (top panel, $z \approx 1.2$ km) and at the height of the tangential wind jet (bottom panel, $z \approx 710$ m). Positive values represent supergradient winds ( $v > V_{gr}$ ), and negative values represent subgradient winds ( $v < V_{gr}$ ). . . . .	75
4.9	Shear-relative quadrants of $r$ - $z$ cross sections of $v$ ( $\text{m s}^{-1}$ ) in Hurricane Irma on 1200 UTC 05 September (top two rows, during IN) and 2100 UTC 05 September (bottom two rows, during WE). Panels are labeled by quadrant (downshear-left, DSL; upshear-left, USL; upshear-right, USR; downshear-right, DSR). The dashed, black line marks the RMW. The bold, black line indicates the axisymmetrized radial inflow layer (as in Figure 4.6). . . . .	76
4.10	Time-radius Hovmöller diagrams of azimuthal tangential wind anomaly ( $v$ minus the azimuthally averaged $v$ in $\text{m s}^{-1}$ ) at $z \approx 710$ m in each shear-relative quadrant from Hurricane Irma. The $x$ -axis represents time, which is labeled by each day at 0000 UTC with the abbreviated month. A timeline shaded by intensity change (red for IN, gray for SS, blue for WE) is drawn at the bottom of each panel. The bold, black line represents the RMW. Panels are labeled by their quadrant abbreviation. . . . .	77
4.11	Radius-azimuth polar plots showing the evolution of Hurricane Irma’s tangential wind anomaly ( $v$ minus the azimuthally averaged $v$ in $\text{m s}^{-1}$ ) at $z \approx 710$ m. Each row of plots represents a different period of intensity change in Irma: IN on 05 September	

	(top), WE on 05 September (middle), and IN on 06 September (bottom). Time increases toward the right at a 2-hour interval. Radius is contoured (gray dashed) every 40 km out to 160 km, and the RMW is contoured in black (solid) near $r = 40$ km. Gray contours of azimuth separate shear-relative quadrants. North points to the top of the figure. Similar to Figure 4.3, deep-layer shear (barb) and storm motion (vector) are superimposed on Irma’s center, and land is hatched in gray. . . . .	79
4.12	Similar to Figure 4.9, but shaded using inertial stability $I^2$ (units $10^{-6} \text{ kg}^{-2} \text{ s}^{-2}$ ). . .	80
4.13	Similar to Figure 4.10, but shaded using inertial stability $I^2$ at $z \approx 510$ m (units $10^{-6} \text{ kg}^{-2} \text{ s}^{-2}$ ). . . . .	81
4.14	Similar to Figure 4.9, but shaded using a gradient wind $v_{ag}$ ( $\text{m s}^{-1}$ ). . . . .	82
4.15	Similar to Figure 4.10, but shaded using a gradient wind $v_{ag}$ at $z \approx 1.2$ km ( $\text{m s}^{-1}$ ). .	83
4.16	Cross sections ( $r$ - $z$ ) of Hurricane Irma’s azimuthally averaged secondary circulation using storm-relative radial wind $u$ , radial divergence $\nabla \cdot (\hat{r} \cdot \vec{U})\hat{r}$ (labeled “RDIV” in the plot), and vertical wind $w$ on 1200 UTC 05 September (left, during IN) and 2100 UTC 05 September (right, during WE). Negative (positive) values in $u$ indicate inflow (outflow). Each row of figures uses the color bar to its right, and each field has its units listed above its panel. The dashed and solid black lines indicate the RMW and azimuthally averaged inflow layer, respectively. The scales used for radial divergence and vertical velocity are geometric about zero (... -4, -2, -1, 0, 1, 2, 4, ... for radial divergence). . . . .	85
4.17	Time-radius Hovmöller plots of Hurricane Irma’s near-surface radial velocity $u$ (at $z \approx 210$ m, top), vertically integrated radial divergence through the <i>asymmetric</i> inflow layer (middle), and vertical motion near the top of the BL inflow $w$ (at $z \approx 1.2$ km, bottom). Each plot uses the color bar to its right, and all fields are expressed in $\text{m s}^{-1}$ . A timeline shaded by intensity change (red for IN, gray for SS, blue for WE) is drawn at the bottom of each panel. The bold, black line represents the RMW. . . . .	87
4.18	Radius-height cross sections of $u$ ( $\text{m s}^{-1}$ ) in each shear-relative quadrant of Hurricane Irma on 1200 UTC 05 September (top two rows, during IN) and 2100 UTC 05 September (bottom two rows, during WE). Panels are labeled by the quadrant they represent. The dashed, black line marks the RMW. The bold, black line indicates the axisymmetrized radial inflow layer (as in Figure 4.16). . . . .	91
4.19	Time-radius Hovmöllers of radial velocity $u$ ( $\text{m s}^{-1}$ ) at $z \approx 210$ m in each quadrant of Hurricane Irma. The $x$ -axis represents time, which is labeled by each day at 0000 UTC with the abbreviated month. A timeline shaded by intensity change (red for IN, gray for SS, blue for WE) is drawn at the bottom of each panel. The bold, black line represents the RMW. Panels are labeled by their quadrant abbreviation. . .	93

4.20	Similar to Figure 4.11, but using radial wind $u$ ( $\text{m s}^{-1}$ ) at $z \approx 210$ m. . . . .	94
4.21	Similar to Figure 4.18, but plotted using radial divergence ( $10^{-4} \text{ s}^{-1}$ ). . . . .	95
4.22	Similar to Figure 4.19, but shaded using vertically integrated radial divergence in the asymmetric radial inflow layer ( $\text{m s}^{-1}$ ). . . . .	96
4.23	Similar to Figure 4.18, but shaded using vertical velocity $w$ ( $\text{m s}^{-1}$ ). . . . .	97
4.24	Similar to Figure 4.19, but shaded using vertical velocity $w$ at $z \approx 1.2$ km ( $\text{m s}^{-1}$ ). . . . .	98
4.25	Time series of upward vertical mass flux ( $10^6 \text{ kg s}^{-1}$ ) in the upshear-left quadrant of Hurricane Irma from 0000 UTC 05 September to 1200 UTC 06 September. The flux is calculated at $z \approx 1.2$ km and averaged between radii of 40 and 80 km. The time series is shaded by intensity change (red for IN, gray for SS, blue for WE). Unequal size, two-sample $t$ -tests comparing the WE phase with each of the IN phases shown found statistically different mean vertical mass fluxes to 99.9% confidence (bold, black lines denote confidence intervals for each IN and WE phase). Statistical significance was also found using $w$ ; it is not shown due to the fact that surface area of cylindrical data cells increases with $r$ , which is not considered in $w$ but is necessary to calculate the mass flux. . . . .	99
4.26	Radius-height cross sections of Hurricane Irma's azimuthally averaged virtual temperature $T_v$ , potential virtual temperature $\theta_v$ , relative humidity $RH$ , and equivalent potential temperature $\theta_e$ on 1200 UTC 05 September (left, IN phase) and 2100 UTC 05 September (right, WE phase). Rows of figures use the color bar to their right, and each plot has its units listed above. The dashed and solid black lines indicate the RMW and azimuthally averaged inflow layer, respectively. . . . .	100
4.27	Time-radius Hovmöller plots of Hurricane Irma's near-surface relative humidity $RH$ (in %, left) and equivalent potential temperature $\theta_e$ (in K, right). The top row of plots depict fields taken at $z \approx 1.85$ km, and the bottom row of plots show fields at $z \approx 210$ m. A timeline shaded by intensity change is drawn at the bottom of each panel. The bold, black line represents the RMW. Each column of plots uses the color bar below the column. . . . .	102
4.28	Quadrant-specific, $r$ - $z$ cross sections of Hurricane Irma's relative humidity $RH$ (%) on 1200 UTC 05 September (top two rows, during IN) and 2100 UTC 05 September (bottom two rows, during WE). Panels are labeled by the representative quadrant. The dashed, black line marks the RMW. The bold, black line indicates the axisymmetrized radial inflow layer. . . . .	104
4.29	Similar to Figure 4.28, but shaded using equivalent potential temperature $\theta_e$ (in K). . . . .	105
4.30	Similar to Figure 4.11, but using $\theta_e$ (K) at $z \approx 1.85$ km (top) and $z \approx 210$ m (bottom) from times associated with the WE phase on 05 September. . . . .	106

4.31	Time-radius Hovmöllers of $\theta_e$ (K) at $z \approx 1.85$ km in Hurricane Irma’s shear-relative quadrants. The $x$ -axis represents time, labeled by each day at 0000 UTC. A timeline shaded by intensity change is drawn at the bottom of each panel. The bold, black line represents the RMW. Panels are labeled by their quadrant abbreviation. . . . .	107
4.32	Similar to Figure 4.31, but using $\theta_e$ (K) at $z \approx 210$ m. . . . .	108
4.33	Volumetric conceptual diagram of Hurricane Irma’s low-tropospheric structure during its weakening phase on 05 September. Vertical, shear, and motion directions are indicated on the left side. Each horizontal plane is labeled by its approximate vertical level on the right side of the figure. Horizontal planes are divided into shear-relative quadrants by thin black lines, and each quadrant is labeled on the surface plane. Bold black ovals represent the RMW as detected at $z \approx 1.8$ km. Tangential vectors (white) and radial vectors (shaded) have magnitudes proportional to their thickness. Radial vectors are shaded by $\theta_e$ using the scale at the bottom. Ascent and descent vectors are colored red and blue, respectively. The yellow shaded region on the horizontal planes represents dry, low- $\theta_e$ air. . . . .	111
5.1	Map illustration of the four domains set at initialization (1200 UTC 28 August 2010) for the WRF-ARW simulation of Hurricane Earl. Contours of mean sea-level pressure (from eta reduction) at initialization time from NCEP FNL Operational Global Analysis data (NCEP 2000) are drawn in blue (hPa, 4 hPa interval). The outermost domain (region containing “D1”) is static with a horizontal resolution of 36 km. Domains labeled “D2,” “D3,” and “D4” are vortex-following with horizontal resolutions of 12 km, 4 km, and 1.333 km, respectively. . . . .	115
5.2	Hurricane Earl’s simulated outgoing longwave radiation at the top of the atmosphere (shaded using the right-side color bar, $W m^{-2}$ ) at various times (labeled at the top of each panel). A storm-motion vector is drawn at Earl’s diagnosed center (shaded by magnitude in knots using the left-side color bar), along with a wind barb denoting the deep-layer shear. Gray hatched areas represent land used in the model. . . . .	116
5.3	Vertical velocity ( $m s^{-1}$ ) in Hurricane Earl, similar to Figure 4.3. Snapshots shown are taken from 1200 UTC 31 August (top panels) and 01 September (bottom panels). . . . .	118
5.4	Hurricane Earl’s simulated center track (red) and HURDAT2 best-track center (black) between 1200 UTC 29 August and 04 September. Circles mark Hurricane Earl’s position at 1200 UTC for a given day. . . . .	120
5.5	Time series of Hurricane Earl’s modeled intensity ( $m s^{-1}$ ) throughout the simulation, shaded by intensity change identifiers (red, intensifying; gray, steady-state; blue, weakening). The 6-hourly HURDAT2 best-track intensity is plotted in black. . . . .	120
5.6	Radius-height cross sections of Hurricane Earl’s azimuthally averaged primary circulation using tangential wind $v$ , absolute angular momentum $M_a$ , inertial stabil-	

	ity $I^2$ , and a gradient wind $v_{ag}$ on 0600 UTC 31 August (left, during intensification) and 0900 UTC 01 September (right, during weakening after peak intensity). Each row of figures uses the color bar to its right, and units are listed above each plot. The bold, black line indicates the radial inflow layer (10% of the maximum inflow). The scale used for $I^2$ is geometric. . . . .	122
5.7	Time-radius Hovmöllers of Hurricane Earl's tangential flow $v$ (top), absolute angular momentum $M_a$ (middle), and inertial stability $I^2$ (bottom) from 0000 UTC 30 August to 1200 UTC 03 September. All fields are taken at the approximate height where the tangential wind jet occurs ( $z \approx 710$ m). A timeline shaded by intensity change (red for IN, gray for SS, blue for WE) is drawn at the bottom of each panel. The bold, black line represents the RMW. Each plot uses the color bar to its right, and units are displayed above each plot. . . . .	124
5.8	Time series of inertial stability $I^2$ ( $10^{-6} \text{ kg}^{-2} \text{ s}^{-2}$ ) outside the RMW in Hurricane Earl between 1200 UTC 30 August and 0000 UTC 03 September. The inertial stability shown here is calculated at $z \approx 970$ m and averaged between radii of 60 and 100 km. The time series is shaded by intensity change (red for IN, gray for SS, blue for WE). A black, dashed line denotes the time of peak intensity (1400 UTC 31 August). . . . .	125
5.9	As in Figure 5.7, except using a gradient wind $v_{ag}$ near the top of the inflow layer (top panel, $z \approx 1.2$ km) and at the height of the tangential wind jet (bottom panel, $z \approx 710$ m). Positive values represent supergradient winds ( $v > V_{gr}$ ), and negative values represent subgradient winds ( $v < V_{gr}$ ). . . . .	126
5.10	Shear-relative quadrants of $r$ - $z$ cross sections of $v$ ( $\text{m s}^{-1}$ ) in Hurricane Earl on 0600 UTC 31 August (top two rows, during IN toward peak intensity) and 0900 UTC 01 September (bottom two rows, during WE after peak intensity). Panels are labeled by shear-relative quadrant. The bold, black line indicates the axisymmetrized radial inflow layer (as in Figure 5.6). . . . .	128
5.11	Time-radius Hovmöller diagrams of azimuthal tangential wind anomaly ( $\text{m s}^{-1}$ ) at $z \approx 710$ m in each shear-relative quadrant from Hurricane Earl. The $x$ -axis represents time, which is labeled by each day at 0000 UTC with the abbreviated month. A timeline shaded by intensity change (red for IN, gray for SS, blue for WE) is drawn at the bottom of each panel. The bold, black line represents the RMW. Panels are labeled by their shear-relative quadrant abbreviation. . . . .	129
5.12	Radius-azimuth polar plots depicting the evolution of Hurricane Earl's $v$ anomaly ( $v$ minus the azimuthally averaged $v$ in $\text{m s}^{-1}$ ) at $z \approx 710$ m. Each row of plots represents a period of intensity change: IN on 31 August (top), WE on 01 September (middle), and WE on 02 September (bottom). Time increases toward the right at a 2-hour interval. Radius is contoured (gray dashed) every 40 km out to 160 km, and the RMW is contoured in black (solid) near $r = 40$ km. Gray contours of azimuth	

	separate shear-relative quadrants. North points to the top of the figure. Deep-layer shear (barb) and storm motion (vector) are superimposed on Earl's center, similar to Figure 5.3. . . . .	131
5.13	Similar to Figure 5.10, but shaded using inertial stability $I^2$ (units $10^{-6} \text{ kg}^{-2} \text{ s}^{-2}$ ). . . . .	132
5.14	Similar to Figure 5.11, but shaded using inertial stability $I^2$ at $z \approx 510 \text{ m}$ (units $10^{-6} \text{ kg}^{-2} \text{ s}^{-2}$ ). . . . .	133
5.15	Similar to Figure 5.10, but shaded using a gradient wind $v_{ag}$ ( $\text{m s}^{-1}$ ). . . . .	134
5.16	Similar to Figure 5.11, but shaded using a gradient wind $v_{ag}$ at $z \approx 1.2 \text{ km}$ ( $\text{m s}^{-1}$ ). . . . .	136
5.17	Cross sections ( $r$ - $z$ ) of Hurricane Earl's azimuthally averaged secondary circulation seen via radial wind $u$ , radial divergence (RDIV), and vertical velocity $w$ on 0600 UTC 31 August (left, during IN) and 0900 UTC 01 September (right, during WE). Each row of figures uses the color bar to its right, with each field's units listed above its panel. The dashed and solid black lines indicate the RMW and azimuthally averaged inflow layer, respectively. The scales used for radial divergence and vertical velocity are geometric about zero. . . . .	138
5.18	Time-radius Hovmöllers of Hurricane Earl's radial velocity $u$ at $z \approx 210 \text{ m}$ (top), vertically integrated radial divergence through the asymmetric inflow layer (middle), and vertical motion near the top of the BL inflow $w$ ( $z \approx 1.2 \text{ km}$ , bottom) from 0000 UTC 30 August to 1200 UTC 03 September. A timeline shaded by intensity change is drawn at the bottom of each panel. The bold, black line represents the RMW. Each plot uses the color bar to its right, and all fields are in $\text{m s}^{-1}$ . . . . .	140
5.19	Radius-height cross sections of radial wind $u$ ( $\text{m s}^{-1}$ ) in Hurricane Earl's shear-relative quadrants on 0600 UTC 31 August (top two rows, during IN) and 0900 UTC 01 September (bottom two rows, during WE). Panels are labeled by the quadrant they represent. The dashed, black line marks the RMW. The bold, black line indicates the axisymmetrized radial inflow layer (see Figure 5.17). . . . .	144
5.20	Similar to Figure 5.12, but using radial wind $u$ ( $\text{m s}^{-1}$ ) at $z \approx 210 \text{ m}$ . . . . .	145
5.21	Hovmöllers ( $t$ - $r$ ) of radial wind $u$ at $z \approx 210 \text{ m}$ in Hurricane Earl's shear-relative quadrants. The $x$ -axis represents time, which is labeled by each day at 0000 UTC with the abbreviated month. A timeline shaded by intensity change is drawn beneath each panel, similar to Figure 5.18. The bold, black line represents the RMW. Panels are labeled by their quadrant abbreviation. . . . .	147
5.22	Similar to Figure 5.19, but shaded using radial divergence ( $10^{-4} \text{ s}^{-1}$ ). . . . .	148
5.23	Similar to Figure 4.18, but shaded using vertical velocity $w$ ( $\text{m s}^{-1}$ ). . . . .	149

5.24	Similar to Figure 5.21, but shaded using vertically integrated radial divergence in the asymmetric radial inflow layer ( $\text{m s}^{-1}$ ). . . . .	151
5.25	Similar to Figure 4.19, but shaded using vertical velocity $w$ at $z \approx 1.2$ km ( $\text{m s}^{-1}$ ). . . . .	151
5.26	Radius-height cross sections of Hurricane Earl’s azimuthally averaged virtual temperature $T_v$ , potential virtual temperature $\theta_v$ , relative humidity $RH$ , and equivalent potential temperature $\theta_e$ on 0600 UTC 31 August (left, IN phase) and 0900 UTC 01 September (right, WE phase). Rows of figures use the color bar to their right, and each plot has its units listed above. The dashed and solid black lines indicate the RMW and azimuthally averaged inflow layer, respectively. . . . .	155
5.27	Time-radius Hovmöller plots of Hurricane Earl’s near-surface relative humidity $RH$ (in %, left) and equivalent potential temperature $\theta_e$ (in K, right). The top row of plots depict fields taken at $z \approx 1.85$ km, and the bottom row of plots show fields at $z \approx 210$ m. A timeline shaded by intensity change is drawn at the bottom of each panel. The bold, black line represents the RMW. Each column of plots uses the color bar below the column. . . . .	157
5.28	Radius-height cross sections of Hurricane Earl’s relative humidity $RH$ (%) in shear-relative quadrants on 0600 UTC 31 August (top two rows, during IN) and 0900 UTC 01 September (bottom two rows, during WE). Panels are labeled by quadrant shown. The dashed, black line marks the RMW. The bold, black line indicates the axisymmetrized radial inflow layer. . . . .	159
5.29	Similar to Figure 5.28, but shaded using equivalent potential temperature $\theta_e$ (in K). . . . .	161
5.30	Time-radius Hovmöllers of $\theta_e$ (K) at $z \approx 210$ m in Hurricane Earl’s shear-relative quadrants. The $x$ -axis represents time, labeled by each day at 0000 UTC. A timeline shaded by intensity change is drawn at the bottom of each panel. The bold, black line represents the RMW. Panels are labeled by their quadrant abbreviation. . . . .	162
5.31	Similar to Figure 5.12, but using $\theta_e$ (K) at $z \approx 210$ m. . . . .	164
5.32	Similar to Figure 5.30, but using $\theta_e$ (K) at $z \approx 1.2$ km. . . . .	165
5.33	Volumetric schematic of Hurricane Earl’s low-level tropospheric structure during its gradual weakening following peak intensity on 31 August. The schematic’s frame is identical to Figure 4.33. Tangential vectors (shaded) and radial vectors (white) have magnitudes proportional to their thickness. Tangential vectors are shaded by their degree of gradient imbalance, with deeper shades of red or blue indicating strongly supergradient or subgradient flow, respectively. Ascent vectors are solid red without an outline, with two regions of ascent shown in the DSR quadrant. The orange and yellow shaded regions indicate areas of very high- and high- $\theta_e$ air, respectively. . . . .	168

- A.1 (left) Schematic of a vortex-centered polar grid, with Cartesian axes  $(x, y)$  drawn over the grid as black vectors; contours of radius  $r$  (concentric circles) and azimuth  $\psi$  (radial rays extending from the center) in gray. Red and blue vectors represent tangential and radial unit vectors, respectively. The green triangle with sides  $X, Y$ , and  $r$  (radius) depicts a conceptual example of calculating  $\psi$  at a position (the black point marked “data”) using trigonometry. (right) Illustration of position error due to assuming  $X = X_{gc}$  and  $Y = Y_{gc}$ , where the solid black dot represents the actual data position and the hollow dot represents the erroneous position calculated. The paths in red represent  $X_{gc}$  and  $Y_{gc}$ , which are computed along lines of latitude and longitude (dashed lines) respectively. The lengths of  $X_{gc}$  and  $Y_{gc}$  are used to approximate  $r$  and  $\psi$  (illustrated by blue dashed lines), resulting in position error. . . 181
- A.2 (left) Eastward and northward unit vectors  $\hat{i}$  (blue) and  $\hat{j}$  (red) superimposed on a vortex-centered polar grid, illustrating deviations of  $\hat{i}$  and  $\hat{j}$  from the Cartesian axes  $(x, y)$ . (right) Example schematic of approximating the projected direction  $\alpha$  (green) of an eastward vector  $\vec{V}$  (red) at some location of data (black dot). Radial and  $x$  unit vectors for the example data are drawn in black. The position of data  $(X, Y)$  is perturbed downstream with the flow, yielding a perturbed position at  $(X', Y')$  (hollow dot). The  $x$  unit vector and a line (in blue) drawn on the projection between  $(X, Y)$  and  $(X', Y')$  are used to form a right triangle, which is used to solve for  $\alpha$ . Note that in this case,  $\alpha$  is not zero—the mathematical direction of an eastward vector on a latitude-longitude grid. . . . . 185

# ABSTRACT

A combination of observational and numerical analyses is used to investigate hurricane boundary layer (BL) structure in the context of intensity change. These analyses refer to hurricanes in three modes of intensity change: intensifying (IN), steady-state (SS), and weakening (WE). Observations from global positioning system (GPS) dropwindsondes launched in Atlantic tropical cyclones between 1998 and 2015 are collected for compositing based on intensity change. After quality control and sorting, 3,091 dropwindsondes were composited—1,086 were released into IN hurricanes, 1,042 were released during WE phases, and the remaining 963 releases were associated with steady-state storms. Lower-tropospheric tangential winds outside the radius of maximum winds (RMW) were stronger in non-intensifying storms than IN storms, which suggests greater inertial stability  $I^2$  outside the RMW in non-intensifying hurricanes. The BL radial inflow is of similar thickness across the three composites, and all composite groups have an inflow maximum situated at the RMW. Non-intensifying hurricanes are associated with stronger near-surface inflow outside the eyewall region, which implies more frictionally forced ascent out of the BL at radii outside the RMW. At greater radii, inflow layer  $\theta_e$  is relatively low in the WE composite, suggesting more local subsidence, downdrafts, and/or reduced sea-surface temperatures.

High-resolution numerical case studies of Hurricane Irma in 2017 and Hurricane Earl in 2010 are used to check results found in the composite analysis and highlight BL azimuthal structure. The Weather Research and Forecasting Model for Advanced Research (WRF-ARW) is employed for these full-physics simulations. Irma's strong tangential winds were relatively confined to the RMW, with weak  $I^2$  outside the eyewall. Aside from land interactions, Irma tended to steadily intensify, with an inflow maximum at the RMW and BL ascent isolated inward of the RMW. A brief WE period in Irma was associated with shear- and motion-induced asymmetry, whereby drier air was able to descend into the BL inflow near the RMW.

Hurricane Earl had a broader tangential wind field, with high  $I^2$  outside the RMW. Earl's strong BL inflow spread over a large radial band, which was associated with widespread BL convergence and shallow ascent outside the RMW. During a prolonged and progressive decay in Earl's inten-

sity, two regions of BL convergence became apparent: one inward of the RMW, and the other well outside the RMW. Descent of low-enthalpy air into the BL near the RMW also occurred during Earl's WE phases. Despite shear and storm motion of comparable magnitude to Irma, asymmetries were more pronounced in Earl's BL. Earl's decline in intensity was often associated with strong low-level outflow in the upshear-right quadrant, which may have led to kinematic and thermodynamic evolution that promoted the aforementioned region of BL convergence outside the RMW, as well as the formation of a secondary eyewall and coincident inner-eyewall collapse.

# CHAPTER 1

## INTRODUCTION

The atmospheric boundary layer (BL) describes a 1–2 km thick layer adjacent to the surface, where turbulent motions on small spatial and temporal scales thoroughly mix kinematic and thermodynamic properties in 3-D space (Kaimal and Finnigan 1994). A simplified schematic of the BL and its assumed structure under uniform flow in the free atmosphere is shown in Figure 1.1. Frictional forcing is integral to turbulent mixing in the BL, which becomes increasingly important with proximity to the Earth’s surface. In tropical cyclones (TCs), frictional dissipation of atmospheric momentum near the surface often occurs in concert with upward-positive fluxes of moisture, latent heat, and sensible heat across an air-sea interface. These fluxes provide potential for a TC to sustain or increase its strength despite the loss of momentum to frictional drag near the surface (Riehl 1954; Ooyama 1969). Maintenance of an organized TC has been explained via its similarity to a Carnot heat engine; whereby internal energy is modulated near the surface via air-sea fluxes, air is drawn toward the TC’s center in the BL, and then air ascends almost pseudoadiabatically from the top of the TCBL to the outflow layer in the upper troposphere (Emanuel 1986).

The apparent importance of air-sea and BL processes on TC structure and strength have not only drawn considerable interest in research, but also in the operational sector tasked with informing and protecting the life and property inhabiting the BL. Due to the warm-core structure of TCs, the most-intense winds in a TC are expected somewhere in the lower troposphere, sufficiently above the frictional sink of momentum at the surface [observations suggest that TCBL winds are maximized at 300–800 m above ground level (AGL) (Franklin et al. 2003; Powell et al. 2003)]. The atmospheric momentum lost to surface drag can be transferred to the ocean beneath the air-sea interface, contributing to wave generation and storm surge. Forecasters and researchers rely on TC observations to diagnose properties of a TC directly (and thus, the potential threat to society), but TC forecasting products intended for the public tend to depend heavily on numerical models.

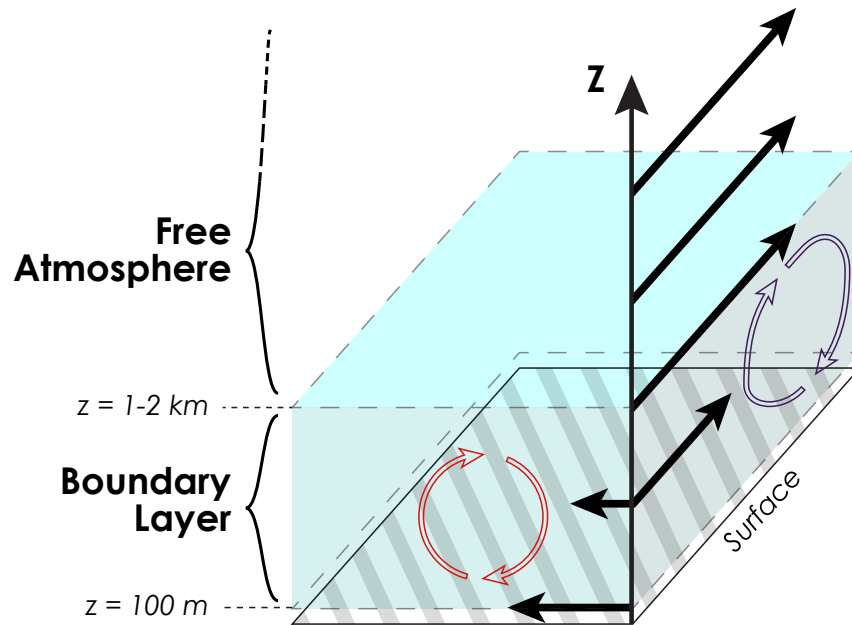


Figure 1.1: Schematic of the boundary layer (BL, shaded light blue) beneath the free atmosphere and above a surface layer. The free atmosphere extends upward from about 1–2 km above the surface, and the surface layer is assumed to be about 100 m thick. Associated with a uniform flow in the free atmosphere (diagonal black arrows above the BL), frictional dissipation in the BL leads to a reduction of momentum and turning of the wind with height (shown with leftward black arrows in the BL). Turbulent motions and horizontal vorticity associated with vertical shear (red and black arrows) mix kinematic and thermodynamic properties throughout the BL.

To reduce forecast errors, the interactions amongst the ocean, the TCBL, and the free atmosphere above the TCBL should be well-represented in TC simulations.

Perhaps unsurprisingly, TC simulations are sensitive to how turbulent processes and air-sea interactions are handled in a model (e.g., Braun and Tao 2000; Foster 2009; Nolan et al. 2009a,b; Smith and Thomsen 2010). Several TCBL modeling configurations were examined by Kepert (2010), highlighting a gamut of assumptions and simplifications assigned to the TCBL that yielded a wide range of results. The breadth of options and differing results illustrates the degree of uncertainty regarding how to handle the TCBL in a model. Determining an appropriate representation of the TCBL for numerical frameworks is reliant on our underlying theories, which could be amended through observational analyses. With a common goal to minimize error in TC track and intensity forecasting, collaborative efforts continue to advance our understanding of TCs and the TCBL

(e.g., DeMaria et al. 2005; Rogers et al. 2006; Black et al. 2007; Chen et al. 2007; Rogers et al. 2013b).

In situ observations in TCs have been collected during flight reconnaissance and research missions for decades, and missions still take place today for storm diagnosis, prognosis, and to further build upon existing TC databases. Doppler radars onboard reconnaissance aircraft sample TCs in three dimensions during flights, and these samples have been used to examine 3-D structures and processes in TCs (e.g., Marks and Houze 1987; Marks et al. 1992; Rogers et al. 2012, 2013a). Despite the ability of Doppler radar to observe wind and precipitation in 3-D space throughout a TC, the data is limited by smoothing and sampling difficulties below 500 m AGL. Doppler radars are also unable to measure many thermodynamic fields reliably (such as potential temperature). These caveats leave arguably critical gaps in the interpretation of TC structure. This is especially true for understanding TCBL structure in particular, where low-level stability and kinematics below 500 m are imperative.

Our ability to measure the TCBL directly is limited, as conditions close to the surface are hazardous to observers (in aircraft or otherwise). To examine the lower troposphere in TCs, reconnaissance missions have made use of global positioning system (GPS) dropwindsondes (dropsondes, sondes), which are released from aircraft to sample TCs as they descend from flight level to the surface (Hock and Franklin 1999). GPS dropsondes can capture accurate, high-resolution vertical profiles of kinematic *and* thermodynamic properties in TCs. Dropsondes have been used in missions flown by the National Oceanic and Atmospheric Administration (NOAA) since 1997, and also in missions conducted by the Air Force Reserve Command (AFRC) since 1998 (Franklin et al. 2003). Since the advent of the dropsonde, analyses using their data have uncovered descriptive structures of the TCBL: low-level tangential jets and supergradient flow (Franklin et al. 2003; Kepert 2006a,b; Bell and Montgomery 2008; Schwendike and Kepert 2008), strong vertical gradients of equivalent potential temperature adjacent to the ocean surface (Barnes 2008), and inconsistency between conventional definitions of BL height (Zhang et al. 2011). These dropsondes are still deployed in missions today, as technological advances lead to improved sampling capabilities.

Considering the observational discoveries and numerical improvements since the turn of the century, as well as the growth of computing power, TC track and intensity forecast errors might be expected to have decreased substantially over time. While errors in TC track seem to have improved since the early 1990s (as shown, for example, in 1–5 day Atlantic basin TC track error in Figure 1.2a), errors in forecasted TC intensity out to 3 days have seen less improvement<sup>1</sup> (Figure 1.2b). Assuming the predictability threshold for TCs has not already been reached (i.e., forecast errors can be realistically reduced further), it is convenient to surmise that the lack of error reduction in TC intensity forecasting reflects an incomplete understanding of TCs and/or deficient modeling frameworks.

The research in the following chapters focuses on the BL of hurricanes specifically—the structure, evolution, and associated physical processes of the hurricane BL that elucidate the two-way interaction between itself and the hurricane’s free atmosphere. The crux of this project is to investigate the hurricane BL during periods of intensity change (or lack thereof), where a storm intensifies, weakens, or remains steady-state. Specifically, a few key questions guide this multifaceted effort:

- Are there robust, observable features of the hurricane BL—kinematic or thermodynamic—associated with some or all phases of intensity change?
- Are observed signals in the hurricane BL explained through contemporary theories and prior research? If not, what signals demand further attention?
- Do full-physics numerical simulations convey observed characteristics of the hurricane BL through phases of intensity change?
- How do large-scale environmental conditions modify the hurricane BL and its role in intensity change?

First, a composite dataset using observations from GPS dropsondes launched since 1998 is built to analyze hurricane BL structure during different modes of intensity change. Second, a numerical simulation of Hurricane Irma in 2017 is completed to examine BL structure and evolution in a case of low environmental wind shear and persistent intensification. Third, the hurricane BL is

---

<sup>1</sup>For more information, see <http://www.nhc.noaa.gov/verification/verify5.shtml>

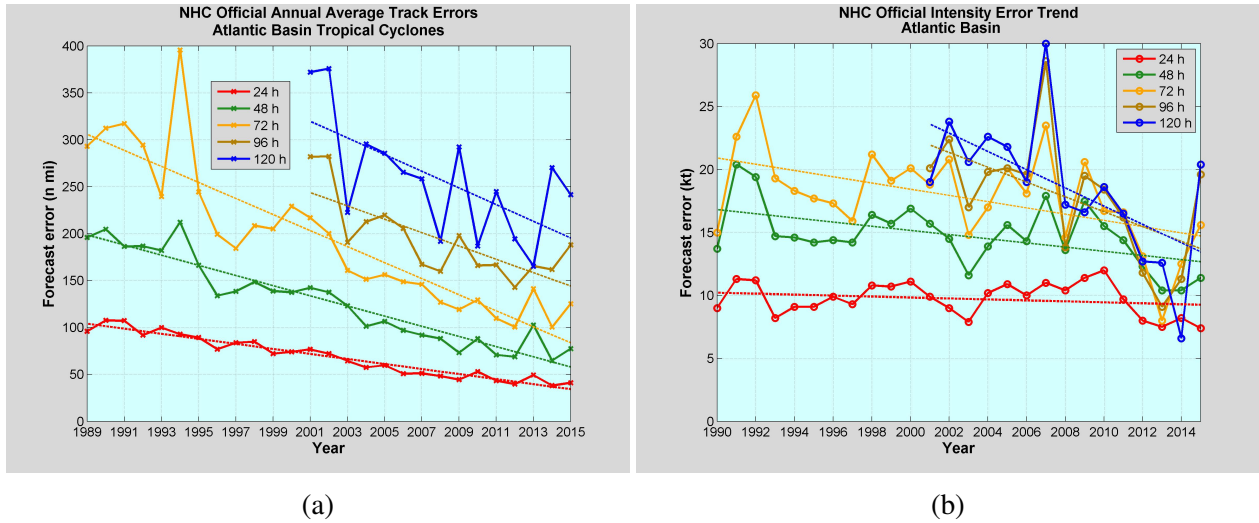


Figure 1.2: Annual average errors of (a) National Hurricane Center (NHC) official Atlantic basin TC forecast track for the period 1989–2015 in nautical miles (n mi), and (b) NHC official Atlantic basin TC forecast intensity for the period 1990–2015 in knots (kt). Line color defines the forecast hour. Dotted lines resemble least-squares trends. These images were gathered from the NHC Forecast Verification webpage (<http://www.nhc.noaa.gov/verification/verify5.shtml>), which contains further information and up-to-date figures.

investigated in a simulation of Hurricane Earl (2010), which was embedded in an environment with moderate shear and was associated with periods of weakening. The results of the simulations are compared against the findings of the composite analysis and prior work, highlighting signals in the simulations that might be specific to the case (and, thus, may not appear in a composite).

The next chapter contains an overview of prior research that motivates this work and provides a compendium of past results with which to compare. The observational composite is described and examined in Chapter 3. Chapters 4 and 5 detail the set-up and results of simulations for Hurricanes Irma (2017) and Earl (2010), respectively. A concluding discussion of the project’s findings is given in Chapter 6. All research in this project uses a particular (and apparently uncommon) transformation of geospatial data to TC-relative space; the appendix covers the background and details of the transformation.

# CHAPTER 2

## BACKGROUND

As discussed in the previous chapter, the atmospheric boundary layer is primarily associated with frictional and turbulent transport of momentum, heat, and moisture near the surface. Turbulent motions mix kinematic and thermodynamic properties vertically and horizontally throughout the BL, and the free atmosphere interacts with the BL in a two-way exchange. In tropical cyclones, these processes occur commonly over open water, so surface turbulent fluxes at the air-sea interface become a critical aspect of the TC dynamical makeup. For simplicity, the work undertaken here will focus on and refer to TCs that are situated over the water (unless explicitly stated otherwise).

This background will detail prior research and theory relevant to this topic, and also serves as the underlying motivation for this research in particular. To reduce the verbosity of this review, we will limit our coverage of previous TCBL studies to those that pertain directly to this research's motivation, findings, and interpretation. This chapter is not a full review of TCs or the TCBL. Past studies that present robust TCBL structures and features are described, and they are used in later chapters to compare with and corroborate our findings. Theories that describe the role of the TCBL are explained, with a focus on ideas that directly tie TCBL processes to TC structure and intensity.

### 2.1 Properties of the TCBL

#### 2.1.1 Agradient Forcing

The winds that comprise a TC's primary circulation are often called the TC's "swirling winds," following from the distinct appearance of the primary circulation in satellite imagery. The tangential wind  $v$  describes a TC's primary circulation. A set of cylindrical momentum and mass continuity equations can be applied to TCs with near-axisymmetric structures, with the origin of the coordinate system coincident with the TC center. Neglecting horizontal turbulent flux terms

and vertical components of Coriolis force, these equations are

$$\frac{Du}{Dt} - \left(f + \frac{v}{r}\right)v = -\frac{1}{\rho} \frac{\partial p}{\partial r} + \frac{\partial \overline{u'w'}}{\partial z}, \quad (2.1)$$

$$\frac{Dv}{Dt} + \left(f + \frac{v}{r}\right)u = -\frac{1}{r\rho} \frac{\partial p}{\partial \psi} + \frac{\partial \overline{v'w'}}{\partial z}, \quad (2.2)$$

$$\frac{Dw}{Dt} = -\frac{1}{\rho} \frac{\partial p}{\partial z} - g, \quad (2.3)$$

$$\frac{\partial \rho}{\partial t} + \frac{1}{r} \frac{\partial \rho r u}{\partial r} + \frac{1}{r} \frac{\partial \rho v}{\partial \psi} + \frac{\partial \rho w}{\partial z} = 0. \quad (2.4)$$

Table 2.1: Definitions of variables and terms used in Equations 2.2–2.4.

Symbol	Description	Symbol	Description
$r$	Radial position from storm center	$u$	Radial velocity
$\psi$	Azimuthal position	$v$	Tangential (azimuthal) velocity
$z$	Vertical position	$w$	Vertical velocity
$\rho$	Air density	$p$	Atmospheric pressure
$f$	Coriolis parameter	$g$	Acceleration of gravity
$\overline{u'w'}$	Vertical turbulent flux of $u$	$\overline{v'w'}$	Vertical turbulent flux of $v$
$t$	Time position		

Although  $\lambda$  and  $\psi$  are respectively used for azimuth and streamfunction by convention, we use  $\psi$  as the azimuthal coordinate to avoid confusion with longitude, which also uses  $\lambda$  by convention and is employed in Appendix A.

In TCs that exhibit axisymmetry, the free atmospheric primary circulation outside strong out-flow regions is often considered to be in approximate gradient wind balance (Chan and Kepert 2010). In other words, an axisymmetric TC's primary circulation in the absence of substantial frictional dissipation, advection of tangential momentum, local tendencies in tangential momentum, and viscous forcing is balanced by the pressure gradient force (PGF), Coriolis force, and centrifugal force. From Equation 2.1, gradient wind balance is derived as an equation quadratic in gradient wind speed  $V_{gr}$  by omitting Lagrangian acceleration of  $u$  and turbulent flux terms:

$$\frac{1}{\rho} \frac{\partial p}{\partial r} = fV_{gr} + \frac{V_{gr}^2}{r}. \quad (2.5)$$

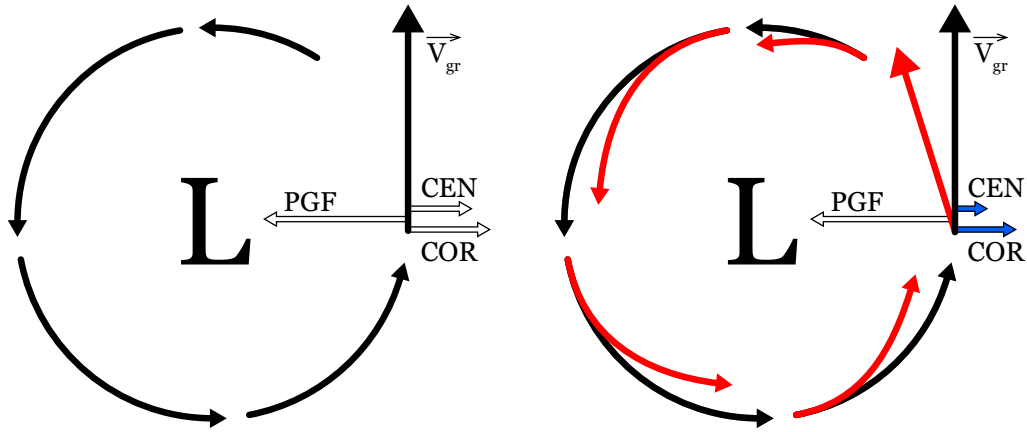


Figure 2.1: Schematics for horizontal flow associated with a common cyclone in gradient wind balance (left) and with negative gradient forcing (right) in the Northern Hemisphere, based on Figure 3.5 in Holton (2004). PGF, COR, CEN, and  $\vec{V}_{gr}$  represent the pressure gradient force, Coriolis force, centrifugal force, and gradient-balanced flow vector, respectively. Black vectors depict flow in gradient balance, whereas red vectors illustrate the otherwise-gradient flow after introducing frictional dissipation. In the left system, the combined effects of Coriolis deflection and centrifugal forcing balance the pressure gradient force. With friction introduced in the right system, the Coriolis and centrifugal terms are relatively reduced, inducing a net inward gradient forcing.

Schematically, this balance of forces is depicted in Figure 2.1 [adapted from an original figure in Holton (2004)]. The assumption of gradient balance is more justifiable outside of the TCBL (where friction, advection, and turbulence upset the balance) and outflow layer (where Lagrangian tendencies in  $u$  can be non-negligible). Willoughby (1990) used observations from several hurricanes to show that the mean axisymmetric hurricane core outside of a surface-adjacent frictional layer is often in near-gradient balance (see Figure 2.2).

Frictional processes in the TCBL lead to a reduction of atmospheric momentum that increases with proximity to the surface. If  $v$  immediately above the top of the TCBL is nearly in gradient wind balance, then it may be assumed that  $v$  in the TCBL would also be in near-gradient balance *if not for frictional drag and its consequences*. By adding a sink of momentum that originates at the surface, tangential winds are slowed, and gradient wind balance breaks down as contributions by Coriolis force and centrifugal force are reduced. Assuming the PGF shown in Figure 2.1 is unaffected, the frictional reduction of Coriolis and centrifugal forcing terms will induce a net

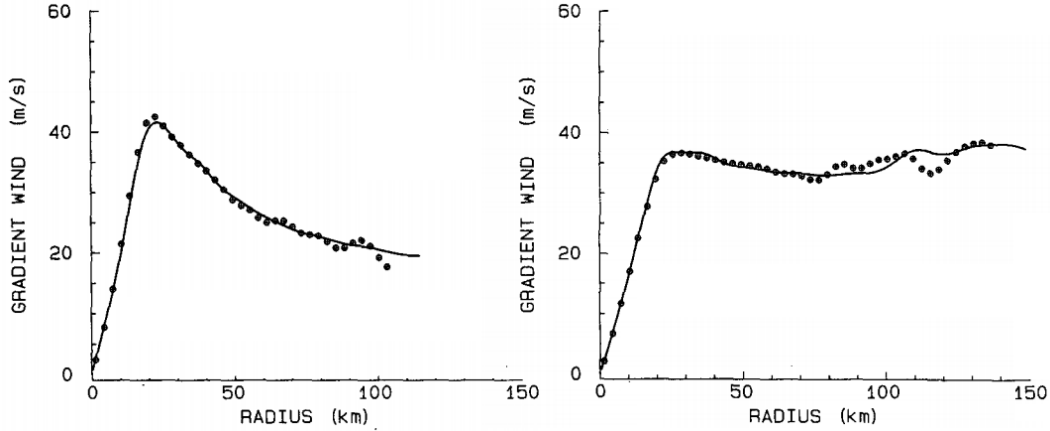


Figure 2.2: Observations of gradient wind balance in (left) rapidly intensifying Hurricane Diana (1984) during a reconnaissance flight from 0228–0903 UTC 11 September at 850 hPa, and (right) weakening Hurricane Gloria (1985) from 1422–2132 UTC 26 September at 700 hPa. Solid curves depict axisymmetrized tangential wind averaged over mission time, and individual marks are calculations of gradient wind. Figures are modified from Willoughby (1990).

forcing directed radially inward toward the center of the cyclone (regardless of hemisphere). This inward forcing evoked by surface drag is called an *agradient force* (AGF), and is defined as the sum of all forces in Equation 2.5 using  $v$  instead of  $V_{gr}$  (Smith et al. 2009):

$$AGF \equiv fv + \frac{v^2}{r} - \frac{1}{\rho} \frac{\partial p}{\partial r}. \quad (2.6)$$

Tangential flow is subgradient if  $AGF < 0$ , supergradient if  $AGF > 0$ , and exactly gradient if  $AGF = 0$ .

The agradient force due to loss of momentum promotes cross-isobaric flow in the TCBL. For air parcels moving closer to the surface where frictional dissipation is stronger, the AGF would be expected to increase in magnitude. This increase in AGF magnitude implies an increase in radial inflow. The frictional near-surface inflow (originating from a loss of tangential momentum) becomes part of a TC’s *secondary circulation*—a toroidal circulation comprised of radial and vertical flow, with an ascending branch at the TC eyewall, outflow extending from the top of the eyewall updraft, and forced subsidence in the central eye [depicted in Figure 2.3, originally from Willoughby (1988)].

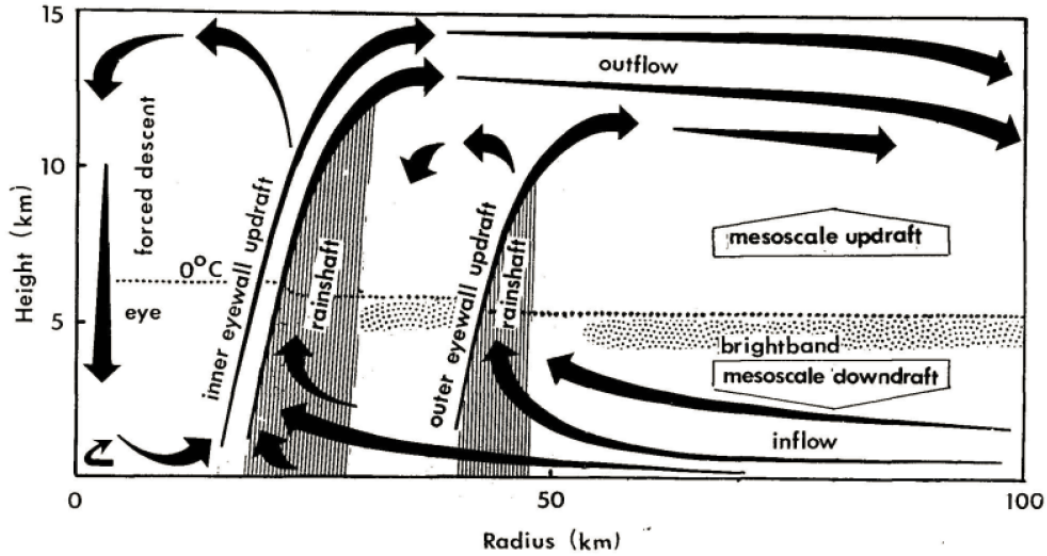


Figure 2.3: Schematic of the secondary circulation (on the  $r$ - $z$  plane) based on radar returns typically observed in the TC core. Heavy-shaded regions indicate rainshafts, situated radially outward of the inner and outer eyewall updrafts. The radar brightband demarcates frozen and liquid hydrometeors (i.e., the melting layer). Original figure in Willoughby (1988).

Figure 2.4 illustrates the lower-tropospheric circulatory properties of an axisymmetric, mature TC volumetrically. The free atmospheric flow above the BL is assumed to be in gradient-wind balance, and the BL flow is expected to be subgradient and directed radially inward. Air ascends out of the BL at the interior, and compensatory subsidence (i.e., via mass conservation) into the BL occurs at the exterior; the BL inflow, interior ascent, and exterior descent are the lower-tropospheric components of the TC's secondary circulation.

The TCBL's inflow has several direct consequences that affect a TC's kinematics and thermodynamics, including (Ooyama 1969):

1. Ascent out of the TCBL in the TC core radially inward of an inflow maximum (which could be abrupt if the inflow maximum is located close to the TC center, as is often the case);
2. Shallow, forced subsidence into the TCBL at radii outside of a radial inflow maximum; and
3. Inward advection of absolute angular momentum, which for inertially stable vortices (like TCs) should be positively oriented.

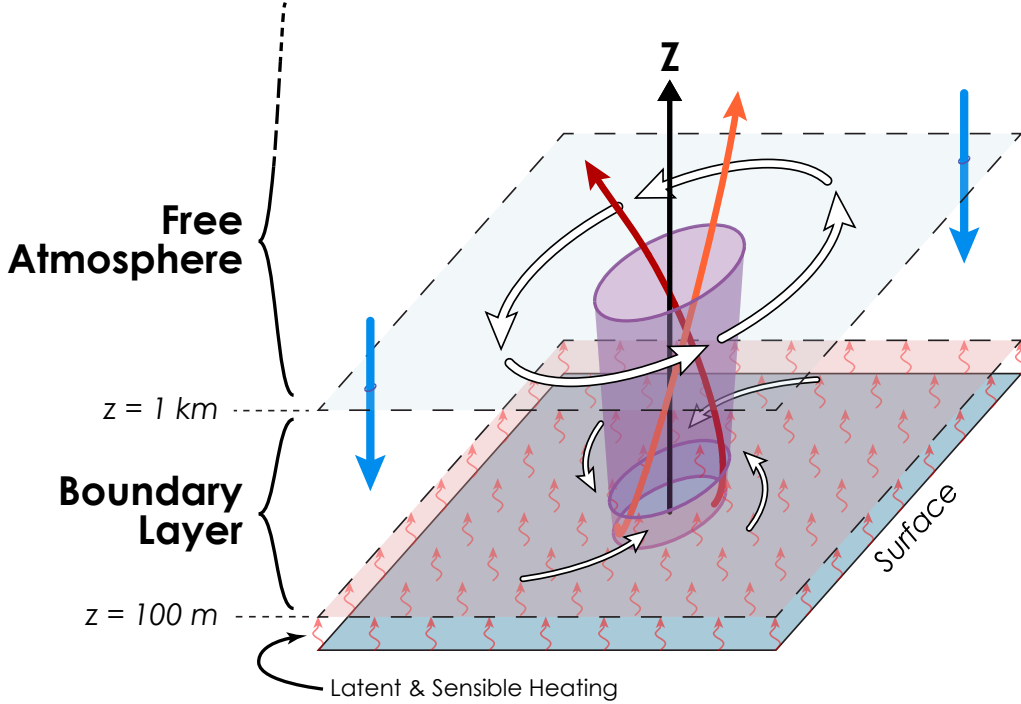


Figure 2.4: Simplified volumetric schematic depicting the low-level structure of an axisymmetric hurricane in the Northern Hemisphere. Horizontal flow (white arrows, magnitudes scaled by thickness) is gradient-balanced in the free atmosphere, and subgradient in the BL outside of the inner eyewall (purple wall). Vertical motions are drawn with bold, colored arrows (red/orange for ascent, blue for descent). Fluxes of latent and sensible heat (red wavy arrows) occur in a surface layer. Heights used to demarcate the free atmosphere, BL, and surface layer are used as reasonable examples, and they do not reflect strict definitions of the boundaries of those layers.

The vertical component of absolute angular momentum per unit mass is defined by

$$M_a = rv + \frac{1}{2}f_0r^2, \quad (2.7)$$

where  $f_0$  is the Coriolis parameter evaluated at the axis of rotation. By itself, positive advection of absolute angular momentum  $M_a$  toward a TC's axis of rotation should spin-up the primary circulation. However, the frictional torque exerted on the atmosphere by the surface destroys atmospheric  $M_a$ , supposedly at a rate that either exceeds or matches precisely the positive  $M_a$  tendencies by advection (e.g., Ooyama 1969, 1982; Kepert 2013). Thus, the frictional inflow has been hypothesized as being unable to amplify a TC's primary circulation directly. On the other hand, Smith et al. (2009) describe the possibility where convergence in the TCBL can cause

*supergradient* flow, which could allow spin-up of tangential winds as a result of frictional inflow. The role and implications of frictional inflow and  $M_a$  advection will be revisited in a forthcoming discussion of supergradient flow (subsection 2.1.3).

## 2.1.2 Transverse Circulation

The frictionally induced radial inflow of the TCBL transports high- $M_a$  air toward the central axis of a TC, but this import of high- $M_a$  air is countered by the loss of momentum due to friction (Ooyama 1969). Smith and Montgomery (2008) argued that earlier studies concluding the inward transport of high  $M_a$  is unable to spin-up a TC's primary circulation have employed balanced or overly simplified modeling frameworks, which is problematic for the naturally unbalanced dynamics of the TCBL. For instance, Ooyama (1969) used a system of linearized, axisymmetrized, and depth-averaged momentum equations for their three-layer TC model. However, simulations using more-relaxed assumptions (e.g., Kepert 2001; Kepert and Wang 2001) have also suggested that the positive inward advection of  $M_a$  in the TCBL is nearly balanced against  $M_a$  loss to frictional torque.

While TCBL inflow may be unable to spin-up a TC (in terms of intensity) via radial advection of  $M_a$ , the field of radial flow can determine areas where frictionally-forced ascent of air with relatively high moist static energy [and possibly, as posed by Smith et al. (2009), relatively high  $M_a$ ] out of the TCBL occurs. The radial convergence integrated through the depth of the TCBL is deterministic of the frictional updraft strength at the BL top (Kepert 2013). Observational and numerical evidence supports the notion that BL convergence favors localized deep ascent in the eyewall, rainbands, and elsewhere (Black et al. 1996; Hazelton et al. 2017b,a; Zhang et al. 2017). Kepert (2017) used a TCBL model to simulate the position of eyewall updrafts relative to the radius of maximum winds (RMW), finding that its displacement from the RMW is roughly regulated by the ratio of 10-m inflow to the square root of inertial stability ( $-u_{10}/I$ ). Because the location and strength of frictional updrafts at the top of the TCBL is linked with localized convection, the spatial distribution of TCBL convergence could have implications in TC intensity and structure (e.g., through regulating the spatial distribution of vertical advection of  $M_a$  or diabatic heating, further examined in subsections 2.1.3 and 2.2.2).

The general structure of the TCBL's transverse circulation has been captured in observational studies. Zhang et al. (2011) composited many GPS dropwindsondes launched in hurricanes over the Atlantic Ocean, and then examined the resulting azimuthally averaged structures of the TCBL. In their composite, the frictional inflow is maximized below 250 m AGL, underneath a peak in tangential wind speed coincident with the RMW. The location of the inflow maximum suggests the strongest radial convergence and frictional ascent out of the TCBL should usually be near or inside the RMW. The most-intense inflow penetrates through the RMW, bringing into focus the potential for inertial overshoot of air through the TC eyewall. The observed signals in Zhang et al. (2011) persist regardless of stratification of data by storm intensity (Figure 2.5). Dropsonde composites were used again by Zhang et al. (2013) to analyze TCBL asymmetric structure; the authors found that the storm quadrant downwind and to the right of the deep-layer shear (i.e., downshear-right or DSR) was associated with the deepest, most intense radial inflow. Rotating counter-clockwise from the DSR quadrant, the inflow layer becomes progressively shallow until a minimum depth (and inflow intensity) is observed in the upshear-right (USR) quadrant (Figure 2.6). Sitkowski and Barnes (2009) used a blend of GPS dropsondes, radar, and in situ data from flights in Hurricane Guillermo (1997) to investigate the storm's rapid intensification (RI), finding that the low-level inflow within a 100–200 km annulus became deeper and more axisymmetrized during the RI period. The inflow layer can become more or less asymmetric due to large-scale effects like

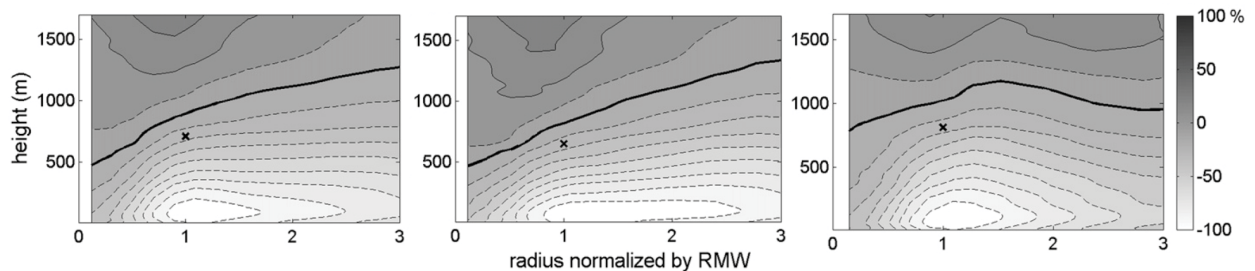


Figure 2.5: Azimuthally averaged dropsonde composite radial velocity fields, normalized by peak radial inflow values for (left) all hurricanes (peak inflow of  $20 \text{ m s}^{-1}$ ), (center) category 1–3 storms (peak inflow of  $17 \text{ m s}^{-1}$ ), and (right) category 4–5 storms (peak inflow of  $25.5 \text{ m s}^{-1}$ ). Negative values indicate inflow, and the contour interval is 10%. The thick black line is the “inflow layer height,” defined here as where inflow is 10% of the peak inflow. The  $\times$  symbol is the location of maximum tangential wind. Figure adapted from Zhang et al. (2011).

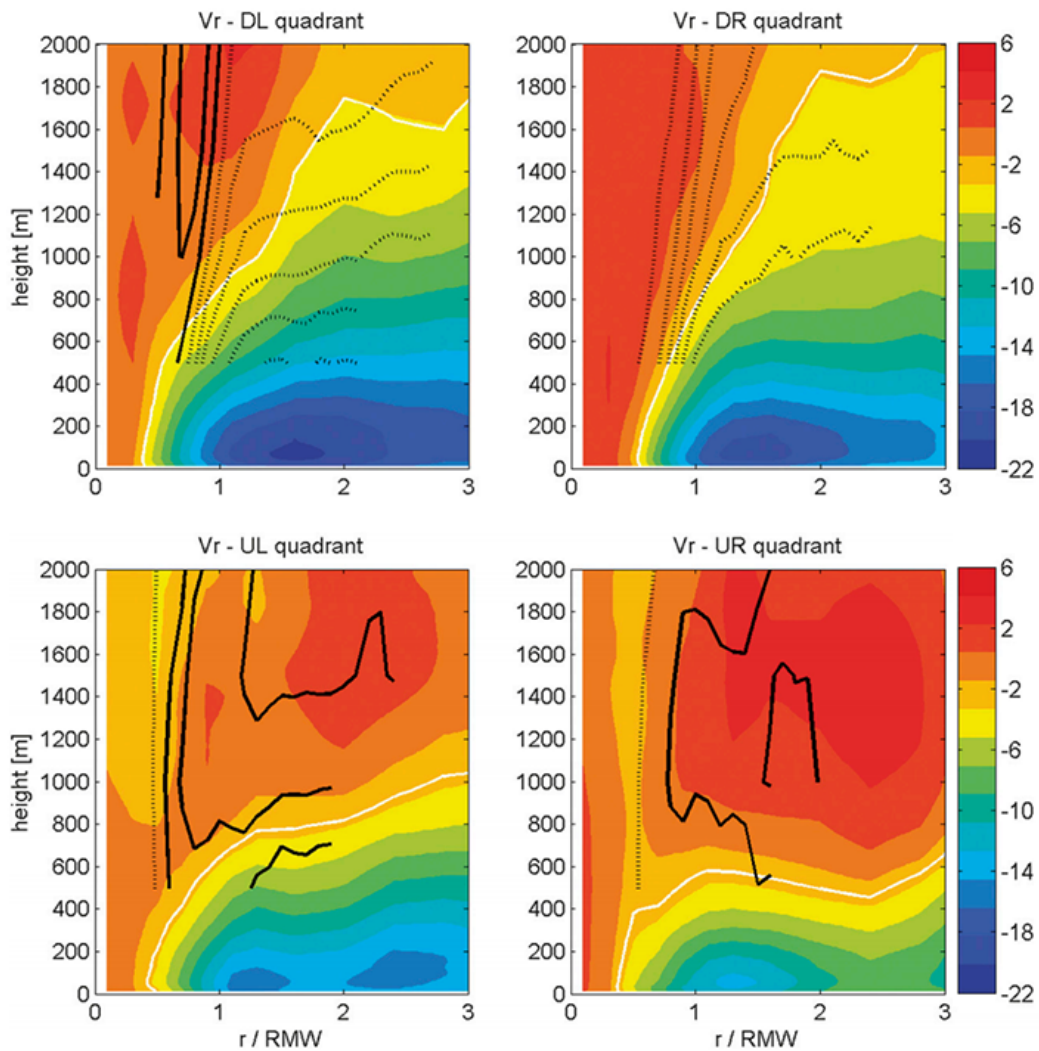


Figure 2.6: Normalized  $r$ - $z$  cross sections of GPS dropsonde composite radial velocity (shaded in  $\text{m s}^{-1}$ ), azimuthally averaged by deep-layer shear-relative quadrant (downshear-left, top-left panel; downshear-right, top-right panel; upshear-left, bottom-left panel; upshear-right, bottom-right panel). Radial distances are normalized by the radius of maximum winds (RMW). Negative values indicate inflow, and the white line represents the height of 10% peak inflow. Composite results using Doppler radar are shown in black contours (interval  $0.5 \text{ m s}^{-1}$ ), where solid and dotted lines indicate outflow and inflow, respectively. Figure adapted from Zhang et al. (2013).

storm motion, imposed environmental vertical shear, and proximity to land (Barnes and Dolling 2013).

While momentum loss due to friction in the TCBL induces the unbalanced flow oriented radially toward a TC's center that is aligned with the TC's secondary circulation, it is important to clarify that at least part of a TC's inflow in the lower troposphere is a result of processes outside of the BL. Additional sources of momentum in the upper troposphere (for example, due to particular interactions with synoptic-scale phenomena such as troughs) can enhance or suppress outflow, affecting the channel(s) through which air flows away from a TC's axis and possibly amplifying or weakening eyewall ascent (and consequently, impacting convergence in the lower troposphere beneath the region of ascent). Sources of heating (presumed to be latent heating) in the eyewall can amplify the ascending branch of the secondary circulation, thereby inciting low-level convergence (and to that effect, enhancing low-level inflow at radii beyond that of the ascending branch) and upper-level divergence. These processes that induce two counter-rotating transverse circulations (the second of which is the indirect circulation radially inward of the ascending branch, where air is forced to descend at the TC's central axis) are definitive of Sawyer-Eliassen dynamics (Schubert and Hack 1982; Holland and Merrill 1984; Smith et al. 2005; Pendergrass and Willoughby 2009). These dynamics provide some avenues through which the TCBL and TC free atmosphere communicate with one another, and illustrate the crucial interplay between a TC's primary and secondary circulations that helps regulate storm intensity.

### **2.1.3 Jets and Supergradient Flow**

The primary circulation of the TCBL has been observed in Doppler radar and GPS dropsonde data. A low-level tangential wind jet is consistently seen in hurricanes (Figure 2.7), located at 300–800 m AGL in the eyewall region, and at 1–2 km AGL at larger radii (Franklin et al. 2003; Knupp et al. 2006; Kepert 2006a,b). Assuming that the top of the frictional inflow layer roughly represents the TCBL top (Kepert 2001; Kepert and Wang 2001; Zhang et al. 2011), the tangential wind maximum is often located within (but near the top of) the TCBL. The total wind decreases near-logarithmically with decreasing height below the jet, due to the increasing impact of surface drag (Powell et al. 2003).

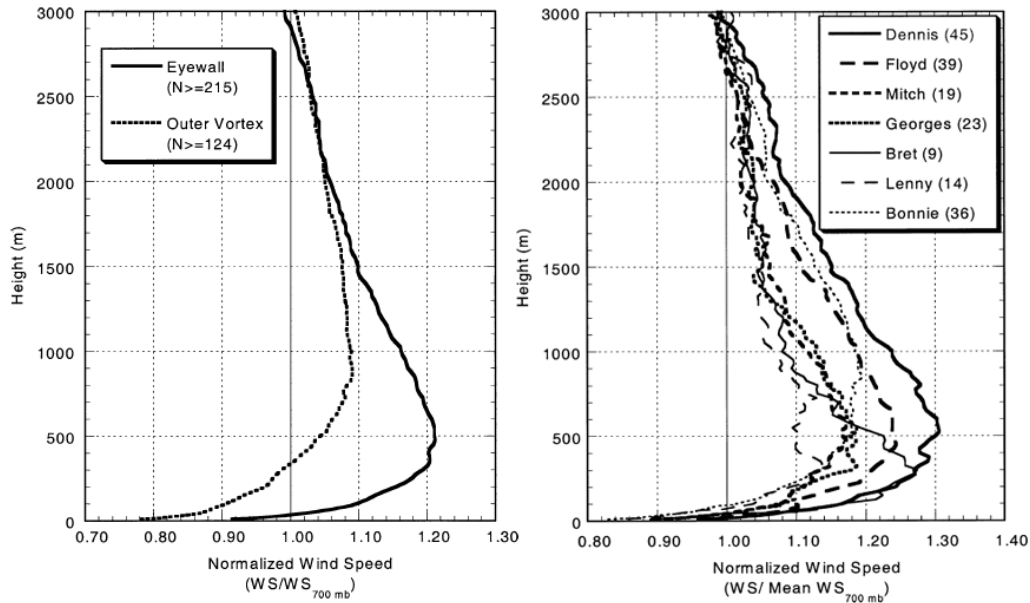


Figure 2.7: (left) Mean GPS dropwindsonde soundings of hurricane wind speed for eyewall (solid line) and outer-vortex (dashed line) regions, and (right) mean dropsonde profiles of eyewall mean wind speed profiles for seven individual hurricanes in 1998 and 1999. All wind speeds are normalized by the 700-hPa wind speed. The minimum number of soundings that represent data throughout each average profile is indicated in parentheses (a “minimum” number is used as the sampling frequency can vary with height). Figure adapted from Franklin et al. (2003).

Tangential flow near the wind jet in the TCBL has the potential to be *stronger* than the locally calculated gradient wind. These winds are considered to be “supergradient” and have been observed in the upper TCBL of some hurricanes (Kepert 2006a,b; Schwendike and Kepert 2008; Bell and Montgomery 2008). Figure 2.8 [modified from Kepert (2006a,b)] shows examples of observed supergradient wind in Hurricanes Georges (1998) and Mitch (1998). The degree to which TCBL winds are supergradient is linked to the radial profile of  $M_a$ —and thus the radial profile of tangential wind (Kepert 2001; Kepert and Wang 2001)—which could explain the difference in observed supergradient flow between the hurricanes depicted in Figure 2.8.

The “peakedness” of the radial profile of gradient wind at the top of the TCBL may determine the distribution and intensity of supergradient winds. Hurricanes with peaked wind profiles will have relatively weak radial gradients of  $M_a$ , and flat gradient wind profiles will have stronger radial

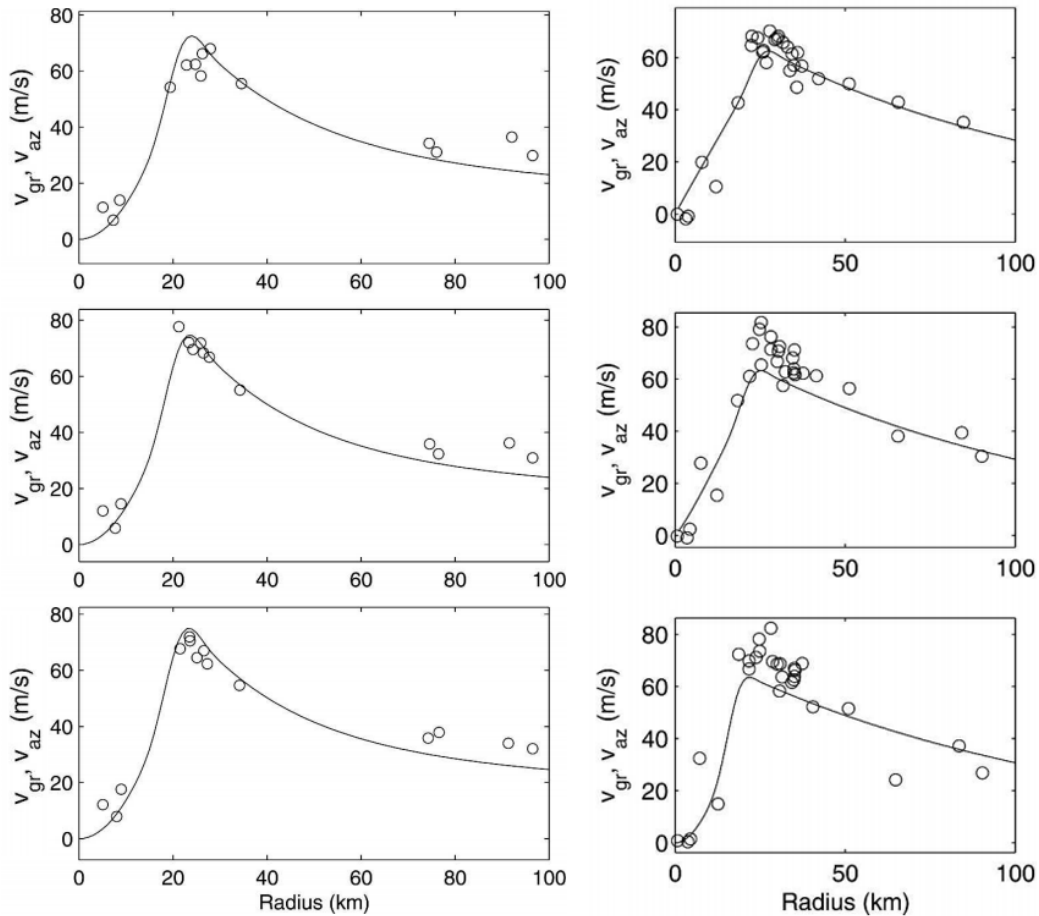


Figure 2.8: Radial profiles of observed tangential wind speeds from GPS dropwindsondes (open circles) and calculated gradient wind speed profiles (solid curves) in (left) Hurricane Georges (1998) and (right) Hurricane Mitch (1998). The top panels are use data at  $z = 2000$  m, while the middle and bottom panels represent data at  $z = 1000$  m and  $z = 500$  m, respectively. Open circles placed above the solid curve indicate supergradient wind speed measurements. Near an apparent radius of maximum winds, Hurricane Mitch is clearly associated with more supergradient winds than Hurricane Georges, which is arguably due to the radial profile of tangential wind speed and associated advection of absolute angular momentum. These figures are scaled together from Kepert (2006a,b).

gradients of  $M_a$ . This difference in  $\partial M_a / \partial r$  indicates a difference in inertial stability

$$I^2 = \frac{1}{r^3} \frac{\partial M_a^2}{\partial r}, \quad (2.8)$$

so storms with peaked profiles of gradient wind at the top of the TCBL will have lower inertial stability  $I^2$  outside the RMW than storms with flat wind profiles. Inertial stability represents resistance of air parcels to radial displacements. In turn, the difference in  $I^2$  allows storms with peaked wind profiles to have stronger inflow at and outside the RMW (i.e., inflow that is impeded less by  $I^2$ ), resulting in faster horizontal transport of  $M_a$  and stronger radial convergence near the highly inertially stable inner eyewall. Hurricanes with flat wind profiles should have weaker, more radially widespread convergence (both as a result of the frictional response to the tangential momentum at the top of the TCBL and the stronger  $I^2$  resisting radial flow).

The dynamics outlined above raise some key questions: Can the inflow be intense enough to import relatively high- $M_a$  air at a rate that overcomes the frictional dissipation of  $M_a$ ? If so, can air with an excess of  $M_a$  escape the frictional inflow via near-surface convergence and subsequent vertical motion before surface drag removes the excess, resulting in a net-positive contribution to  $M_a$  near the top of the TCBL (and, assumedly, supergradient flow via tangential spin-up)? Kepert (2006a,b) argues that, yes, the horizontal and vertical advection of  $M_a$  (and their relation to  $I^2$ ) can explain the difference between observed supergradient winds in Hurricanes Georges and Mitch in 1998—and the difference can ultimately be tied back to the radial profile of gradient wind near the top of the TCBL. In summary, peaked gradient wind profiles are linked to confined, strongly supergradient flow near the RMW the top of the TCBL; flat wind profiles are associated with broader, weakly supergradient flow.

Convergence of absolute angular momentum in the TCBL has also brought forth the question of whether it can spin-up a TC's primary circulation. As explained in subsections 2.1.1 and 2.1.2, radial advection of  $M_a$  in the TCBL is theorized to be unable to directly spin-up a TC due to the counteracting spin-down tendencies of frictional torque. However, Smith et al. (2009) and Smith and Montgomery (2016) posit that not only can TCBL convergence force ascent of inwardly flowing air with an excess of  $M_a$  (and result in supergradient flow), but that the development of supergradient flow by this process should lead to axisymmetric spin-up above the BL (i.e., TC spin-up could be explained as a *consequence* of  $M_a$  convergence, and TC spin-up can *originate* in the

TCBL). Ascent through the TCBL inside a TC's RMW would imply inflow across the RMW near the surface, which should import relatively high- $M_a$  into the RMW (and theoretically, the inflow may be deflected vertically by high  $I^2$ , allowing positive vertical advection of  $M_a$  inside the RMW and local tangential spin-up). On the other hand, ascent outside the TC's RMW suggests outflow tendencies across the RMW (due to the implied near-surface convergence outside the RMW), which would pull relatively low- $M_a$  air into the RMW (thus, inducing local spin-down there). The dynamics of the jet in the TCBL (and especially its role in TC intensity) is an open and hotly contested topic (Stern et al. 2015; Heng et al. 2017; Montgomery and Smith 2018; Montgomery et al. 2018).

#### 2.1.4 Thermodynamics

Given the importance of low-level atmospheric stability in convection and air-sea surface turbulent fluxes in TC energetics, thermodynamic properties of the TCBL cannot be ignored. In case studies of the quite intense Hurricane Isabel (2003), Montgomery et al. (2006b) and Bell and Montgomery (2008) examined low-level thermodynamic structure using a mix of flight-level and GPS dropsonde data. The azimuthally averaged inner-core structure of Hurricane Isabel exhibited a generally negative radial differential of equivalent potential temperature  $\theta_e$  (i.e.,  $\partial\theta_e/\partial r < 0$ )—especially in the region between the RMW and the eye (Figure 2.9). Parcels in the strong near-surface inflow have the potential to overshoot the high inertial stability of the eyewall (as was seen in Hurricane Isabel), thereby entering the relatively high- $\theta_e$  eye region. Parcels in the eye can then mix horizontally with the encapsulating eyewall after increasing their  $\theta_e$ , providing an avenue by which buoyancy can be added to eyewall convection (and, by consequence of an amplified ascending branch of the secondary circulation, a spin-up of the mean tangential wind field).

Barnes (2008) analyzed boundary layer thermodynamic profiles captured from dropsondes launched in Hurricanes Bonnie (1998), Mitch (1998), and Humberto (2001). Properties unique to the hurricane BL were found in the dropsonde soundings—example soundings from their work are shown in Figure 2.10. First, the thermodynamic profiles near the top of the low-level inflow layer revealed a generally positive vertical differential of  $\theta_e$ . Barnes states that within 100–200 km of the hurricane center, inflowing air parcels with relatively low  $\theta_e$  can undercut rotational air

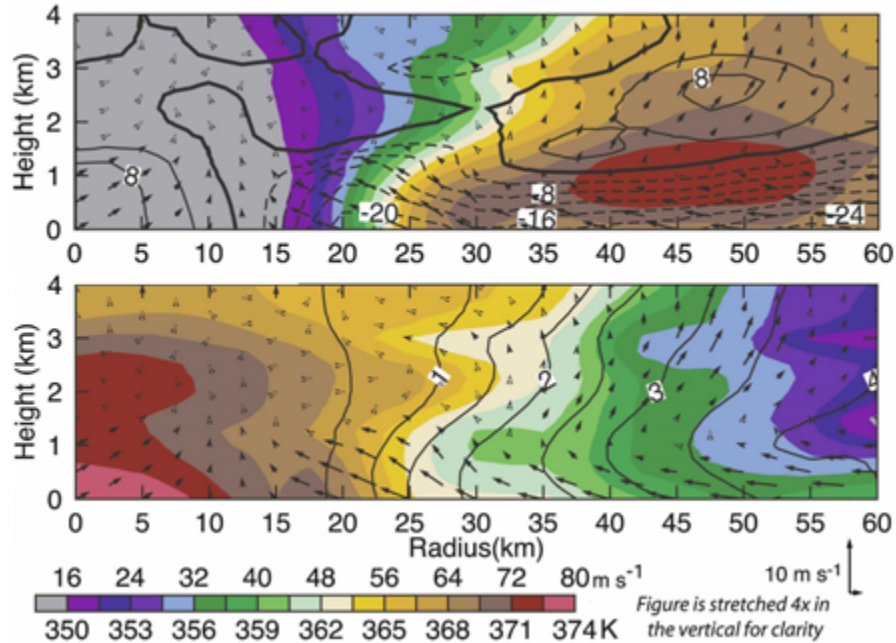


Figure 2.9: (top) Radius-height cross sections of axisymmetrized storm-relative (top) tangential velocity (shaded,  $\text{m s}^{-1}$ ) and radial velocity (contour,  $\text{m s}^{-1}$ ) from observations in Hurricane Isabel. (bottom) Axisymmetrized equivalent potential temperature  $\theta_e$  (shaded, K) and absolute angular momentum  $M_a$  (contour,  $\text{m}^2 \text{s}^{-1} \times 10^6$ ) from the same case. Both panels depict the transverse secondary circulation with vectors ( $\text{m s}^{-1}$ ; see legend at bottom-right of figure). All data are derived from a blend of GPS dropwindsonde and flight-level data on 13 September 2003 in Hurricane Isabel. Figure adapted from Bell and Montgomery (2008).

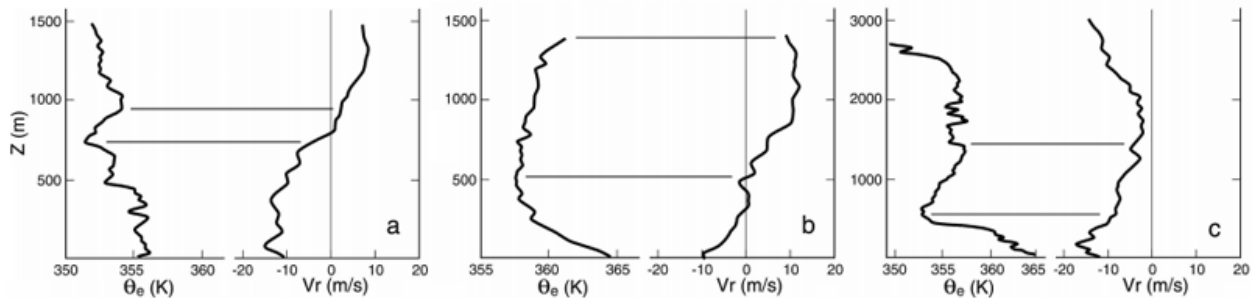


Figure 2.10: Three GPS dropwindsonde vertical profiles of equivalent potential temperature  $\theta_e$  (in K, left-side profile in each panel) and storm-relative radial velocity (in  $\text{m s}^{-1}$ , right-side profile in each panel) from Hurricane Bonnie (1998). Negative radial velocities indicate inflow. Horizontal lines between dual-sounding plots delineate distinct layers where  $\theta_e$  increases with height. Figure adapted from Barnes (2008).

that has been in close proximity with the high- $\theta_e$  eyewall over time, thereby establishing the layer where  $\partial\theta_e/\partial z > 0$  near the top of the inflow. The aforementioned layer may insulate the undercutting inflow—where positive upward fluxes of heat and moisture from the air-sea interface may transpire—from loss or dilution of entropy via entrainment or subsidence into the inflow. Second, the soundings showed a sharp decrease of  $\theta_e$  with height and near-superadiabatic conditions in a  $\sim 100$ -m deep surface layer. Barnes hypothesizes that water loading from sea spray and a subsequent increase of parcel residence time in the surface layer explains this result. Third, moist absolutely unstable layers [MAULs, described by Bryan and Fritsch (2000)] were sometimes observed adjacent to the eyewall, in convective rainbands, and within hub clouds [low-level stratocumulus (Simpson and Starrett 1955; Schubert et al. 2007)] in the center of the hurricane eye.

The axisymmetric thermodynamic structure of the TCBL was investigated in Zhang et al. (2011) using their dropsonde composite. Surfaces of constant virtual potential temperature  $\theta_v$  were shown to slope upward gently with increasing radius, with  $\theta_v$  generally increasing with height. Their results suggest considerable dry static stability near the top of the inflow layer, and often statically stable conditions throughout. An exception to this property is observed below 200 m AGL in some areas, where the vertical gradient of  $\theta_v$  becomes nearly zero (neutral) or negative (unstable). Kepert et al. (2016) used the axisymmetric CM1 model (Bryan and Rotunno 2009) to probe the processes behind the TCBL’s observed dry thermodynamic structure (and in particular, the dry static stability at the top of the inflow layer). They concluded that the observed dry static stability at the inflow layer top is primarily a result of two processes:

1. Diabatic heating and cooling associated with condensation of moist air above the inflow and evaporating rainfall within the inflow, respectively; and
2. Differential horizontal advection of potential temperature  $\theta$ , where inward advection of relatively low- $\theta$  air is maximized near the surface (coincident with maximized inflow) and weakens or reverses sign with height (as the inflow weakens or reverses orientation with height).

These two processes promote  $\partial\theta/\partial z > 0$  above the height of maximum radial inflow (suggested to be around 100 m AGL). The near-superadiabatic conditions observed below the maximized inflow

could be partially due to weakening low- $\theta$  advection (a result of decreasing inflow with decreasing height between 0–100 m AGL).

Zhang et al. (2013) expanded their original composite of dropsondes to analyze shear-relative asymmetric structure in the inner-core TCBL. The near-surface  $\theta_e$  field was maximized in the downshear-right quadrant (DSR), and minimized in the upshear-left quadrant (USL). The authors surmise that the observed asymmetry of near-surface  $\theta_e$  is related to asymmetric patterns of TC convection (Black et al. 2002; Corbosiero and Molinari 2002, 2003; Chen et al. 2006; Reasor et al. 2013; DeHart et al. 2014; Hazelton et al. 2017a; Nguyen et al. 2017). In this framework, convection is assumed to initiate between the DSR and DSL quadrants where BL inflow is maximized (Figure 2.6), and downdrafts carrying low- $\theta_e$  air form downstream (rotating counter-clockwise in the Northern Hemisphere) in the USL quadrant. Air parcels in the TCBL may recover their enthalpy through air-sea fluxes as they rotate through the USL and USR quadrants (where integrated inflow and thus radial convergence is minimized), before reaching a  $\theta_e$  maximum in the DSR quadrant where convection can initiate again, thus completing a cyclical process. Observational evidence shown in Hense and Houze (2011), Reasor et al. (2013), and DeHart et al. (2014) corroborate the pattern of vertical motion described by Zhang et al. (2013).

In comparison to the breadth of analysis of TCBL kinematics, the amount of information and theory explaining TCBL thermodynamics is relatively limited. A key reason for this is the difficulty in volumetrically sampling the TCBL's thermodynamic fields. For example, Doppler radar can reliably sample winds through 3-D space, but not temperature or moisture. Dropsondes can measure thermodynamic fields as they fall from reconnaissance aircraft, but only along their trajectory (and thus, they can only instantaneously sample at one point in space). Regardless, it would be neglectful to dismiss the effects of thermodynamics in a TC. At least, the processes of acquisition and distribution of heat and moisture throughout the frictional boundary layer should remain in focus for future research. The studies described herein sometimes attempt to connect TCBL kinematics and thermodynamics (Montgomery et al. 2006b; Barnes 2008; Zhang et al. 2013), but coupling both aspects of the TCBL cogently proves difficult.

## 2.2 TC Maintenance and Intensification

As previously discussed, the effects of surface drag deplete a TC's momentum, which is transferred to the ocean below. Despite the surface acting as a sink of momentum that directly spins down a TC, the boundary layer could serve to amplify a TC's circulation through direct or indirect means. The import of high-entropy air by BL inflow can modulate a TC's warm-core structure and associated wind field through their relationship to the pressure gradient force. Additionally, convection can generate diabatic heating and vertical vorticity that lead to changes in vortex structure and intensity.

### 2.2.1 Air-sea Interaction

Riehl (1954) suggested that latent and sensible heat fluxes from the ocean are imperative to consider in TC theory. Emanuel (1986) theorized that latent and sensible heat fluxes induced through the TC's own wind field modulate exclusively the maintenance of mature steady-state TCs. As an analog to the classical Carnot heat engine, heat is extracted from the underlying ocean in horizontal inflow, and then ascends slantwise along a moist-neutral thermodynamic profile from the top of the BL to the height of TC outflow where heat is given off amongst much lower surrounding temperatures. The efficiency of this TC engine is expressed as a function of the difference between temperature at the BL top and the outflow temperature (near the periphery between the troposphere and stratosphere for mature TCs). The production of energy associated with the engine counters energy lost via friction and downdraft mixing in the boundary layer. This theory of wind-induced surface heat exchange [termed WISHE by Yano and Emanuel (1991)] is unique in that the convective branch of the secondary circulation merely redistributes heat acquired from the ocean—it does not intensify the TC directly through conversion of convective available potential energy (CAPE) to kinetic energy.

While the details of air-sea exchange processes are quite important to the inner workings of a TC, such details are particularly difficult to examine with observations. Powell et al. (2003) and Donelan et al. (2004) used observational data and laboratory experiments to study the effects of high wind speeds on the surface roughness of water for the purpose of improving our understanding of air-sea interactions in TCs. Both studies concluded that the bulk surface drag coefficient should

not increase at a linear or persistent rate with increasing near-surface wind speed. Using dropsonde data, Powell et al. (2003) reported that surface stress (and the associated surface drag coefficient  $C_D$ ) *decreases* with increasing wind speed when the wind speed is in excess of  $40 \text{ m s}^{-1}$ . Laboratory results from Donelan et al. (2004) echo the observational findings of Powell et al. (2003), suggesting that the properties of high velocity flow (wind speeds exceeding  $33 \text{ m s}^{-1}$ ) are different such that aerodynamic roughness over water becomes “saturated.” The Coupled Boundary Layer Air-Sea Transfer (CBLAST) experiment included a focus on air-sea interactions in hurricanes (Black et al. 2007). The CBLAST project corroborated the tendencies found in Powell et al. (2003) and Donelan et al. (2004), although the drag coefficient was suggested to level off at much weaker near-surface wind speeds of  $22\text{--}23 \text{ m s}^{-1}$ . Zhang et al. (2008) analyzed CBLAST measurements of enthalpy flux in the TCBL, finding no significant dependence of the enthalpy exchange coefficient  $C_k$  on wind speed up to  $30 \text{ m s}^{-1}$ . Theoretical and numerical evidence has implied that hurricane intensity is strongly dependent on the ratio of  $C_k$  to  $C_D$ , but the results of Zhang et al. (2008) suggest that the observed ratio is significantly below the lowest threshold necessary for development. Sea spray and lateral fluxes from the TC warm core were cited as possible contributors to TCBL enthalpy that could erode the deficit in enthalpy flux implied by their observations of  $C_k$ .

The contrasting effects of surface drag and enthalpy transfer at the air-sea interface have been highlighted in studies assuming unbalanced hurricane BL dynamics (i.e., not assuming gradient wind balance). Montgomery et al. (2010) tested the sensitivity of TC behavior to  $C_D$  in 3-D model simulations without imposing gradient wind balance. For a regime of small to moderate values of  $C_D$ , TC intensity can increase in tandem with increasing  $C_D$  due to gradient wind imbalance and the enhanced BL inflow therefrom. However, Bryan (2012) argued that the simulations of Montgomery et al. (2010) did not integrate far enough forward in time to reach a quasi-steady state, so their results may not be necessarily valid in comparisons to steady-state theories [e.g., intensity-related theories posed in Emanuel (1986) and Emanuel (1995)]. Smith et al. (2014) revisited questions regarding the roles of  $C_D$  and  $C_k$  in TC simulations, and found that increasing or decreasing wind speed-dependent  $C_D$  by a factor of 2 yields reduced maximum tangential winds. Their result implied that there exists an optimal bulk surface drag coefficient for simulating maximized TC intensity. The non-linear nature of TC intensity’s dependence on  $C_D$  is arguably due

to two competing factors: the advection of high- $M_a$  air by frictional inflow that represents spin-up potential, and the direct loss of  $M_a$  to friction that acts as the key spin-down process. Zhang and Emanuel (2016) investigated the effects of enforcing a wind speed cap on calculations of enthalpy flux in TCs (i.e., imposing an upper-limit to wind speeds used in flux calculations); their research showed that this restriction on enthalpy flux tends to reduce simulated maximum wind speed in idealized and real-world hurricane simulations.

Due to the difficulty in fully understanding the competing processes of frictional dissipation and enthalpy flux, a complete theory that describes how air-sea interactions affect TCs and their boundary layers remains elusive. Numerical studies continue to test the effects of  $C_D$  and  $C_k$  (and other representations of frictional drag and enthalpy flux) on TC intensity and structure.

### **2.2.2 Convection, Heating, and Vorticity Conversion**

Convection can generate vertical vorticity perturbations on the scale of convection, whether it be induced via frictional convergence or other mechanisms. Vertical motions can stretch pre-existing vertical vorticity, tilt horizontal vorticity (i.e., shear vorticity) to align with and become vertical vorticity, and baroclinicity. Strong vertical wind shear near the surface in the TCBL acts as a source of vorticity that can be oriented into the vertical direction via convection. Convection-generated vertical vorticity becomes embedded with a TC's background swirling wind field, which can enhance tangential flow.

Black et al. (1996) derived vertical motion fields from airborne Doppler radar data, finding the broadest and narrowest distributions of vertical motion in the eyewall and stratiform rain regions, respectively. Slightly negative mean vertical motions are observed in the stratiform region below 3 km AGL. Updrafts are more frequently seen in the eyewall than in rainbands and stratiform rain. While the swaths of vertical velocity associated with rainbands contribute more to the net vertical mass flux than the eyewall, other research has noted that the *locations* of vertical motions are important to the maintenance and evolution of TCs. Shapiro and Willoughby (1982) added sources of heat as a proxy for convection to simulated hurricane-like vortices, demonstrating that vortex intensification would occur only if heat sources were placed sufficiently close to the RMW. Pendergrass and Willoughby (2009) and Vigh and Schubert (2009) reverberate the important role

of position in diabatic heating, while adding that TC strength and structure also bear roles in vortex intensification [Rogers et al. (2013a) confirmed these conclusions in their observational analysis of steady-state and intensifying hurricanes using Doppler radar data].

Other numerical studies by Nolan and Montgomery (2002), Nolan and Grasso (2003), and Nolan et al. (2007) have examined vortex responses to asymmetrically distributed heating, concluding that vortex intensification is approximately a symmetric response to the azimuthally averaged heating; asymmetric modes of heating almost always led to a spin-down of the azimuthally averaged vortex. In contrast, vortex simulations that added perturbations of vertical vorticity in lieu of heating sources (e.g., Montgomery and Kallenbach 1997; Möller and Montgomery 2000; Shapiro 2000) have led to vortex intensification. These vorticity-perturbed model results imply that the consequences of asymmetric convection (presumably vertical vorticity generation, hence the alternative use of vorticity perturbations) can induce vortex spin-up via axisymmetrization of convectively generated potential vorticity near the RMW by vortex Rossby waves (Montgomery and Kallenbach 1997). Krishnamurti et al. (2005) used trajectories to track  $M_a$  of air parcels as they traveled inward toward a hurricane's center, concluding that the eventual  $M_a$  of air as it approached the center seemed to determine the storm's intensity.

In mature TCs with an organized inner core, the transfer of air in the calm TC eye into the ascending branch of the eyewall can affect vortex dynamics. Persing and Montgomery (2003) focused on eye-eyewall interactions in their paper outlining how hurricanes could become more intense than the theoretical upper-bound of intensity for steady-state axisymmetric hurricanes (maximum potential intensity, or MPI) proposed by Emanuel (1986). A hurricane's near-surface inflow has the potential to overshoot through the eyewall and into the high-entropy eye. Inwardly flowing air parcels that overshoot into the hurricane's eye can then increase their equivalent potential temperature  $\theta_e$  via air-sea heat fluxes and mixing with the high-entropy air in the eye, all before returning to the encompassing eyewall in low-level outflow. This mechanism can add internal energy and buoyancy to a hurricane's eyewall, amplifying eyewall convection and thereby affecting the secondary circulation and warm-core structure to sustain a stronger vortex at steady-state (Shapiro and Willoughby 1982). Superintensity was revisited in the observational analysis of Hurricane Isabel (2003) by Montgomery et al. (2006b), which found a strong radial gradient of tangential

velocity across the inner eyewall, indicating a potential for Kelvin-Helmholtz instability and lateral mixing between the eyewall and eye (they corroborated these findings using radar and satellite imagery). For the period highlighted, Isabel's inflow below 1 km AGL also extended across the diagnosed eyewall, suggesting an overshoot of air into the hurricane's eye.

Deep and localized convective cores [hot towers (HTs), or *vortical* hot towers (VHTs) if accompanied by rotation] have been observed in some TCs, and are usually studied in the context of tropical cyclogenesis and intensification (e.g., Hendricks et al. 2004; Montgomery et al. 2006a; Nolan et al. 2007). Hot towers in TCs have been found to add a potentially significant amount of vertical vorticity to the background mean vortex (Reasor et al. 2005; Montgomery et al. 2006a; Houze et al. 2009). In an analysis of Hurricane Dennis (2005), Guimond et al. (2010) studied the effects of HTs on Dennis' rapid intensification, reporting that the strengthening of the hurricane's warm core and axisymmetrization of the vortex was possibly due to vortex Rossby wave dynamics (Montgomery and Kallenbach 1997) following an outbreak of HTs and deep convection.

The mechanisms outlined in this subsection supposedly have substantial implications for TC intensity and structure; while these mechanisms may not necessarily take place *within* the TCBL, most of them involve TCBL properties or processes to some degree. Subsection 2.1.2 explained that a TC's frictionally induced transverse circulation may not directly initiate or deepen strong convection, but the field of radial convergence associated with the frictional inflow can determine where deep convection is more or less likely to occur. The spatial distribution of convection in a TC is likely critical to TC intensity and structure. In addition, strong BL inflow can extend through the highly inertially stable inner core of mature TCs, leading to eye-eyewall interactions that directly affect the ascending branch of the secondary circulation. The import of high- $M_a$  air into the eye by overshooting inflow may also have consequences in the eye (Emanuel 1997). This section motivates the research described in the forthcoming chapters, and the importance of examining and analyzing 3-D TCBL kinematics and thermodynamics in the context of TC maintenance and evolution.

# CHAPTER 3

## OBSERVATIONAL COMPOSITE OF THE HURRICANE BOUNDARY LAYER

We used an observational approach to analyze the TCBL directly. Observations are composited and framed such that they represent TCs undergoing particular modes of intensity change. Here, we focus specifically on hurricane-strength TCs situated over water, as we are concerned most with intensity change in storms beyond a state of cyclogenesis—the dynamics regulating intensity in an under-developed TC are quite different than those in a mature hurricane. The observational composite provides a broad depiction of the mean, azimuthally averaged hurricane BL as hurricanes undergo changes (or stagnation) in intensity. The methodological background, results, and interpretation are detailed below.

### 3.1 Methodology

#### 3.1.1 Data

Observational data are collected from GPS dropwindsondes, which act as the central element of this composite analysis. These dropsondes were developed by the National Center for Atmospheric Research (NCAR), and have been deployed from aircraft in TC reconnaissance and research missions since 1998 (Hock and Franklin 1999). At a nominal sampling rate of 2 Hz and a near-surface fall speed of 11–12 m s<sup>-1</sup>, these dropsondes yield Lagrangian profiles of kinematic and thermodynamic variables with a vertical resolution of about 5 m (Franklin et al. 2003, hereafter F03). Each sample along a dropsonde’s trajectory can provide measurements of location, pressure, air temperature, relative humidity, wind direction and speed, vertical velocity of the instrument, and geopotential altitude. The estimated typical errors associated with NCAR dropsondes are 1 hPa for pressure, 0.2 °C for temperature, < 5% for relative humidity, and 0.5–2.0 m s<sup>-1</sup> for wind speed.

A detailed background and assessment of NCAR dropsondes can be found in Hock and Franklin (1999).

The GPS dropsondes used for this study were collected directly from the Hurricane Research Division (HRD) storm pages archives<sup>1</sup>; all dropsonde data from Atlantic hurricanes between 1998 and 2015 are considered initially for compositing the inner-core structure of the hurricane BL. Initial processing and quality control is performed for the data using NCAR's Atmospheric Sounding Processing Environment program (ASPEN-QC)<sup>2</sup>. In total, 12,045 individual dropsondes were processed in ASPEN-QC, but not all soundings were used in this study due to further data filtering in the compositing technique. To our knowledge, we have considered all available Atlantic dropsonde data from missions between 1998 and 2015 that reported surface wind data using a stepped frequency microwave radiometer (SFMR; Uhlhorn and Black 2003; Uhlhorn et al. 2007; Klotz and Uhlhorn 2014), which are required in the compositing technique for establishing the composites' radial coordinate.

### 3.1.2 Compositing Technique

All dropsonde data are reviewed to ensure that they are suitable for our analysis. Dropsonde data from TC reconnaissance and research are considered eligible for compositing if, at the time of observation,

- The dropsonde and the subject storm's center were located over water,
- The storm was tropical and of hurricane intensity, and
- All required auxiliary data for sorting and positioning (e.g., surface wind data from SFMR) are available.

The center of a TC is defined via linear interpolation between 2-minute storm track data, which were created from a fit of flight-level wind center fixes (Willoughby and Chelmon 1982). If a dropsonde or the subject TC's center were located over land at any time during the dropsonde's flight, the dropsonde is omitted from compositing and analysis. A spatial mask representing land

---

<sup>1</sup> Accessed via [http://www.aoml.noaa.gov/hrd/data\\_sub/hurr.html](http://www.aoml.noaa.gov/hrd/data_sub/hurr.html)

<sup>2</sup> Accessed via <https://www.eol.ucar.edu/software/aspn>

and non-land points is taken from ERA-interim (Dee et al. 2011) to carry out this check for contamination by land—the coarse grid is used to more aggressively filter out observations near or over land. To determine if a sampled storm was both tropical and of hurricane intensity, we use the revised Atlantic hurricane database (HURDAT2; Landsea and Franklin 2013). The HURDAT2 database gives “status of system” information (e.g., a system can be tropical, extratropical, etc.) and estimates of maximum sustained winds  $V_{max}$  (interchangeable with intensity), often on a 6-hourly interval. Every dropsonde measurement occurs between two HURDAT2 records in time; if either of these two HURDAT2 records indicate that the sampled storm was not tropical, or if both records suggest that the storm was not of hurricane intensity ( $V_{max} > 64$  kt), then the sample is ineligible for compositing.

After ineligible data have been removed from the initial group of 12,045 dropsondes, eligible data are regridded from Earth-relative coordinates to cylindrical coordinates with the following default properties:

- The central axis coincides with the sampled storm’s center,
- Azimuth  $\psi$  is rotated to be relative to the heading of environmental deep-layer vertical shear ( $\psi_s$ ),
- Radius  $r$  is normalized by the radius of maximum winds to yield  $r_\star = r/RMW$ , and
- The vertical coordinate is height above ground level  $z$ .

Regridding is applied individually to measurements along a dropsonde’s trajectory to consider horizontal translation during descent (or ascent in strong updrafts). Data are transposed to  $(\psi, r, z)$  coordinates using the technique outlined in section A.2. The nearest-in-time analysis output from the Statistical Hurricane Intensity Prediction Scheme (SHIPS; DeMaria et al. 2005) is consulted to declare the heading of environmental shear and thus determine  $\psi_s$ ; the parameter for 850–200 hPa vertical shear over a TC-centered 200–800 km annulus is used as this heading.

The radial coordinate, normalized radius  $r_\star$ , is used over physical radius  $r$  to account for differences in TC eye size. This radial normalization has been used for similar purposes in prior studies of TC structure and intensity (Zhang et al. 2011; Rogers et al. 2013a; Zhang et al. 2013). To determine the radius of maximum winds necessary in computing  $r_\star$ , we compiled a catalog of

observationally detected surface-level RMW data for the sampled Atlantic storms between 1998 and 2015. Surface wind data from SFMR onboard research and reconnaissance aircraft are used to build the RMW database. Due to eyewall slope, it is expected that the RMW data derived with SFMR will differ from flight-level RMW data used in prior studies (e.g., Zhang et al. 2011; Rogers et al. 2013a; Zhang et al. 2013). Namely, RMWs calculated here should generally be smaller than RMWs calculated at flight-level. The SFMR measures nadir brightness temperature in six C-band frequencies at a sampling rate of 1 Hz, and uses a geophysical model function relating surface emissivity and wind speed to calculate surface wind speed along the flight path. To reduce transient gustiness and noise in the surface wind time series, we apply a 60-second box smoother to the data (i.e., each SFMR measurement is replaced with an average of all measurements in a 60-second window centered on the sampling time).

The surface-level RMW data is determined using a subjective—but robustly tested—method. During a TC research or reconnaissance flight (and assuming the flight is not an upper-level or large-scale environment mission), the aircraft will often make several passes through the TC’s eyewall. From each “leg” across the TC’s center, an SFMR-based determination of RMW is possible provided that valid data exist. To find the RMW for a given pass, we make a liberal first-guess at the annular or ring-like area likely to contain the RMW (an example is shown in Figure 3.1). The region’s inner wall  $R_{in}$  is defined using either a minimum distance or wind speed threshold (hence the region would become “ring-like,” which is ideal for hurricanes with calm eyes). The outer wall of the area  $R_{out}$  is assigned using a maximum distance threshold. When the aircraft first enters the region through  $R_{out}$ , we begin scanning for the maximum surface wind speed and its great-circle distance from the TC center (we will call this distance  $r_i$ ). If the aircraft exits the search region through  $R_{in}$ ,  $r_i$  is recorded for the leg. Provided that  $R_{in}$  is well-defined, the aircraft *must* reenter the search region through  $R_{in}$  (i.e., it must exit the center of the TC), whereupon we scan again for a maximum surface wind speed and its great-circle distance from the TC center (called  $r_f$ ). If the aircraft leaves the search region through  $R_{out}$  before the SFMR record ends, then  $r_f$  is ascertained and the RMW at time  $t_{RMW}$  is calculated simply as

$$RMW(t_{RMW}) = \frac{r_i + r_f}{2}. \quad (3.1)$$

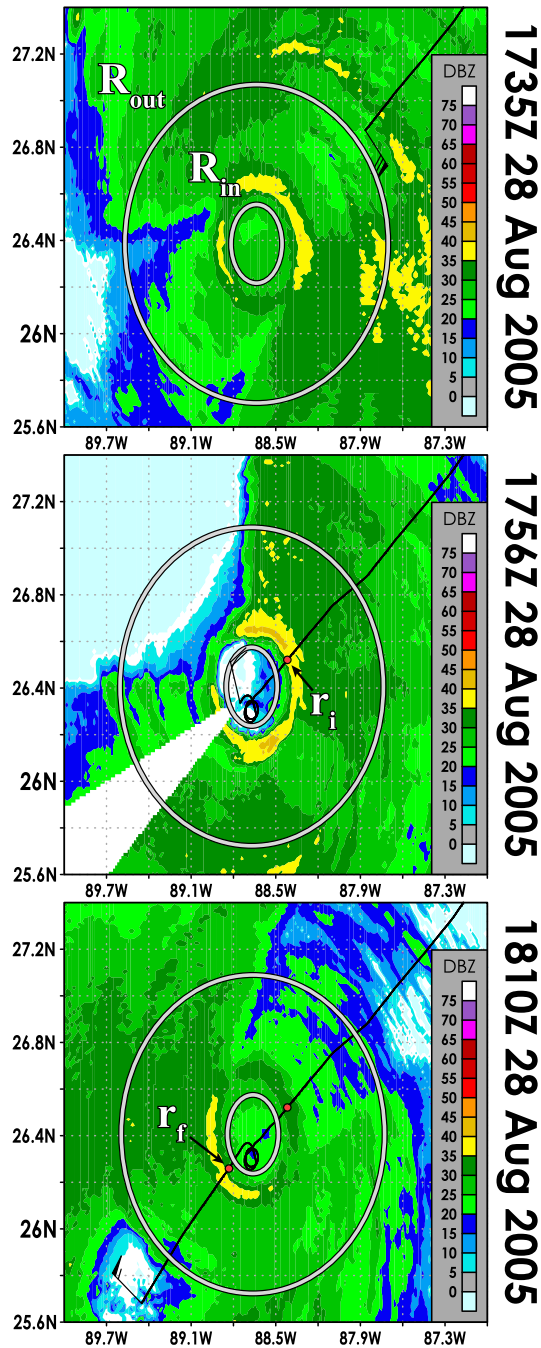


Figure 3.1: Schematic depiction of determining the RMW for a storm using Hurricane Katrina for example [lower fuselage radar reflectivity (dBZ) shaded]. The black line is the aircraft flight path, and the barb represents flight level wind speed (kt) and direction. White ovals ( $R_{out}$  and  $R_{in}$ ) are borders of the area where RMW searches occur. (top) Scanning for  $r_i$  begins after the aircraft enters the area via  $R_{out}$ . (center)  $r_i$  is recorded after plane exits the area through  $R_{in}$ ; searching for  $r_f$  starts when the plane reenters the area. (bottom) Searching for  $r_f$  ends, and RMW is calculated.

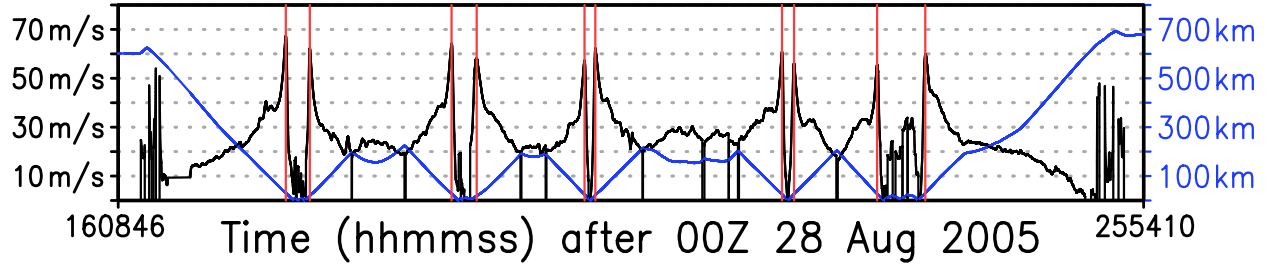


Figure 3.2: Time series of 60-second averaged surface wind speed (black, left axis) and great circle distance from interpolated 2-minute track position (blue, right axis), taken from the stepped frequency microwave radiometer (SFMR) onboard NOAA aircraft 43RF during its mission into Hurricane Katrina on 28 August 2005 (same flight in Figure 3.1). Times of recorded  $r_i$  and  $r_f$  values are marked with red lines.

The time  $t_{RMW}$  assigned to the calculated RMW is equal to the time when  $r_f$  was measured. An example result from this procedure is provided in Figure 3.2; it shows time series of surface wind speed and great-circle distance from the flight in Figure 3.1, along with times when  $r_i$  and  $r_f$  were detected. The nearest RMW in time is assigned to a given dropsonde datum (which, in turn, is used to compute  $r_*$ ). If a dropsonde’s launch time is more than 12 hours separated from the nearest RMW on record, it is removed from the composite pool, as the RMW could change significantly in that time period. The analysis results were robust to several other cutoffs for temporal separation (6, 18, and 24 hours) between RMW detection and sonde sampling time.

After all dropsonde data are mapped to  $(\psi_s, r_*, z)$  coordinates, we use HURDAT2 intensity data to separate the sonde data into groups based on intensity trends. First, we assign a composite identifier to every period between consecutive HURDAT2 records. The intensity tendency for a given period is just the difference in intensity over the time elapsed during the period. Following Rogers et al. (2013a) as a baseline, we define three composite identifiers:

- Intensifying (IN):  $\frac{\Delta V_{max}}{\Delta t} \geq \frac{20 \text{ kt}}{24 \text{ h}}$
- Steady-state (SS):  $\frac{20 \text{ kt}}{24 \text{ h}} > \frac{\Delta V_{max}}{\Delta t} \geq -\frac{10 \text{ kt}}{24 \text{ h}}$
- Weakening (WE):  $\frac{\Delta V_{max}}{\Delta t} < -\frac{10 \text{ kt}}{24 \text{ h}}$

Each dropsonde sample is then tagged with the composite identifier associated with the time of measurement. Three composites (IN, SS, and WE) are made by averaging all like-tagged data in every  $(\psi_s, r_*, z)$  bin.

Due to the spatial density of data and the focus of this research, we limit our analysis to observations at or below 2.5 km AGL and at  $r_* \leq 3.0$ . By default, the composite grids have 0.25 RMW radial resolution,  $90^\circ$  azimuthal resolution, and 25 m vertical resolution. For storm-relative velocities, storm motion is calculated from 2-minute track data using the TC's positional difference over the time interval containing a dropsonde sample. Radial and tangential components of wind are derived following the procedure in section A.3.

In the following section, we examine the resulting data climatology to aid our later physical interpretations of the data, and a detailed analysis of azimuthally averaged hurricane BL structures in all three composites is presented.

## 3.2 Data Climatology

Before we examine our composite results directly, let us first consider the makeup of data used in the composites. Since the composites combine data from missions undertaken in 50 different Atlantic hurricanes over nearly two decades, the composite metadata is important to recognize in its potential to skew physical interpretation. For example, the intensifying storms' composite (shortened to IN composite or group) includes more data from weaker hurricanes on average, which would be expected to manifest in the resulting primary circulatory structure at least—and as shown in subsection 3.3.1, the tangential wind field of the IN composite indeed differs as expected from the SS and WE composites. In addition, the spatial consistency of data *within composite space* is investigated. For the sake of argument, consider the possibility that a composite's data at radii inside the RMW consist of samples from hurricanes that are different (e.g., far more intense) from measurements composited outside the RMW. In this situation, carelessly combining data from multiple radii to make an argument *vis-à-vis*, for instance, the inner-core primary circulation may be misleading or invalid. To address these caveats, we consider the launch locations of Atlantic dropsondes in all composites, thereby highlighting the potential for composite structures

to be skewed by environmental factors like land, latitude, and sea-surface temperature (SST). We breakdown the relative sampling frequencies of storm intensity and deep-layer shear magnitude across composite space for each group.

In total, data from 3,091 out of the original pool of 12,045 quality-controlled Atlantic dropsondes (25.7%) are included in our composite analysis. From the remaining sondes, 1,086 (963/1,042) were launched into a hurricane during intensification (steady-state/weakening). The launch position of each of these dropsondes is mapped in Figure 3.3. Hurricane sampling occurs mostly in the western Atlantic basin, the Gulf of Mexico, and the Caribbean Sea. Most of the sondes from the southwestern Gulf of Mexico and the Caribbean Sea were launched in intensifying cases. This is contrasted with the relatively sporadic spread of intensity change associated with sondes from the northern Gulf of Mexico and east of the United States; this is likely due to the increased potential for interaction with land, external synoptic weather patterns, and less-favorable SSTs. Storm-relative dropsonde launch locations (on a  $\psi_s$ - $r_*$  plane) are shown in Figure 3.4. Generally, launches are concentrated immediately about the TC center, with a relatively high spatial density of sondes launched at  $r_* \leq 1.5$  when compared to outside this area. All shear-relative quadrants are reasonably sampled in each composite, although launches are somewhat more concentrated to the left of the deep-layer shear. Based on the distribution of sondes, the axisymmetric fields should not be heavily influenced by data in any particular quadrant.

The dropsonde data originate from missions flown in 50 Atlantic hurricanes. Of these cases, the most dropsonde launches occurred in Hurricanes Rita in 2005 (212 sondes), Ike in 2008 (191), Irene in 2011 (190), Earl in 2010 (184), Isabel in 2003 (176), and Sandy in 2012 (155). Hurricanes Ike and Earl are associated with the most sonde launches during IN (78 and 74 sondes, respectively). In the WE group, most sonde launches come from Hurricanes Rita (138) and Isabel (96). Bonnie in 1998 (138) and Irene (106) contribute the most launches to the SS composite. A summary of these 50 storms, including best-track intensity and RMW information at the times of sampling, is given in Table 3.1. Average at-launch environmental characteristics [e.g., low-level relative humidity (RH)] for each composite are listed in Table 3.2. In the mean, IN storms have the smallest RMWs, weakest deep-layer shear, most low-level RH, and highest SSTs. In contrast, the

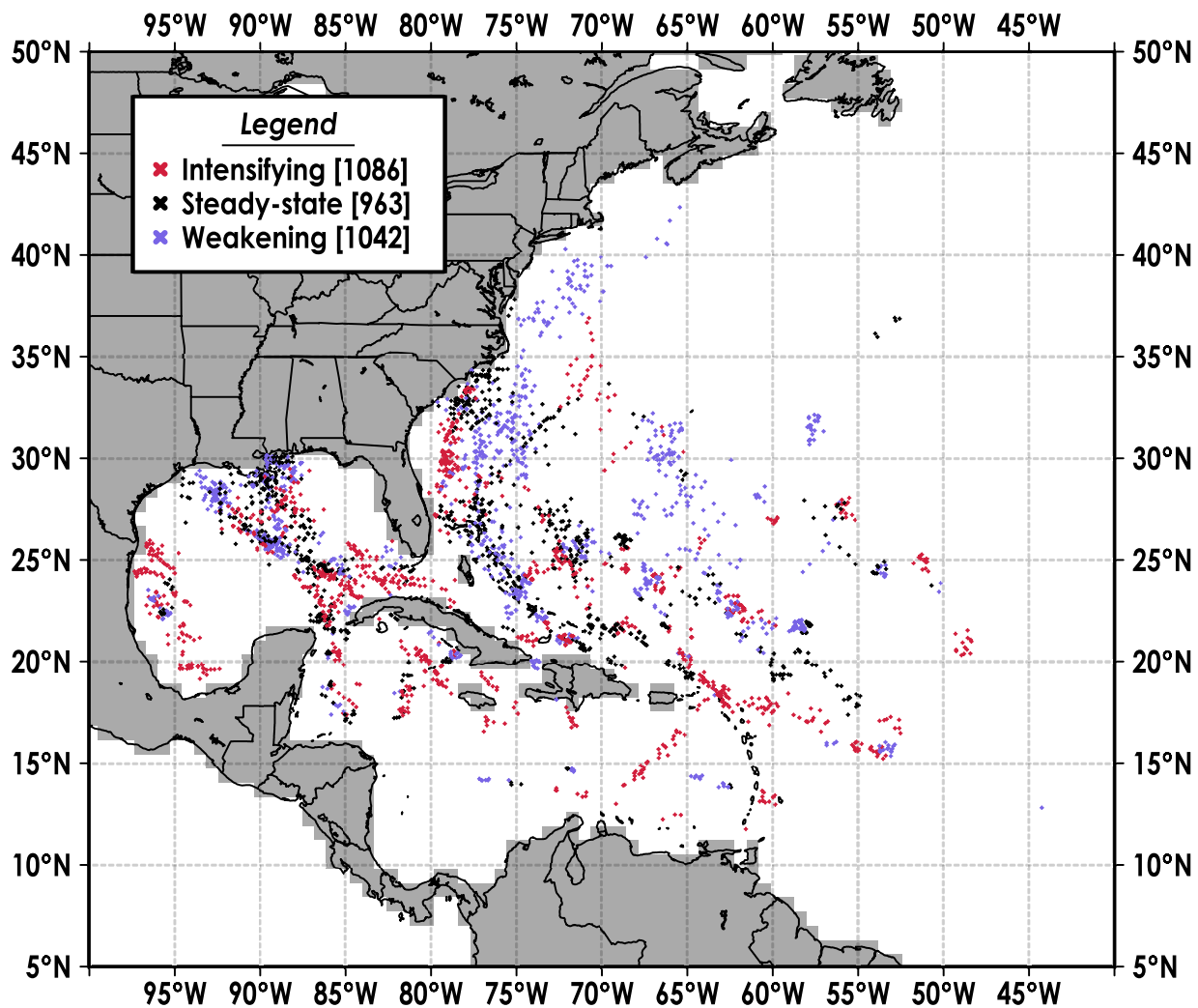


Figure 3.3: Launch positions of all composited dropsondes for Atlantic hurricanes from 1998 to 2015. Each dot is colored, representing the intensity change identifier associated with a dropsonde at launch time (summarized in the legend). The amount of dropsondes utilized in each composite is contained in brackets next to each descriptor in the legend. Landmask for determining whether dropsonde data or storm centers were over land (and thus discarded) is colored in gray.

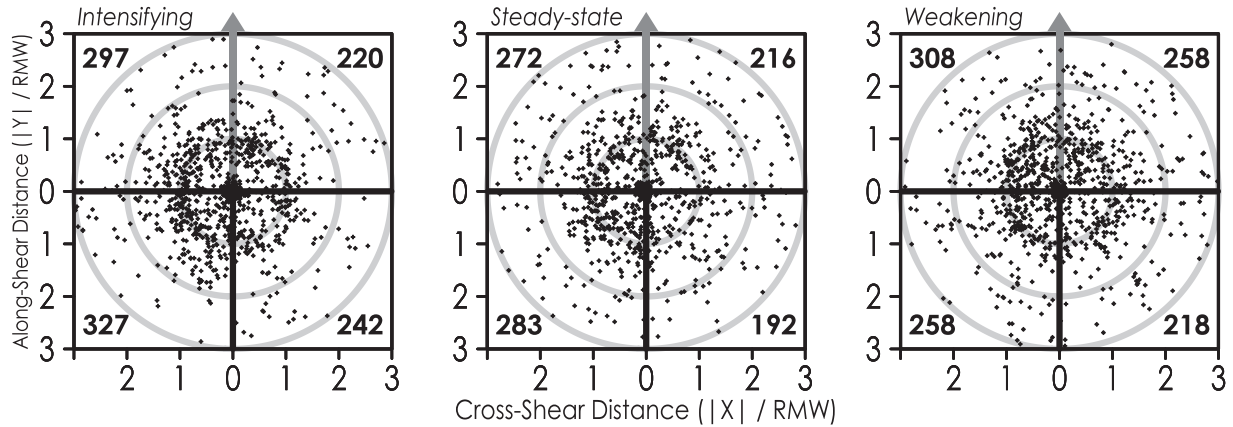


Figure 3.4: Composited dropsonde launch positions on the horizontal plane for (left) intensifying, (center) steady-state, and (right) weakening Atlantic storms. The  $x$  and  $y$  distances from the storm center are expressed in multiples of detected RMW. Concentric dividers represent contours of  $r_*$  with an interval of 1. The bold gray vector represents the environmental wind shear as determined from SHIPS. The number in the corner of each shear-relative quadrant represents the number of sondes launched in that quadrant.

WE composite uses data from cases with the strongest deep-layer shear, least low-level RH, and coldest SSTs.

As mentioned earlier, the level of consistency in storms sampled on average across composite space should also be considered. The composites' representations of the hurricane BL may lose meaning if the included storms were both highly unique and sampled unevenly across space. We examine this potential for data heterogeneity by decomposing composited system and environmental data in space. Figure 3.5 breaks down the relative frequency of occurrence for hurricane intensity ranges as a function of normalized radius  $r_*$ , expressed as a fraction of total launches within a given radial bin (i.e., each column of values in Figure 3.5 sums to unity). In the IN group, samples at  $r_* > 2.0$  are generally more associated with weaker storms (60–70 kt) compared to inner radii—some bins at these outer radii have more than 40% of their data originating from hurricanes of this intensity. Dropsonde launches from the SS composite originate mostly from storms with  $V_{max} < 120$  kt, with a relative sampling maxima in the 100–105 kt intensity range in most radial bins. Sondes from the WE group are taken from a somewhat diverse range of intensities; relative sampling maxima are seen in the 135–140 kt intensity bin for  $r_*$  between 0.75 and 1.5,

Table 3.1: List of Atlantic hurricanes included in composites. Number of used dropsondes are shown, as well as the amount of dropsondes launched under each intensification identifier. Ranges of best-track storm intensity and SFMR-detected radius of maximum winds at times of observation are disclosed.

Name	Year	All sondes	IN sondes	SS sondes	WE sondes	$V_{max}$ (kt)	$RMW$ (km)
Rita	2005	212	62	12	138	60 – 146	14.6 – 39.7
Ike	2008	191	74	98	19	65 – 115	9.3 – 113.2
Irene	2011	190	22	106	62	65 – 105	18.3 – 112.6
Earl	2010	184	78	30	76	60 – 125	16.5 – 67.6
Isabel	2003	176	50	30	96	130 – 140	25.8 – 41.8
Sandy	2012	155	33	61	61	62 – 95	26 – 89.6
Bonnie	1998	146	0	138	8	95 – 100	56.3 – 67.7
Gonzalo	2014	115	47	23	45	64 – 125	6.6 – 49.5
Ophelia	2005	108	47	0	61	55 – 71	14.8 – 100.1
Frances	2004	98	21	41	36	85 – 125	18.5 – 66.5
Gustav	2008	95	34	38	23	59 – 126	14.7 – 49.8
Arthur	2014	90	50	12	28	60 – 85	24.2 – 79.8
Isaac	2012	85	42	42	1	69 – 70	36.5 – 88.3
Ivan	2004	79	1	51	27	105 – 140	14 – 49.9
Katrina	2005	79	7	18	54	100 – 150	26.6 – 64.4
Bill	2009	66	18	29	19	73 – 115	27.2 – 44.1
Joaquin	2015	64	27	6	31	68 – 135	20.9 – 47.1
Lili	2002	63	52	11	0	65 – 125	14 – 31.6
Ingrid	2013	61	34	7	20	60 – 72	14 – 36.7
Edouard	2014	61	26	12	23	72 – 102	18.4 – 42.5
Georges	1998	58	25	17	16	78 – 135	19.1 – 68.6
Wilma	2005	53	37	8	8	85 – 110	51.4 – 61.6
Dennis	2005	52	44	0	8	75 – 130	14.1 – 26.2
Helene	2006	46	13	16	17	80 – 101	21.6 – 94.4
Danielle	1998	45	0	24	21	65 – 70	32.9 – 43.1
Ida	2009	42	31	3	8	60 – 90	22.3 – 34
Tomas	2010	42	20	2	20	60 – 85	21 – 53.7
Isidore	2002	40	0	40	0	~ 110	18.2 – 24.5
Paloma	2008	37	20	10	7	65 – 125	10.6 – 29.1
Omar	2008	35	33	0	2	60 – 109	13.5 – 27.6
Paula	2010	34	5	16	13	65 – 90	10.3 – 20.1
Dolly	2008	32	32	0	0	60 – 71	25.2 – 40.2
Fabian	2003	32	6	14	12	105 – 120	19.5 – 31.6
Alex	2010	29	23	6	0	65 – 81	14.3 – 24.4
Jeanne	2004	28	0	28	0	85 – 105	28.7 – 59.9

Table 3.1 – continued.

Name	Year	All sondes	IN sondes	SS sondes	WE sondes	$V_{max}$ (kt)	RMW (km)
Karl	2010	24	24	0	0	56 – 86	17.3 – 28.4
Igor	2010	21	0	0	21	69 – 90	57.2 – 89.6
Felix	2007	21	11	3	7	62 – 150	9.9 – 21.3
Rina	2011	16	0	8	8	79 – 100	17 – 22.8
Rafael	2012	15	7	2	6	60 – 80	24.7 – 74.1
Danny	2015	15	0	0	15	64 – 65	11.4 – 15.2
Katia	2011	14	0	0	14	93 – 104	80.6 – 82.5
Danielle	2010	14	8	0	6	98 – 113	17.8 – 62.9
Kyle	2008	12	11	1	0	60 – 70	25.4 – 43.4
Ernesto	2012	5	5	0	0	61 – 68	26.3 – 37.2
Leslie	2012	3	0	0	3	60 – 61	~ 95.1
Fay	2014	3	3	0	0	60 – 61	~ 95.2
Kate	2015	3	3	0	0	62 – 63	~ 18.3
Karen	2007	1	0	0	1	61 – 62	~ 29.6
Bertha	2008	1	0	0	1	66 – 67	~ 70.8

Table 3.2: Mean environmental conditions at launch of dropsondes in IN, SS, and WE composites. Standard deviations are given in parentheses. Shear, SST, and low-level relative humidity data are pulled from SHIPS data.

Quantity	IN	SS	WE
850–200 hPa shear ( $\text{m s}^{-1}$ )	7.66 (4.31)	8.97 (5.13)	9.76 (5.12)
SST ( $^{\circ}\text{C}$ )	29.20 (0.82)	28.93 (0.80)	28.71 (1.39)
850–700 hPa relative humidity (%)	68.95 (7.64)	67.61 (5.68)	66.70 (6.36)
RMW (km)	34.57 (19.17)	43.75 (22.60)	41.15 (21.23)
Intensity $V_{max}$ ( $\text{m s}^{-1}$ )	44.41 (12.31)	49.96 (10.08)	51.92 (12.76)
Storm latitude ( $^{\circ}\text{N}$ )	23.21 (4.60)	25.51 (4.34)	26.89 (5.13)
Storm longitude ( $^{\circ}\text{W}$ )	76.61 (11.99)	77.07 (10.20)	75.44 (11.04)

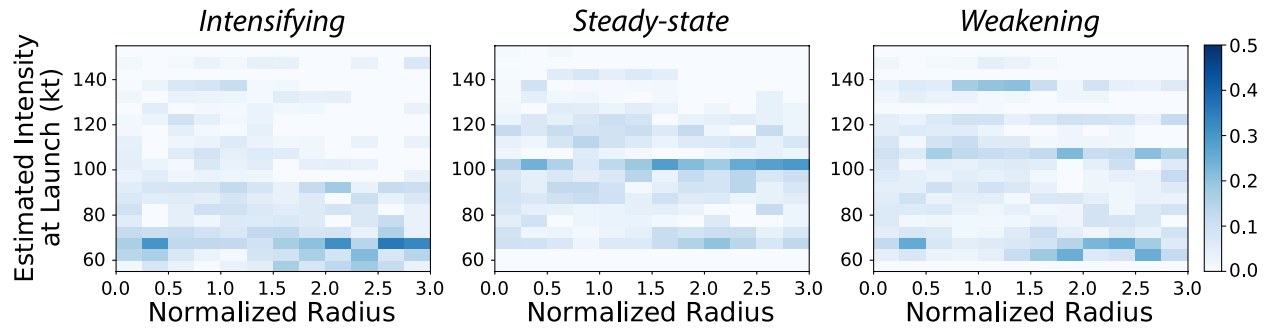


Figure 3.5: Relative frequency of at-dropsonde-launch (hereafter “at-launch”) estimated storm intensity (5-kt bin width) for each radial bin. The value of a shaded cell at  $(r_*, V_{max})$  represents the ratio of dropsondes launched at  $r_*$  with storm intensity  $V_{max}$  to the total number of launches at  $r_*$ . Thus, the sum of all values in a column is unity. Variability across  $r_*$  signifies radial heterogeneity in sampling for given  $V_{max}$ , whereas variability across  $V_{max}$  implies diverse sampling of storm intensity for given  $r_*$ .

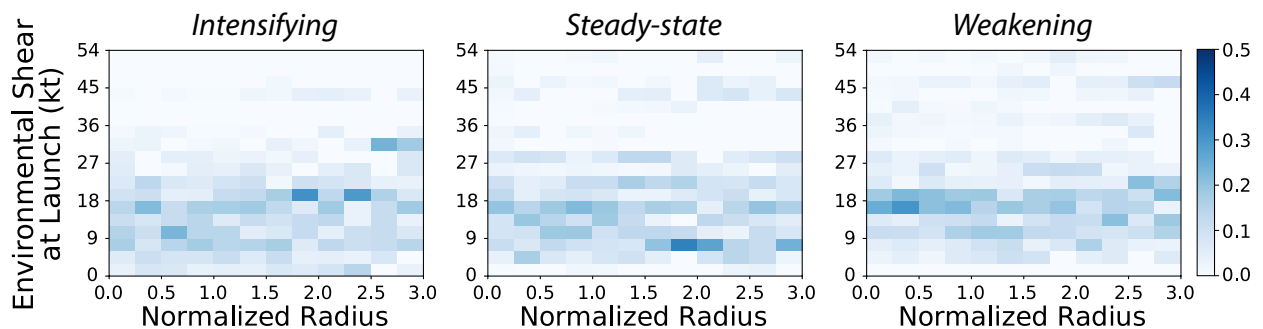


Figure 3.6: Similar to Figure 3.5, except the y-axis represents the at-launch environmental vertical wind shear magnitude (as estimated with SHIPS data). The bin width used for shear data is 3 kt.

and in the 60–70 kt intensity range for  $r_*$  between 1.75 and 2.75. Loosely speaking, the IN and WE composites both exhibit a similar property: Relatively weak storms (from the perspective of intensity, which could be explicitly representative only of wind near the RMW) are sampled more often at greater radii. Assuming the radial profile of wind associated with each sample has similar peakedness, these sampling trends suggest that the resulting tangential winds of IN and WE composites may be biased toward looking more peaked.

The spatial sampling trends of at-launch deep-layer wind shear are shown in Figure 3.6, framed in a fashion similar to Figure 3.5. For the IN group, relative sampling frequency is mostly concentrated between 6–21 kt, except at  $r_* > 2.5$  where sampling maxima appear in the 30–33 kt shear range. The SS composite has a wider range of shear magnitudes across  $r_*$ , with most sondes launched when the deep-layer shear is between 6 and 30 kt. A small amount of sondes at outer radii in the SS group ( $\lesssim 10\%$ ) are launched when the shear is quite strong ( $\geq 42$  kt). The WE group has a similar signal of strong shear at outer radii, and most sondes in the WE composite are launched when the deep-layer shear magnitude is 9–27 kt. With respect to shear, there appears to be less heterogeneity in sampling across  $r_*$ , so we do not expect sampling biases in shear to affect results of each composite. However, they *may* affect comparisons between the composites due to the tendency for higher shear to be seen in storms that are weakening (Table 3.2).

### 3.3 Axisymmetric Analysis

For this section’s analysis, we sum all measurements of variables from all quadrants in each  $(r_*, z)$  bin, and then divide each result by the total number of observations in all quadrants from the given  $(r_*, z)$  bin (i.e., the variables are azimuthally averaged). To that effect, most of these results are depicted with normalized radius-height cross sections. All wind fields shown are storm-relative unless stated otherwise.

#### 3.3.1 Primary Circulation

Azimuthally averaged storm-relative tangential wind is shown for all composites in Figure 3.7. All composites exhibit a low-level tangential wind jet at the RMW, which is situated between 250 m and 1250 m AGL. These signals were also observed by F03 in eyewall dropsondes; F03 found

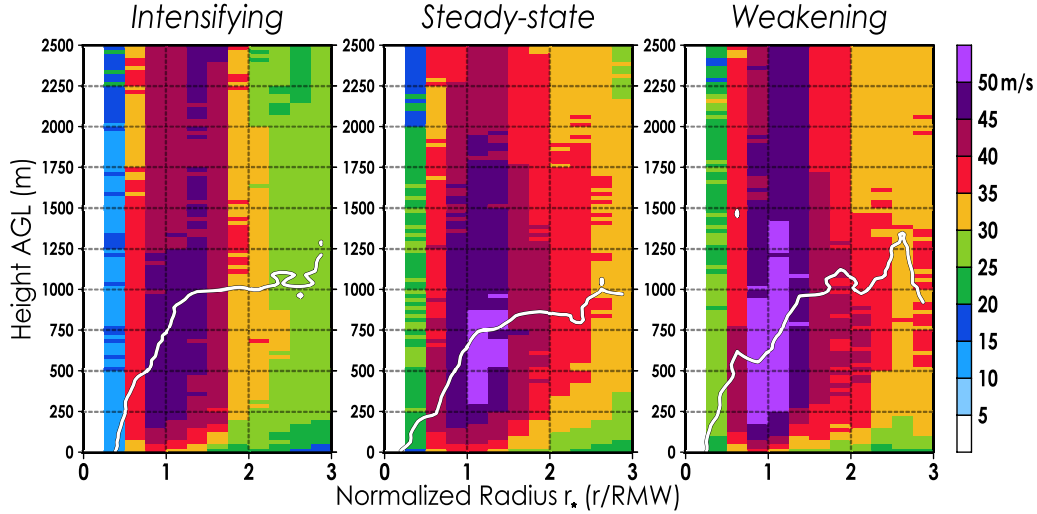


Figure 3.7: Normalized radius-height cross sections of azimuthally averaged, storm-relative tangential velocity  $v$  (in  $\text{m s}^{-1}$ ) for all composites. The solid, white contour highlights the radial inflow layer adjacent to the surface. For defining the inflow layer, storm-relative radial velocity is smoothed 5 times with a 1-2-1 filter and then normalized by peak inflow. The inflow layer is where the normalized radial velocity is at least 10% of the peak inflow (omitted above  $z = 1500$  m).

the strongest eyewall winds to be at about 500 m AGL. Although F03 notes a sampling bias in their data, these low-level wind maxima are presumably a consequence of warm-core cyclone structure. The jet magnitude is weakest in the IN composite ( $v \approx 48 \text{ m s}^{-1}$ ) and strongest in the WE composite ( $v \approx 53 \text{ m s}^{-1}$ ); the SS composite’s jet has wind speeds between the jets in IN and WE ( $v \approx 51 \text{ m s}^{-1}$ ). Regardless of stratification by intensity change, the radial position of  $v$  maxima at a given height shifts outward with altitude, indicating a slope in the tangential wind maximum. Tangential winds weaken rapidly with decreasing height below  $v$  maxima, consistent with prior observational studies (e.g., Franklin et al. 2003; Powell et al. 2003; Zhang et al. 2011). At greater radii ( $r_* > 1.75$ ), the IN composite’s tangential winds are weaker in comparison to SS and WE, which could be due to sampling biases shown in Figure 3.5. As a function of  $r_*$ , the height of maximum  $v$  generally increases with  $r_*$  in all groups—rapidly so near the RMW and levelling off at greater radii.

Differences in  $v$  between composites are partly a result of sampling trends, as discussed in section 3.2. Figure 3.8 shows the azimuthally averaged storm intensity, which is calculated by

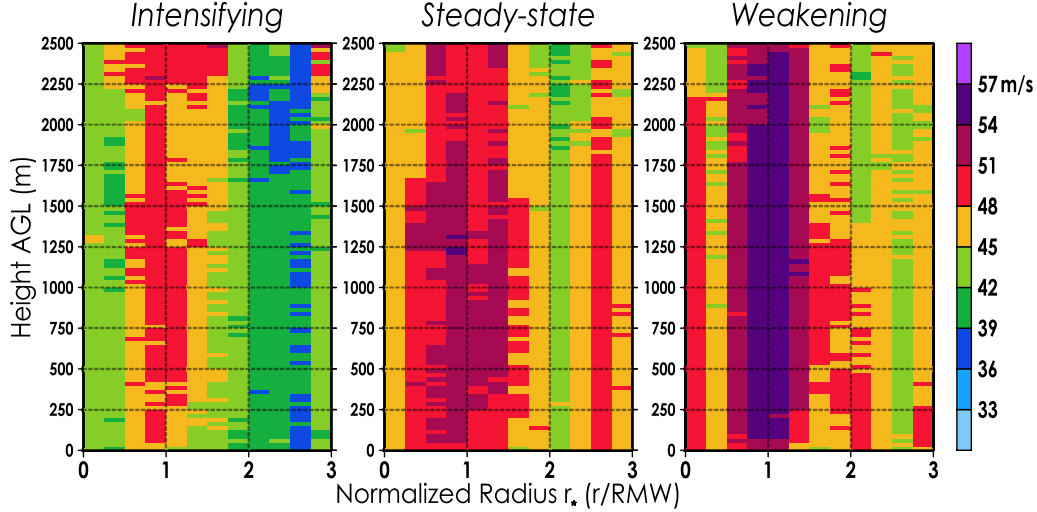


Figure 3.8: Axisymmetrized, normalized radius-height cross sections of estimated storm intensity  $V_{max}$  (in  $\text{m s}^{-1}$ ) at the time of sampling, interpolated from HURDAT2 data. Values of  $V_{max}$  associated with all samples in a given  $r_*$ - $z$  bin are averaged to yield this figure.

compositing estimated  $V_{max}$  from HURDAT2 at sampling time (these estimates are assigned to the spatial bin associated with the *dropsonde's* position, although  $V_{max}$  estimates are expected to represent winds at the RMW). On average, observations near the RMW in the IN group are from hurricanes of lesser intensity ( $45 - 51 \text{ m s}^{-1}$ ) compared to similarly positioned observations in the SS composite ( $48 - 54 \text{ m s}^{-1}$ ) and WE composite ( $54 - 57 \text{ m s}^{-1}$ ). Generally,  $V_{max}$  from IN is lower compared to non-intensifying composites for a given  $(r_*, z)$  bin, which explains (to some degree) the composite differences in azimuthally averaged  $v$ . Near the center and at  $r_* > 1.5$ , azimuthally averaged  $V_{max}$  is weaker relative to averaged  $V_{max}$  adjacent to the RMW in every composite. These sampling trends in storm intensity obfuscate our interpretation of the primary circulation directly—both in assessment of composites independently and the comparisons between them.

The radial profile of  $v$  can be used to interpret a vortex's inertial stability. In the lower troposphere, inertially stable conditions are typical of hurricanes ( $I^2 > 0$ ). Radial displacements of fluid are resisted in an inertially stable system. Inertial stability is proportional to the radial differential of squared absolute angular momentum per unit mass:

$$I^2 = \frac{1}{r^3} \frac{\partial M_a^2}{\partial r} = \frac{1}{r^2} (r^2 f_0^2 + 3rvf_0 + 2v^2) + \frac{1}{r} \frac{\partial v}{\partial r} (rf_0 + 2v). \quad (3.2)$$

A vortex with a relatively sharp decrease of  $v$  along the radial direction (i.e., a peaked wind profile) would yield smaller  $\partial M_a / \partial r$  (and thus  $I^2$ ) as it offsets the increase in  $M_a$  by increasing  $r$ . Inertial stability may at first seem like a natural property to examine in our composites, but our composite framework precludes direct calculation of  $I$  due to the use of normalized radius. Simply put, an exact determination of any radial derivative using discrete observations is not viable for this analysis for a multitude of reasons—variable intensity across composite space is one of the more pressing reasons.

We account for the spatial variability in  $V_{max}$  by assessing the difference between  $V_{max}$  and  $v$ . The resulting difference  $\delta v$  shown in Figure 3.9 represents the departure of  $v$  from the estimated maximum wind located presumably at  $r_* = 1$ . In turn,  $\delta v$  can be used to interpret the radial variation of tangential wind relative to wind at the RMW, which we use as a conceptual proxy for  $\partial M_a / \partial r$ . For example, a rapid increase in  $\delta v$  with radius implies a smaller radial differential of  $M_a$ , and thus weaker inertial stability.

In the IN composite, tangential winds between 250–1500 m AGL at  $r_* = (0.75, 1.75]$  are often within  $3 \text{ m s}^{-1}$  of  $V_{max}$ , implying a local weak radial gradient of  $v$ . The SS and WE composites show a stronger radial gradient of  $\delta v$  in the same area. These differences are somewhat due to samples in non-intensifying groups being associated with hurricanes that had larger RMWs. The actual radial distance spanning the area where  $\delta v < 3 \text{ m s}^{-1}$  in the SS composite is closer to that of the IN group—both composites have this area extend to about 20–25 km outward from the RMW, whereas this region extends to roughly 10–15 km outward from the RMW in the WE composite. The tangential wind jet (represented as areas where  $\delta v$  is near zero) is deepest in the IN composite and shallower in non-intensifying groups, which may indicate that stronger vertical mixing or turbulence occurs in this region during intensification. These results imply that the eyewall region has relatively high  $I^2$  in intensifying hurricanes when compared against non-intensifying hurricanes of similar intensity.

At  $r_* > 1.75$ ,  $\delta v$  increases the least with increasing  $r_*$  in the WE composite. Due to larger RMWs on average compared with the IN composite, the physical radii associated with the outer radial bins are larger in non-intensifying groups; combined with the relatively low  $\partial(\delta v) / \partial r_*$  in the WE composite, these results suggest that the weakest  $\partial v / \partial r$  at  $r_* > 1.75$  is found in weakening

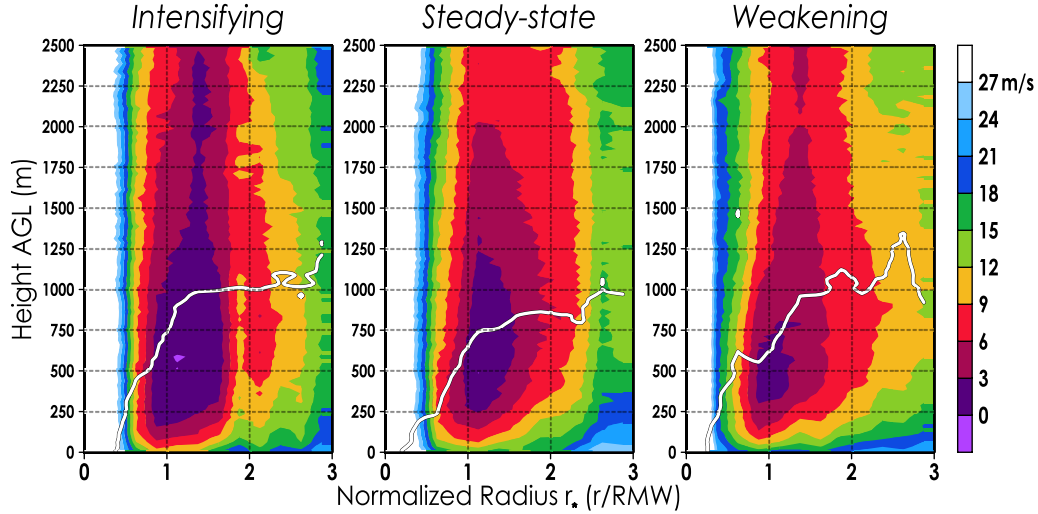


Figure 3.9: Azimuthally averaged, normalized radius-height cross sections of the difference between estimated storm intensity and storm-relative tangential velocity, defined as  $\delta v \equiv V_{max} - v$  (in  $\text{m s}^{-1}$ ). The white contour marks the inflow layer height as defined in Figure 3.7.

hurricanes. Thus, the implied local inertial stability from these patterns is maximized in the WE composite. As inertial stability represents a resistance to radial displacement of fluid, low-level radial convergence should be modulated by the local  $I^2$ . Radially translating air that encounters high  $I^2$  at  $r_* > 1.75$  should therefore have a higher tendency to be deflected into the vertical due to implied radial convergence, possibly enhancing transport between the high-enthalpy near-surface inflow and the relatively dry air above the inflow layer. Forced shallow ascent of relatively moist and warm air out of the BL may reduce conditional stability just above the BL in the vicinity of ascent. These processes corroborate prior observed differences in the radial location of deep convection between intensifying and non-intensifying storms (Rogers et al. 2013a).

Our interpretation of composite  $I^2$  rests on the assumption that an inverse relationship exists between  $\partial(\delta v)/\partial r$  and  $I^2$ . This relationship is examined using bin-averaged dropsonde data from the well-sampled Hurricane Earl in 2010 during its intensification and decay. Figure 3.10 shows vertical profiles of  $\partial(\delta v)/\partial r$  and  $I^2$  calculated at several radial ranges during Hurricane Earl's intensification and weakening (with data categorized and sorted as explained in subsection 3.1.2). With the exception of data at  $r_* = (1.5, 2]$ ,  $\partial(\delta v)/\partial r$  apparently has a non-linear inverse relation-

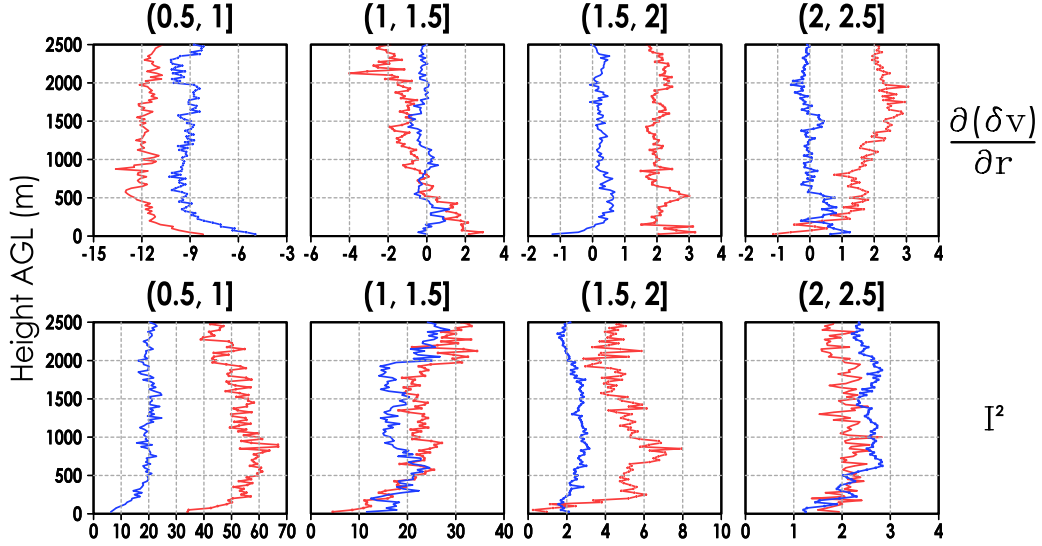


Figure 3.10: Vertical profiles of (top)  $\partial(\delta v)/\partial r$  (in  $10^{-4} \text{ s}^{-1}$ ) and (bottom) inertial stability  $I^2$  (in  $10^{-7} \text{ kg}^{-2} \text{ s}^{-2}$ ) using azimuthally averaged dropsonde data from Hurricane Earl (2010) during intensification (red profiles) and weakening (blue profiles). The top of each plot is labeled with the interval of  $r_*$  displayed. Both calculations used bin-averaged values for  $r$ ,  $v$ , and  $M_a$ , with a 0.5 RMW radial resolution.

ship with  $I^2$ . Inside the RMW, Hurricane Earl's inertial stability was greatest during intensification, in qualitative agreement with the composite  $\delta v$  field. At  $r_* = (2, 2.5]$  and above  $z = 250 \text{ m}$ , inertial stability was weakest during intensification. The breakdown of the relationship between  $\partial(\delta v)/\partial r$  and  $I^2$  apparent at  $r_* = (1.5, 2]$  is due to a strong radial gradient of sampled RMW in this range during Hurricane Earl's weakening; the sampled RMW increases from about 45 km at  $r_* = 1.25$  to over 60 km at  $r_* \geq 1.75$ , which is almost double the RMW found during Hurricane Earl's intensification at the same radial range. With the strong dependence of  $I^2$  on  $r^{-1}$ , the inertial stability calculated for Hurricane Earl at  $r_* = (1.5, 2]$  during weakening is considerably lower than  $I^2$  during intensification due to the RMW sampling bias. However, while this relationship breakdown due to RMW sampling suggests that a bulk calculation of  $I^2$  is sensitive to sampling biases (particularly in  $r$ ), it does not necessarily suggest that  $\partial(\delta v)/\partial r$  is a better metric for inertial stability using biased data.

### 3.3.2 Secondary Circulation

Each composite's secondary circulation is depicted in Figure 3.11, using the storm-relative radial velocity normalized by the magnitude of peak inflow in  $r_*$ - $z$  space. The inflow layer is defined using the  $-0.1$  normalized radial wind contour, which follows the definition used in Zhang et al. (2011). A surface-adjacent inflow layer is evident in each composite, with the strongest inflow located just outside the RMW. Relatively weak radial winds were observed throughout much of the area outside of the inflow layer. The near-surface inflow extends from  $r_* = 0.5$  to the outer edge of the composite domain, with the layer deepening markedly with increasing radius at  $r_* \leq 1.0$ . As a function of  $r_*$ , wind speed maxima are often found near the top of the inflow layer; this is simply explained by the effects of frictional dissipation and substantial agradient forcing occurring in tandem with one another (Ooyama 1969; Smith et al. 2009).

At radii beyond the RMW, the inflow layer is roughly 750–1250 m thick. The IN composite's inflow layer is of greater or nearly equal thickness to inflow layers in the SS and WE composites outside of  $r_* = 1.0$ , despite the greater intensity of storms composited in the non-intensifying groups. This implies that the vertically integrated radial convergence, given by

$$-\int_0^{Z_{BL}} \nabla \cdot (\hat{r} \cdot \vec{U}) \hat{r} dz = -\int_0^{Z_{BL}} \left( \frac{u}{r} + \frac{\partial u}{\partial r} \right) dz \quad (3.3)$$

where  $\vec{U}$  is the 3-D wind vector and  $Z_{BL}$  is the height of the top of the kinematic boundary layer, is relatively high at and immediately inward of the RMW during intensification for a given storm intensity. In the area where  $r_* = (1.25, 2.75]$ , the IN and WE composites' inflow layers are approximately 1 km thick. If the depth scale  $\delta$  of the frictionally induced inflow is linked to the ratio of turbulent diffusivity  $K$  to inertial stability [i.e.,  $\delta = \sqrt{2K/I}$  as discussed in Kepert (2001) and Kepert and Wang (2001)], then vertical diffusion in the WE composite should be greater than IN at these outer radii (to compensate for enhanced  $I^2$  implied in Figure 3.9).

All composites have their maximum inflow located near the surface and just outside the RMW. Inward of these maxima, inflow weakens rapidly with decreasing  $r$  due to reduced  $v$  (and thus AGF) and strong resistance associated with  $I^2$ . The radial span of normalized inflow less than  $-0.7$  is most pronounced in SS and WE composites. Strong inflow at radii outside of the RMW may be indicative of tendencies for radial convergence to be enhanced at these radii. For instance, a local

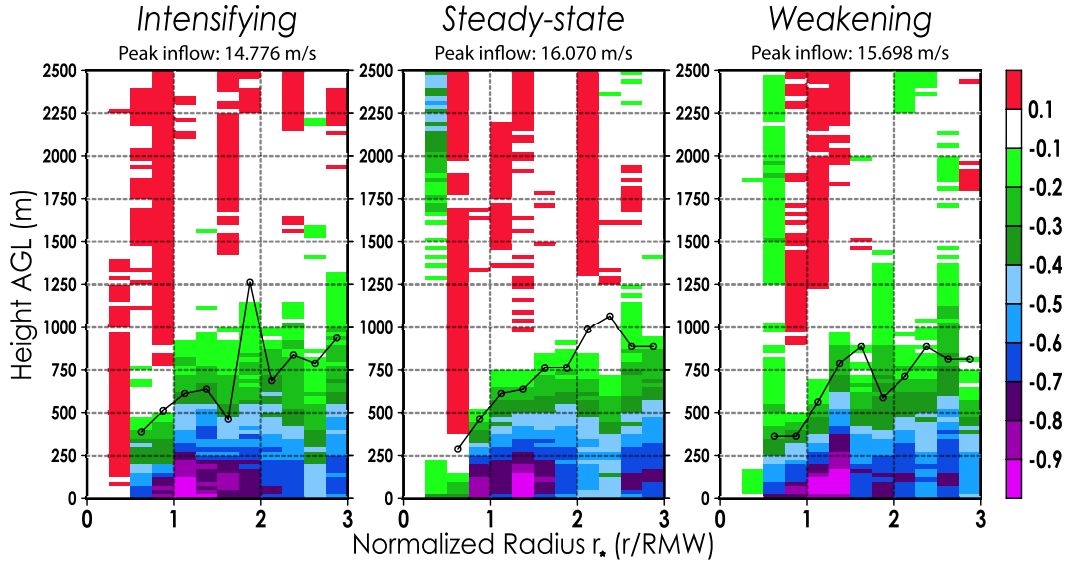


Figure 3.11: Normalized radius-height cross sections of azimuthally averaged, storm-relative radial velocity divided by the magnitude of peak inflow in each group (listed at the top of each panel). Negative values indicate inflow. Black lines connect black circles representing the height at which  $v$  (smoothed with a 1-2-1 filter 5 times) is maximized at each radial bin outside of  $r_* = 0.5$ .

maximum of inflow is apparent at  $z = 250$  m AGL and  $r_* > 2.5$  in the SS and WE groups, which is a sign of enhanced convergence there due to increased  $-u/r$  and  $-\partial u/\partial r$ . Note that sampling biases in  $V_{max}$  can translate to  $u$  in the BL, as BL inflow is heavily influenced by a gradient forcing dependent on frictional destruction of momentum aloft.

Prior studies have concluded that convective diabatic heating located inside the RMW may be conducive for intensification (Shapiro and Willoughby 1982; Pendergrass and Willoughby 2009; Vigh and Schubert 2009). Conversely, diabatic heating situated radially outward of the RMW may reduce a hurricane's intensity, arguably because that heating would reduce the radial temperature gradient between the TC core and its surroundings. The warm anomaly associated with the TC center would be weakened, reducing  $\partial p/\partial r$  in the inner core and thereby affecting the tangential wind. Our cross sections of  $u$  and  $\delta v$  suggest that the WE composite has stronger radial convergence and inertial stability at radii outside the RMW, which could increase the likelihood of convection outside the RMW [as shown in numerical studies by Hazelton et al. (2017b,a)] that would distribute diabatic heating over a larger area outside the principal eyewall. Such a distri-

bution of convection may lead to a less pronounced TC core temperature anomaly, which could weaken the mean vortex. An alternate,  $M_a$ -based perspective regarding the impact of the spatial distribution of convergence and convection leads to a similar conclusion: Ascent out of the hurricane BL inside the RMW is associated with near-surface inflow that advects relatively high- $M_a$  surfaces from higher radii toward the RMW, leading to tangential wind spin-up (Smith and Montgomery 2016). In contrast, ascent out of the BL *outside* of the RMW should lead to spin-down tendencies at the RMW, as relatively low- $M_a$  surfaces would be pulled from lesser radii toward the RMW.

If radial convergence and forced shallow ascent occur outside of the RMW, it is possible that the ascending air escapes the BL and—pending its enthalpy in comparison to the air immediately aloft—continues to rise in an updraft. The originally inflowing, high- $\theta_e$  air that is deflected upward and escapes the BL is replaced by relatively low- $\theta_e$  air in the free atmosphere, which results in a reduction of the inflow’s moist static energy (MSE). The low- $\theta_e$  air from above the BL replaces inflowing air via forced subsidence, which could be located inward of BL convergence outside of the RMW. Additionally, convective downdrafts and turbulent mixing can import low-enthalpy air from aloft into the near-surface inflow. In sum, these processes can reduce MSE of inwardly moving air that arrives at the principal eyewall, possibly affecting inner-core conditional stability and diabatic heating. The thermodynamics of our three composites will be examined in more detail in the next subsection, which will touch upon the ideas posed above.

### 3.3.3 Thermodynamic Structure

Since our composites’ framework uses height for its vertical coordinate, examining dry and moist static stability is relatively simple compared to interpreting  $I^2$ . Virtual potential temperature  $\theta_v$  is plotted in Figure 3.12. All composites exhibit a low-level, virtually warm-core structure typical of hurricanes. The  $\theta_v$  inside the RMW is up to about 2 K warmer in the SS and WE composites compared to the IN composite. Noting that the non-intensifying composites are comprised of data from more-intense hurricanes relative to the IN group on average, these differences in  $\theta_v$  are sensible and corroborate the results of Zhang et al. (2011).

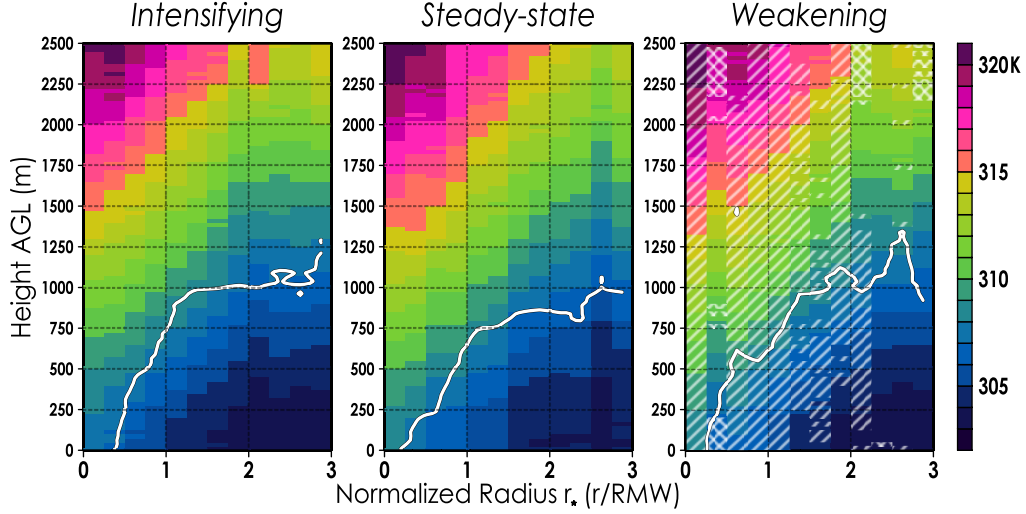


Figure 3.12: Similar to Figure 3.7, except virtual potential temperature  $\theta_v$  (in K) is shaded. Differences between IN and WE with statistical significance (to 95% confidence) are depicted with diagonal lines (where  $\theta_v$  is greater in WE) or cross hatching (where  $\theta_v$  is greater in IN) in the WE panel.

To calculate dry static stability, we lower the vertical resolution of the composites to 100 m to reduce noise. The dry static stability is defined and calculated as

$$N^2 = \frac{g}{\theta_v} \frac{\partial \theta_v}{\partial z}, \quad (3.4)$$

where  $N^2$  is the Brunt-Vaisälä frequency (note the word “dry” is used as this buoyancy frequency refers generally to unsaturated air). The vertical differential is evaluated using centered finite differencing; the resulting  $N^2$  from the reduced resolution composites is shown in Figure 3.13. A layer of weaker dry static stability is apparent near the surface in all composites. In all composites, the layer of relatively low  $N^2$  is most thick at greater radii and becomes thinner with decreasing radius until reaching a minimum inside the RMW. A shallow, surface-adjacent, near-superadiabatic area is seen in all composites near  $r_* = 2.5$ . In the lowest 750 m,  $N^2$  is largest inside the RMW in all groups. In the IN composite, a locally weak region of static stability is present at  $r_* \leq 0.5$  and below 400 m, which coincides with the hurricane’s eye region. Similarly, static stability is locally reduced in the same area in the other composites, though to a lesser degree. Above the inflow layer, more statically stable conditions are observed. Prior observational and numerical

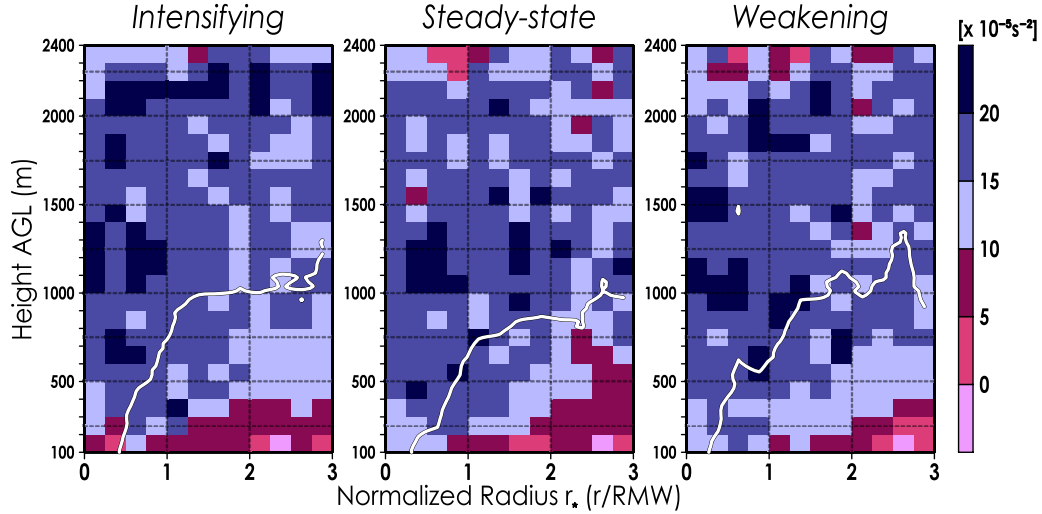


Figure 3.13: Axisymmetric, normalized radius-height cross sections of static stability  $N^2$  plotted between 100 m and 2400 m AGL (shaded in  $10^{-5} \text{ s}^{-2}$ ). The data in this figure were composited into lower resolution vertical bins with 100 m thickness to reduce noise. The vertical derivative of  $\theta_v$  is calculated using a centered finite difference. The white line is defined identically as in Figure 3.7.

analyses have also identified dry stability at the top of the frictional inflow in hurricanes (Zhang et al. 2011, 2013; Kepert et al. 2016). Kepert et al. (2016) concluded that the dry static stability is a result of diabatic cooling from rain falling and evaporating near the top of the BL, and cold-air advection decreasing with height (radial inflow advecting low- $\theta_v$  surfaces inward, which weakens and eventually reverses sign with increasing height). At  $r_* > 2$  above the inflow layer, SS and WE composites have generally lower  $N^2$  than the IN composite. If deeper vertical oscillations are more frequent in this area, then momentum and entropy above and near the top of the hurricane BL may have more potential to mix with the near-surface inflow. In this case, the entropy of inflowing parcels would likely be reduced before arriving at the eyewall, assuming they are not evacuated from the inflow via frictional ascent or convection.

Moist static stability can be assessed using equivalent potential temperature  $\theta_e$ , which is plotted in Figure 3.14. All groups have a core of high- $\theta_e$  air inward of the RMW. Although this feature of the low-level hurricane center has been noted previously (Bell and Montgomery 2008), there are apparent differences between the composites. Inside the RMW, the IN composite has the low-

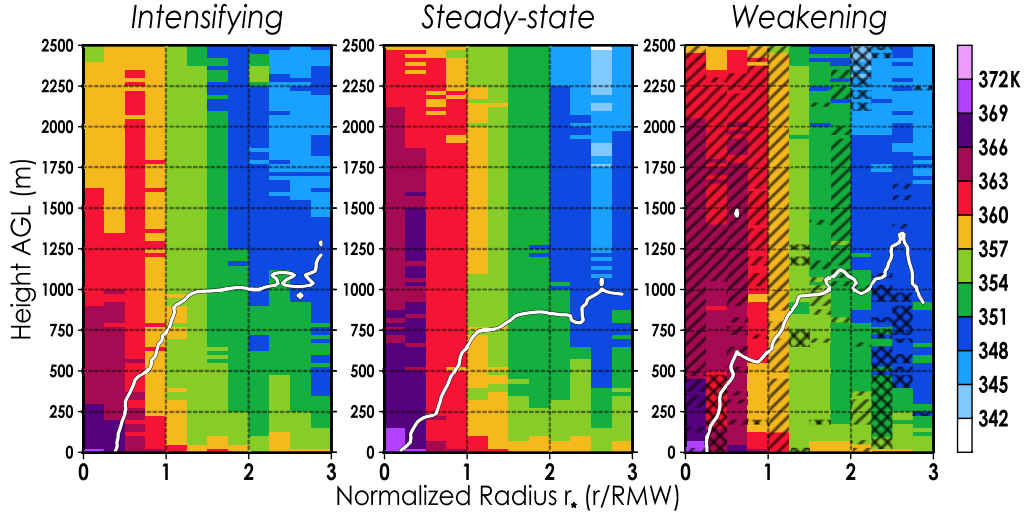


Figure 3.14: Similar to Figure 3.7, except equivalent potential temperature  $\theta_e$  (in K) is shaded. Statistically significant differences between IN and WE are plotted the same as in Figure 3.12 (using a darker color for clarity).

est  $\theta_e$  and the most-negative  $\partial\theta_e/\partial z$ . In contrast, the SS and WE composites have greater  $\theta_e$  and a weaker vertical gradient of  $\theta_e$  in the same area, usually between 360 and 366 K (about 3 K higher than seen in the IN group). In the WE composite,  $\theta_e$  is often significantly greater than IN inside the RMW and above  $z = 1$  km. All composites exhibit  $\partial\theta_e/\partial z < 0$  in most of the area below  $z \approx 500$  m outside the RMW [similar properties were found by Barnes (2008)]. The highest values of  $\theta_e$  are seen at  $r_* \leq 0.5$  near the surface in all groups. Inflowing parcels may overshoot past the RMW and interact with this region of maximized moist entropy, thereby increasing their  $\theta_e$  (apparent from the radial gradient of  $\theta_e$  across  $r_* = 0.5$ ). Assuming that the area where  $r_* \leq 0.5$  roughly represents the eye region, parcels that enter or interact with this region have to exit eventually, with the eyewall updraft being the likely avenue taken. In doing so, the parcels transport additional moist entropy acquired from the low-level hurricane eye. The degree to which a parcel's  $\theta_e$  changes while interacting with the high-entropy eye depends on residence time, the amount of local turbulence, and the difference in  $\theta_e$  between the parcel and its surroundings (Cram et al. 2007; Bell and Montgomery 2008; Guimond et al. 2016; Hazelton et al. 2017b,a).

In the IN composite, an area of  $\theta_e \gtrsim 366$  K is located near the surface adjacent to the inner-most

boundary of the inflow layer. As described earlier, inflowing air may overshoot into this high- $\theta_e$  area and increase its enthalpy via entrainment, all before returning to the eyewall. The moist static stability inside the RMW is lowest in the IN group (by virtue of having the highest  $\partial\theta_e/\partial z$ ); in this situation, eye-penetrating parcels that mix with the inner eyewall after spending time in the eye may more easily become buoyant, ascend above the BL, and release latent heat in the high- $I^2$  core. By comparison, the SS and WE composites have a weaker vertical gradient of  $\theta_e$  inside the RMW, indicating stronger moist static stability. Therefore, overshooting parcels from the non-intensifying groups may return to the inner eyewall and encounter greater conditional stability, unless they can acquire more enthalpy. The non-intensifying composites have a shallow near-surface area in the eye where  $\theta_e > 369$  K, so it is possible for overshooting parcels to increase their  $\theta_e$  to a higher value than in the IN group.

On the inner periphery of the WE composite's RMW, there are signs of conditional stability where  $\theta_e$  apparently increases with height (assuming that the air in the near-surface eyewall is saturated or nearly saturated). The inflow layer at this radius ( $r_* \approx 0.875$ ) has lower enthalpy in the WE composite than the SS composite, despite being associated with hurricanes of greater intensity on average. This implies some difference in the thermal properties of the eyewall in the frictional transverse circulation. Air parcels overshooting into the eye during weakening may have to acquire more enthalpy than during steady-state or intensification if they are to be locally buoyant (or at least moist-neutral) upon reaching saturation. If these parcels are *forced* to ascend at or within the RMW—for instance, because of ongoing eyewall convection—and are still conditionally stable, then reaching saturation would not prevent these parcels from decelerating pre-existing vertical motions in the eyewall. Alternatively, such air parcels could move outside of the RMW to an environment with lower  $\theta_e$  to attain moist neutrality or instability, which would imply a more-slantwise ascending trajectory in the eyewall. However, this nature of ascent would be expected to weaken the inner-core primary circulation. Parcels that become buoyant upon moving outside of the RMW may release diabatic heat there and reduce the temperature gradient across the RMW, which would result in a thermal wind adjustment of the primary circulation below the reduced temperature gradient that results in spin-down. Additionally, parcels moving across the RMW

from lower radii to “escape” conditional stability would also pull relatively low- $M_a$  air into the RMW, leading to locally direct spin-down.

The SS composite exhibits nearly moist-neutral profiles between  $r_* = (0.5, 1]$  between the surface and about 2 km AGL. Air that enters the low-level eye from the inflow layer appears to originate from an almost conditionally neutral environment. A near-surface layer of air in the eye where  $\theta_e > 366$  K is observed up to roughly 1.5 km AGL, representing a larger volume of high-entropy air with which overshooting parcels can interact. It is not apparent how to discern from this data how much these parcels may interact with the higher  $\theta_e$  environment above the surface. Regardless, the moist-neutral conditions above the inflow layer near the RMW suggest that there are less overshooting parcels in the SS composite that could mix with the inner eyewall and considerably affect local vertical motion upon reaching saturation.

At radii beyond  $r_* = 2.25$ ,  $\theta_e$  is relatively reduced in the inflow layer. This reduction is most evident in the WE composite, where  $\theta_e$  is significantly lower than that of the IN composite. The lower  $\theta_e$  may be a result of forced subsidence into the hurricane BL due to convergence and subsequent shallow ascent out of the BL at inner radii (Ooyama 1969; Kepert 2013), increased turbulent mixing in vertical shear (Kepert 2010), or convective downdrafts. By these mechanisms that bring lower enthalpy air into the BL, low- $\theta_e$  air may entrain with the strong near-surface inflow. Air parcels in the inflow will travel toward the RMW as their enthalpy is reduced, possibly affecting the core’s thermal properties upon arrival (and perhaps explaining the layer where  $\partial\theta_e/\partial z > 0$  is seen on the inside of the RMW in WE). Of course, it is still possible that inflowing air at outer radii recovers its enthalpy via heat fluxes before arriving at the RMW.

### 3.4 Summary

To improve our understanding of the hurricane BL and its role in vortex intensification, decay, and maintenance, soundings from Atlantic basin dropwindsondes launched between 1998 and 2015 were collected and composited based on intensity change. Three composites were created: intensifying (IN), steady-state (SS), and weakening (WE) storm composites. From an original pool of 12,045 gathered soundings, 3,091 were used in our composite analysis following quality control

and imposing spatial restrictions on data. The composites utilized an array of external data in their construction, including SFMR for compiling an RMW database (Uhlhorn and Black 2003; Uhlhorn et al. 2007; Klotz and Uhlhorn 2014), HURDAT2 for discerning intensity and intensity change (Landsea and Franklin 2013), SHIPS for shear-relative positioning (DeMaria et al. 2005), and 2-minute track data for TC location (Willoughby and Chelmow 1982).

The composite datasets are composed of samples from various hurricanes with varying properties of intensity, size, motion, and general structure. A climatology of the data showed that most hurricane sampling in the Caribbean Sea and southwestern Gulf of Mexico is associated with intensifying storms, suggesting that the environment is likely more conducive for intensification [e.g., high oceanic heat content (OHC) (Leipper and Volgenau 1972), weak deep-layer shear (DeMaria 1996; Gallina and Velden 2002; Paterson et al. 2005)]. A considerable amount of data originates elsewhere in the Gulf of Mexico and near the eastern United States coastline, where influences of land, large-scale extratropical systems, and spatially variable SSTs [even on the vortex-scale, as suggested in Shi and Bourassa (2019)] may affect hurricane intensity positively or negatively. Most dropsondes appear to be launched in the eye and eyewall regions, and less sampling occurs outward of the eyewall. Some spatial heterogeneity in sampling hurricane intensity was observed in the three composites, which we concluded may obfuscate interpretations of the data.

All azimuthally averaged composites showed a low-level tangential wind just below 1250 m AGL, and a nearly logarithmic decrease of  $v$  with decreasing altitude below the jet [in agreement with F03 and Powell et al. (2003)]. The WE composite exhibited the strongest inner-core primary circulation, while the IN group was associated with generally weaker  $v$  across the composite field. Intensity sampling in each composite showed that these differences in  $v$  are driven somewhat by sampling biases; on average, weaker storms are sampled during intensification, while intense storms are more often associated with weakening. To account for these sampling issues, we computed a difference field between  $V_{max}$  and  $v$  (named  $\delta v$ ). In the difference field, the IN composite was associated with the deepest jet in the eyewall region, indicating stronger local vertical motion or turbulence compared to the SS and WE storms. Inertial stability was inferred from the difference field; the IN composite's eyewall region appeared more inertially stable, and the area above the inflow layer and outside of the eyewall was less inertially stable when contrasted with non-

intensifying groups. These results suggest that non-intensifying hurricanes may be more likely to have low-level ascent outside the RMW than intensifying hurricanes. The deep tangential wind jet in the IN group, along with apparently high  $I^2$  in the eyewall and low  $I^2$  outside the eyewall, indicates that convection may be confined about the RMW during intensification.

Azimuthally averaged secondary circulations from the composites were evaluated. All composites showed a surface-adjacent inflow layer, often situated beneath a radially local tangential wind maximum. All groups had intense near-surface inflow close to the RMW. Every composite showed inflow that extended inward through the RMW, suggesting eyewall penetration near the surface. Strong inflow at larger radii was seen more in the non-intensifying composites, which would be linked to differences in the radial convergence field and subsequent forced ascent. The stronger inflow at outer radii may be tied to enhanced radial convergence at these radii in SS and WE storms, which could lead to local ascent and possibly convection outside the RMW. The results of the axisymmetrized secondary circulation analysis are likely impacted somewhat by sampling biases in intensity.

Axisymmetric dry thermodynamics were examined in the composites using virtual potential temperature. Non-intensifying storms appeared to have the warmest  $\theta_v$  inside the RMW, likely due to the greater average storm intensity relative to IN. Measures of dry static stability were minimized in the inflow layer of each composite and greater above the inflow layer, corroborating prior analyses (Zhang et al. 2011; Kepert et al. 2016). At outer radii in non-intensifying composites,  $N^2$  was generally reduced above the inflow layer compared to the IN composite. Based on the dry static stability observed at outer radii, vertical motions between the inflow layer and the free atmosphere aloft might be more likely in non-intensifying storms at these radii. Assuming the free atmospheric air has less moist entropy than inflowing air, the vertical exchange of air between the BL and the air aloft would reduce the MSE of inflow toward the eyewall.

Similarly, moist thermodynamics were also highlighted in an axisymmetrized framework. All composites had areas of high- $\theta_e$  in the eye region, with an often negative  $\partial\theta_e/\partial z$  inside the RMW. The IN group had the most pronounced vertical gradient of  $\theta_e$  (and thus the most conditional instability) in the eye. Horizontal mixing along a hurricane's inner eyewall may mix high-entropy air of the low-level eye into the eyewall, introducing a source of buoyancy and affecting local con-

vection (Montgomery et al. 2006b). If horizontal mixing occurred along the inner eyewall through some depth of the lower troposphere, then the profiles of conditional stability in the eye and eyewall should tend toward one another. The eye with the most-negative  $\partial\theta_e/\partial z$  was observed in IN, implying that conditional instability could be most readily imported to the eyewall via horizontal mixing during intensification. At greater radii, relatively low  $\theta_e$  air is found in the inflow layer of all composites; this property is most apparent in the WE composite, where local  $\theta_e$  is significantly lower than that found in the IN composite. Low-entropy air from outside the hurricane BL may entrain with the frictional inflow more effectively during weakening phases, which we hypothesize can affect the air that eventually arrives at the RMW. The composite differences in  $\theta_e$  in the inflow layer at outer radii may be due to differences in OHC and heat fluxes, vertical motion near the top of the BL due to frictionally forced ascent and descent, convective downdrafts, and vertical diffusion from vertical shear.

Based on the results of this composite analysis, a simple schematic summary of the azimuthal-mean BL structures of intensifying and non-intensifying hurricanes is provided in Figure 3.15. The structures differ in their primary circulation (and thus inertial stability, which is greater outside the RMW in non-IN hurricanes), secondary circulation (and thus BL convergence, potentially leading to convective motions above the BL), and thermodynamics. Loosely speaking, the differences between IN and non-IN hurricanes imply that non-IN storms tend to experience hindrances to inner-eyewall convection. Such hindrances could affect the hurricane's intensity directly via reduction of the vertical advection of  $M_a$ , or indirectly through weakening the hurricane's warm-core structure by reducing MSE at the root of inner-eyewall convection.

### 3.5 Discussion

Among the caveats associated with our composite analysis, the most pressing ones are linked to a limited number of observations. To combat this limitation, we combined thousands of samples from many different hurricanes, which is itself problematic because no two hurricanes are entirely alike and no hurricane assumes an actual state of stasis. Even with this compromise, we were unable to perform a detailed asymmetric analysis of the inner-core hurricane boundary layer using

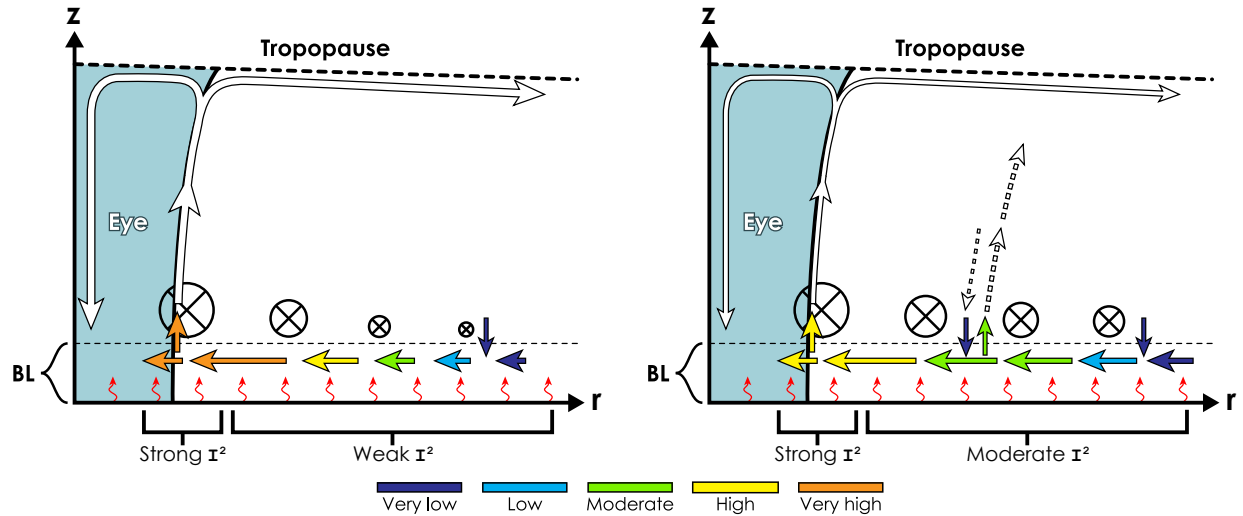


Figure 3.15: Radius-height conceptual diagrams of the azimuthal-mean tropospheric structure in (left) IN hurricanes and (right) non-IN hurricanes, based on the composite analysis. Circles with crosses indicate tangential flow (into the page), and their sizes are proportional to their magnitude. Regions of differing inertial stability are marked along the radial axis. Vectors in the BL are shaded by MSE using the scale at the bottom of the figure. Radial vectors in the BL have lengths proportional to radial wind speed. Red wavy vectors at the surface indicate upward heat fluxes at the air-sea interface. Above the BL, dashed vectors indicate possible convective motions, and solid vectors represent the secondary circulation in the free atmosphere with boldness proportional to circulation strength.

our composites due to a lack of data. The weaknesses of our composite analysis leave us with a few critical questions; those most apparent and within the scope of this endeavor include:

- Would the interpretations of our composite analysis be supported in analyses of individual hurricanes?
- How does the asymmetric structure of the hurricane BL differ between modes of intensity change?
- How is the asymmetric BL structure modulated by environmental factors like far-field vertical wind shear?

While these questions would be quite difficult to address with the observations currently available due to data limitations, they could be addressed in case studies using numerical simulations (assuming that the employed model appropriately represents the physics). In Chapters 4 and 5,

we will examine the BL structure of individual Atlantic basin hurricanes using high-resolution simulations from the Weather Research and Forecasting model for advanced research (Skamarock et al. 2008). Our case studies will assess the axisymmetric *and* asymmetric structures of the hurricane BL. We will analyze the effect of differing environmental vertical wind shear on hurricane BL structure by simulating two cases: Hurricanes Irma in 2017 and Earl in 2010, which were associated with generally weak and moderate deep-layer vertical shear, respectively.

# CHAPTER 4

## LOW-SHEAR NUMERICAL ANALYSIS: HURRICANE IRMA (2017)

The findings and limitations of our composite analysis in Chapter 3 lead us to this case study of Hurricane Irma in 2017. This simulation [and that of Hurricane Earl (2010) in Chapter 5] allows us to address some of the weaknesses of the composite analysis, including whether azimuthal-mean BL structure in individual hurricanes is at all consistent with the observational composite. The numerical analysis also allows us the freedom to investigate azimuthal structure of the hurricane BL, which was omitted from our composite analysis due to data limitations. Hurricane Irma is chosen to represent a situation where a well-developed hurricane is contained in an environment of weak-to-moderate deep-layer vertical shear, which should affect vortex and BL structure (e.g., Zhang et al. 2013; Barnes and Dolling 2013; DeHart et al. 2014).

### 4.1 Methodology

For this case study, we will use version 3.9 of the Weather Research and Forecasting model for advanced research (WRF-ARW) to simulate Hurricane Irma well prior to landfall in 2017. A very high-resolution domain is necessary to capture mesoscale features of interest in the hurricane BL. We use four domains of progressively enhanced horizontal resolution: 36 km in the outermost domain, 12 km in the second domain, 4 km in the third domain, and 1.333 km in the innermost domain. Additionally, the four domains use progressively smaller integrative timesteps to ensure numerical stability, with each domain assuming a timestep in seconds equal to its horizontal resolution in km multiplied by 3 (e.g., the outermost domain uses a 108 second timestep, and the innermost nest uses a 4 second timestep). The model uses a 20 hPa top with 71 terrain-following ( $\eta$ ) vertical levels. The simulation time spans from 0000 UTC 03 September to 0000 UTC 11 September, with complete output for the innermost domain every 15 minutes.

To minimize computation time and the size of output data, we choose the vortex-following domain option for WRF-ARW, which allows spatial domains to move in tandem with a mid-level vortex signature (and thus, eliminate the need for an unreasonably large domain of very high resolution). For the purposes of repositioning the center of a domain, the vortex's position is calculated as the minimum geopotential detected on a particular vertical level in the middle troposphere. The model chooses the vertical level with a base-state geopotential closest to that at 600 hPa. The domains specified at initialization are shown in Figure 4.1. Initial and boundary conditions are provided through National Centers for Environmental Prediction (NCEP) Final (FNL) Operational Model Global Tropospheric Analyses (NCEP 2000). These data are available every six hours and have  $1^\circ$  spatial resolution. Two-way feedback across the boundaries of each domain is permitted, and no grid nudging at the boundaries is used.

The Yonsei-University (YSU) planetary boundary layer physics scheme (Hong et al. 2006) is used for this simulation. Exchange coefficients (e.g.,  $C_D$ ) are calculated using Monin-Obukhov similarity theory in the revised MM5 surface layer scheme (Jiménez et al. 2012). To account for observed wind-speed dependencies in bulk surface exchange coefficients, we use the model's alternative formulation for these exchange coefficients intended for TC applications. In the two outermost domains (with 36 km and 12 km resolution, respectively), the Kain-Fritsch cumulus convection parameterization scheme is employed (Kain 2004); the two inner-most domains use no cumulus parameterization, and thus attempt to resolve convection explicitly. Land surface physics are represented using the unified NOAH land surface model (Tewari et al. 2004). Longwave and shortwave radiation are handled with the RRTMG radiation schemes (Iacono et al. 2008). The Morrison 2-moment microphysics scheme (Morrison et al. 2009) is used. A summary of the physics packages and options used for this simulation (with other model details) is given in Table 4.1.

Using the WRF-ARW post-processing program (ARWpost), model output is converted from its staggered Arakawa C-grid with a terrain-following vertical coordinate to a longitude-latitude coordinate system with height surfaces. During our initial analysis, the WRF-diagnosed vortex center (based on the 600-hPa geopotential minimum) was found to oscillate about a near-central point in the hurricane with an approximate period of 1 hour, resulting in an apparent artificial wave-like signal in the asymmetric structure. To remedy this, we used an iterative method that calculates

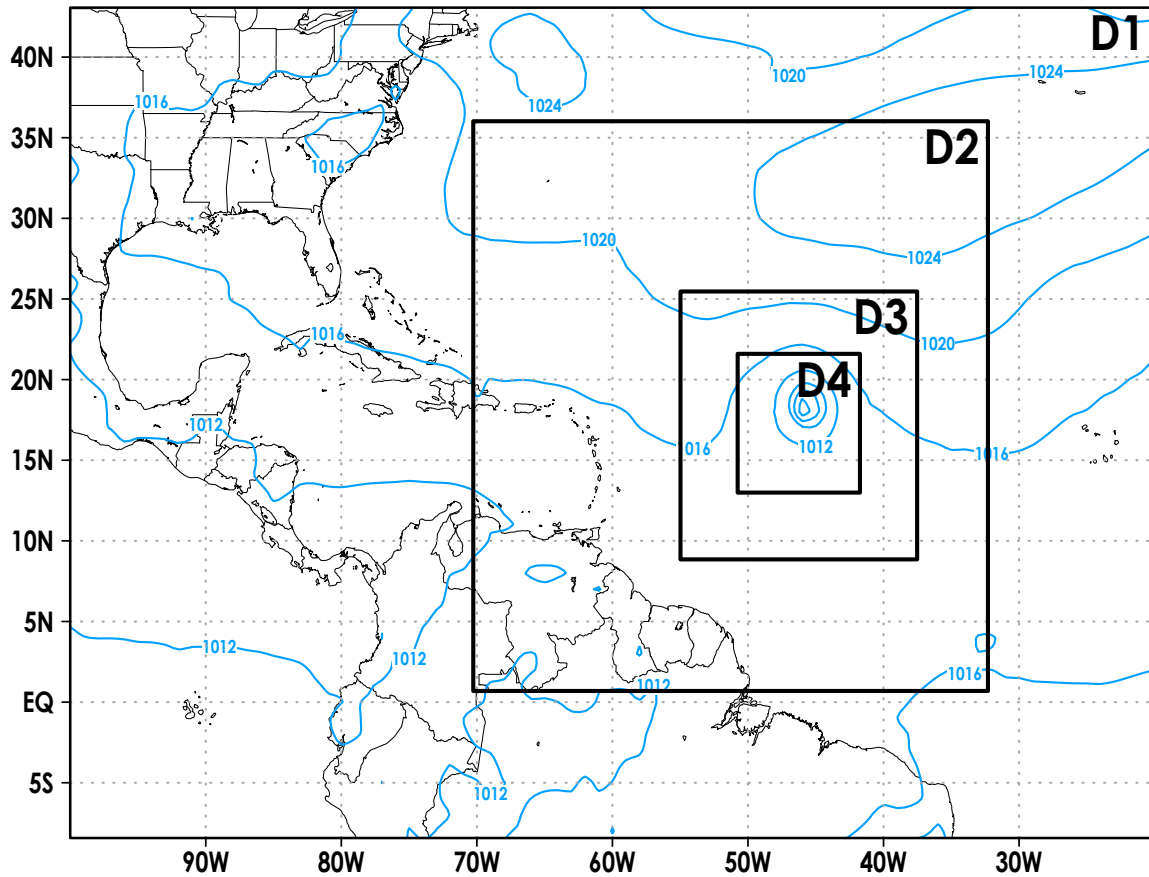


Figure 4.1: Map illustration of the four domains set at initialization (0000 UTC 03 September 2017) for this WRF-ARW simulation of Hurricane Irma. Contours of mean sea-level pressure (from eta reduction) at initialization time from NCEP FNL Operational Global Analysis data (NCEP 2000) are drawn in blue (hPa, 4 hPa interval). The outermost domain (region containing “D1”) is static with a horizontal resolution of 36 km. Domains labeled “D2,” “D3,” and “D4” are vortex-following with horizontal resolutions of 12 km, 4 km, and 1.333 km, respectively.

the hurricane center based on a pressure centroid at  $z \approx 1.84$  km (Nguyen et al. 2014). This method to calculate the storm center has been found to minimize apparent vortex tilt in hurricanes (Ryglicki and Hart 2015). The WRF-diagnosed vortex center was used as the first-guess center in this method, and the environmental pressure (required by the method) was calculated using a 10-km wide annulus centered at  $r = 500$  km (the nearest-in-time output from the third domain with 4-km and 6-hour resolution was used to calculate environmental pressure). The new center

Table 4.1: Summary of details and specifications for the WRF model used to simulate Hurricanes Irma (2017) and Earl (2010). The simulations for Hurricanes Irma and Earl differ only in simulation time and domain specification.

Dynamical core	Advanced Research WRF (Skamarock et al. 2008)
Version	3.9
Domain type	Vortex-following
Horizontal resolution	36 km (D1), 12 km (D2), 4 km (D3), 1.333 km (D4)
Vertical levels	71 with 20 hPa model top
Timestep	108 s (D1), 36 s (D2), 12 s (D3), 4 s (D4)
Initial-boundary conditions	6-hourly NCEP FNL (NCEP 2000)
Feedback option	Two-way domain feedback
Planetary boundary layer	YSU (Hong et al. 2006)
Surface layer	Revised MM5 (Jiménez et al. 2012) with exchange coefficients for TC applications
Land surface model	Unified NOAH (Tewari et al. 2004)
Cumulus parameterization	Kain-Fritsch (D1 and D2, Kain 2004); none (D3 and D4)
Radiation physics	RRTMG (Iacono et al. 2008)
Microphysics	Morrison 2-moment (Morrison et al. 2009)

was determined after 15 iterations. Radial distance is calculated as outlined in section A.2.

Generally, the flow analyzed here will be relative to storm motion. The storm’s zonal and meridional motions are calculated using 6-hour time-centered differences of central longitude and latitude, respectively. Azimuthal structure will be analyzed relative to deep-layer shear direction. We calculate the shear by first averaging the horizontal wind over a storm-centered 200–800 km annulus on height surfaces closest to 850 hPa and 200 hPa, and then we subtract the  $\sim$ 850 hPa annulus-mean wind from the  $\sim$ 200 hPa annulus-mean wind to yield the shear vector. We follow this method to be comparable with the deep-layer shear parameter from SHIPS data (DeMaria et al. 2005). Because of the size of the annulus, we must use winds from the third domain, which has 6-hourly output. Thus, the shear vector is calculated explicitly every six hours. We use temporal linear interpolation to estimate the shear every 15 minutes between 6-hourly intervals when shear is calculated explicitly.

The ARWpost-processed data are then regridded to a storm-centered cylindrical coordinate

system with radius  $r$ , shear-relative azimuth  $\psi_s$ , and height  $z$  following section A.2. The cylindrical grid extends outward to  $r = 200$  km and has 2 km radial resolution,  $90^\circ$  azimuthal resolution (quadrants), and a vertical grid identical to that output by ARWpost. The maximum azimuthally averaged, storm-relative tangential wind at  $z \approx 1.84$  km is used to determine storm intensity  $V_{max}$ , the radius of maximum winds (RMW), and all their derivative forms.

For the purposes of finding the rate of intensity change, the intensity data are temporally smoothed with a time-centered 3-hour box smoother. To determine the rate of intensity change for a given output time, we calculate the linear best-fit line of smoothed intensity versus time using data from the immediate output time with both the preceding and following six hours of output time (i.e., a 12-hour time-centered linear regression, with  $N = 49$ ). The hurricane is deemed to be either in an intensifying (IN), weakening (WE), or near-steady state (SS) using the slope of the best-fit line following Rogers et al. (2013a) (in line with our earlier composite analysis):

- Intensifying (IN):  $\frac{\Delta V_{max}}{\Delta t} \geq \frac{20 \text{ kt}}{24 \text{ h}}$
- Steady-state (SS):  $\frac{20 \text{ kt}}{24 \text{ h}} > \frac{\Delta V_{max}}{\Delta t} \geq -\frac{10 \text{ kt}}{24 \text{ h}}$
- Weakening (WE):  $\frac{\Delta V_{max}}{\Delta t} < -\frac{10 \text{ kt}}{24 \text{ h}}$

As this analysis intends to detail and explain azimuthal structure, we will need to refer to features (e.g., convection) in system- and environment-based reference frames, such as those relative to storm motion or deep-layer shear. We will use the following terminology to refer to certain frames of reference:

- “Downshear” and “upshear” are used respectively to reference areas ahead of and behind the heading of 850–200 hPa shear,
- “Downstream” and “upstream” are similarly used to reference areas relative to the *heading of storm motion*, and
- “Downwind” and “upwind” are used to reference areas relative to the actual wind.

To allow the model time to “spin up” the hurricane (i.e., to develop vortex structure at model resolution, starting from relatively coarse initial conditions), we will not analyze the first day of

model output in detail. For this study, we want to avoid analyzing data associated with strong TC-land interactions (particularly, those between Hurricane Irma and the islands of Hispaniola and Cuba). Thus, we will limit our analysis also to periods when such interactions are not occurring obviously. Unless otherwise noted, analyses and results refer to data taken from the innermost (fourth) domain.

## 4.2 General Overview

First, we examine the broader aspects of the simulation result to add context to our analyses of boundary layer structure. The outgoing longwave radiation (OLR) field is used as an analog to infrared satellite imagery, and is shown at multiple times in Figure 4.2. For the analysis period, the simulated Hurricane Irma tracks west-northwestward at 8–18 kt, moving to the north of Puerto Rico and Hispaniola. On 05 September, weak-to-moderate shear is directed south-southwestward, and the lowest OLR (i.e., lowest brightness temperatures, implying more-elevated cloud tops) is visible in Irma’s outer core downstream-left of the storm motion, as well as downshear and to the left of shear in Irma’s inner core. Deep convective termini can be associated with these lowest values of OLR in the inner core, so it appears that inner-core convection may initiate downshear-right and end primarily to the left of shear. Over time, the shear rotates counter-clockwise until becoming almost antiparallel with the storm motion on 08 September. As the shear orients itself against the storm motion by 07 September, the inner-core asymmetry in OLR is minimized, suggesting relatively axisymmetric convective structure.

Prior work suggests that BL inflow is asymmetrically stronger (i.e., deeper and/or more intense) downstream of the storm motion, downstream of the deep-layer shear, and downwind from nearby land (Barnes and Dolling 2013). Thus, ignoring the effects of nearby land, one might expect that the BL inflow is strongest downstream and to the right of the shear vector at the start of the analysis period, and then becomes more axisymmetric as the shear becomes east-southeastward. By 08 September, however, Irma is tracking about 100 km to the north of Hispaniola; at this distance, Hispaniola should have a substantial frictional effect on Irma’s inner core. Including the expected effects of land on 08 September, it is expected that the BL inflow is strongest downshear at that

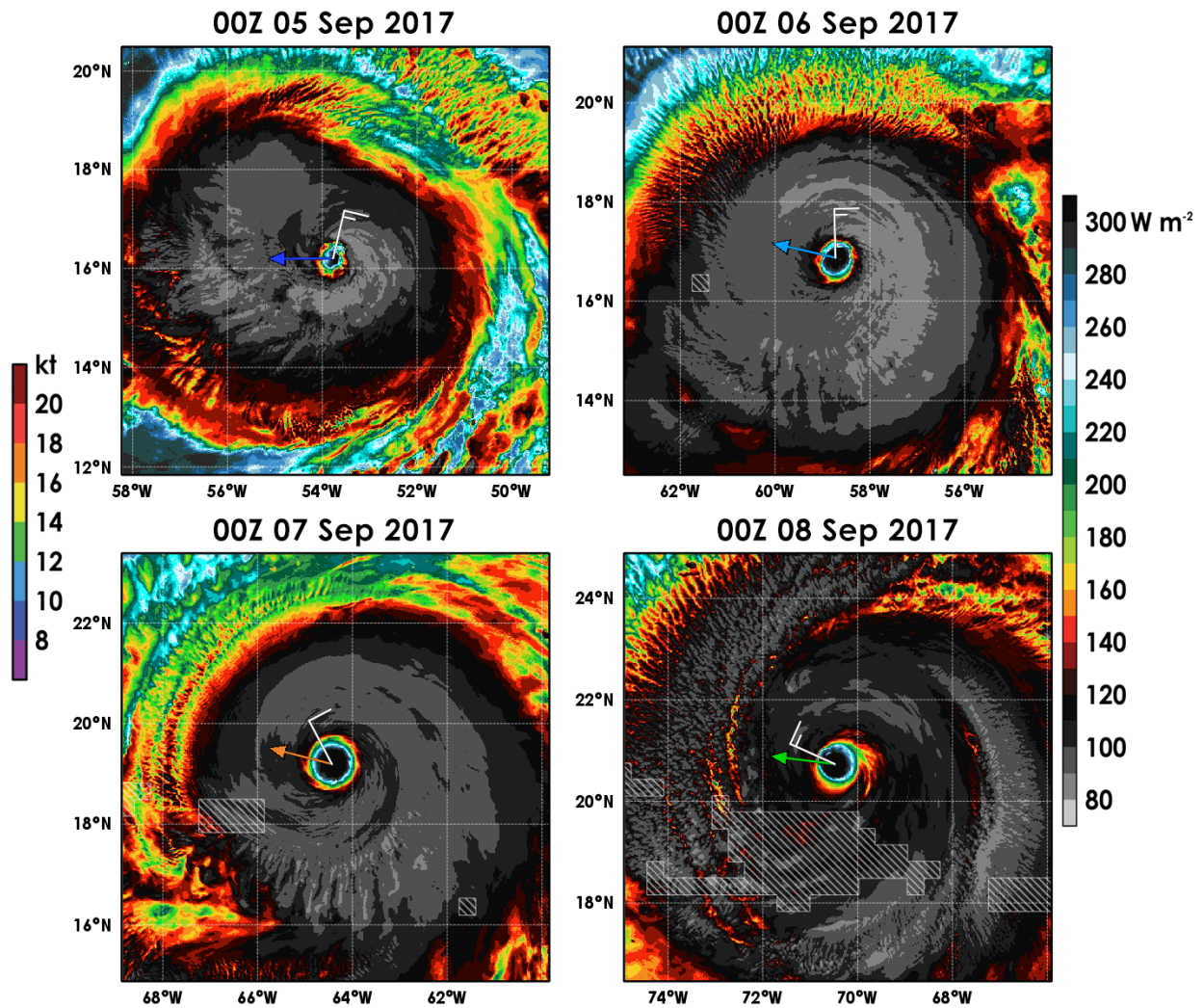


Figure 4.2: Simulated outgoing longwave radiation at the top of the atmosphere (shaded using the right-side color bar,  $W m^{-2}$ ) at various times (labeled at the top of each panel). A storm-motion vector is drawn at the diagnosed center of Hurricane Irma (shaded based on magnitude in knots using the left-side color bar), along with a wind barb denoting the deep-layer shear. Gray hatched areas represent land used in the model.

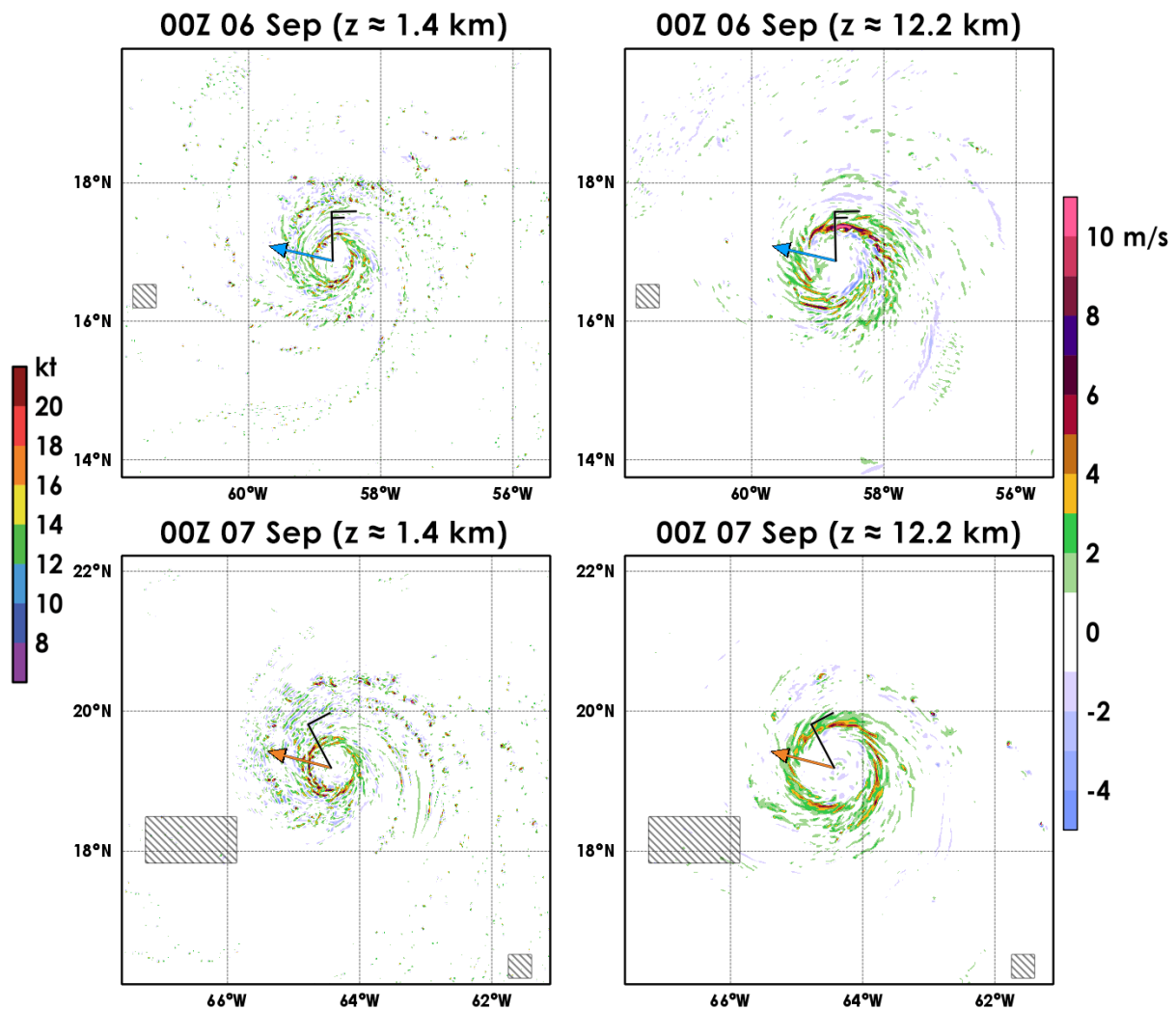


Figure 4.3: Vertical velocity ( $\text{m s}^{-1}$ ) at the model levels closest to 850 hPa ( $z \approx 1.4$  km, left panels) and 200 hPa ( $z \approx 12.2$  km, right panels) in Hurricane Irma, shaded using the right-side color bar. The snapshots are taken from 0000 UTC 06 September (top panels) and 07 September (bottom panels). The storm-motion vector is drawn at the center of the hurricane (shaded using the left-side color bar). A wind barb representing the deep-layer shear is drawn in black at the center. Gray hatched areas represent land used in the model.

time. The BL inflow is directly tied to radial convergence and thus vertical motion. To examine these ideas directly, Figure 4.3 depicts the simulated vertical velocity in the lower- and upper-troposphere on 0000 UTC 06 September and 07 September, as the shear turns counter-clockwise from orthogonal and pointing left of the storm motion. The storm motion increases over the same time period. Low-level eyewall convection on 06 September appears more prevalent downstream and to the right of storm motion, as well as in the downshear-left quadrant. At the same time, strong upper-level vertical motion is generally concentrated upshear and to the left of shear, with some wave-like features with strong upward motion immediately downshear. Based on the vertical structure of convection on 06 September, it appears that the upshear and downshear convective tops are linked with low-level convection downshear-left and right of the storm motion, respectively. By 07 September when shear becomes weaker and more antiparallel with Irma’s increased translational speed, the low-level convection is strongest to the right of shear and downstream of Irma’s motion. Upper-level vertical velocity is quite axisymmetric in appearance at this time, which may be related to more axisymmetric BL convergence.

Hurricane Irma’s simulated track is drawn in Figure 4.4, along with best track data from HURDAT2 (Landsea and Franklin 2013) for the simulated time period. The simulated storm generally follows the best track, but also lags the track by about 6 to 12 hours. Irma approaches and eventu-

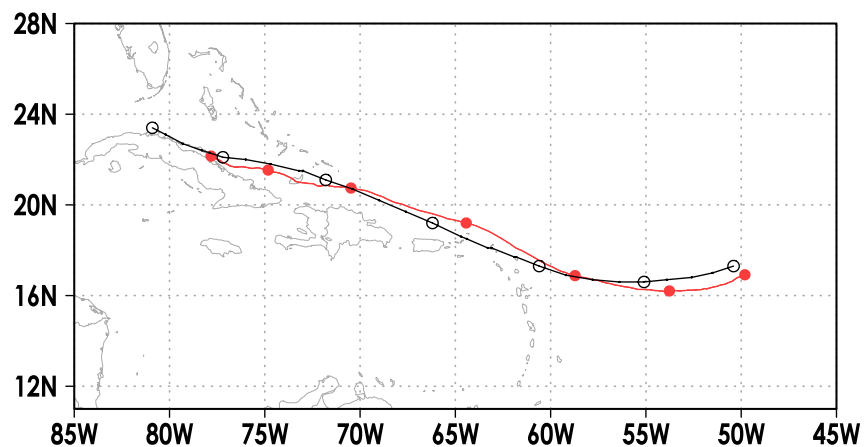


Figure 4.4: Hurricane Irma’s simulated center track (red) and HURDAT2 best-track center (black) as it generally moved westward between 04 September and 10 September. Circles mark Hurricane Irma’s position at 0000 UTC for a given day.

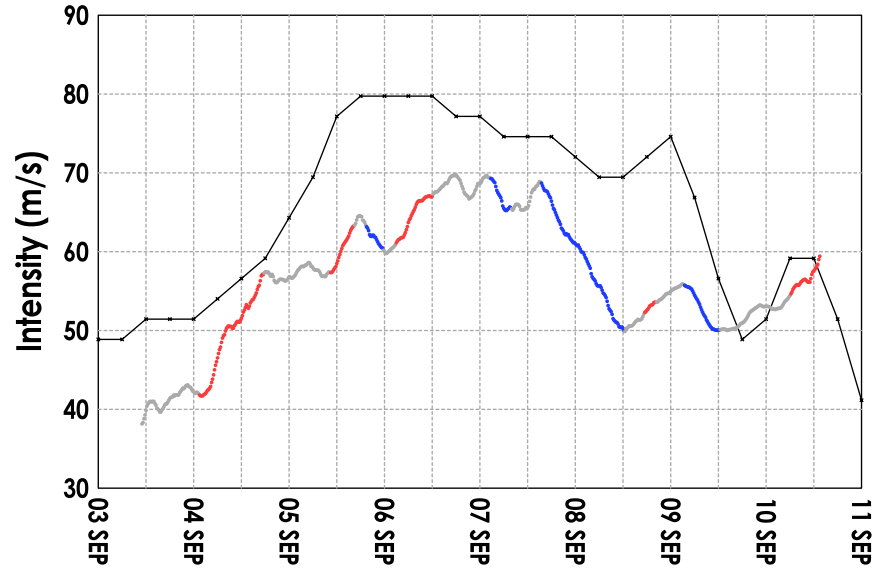


Figure 4.5: Time series of Hurricane Irma’s modeled intensity ( $\text{m s}^{-1}$ ) throughout the simulation, shaded by intensity change identifiers (red, intensifying; gray, steady-state; blue, weakening). The 6-hourly HURDAT2 best-track intensity is plotted in black.

ally makes landfall in Cuba on 10 September in the model, which deviates from Irma’s real track (although Irma did closely follow the Cuban coastline in reality). Figure 4.5 shows Irma’s modeled intensity in comparison to best track data; the simulation reasonably follows Irma’s evolution to major-hurricane status, and captures Irma’s sustained high intensity prior to moving north of Hispaniola. With the exception of one weakening period late on 05 September, the modeled intensity generally increases or remains neutral over time between 04 September and 07 September. Between 1200 UTC 05 September and 1200 UTC 06 September, Irma’s modeled intensity is considerably less than observed, possibly due to the way  $V_{max}$  is determined here (which smooths wind data over time and space). The simulated storm’s intensity begins to fall rapidly around 1500 UTC 07 September, during its pass by Hispaniola. In observations, when Irma moved north of Hispaniola between 1200 UTC 07 September and 1200 UTC 08 September, it did weaken, though not as dramatically as simulated. The discrepancy between Irma’s simulation and reality may be due to Hispaniola’s low-resolution representation in the model, which is forced to share resolution with the parent nest (36 km).

While the simulation does not (and indeed, could not be expected to) replicate Irma’s track and intensity exactly, it reasonably represents Irma’s development, appearance, and environment prior to 08 September. We clarify that this research (as well as the forthcoming analysis of Hurricane Earl) endeavors *not* to replicate the physics and dynamics of Hurricane Irma as observed, but to reasonably represent the case in the context of its environment and development for the sake of analysis relative to diagnostics from the model results. In other words, the BL analysis is conducted not in reference to Irma as observed—it is conducted in reference to the model’s representation of Irma.

## 4.3 Primary Circulation

### 4.3.1 Axisymmetric Structure

From prior dropsonde-based observational analyses (Franklin et al. 2003; Zhang et al. 2011, 2013, as well as our own analysis in Chapter 3), the strongest BL tangential winds are often at  $\sim 700$  m AGL. Figure 4.6 shows that Hurricane Irma’s azimuthally averaged primary circulation possesses that attribute, which prevails throughout most of the simulation. Generally, Irma’s tangential winds weaken with increasing  $r$  outside the wind jet near  $r = 35$  km, and  $v$  also weakens with decreasing altitude inside the radial inflow layer. The  $r$ - $z$  profiles of absolute angular momentum  $M_a$  show a strong radial gradient of  $M_a$  near the RMW, and a weaker gradient of  $M_a$  outside of  $r \approx 60$  km. At a given radius outside of the RMW,  $M_a$  tends to be greatest near the top of the kinematic BL (represented as a “nose” of  $M_a$  along the top of the radial inflow layer), with a logarithmic vertical profile of  $M_a$  within the BL in coincidence with the expected frictional dissipation of momentum. Near the top of the radial inflow layer, the advection of high- $M_a$  air seems to outweigh the dissipation of  $M_a$  by friction, as evidenced by the weakly supergradient flow there (bottom of Figure 4.6). Although our earlier composite analysis precluded a direct examination of inertial stability, we are free to analyze that property for this simulation (shown also in Figure 4.6). High inertial stability is situated within and inward of the eyewall, as is typical and expected for mature hurricanes given their radial profiles of  $M_a$ . The greatest values of  $I^2$  are located inward of the tangential wind jet, owing to the strong positive radial gradient of  $M_a$  and relatively low  $r$ .

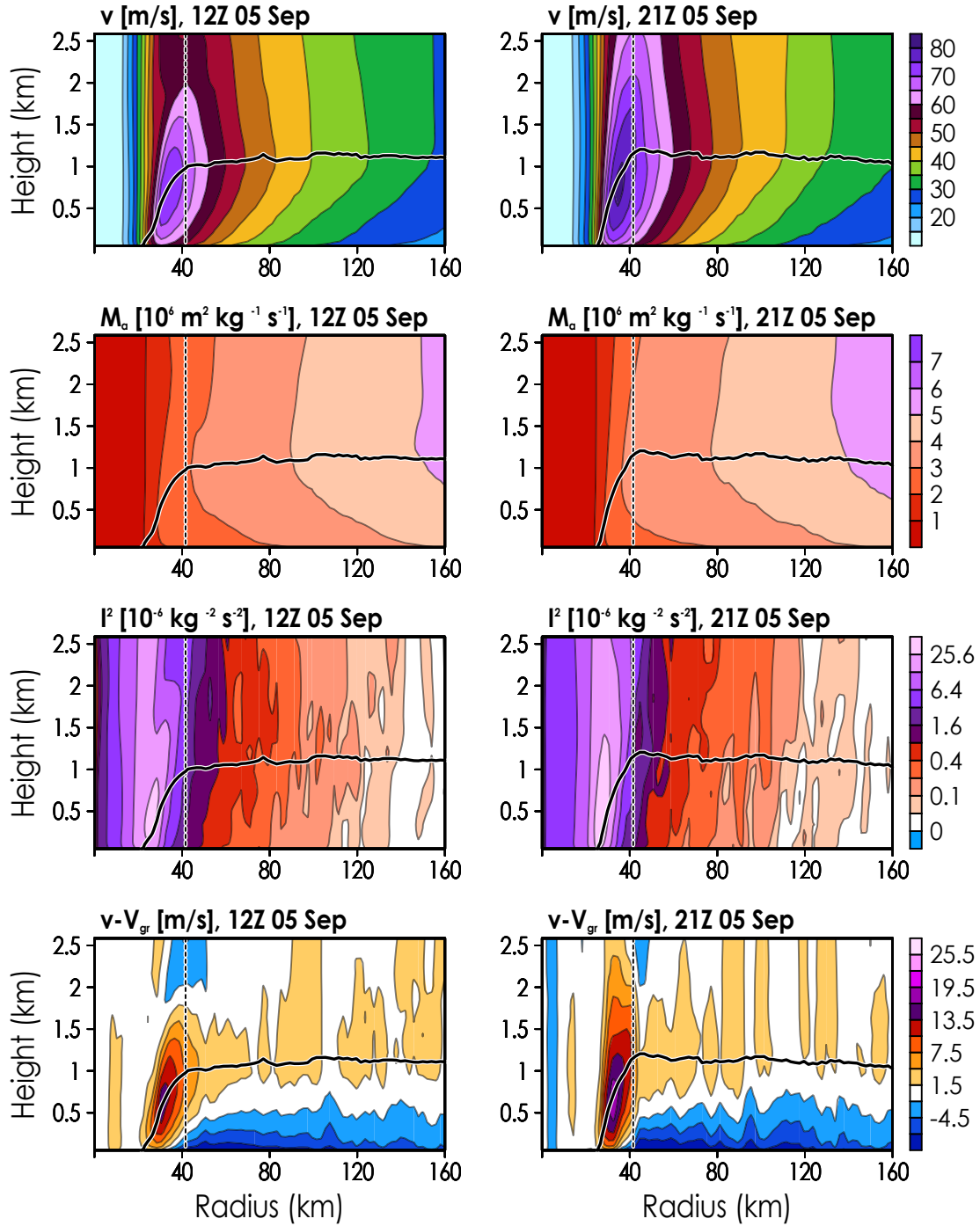


Figure 4.6: Radius-height plots of Hurricane Irma’s azimuthally averaged primary circulation using storm-relative tangential wind  $v$ , absolute angular momentum  $M_a$ , inertial stability  $I^2$ , and agradient wind  $v_{ag} \equiv v - V_{gr}$  on 1200 UTC 05 September (left, during IN) and 2100 UTC 05 September (right, during WE). Each row of figures uses the color bar to its right; units are given above each plot. The dashed, black line marks the RMW. The bold, black line indicates the radial inflow layer (10% of the maximum inflow). The scale used for  $I^2$  is geometric (0, 0.05, 0.1, 0.2, 0.4, ...).

Inertial stability tends to decrease with increasing radius outside of the RMW, though local areas of enhanced or reduced  $I^2$  are apparent. Radial variability of BL  $I^2$  seems to fluctuate over time, presumably due to convective and turbulent transport of momentum.

Assuming a near-gradient balance of tangential winds in the free atmosphere, an assessment of supergradient and subgradient tangential flow can be useful in identifying local or widespread dynamical imbalances where the advection of  $M_a$  (primarily by radial flow, presumably) outweighs or is outweighed by frictional dissipation. The bottom row of  $r$ - $z$  cross sections in Figure 4.6 reveals the presence of supergradient and subgradient flows. In the radial inflow layer, the flow becomes substantially subgradient with decreasing altitude due to friction. The tangential wind jet is strongly supergradient as the advection of greater  $M_a$  is likely maximized there (whether through radial advection of  $M_a$  at the level of the wind jet, vertical advection of  $M_a$  originating from the surface inflow layer below the jet, or a combination of both). The supergradient jet late on 05 September during a brief WE phase is more vertically oriented than the jet during IN periods before and after this time. It may be possible that low-level eyewall convection becomes less slantwise during this WE period, and then becomes more slantwise (as was apparent in the prior IN phase) afterward. This would lead to high- $M_a$  air from the BL being advected upward into an area radially inward of the pre-existing maximum  $v$  aloft, instead of into that area of maximum  $v$ . Near and above the top of the BL inflow, tangential winds fluctuate between near-gradient and weakly supergradient. As implied by the  $M_a$ -field, the supergradient flow at the top of the BL could be a result of positive  $M_a$  advection outweighing frictional/turbulent dissipation. The strongly supergradient wind jet near the RMW becomes more supergradient as it intensifies toward peak intensity, reflective of increasing positive  $M_a$  advection there during IN (not shown). The radial inflow near the RMW is expected to strengthen in response to Irma's intensification as more momentum is dissipated by friction (and thus enhancing a gradient forcing).

Axisymmetrized, storm-relative tangential winds are plotted at the height of the wind jet ( $z \approx 710$  m) as a function of time and radius in Figure 4.7. Between 04 September and 07 September, Irma's low-level  $v$ -field tends to intensify steadily (except in the calm eye), and Irma reaches its peak intensity near the end of 06 September. As Irma intensifies, high- $M_a$  surfaces from outer radii in the BL are drawn toward the RMW (shown also in Figure 4.7), perhaps as a result of the

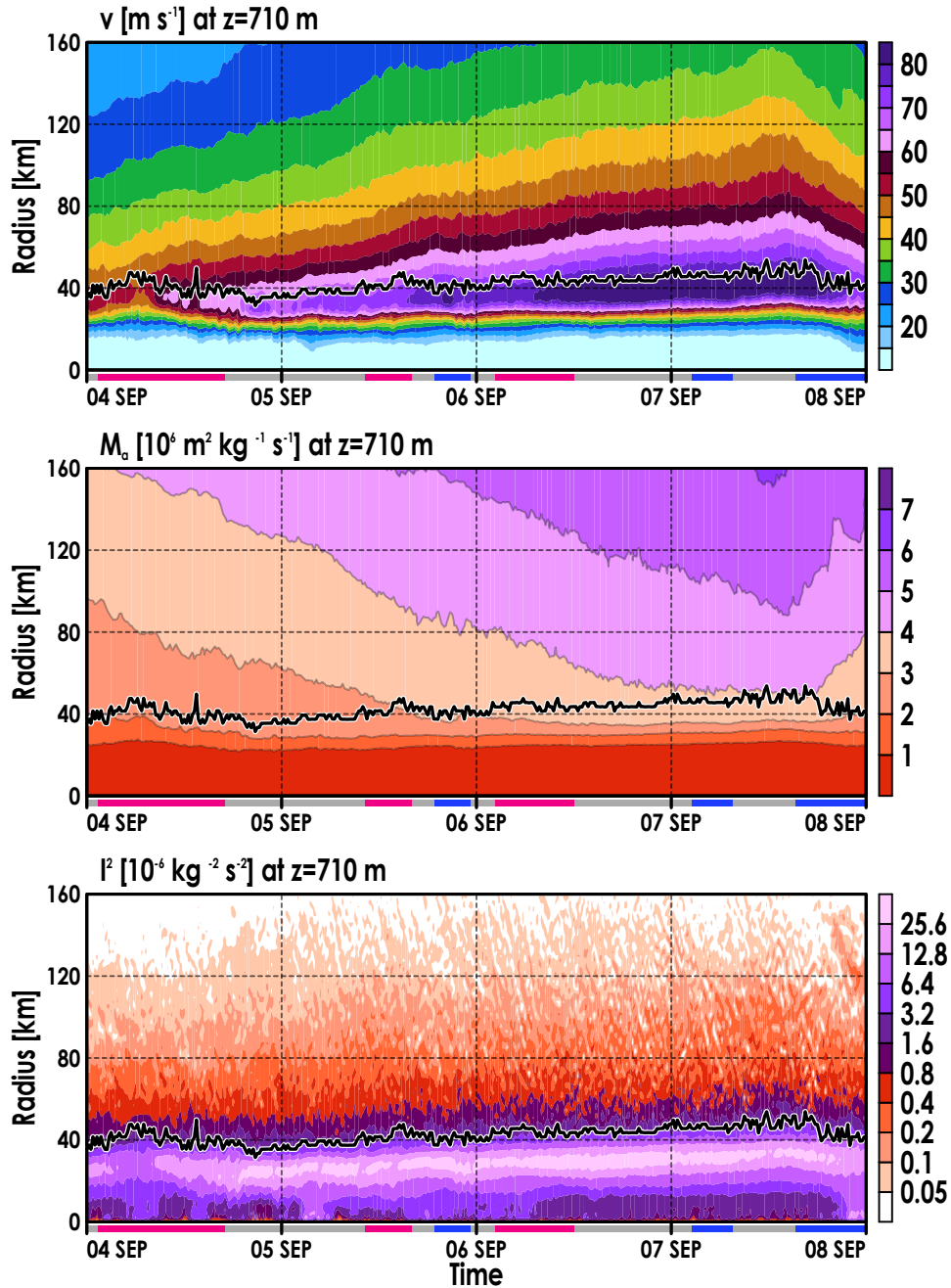


Figure 4.7: Time-radius Hovmöller diagrams of Hurricane Irma’s storm-relative tangential flow  $v$  (top), absolute angular momentum  $M_a$  (middle), and inertial stability  $I^2$  (bottom). All fields are taken at the model height where the tangential wind jet occurs ( $z \approx 710$  m). A timeline shaded by intensity change (red for IN, gray for SS, blue for WE) is drawn at the bottom of each panel. The bold, black line represents the RMW. Each plot uses the color bar to its right, and units are displayed above each plot.

vortex deepening (and associated increase in gradient-balanced wind aloft) and/or unbalanced dynamics related to BL inflow. During non-intensification periods near the end of 05 September and after 1200 UTC 06 September,  $M_a$  surfaces stagnate at outer radii (including at  $r > 100$  km prior to the WE phase on 05 September). The most-inertially stable BL air remains confined inward of the RMW throughout the analysis period. Aside from a subtle increase in  $I^2$  at all radii over time, Irma's radial distribution of  $I^2$  within the BL has little obvious evolution. Irma likely weakened around 0300 UTC 07 September due to a close approach with Puerto Rico, and Hispaniola's proximity to Irma likely explains the rapid deterioration of  $v$  after 1200 UTC 07 September.

Figure 4.8 shows the azimuthally averaged agradient flow  $v_{ag}$  near the top of the inflow layer outside the RMW. At  $r < 80$  km, weak supergradient flow persists near the top of the inflow throughout the analysis. At the same height and inward of the RMW, strong supergradient flow develops hours prior to and immediately following an intensification period near 1200 UTC 05 September. The strong supergradient wind after that IN period extends into a weakening period near the end of 05 September, perhaps due to an adjustment of gradient-balanced flow (e.g., from a weakened pressure gradient). During the IN period on 06 September, more-intense supergradient winds inside the RMW develop, which last until Irma's land-induced decay on 07 September.

Agradient wind at  $z \approx 710$  m (at the height of the BL jet; Figure 4.8) suggests that as Irma intensifies between 05 September and 07 September, the BL inflow deepens at  $r > 80$  km, evidenced by the increasing prevalence of subgradient flow. It also appears likely that the supergradient flow near the RMW at  $z \approx 1.2$  km is constrained by the degree of gradient imbalance in the BL jet, which could be "advected" upward (i.e., vertical advection of  $M_a$  that would increase  $v$ ).

Prior to land interactions on 07 September, Hurricane Irma's low-level primary circulation does not show substantial radial evolution over time in the azimuthal mean. With the exception of a brief weakening period on 05 September, Irma's azimuthal-mean primary circulation gradually intensified over open waters. The most-intense, most-supergradient winds were consistently located at  $z \approx 710$  m, just inward of the RMW. The asymmetric effects of shear and storm motion should affect Irma's azimuthal structure, which is lost in this axisymmetric analysis. The azimuthal structure of Irma's low-level primary circulation can change over time (e.g., though changes in en-

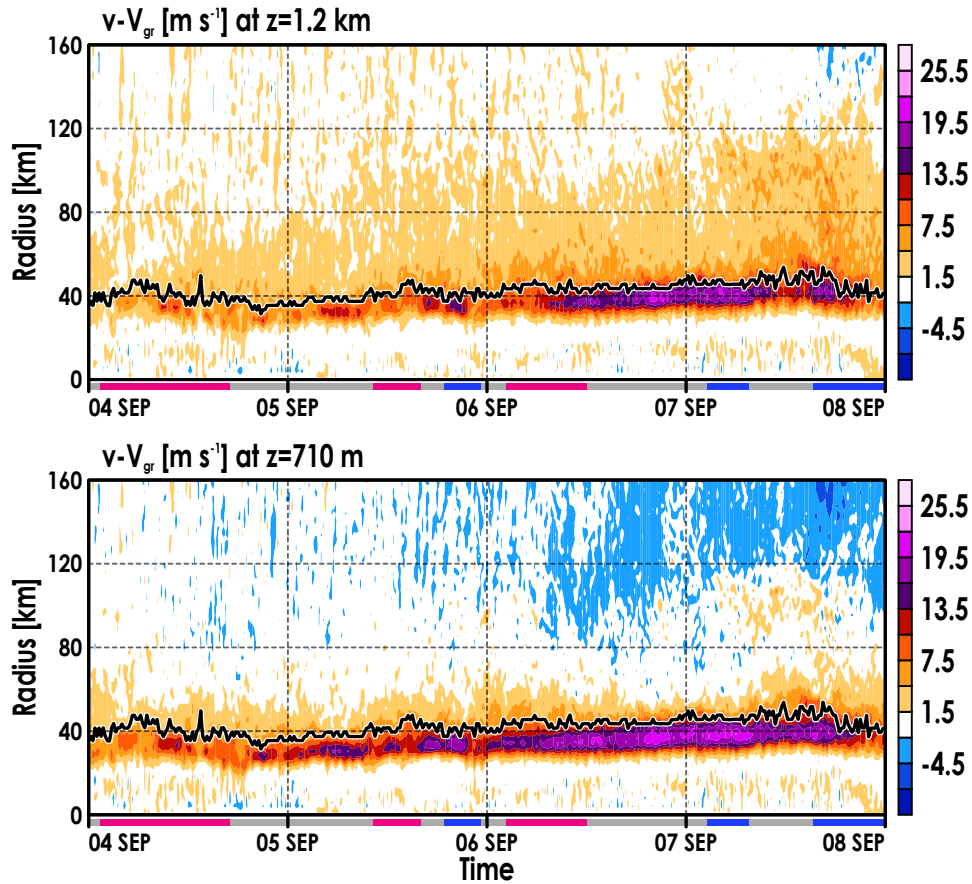


Figure 4.8: Similar to Figure 4.7, except using a gradient wind  $v_{ag}$  near the top of the inflow layer (top panel,  $z \approx 1.2$  km) and at the height of the tangential wind jet (bottom panel,  $z \approx 710$  m). Positive values represent supergradient winds ( $v > V_{gr}$ ), and negative values represent subgradient winds ( $v < V_{gr}$ ).

environmental forcing or large-scale vortex structure), which may provide hints toward explaining Irma’s IN and WE phases on 05 and 06 September.

### 4.3.2 Asymmetric Structure

Snapshots of Hurricane Irma’s storm-relative tangential wind averaged in shear-relative quadrants are shown in Figure 4.9. Throughout the analysis time, Irma’s primary circulation appears mostly axisymmetric. As Irma intensifies on 05 September, the strongest  $v$  is located downshear-right (DSR)—this quadrant also has the weakest  $v$  above the BL at  $r > 80$  km. During Irma’s weakening on 05 September, its maximum BL tangential wind moves into the upshear-left (USL)

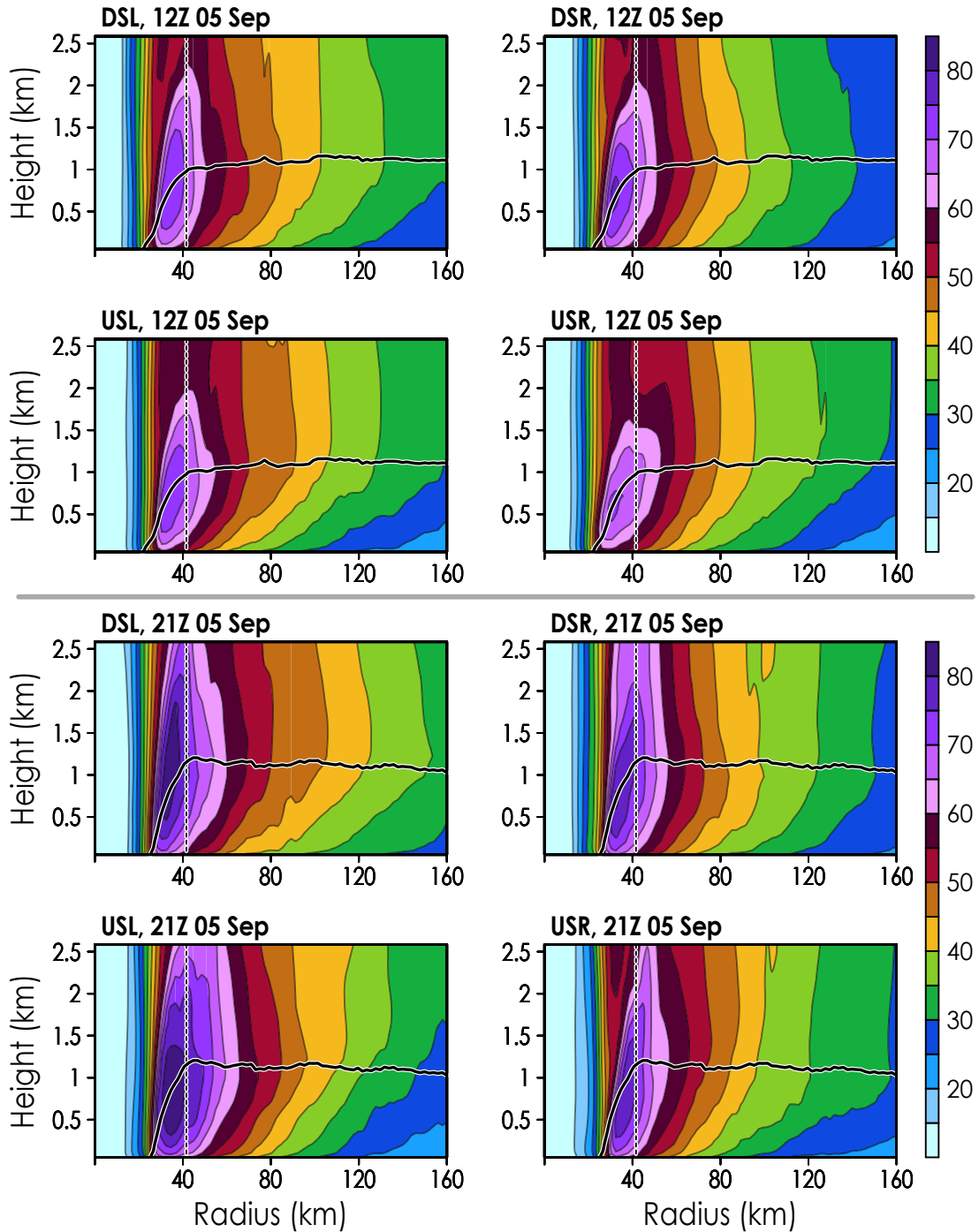


Figure 4.9: Shear-relative quadrants of  $r$ - $z$  cross sections of  $v$  ( $\text{m s}^{-1}$ ) in Hurricane Irma on 1200 UTC 05 September (top two rows, during IN) and 2100 UTC 05 September (bottom two rows, during WE). Panels are labeled by quadrant (downshear-left, DSL; upshear-left, USL; upshear-right, USR; downshear-right, DSR). The dashed, black line marks the RMW. The bold, black line indicates the axisymmetrized radial inflow layer (as in Figure 4.6).

quadrant, and the radial gradient of low-level  $v$  outside the RMW is strongest USL. In the same WE period,  $v > 60 \text{ m s}^{-1}$  extends above  $z = 2.5 \text{ km}$ , with strong radial gradients of  $v$  in the eyewall above the BL in the DSL and USR quadrants. Near peak intensity at 0600 UTC 07 September, Irma's BL jet is quite axisymmetric, with intense winds in excess of  $80 \text{ m s}^{-1}$  near  $r = 30 \text{ km}$  in all quadrants (not shown).

To assess the time evolution of asymmetric tangential velocity in the BL, Figure 4.10 frames the azimuthal anomaly of  $v$  at  $z \approx 710 \text{ m}$  in shear-relative quadrants with time-radius Hovmöllers. Most of Irma's intensification periods are associated with near-axisymmetric tangential wind outside the RMW, except on 04 September and toward the end of the IN phase on 05 September. At the end of that IN period, stronger  $v$  is seen DSL at  $r > 80 \text{ km}$  and USL at  $r < 80 \text{ km}$ , while relatively weak  $v$  appears USR at  $r > 60 \text{ km}$  and DSR at  $r < 80 \text{ km}$ . The asymmetry persists through the WE period

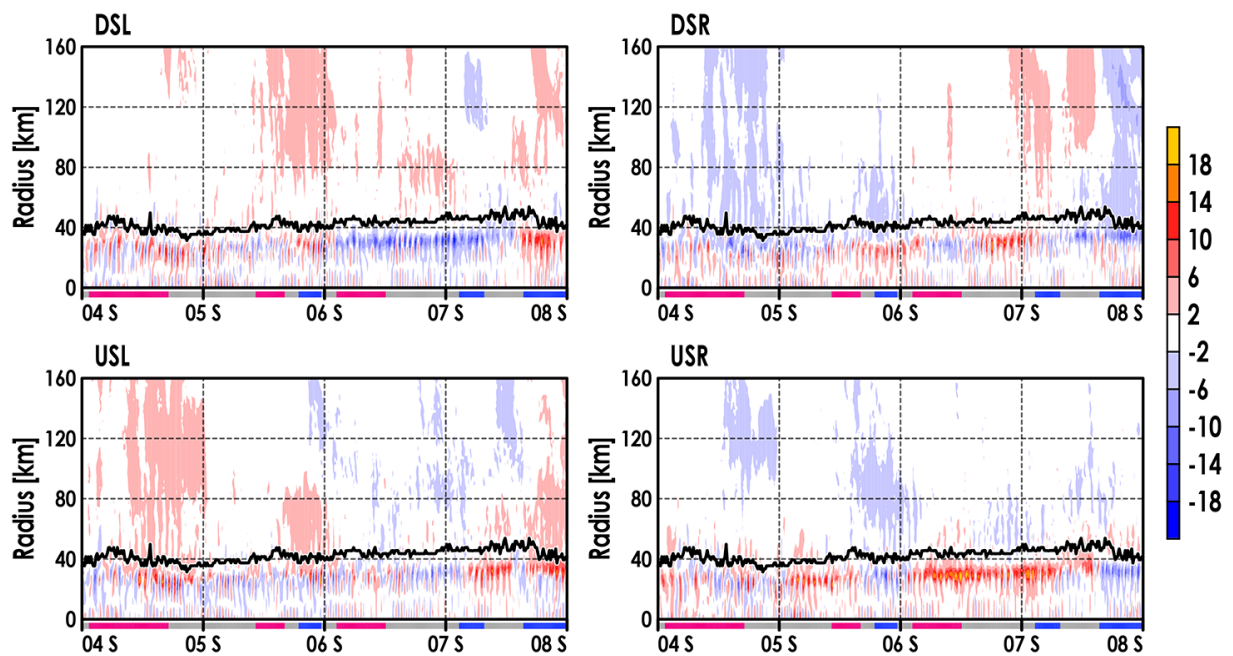


Figure 4.10: Time-radius Hovmöller diagrams of azimuthal tangential wind anomaly ( $v$  minus the azimuthally averaged  $v$  in  $\text{m s}^{-1}$ ) at  $z \approx 710 \text{ m}$  in each shear-relative quadrant from Hurricane Irma. The  $x$ -axis represents time, which is labeled by each day at 0000 UTC with the abbreviated month. A timeline shaded by intensity change (red for IN, gray for SS, blue for WE) is drawn at the bottom of each panel. The bold, black line represents the RMW. Panels are labeled by their quadrant abbreviation.

that follows, and then disappears in coincidence with the start of the IN period on 06 September. During the last IN phase, Irma’s BL jet is strongest in the USR quadrant and weakest in the DSL quadrant—these features continue until Irma’s land interactions.

Figure 4.11 shows multiple frames of the full horizontal structure of Hurricane Irma’s tangential wind anomaly at  $z \approx 710$  m. As Figure 4.10 suggests, Irma’s IN periods are generally associated with less tangential wind asymmetry outside of the inner eyewall than during Irma’s WE phase on 05 September. Over time during the 05 September IN phase, asymmetrically strong  $v$  appears left of shear, while weaker  $v$  becomes persistently oriented right of shear. As the 05 September WE phase begins, anomalously strong  $v$  wraps from outer radii in the DSL quadrant to inner radii upshear. Moderate northerly shear persists through most of 05 September, which should be associated with an asymmetric response in BL inflow—namely, the development of stronger low-level inflow downshear and weaker inflow upshear. The asymmetric BL inflow could be associated with strong positive advection of  $M_a$  downshear; the strongest winds would be downwind of that asymmetrically strong inflow (i.e., upshear), thus establishing the asymmetric profile of  $v$  seen during Irma’s WE phase on 05 September. During IN on 06 September, the anomalously intense BL jet in the USR quadrant seen in Figure 4.10 is perhaps due to a change in Irma’s storm motion, which became stronger and turned to point USR. The change in Irma’s motion would be expected to induce changes in BL azimuthal structure relative to shear. In this case, we would expect storm motion to induce stronger BL inflow (and subsequent radial convergence) in the USR quadrant, and weaker BL inflow in the DSL quadrant.

Figure 4.12 shows the inertial stability for the given  $v$ -field in Figure 4.9. As implied by  $v$ , the inertial stability inside  $r = 40$  km (near the RMW) appears mostly axisymmetric. At greater radii,  $I^2$  becomes generally less positive and more sporadic over space and time, perhaps as a result of  $M_a$  advection via radial flow and/or convective updrafts/downdrafts. Instances of inertial instability occur throughout the domain outside the RMW, though these instances are often below 1 km AGL. During Irma’s weakening on 05 September, inertial instabilities appear more prominently in the upshear semicircle. Figure 4.13 provides time-radius Hovmöllers of  $I^2$  for all shear-relative quadrants at  $z \approx 510$  m. Throughout the analysis,  $I^2$  is nearly axisymmetric in the eyewall region, and some asymmetry is seen between upshear and downshear semicircles outside

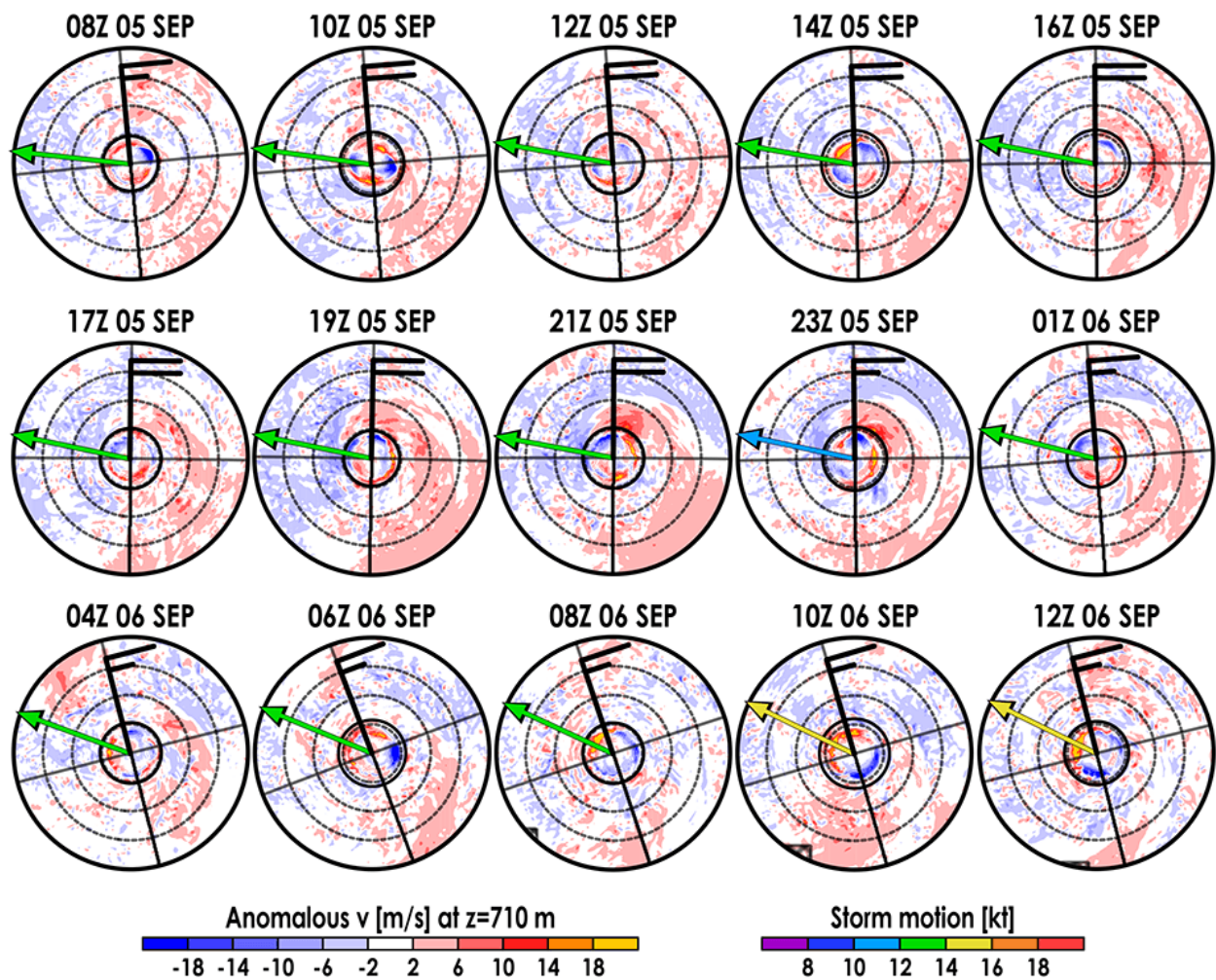


Figure 4.11: Radius-azimuth polar plots showing the evolution of Hurricane Irma's tangential wind anomaly ( $v$  minus the azimuthally averaged  $v$  in  $\text{m s}^{-1}$ ) at  $z \approx 710$  m. Each row of plots represents a different period of intensity change in Irma: IN on 05 September (top), WE on 05 September (middle), and IN on 06 September (bottom). Time increases toward the right at a 2-hour interval. Radius is contoured (gray dashed) every 40 km out to 160 km, and the RMW is contoured in black (solid) near  $r = 40$  km. Gray contours of azimuth separate shear-relative quadrants. North points to the top of the figure. Similar to Figure 4.3, deep-layer shear (barb) and storm motion (vector) are superimposed on Irma's center, and land is hatched in gray.

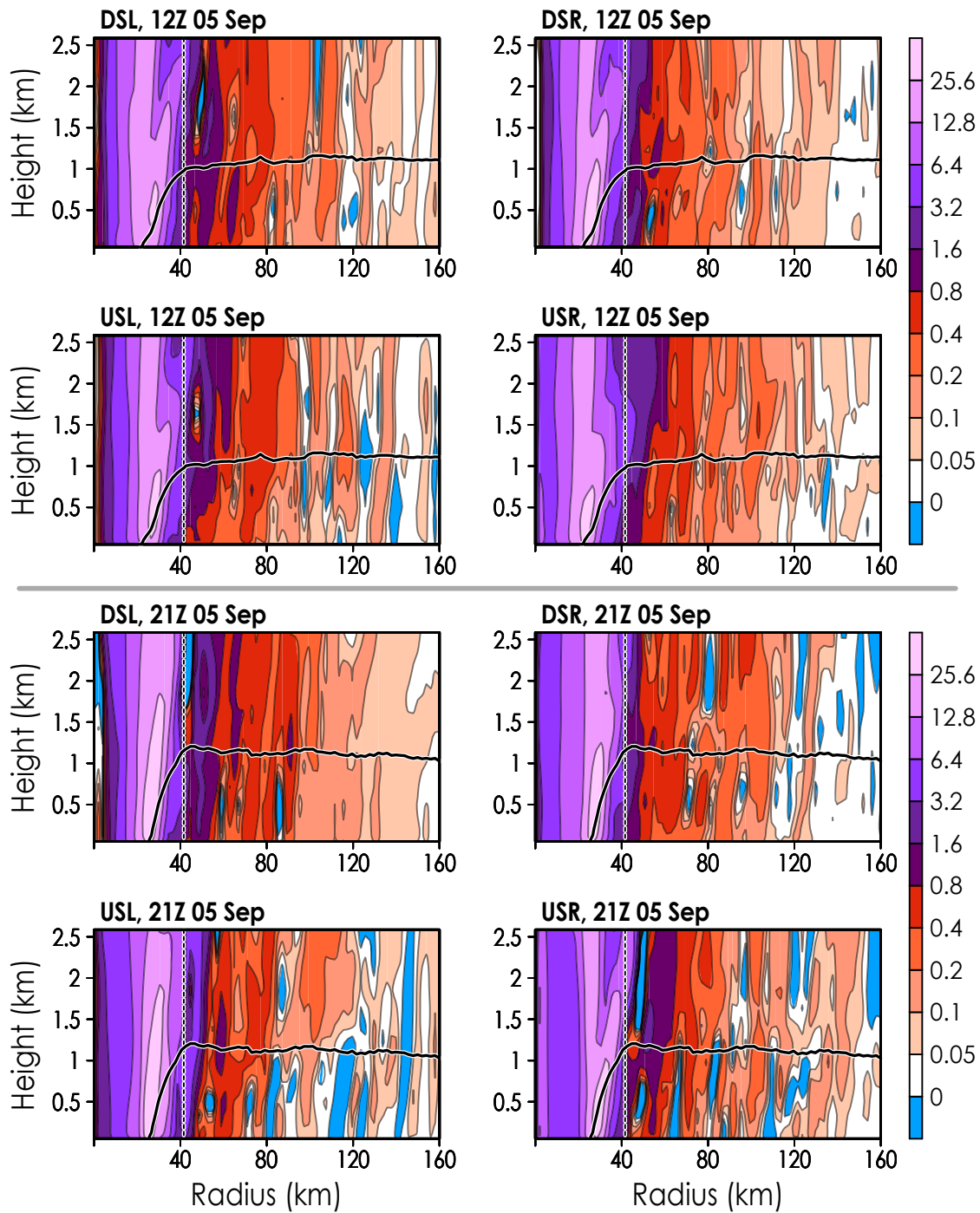


Figure 4.12: Similar to Figure 4.9, but shaded using inertial stability  $I^2$  (units  $10^{-6} \text{ kg}^{-2} \text{ s}^{-2}$ ).

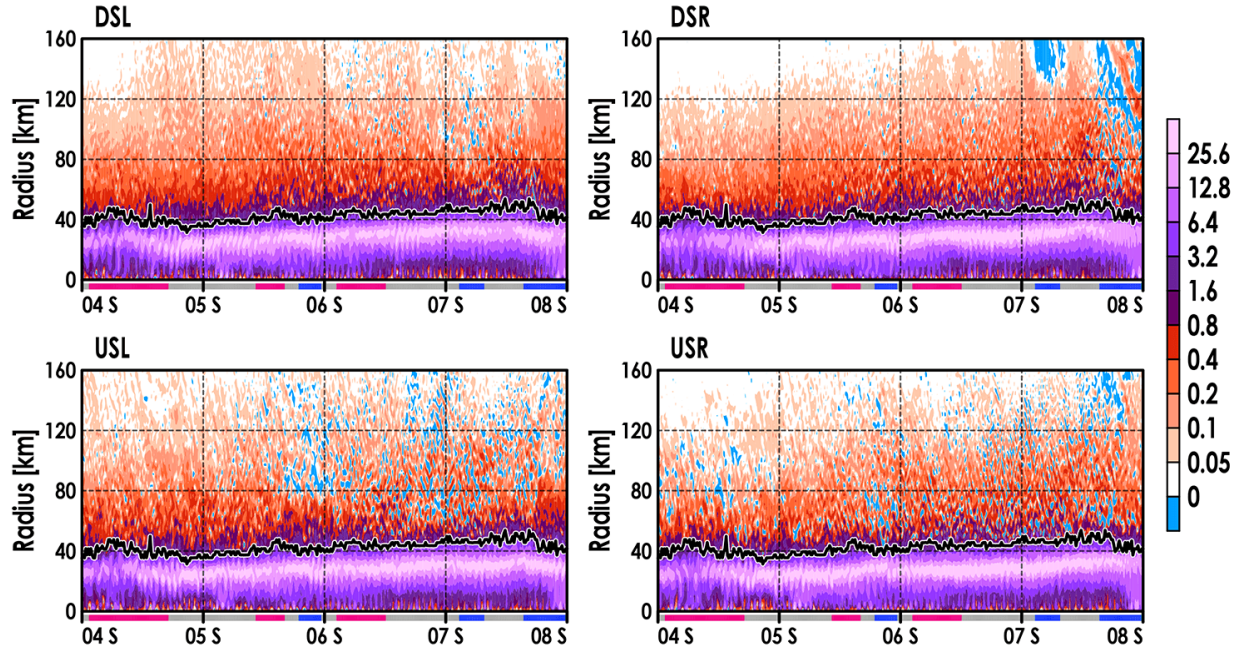


Figure 4.13: Similar to Figure 4.10, but shaded using inertial stability  $I^2$  at  $z \approx 510$  m (units  $10^{-6} \text{ kg}^{-2} \text{ s}^{-2}$ ).

the eyewall. Transient inertial instabilities in the BL occur more frequently upshear, and they are mostly situated well outside the RMW except in the USR quadrant [where we would expect convective downdrafts to be more frequent (DeHart et al. 2014)]. Downdrafts can push high- $M_a$  air from above the BL into the near-surface inflow, leading to local increases in  $M_a$  that can result in  $\partial M_a / \partial r < 0$  nearby. The frequency of inertial instabilities at this height increases after its intensification on 05 September. On 07 September, a strong and relatively persistent inertial instability appears in the DSR quadrant at  $r > 120$  km in coincidence with weakening. At that time, Puerto Rico is about 120 km to the south-southwest of Irma with shear out of the northwest, so this signal is likely associated with land-based frictional drag that would lead to  $\partial M_a / \partial r < 0$  radially inward of that surface drag. Thus, it is plausible that Irma’s proximity to Puerto Rico may explain Irma’s WE period early on 07 September.

Asymmetric agradiant wind is plotted in Figure 4.14, similar to Figures 4.9 and 4.12. During the IN phase of 05 September, the tangential wind jet is most supergradient in the DSR quadrant and least supergradient in the USL quadrant. Near the top of and above the azimuthally averaged

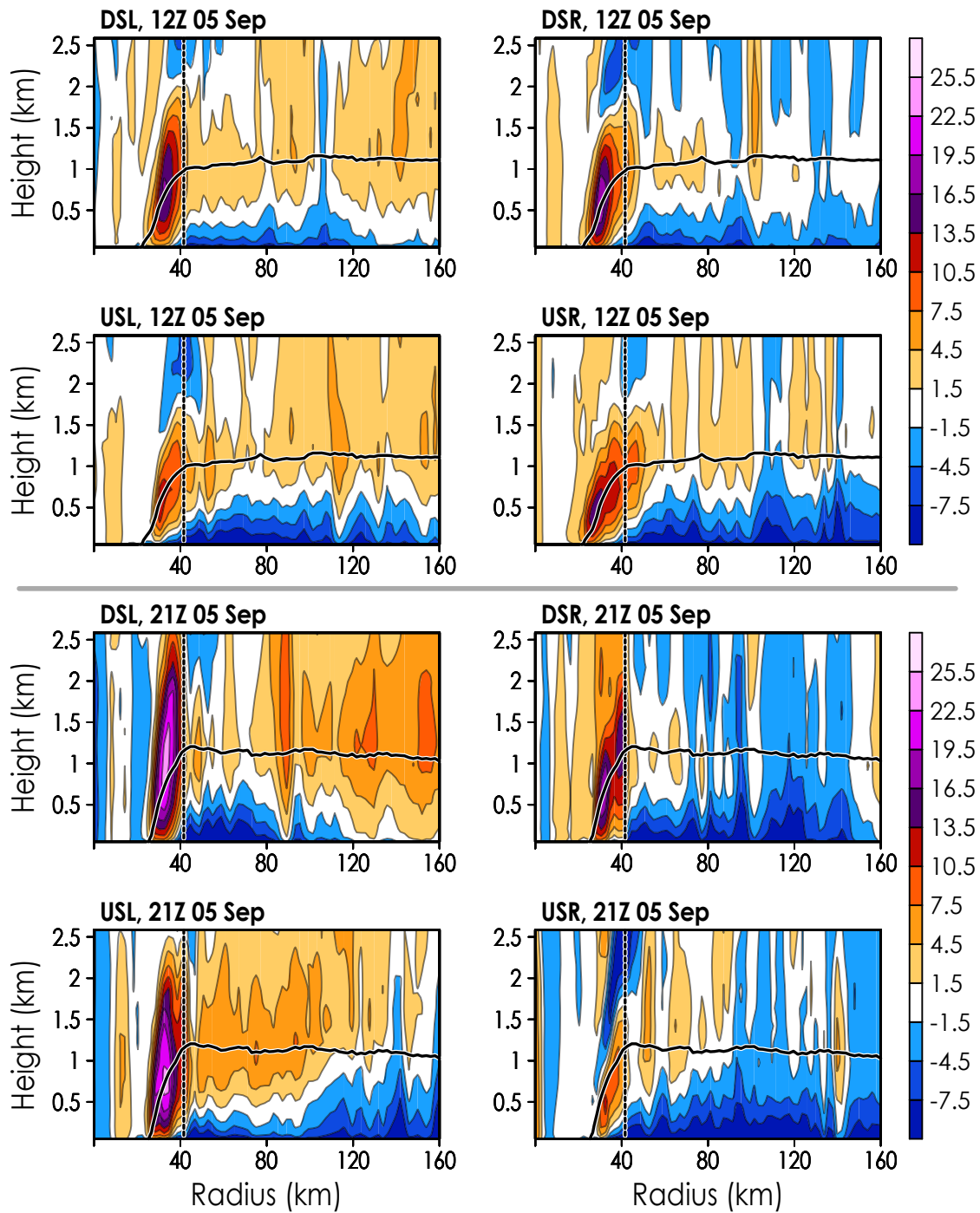


Figure 4.14: Similar to Figure 4.9, but shaded using a gradient wind  $v_{ag}$  (m s<sup>-1</sup>).

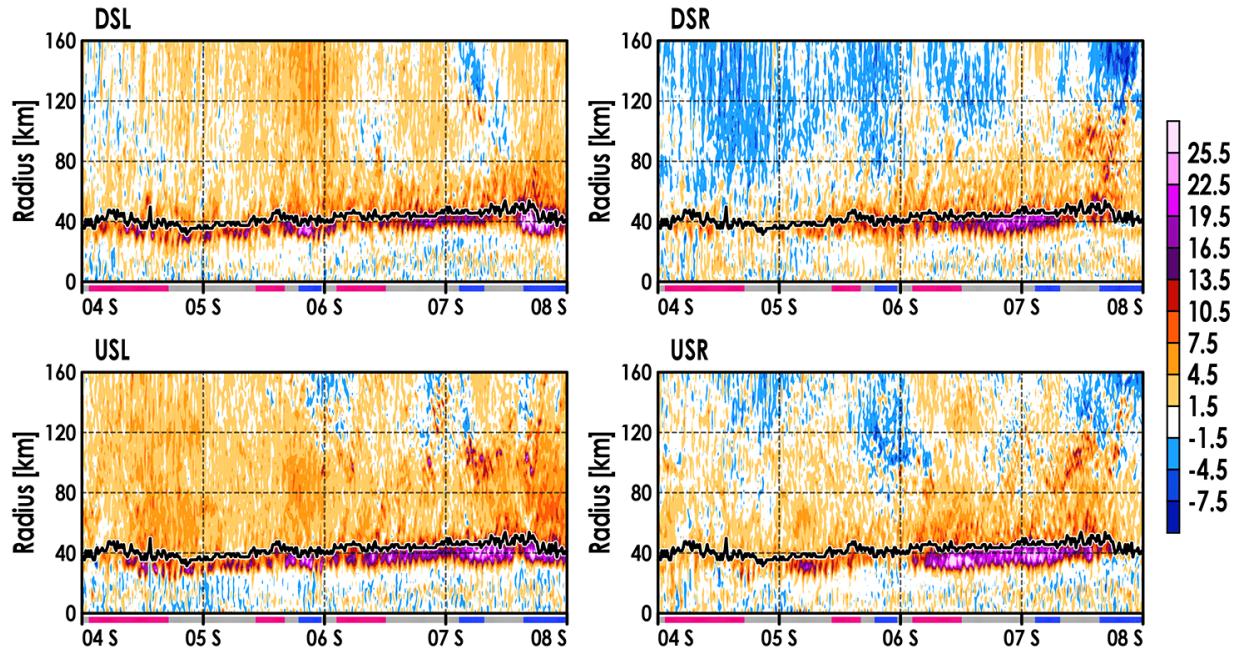


Figure 4.15: Similar to Figure 4.10, but shaded using a gradient wind  $v_{ag}$  at  $z \approx 1.2$  km ( $\text{m s}^{-1}$ ).

BL inflow, weak (but relatively deep) supergradient flow is seen at most radii left of shear during this IN period. As Irma enters its weakening period on 05 September, the peak supergradient flows are seen in the DSL and USL quadrants, with the weakest supergradient jet in the USR quadrant. Outside the RMW during this WE phase, the winds near the top of the azimuthally averaged inflow layer are more supergradient at  $r > 80$  km DSL and at  $r < 100$  km USL. These differences between supergradient winds in the IN and WE phases (which are separated by a few hours) may indicate some shift in the azimuthal distribution of low-level inner-core convection, a change in the azimuthal structure of the BL inflow that would affect  $M_a$  advection, or a change in the radial distribution of  $M_a$  in the BL well outside the RMW (which would also affect advection of  $M_a$ ).

Quadrant-specific Hovmöllers of a gradient flow at  $z \approx 1.2$  km are provided in Figure 4.15. Quadrants left of shear have supergradient flow for most of the analysis time at all radii outside Irma's eye, while the DSR quadrant experiences subgradient flow at  $r > 80$  km most of the time. During and leading up to the WE period on 05 September, the USR quadrant has subgradient flow at outer radii, while the tangential wind inside the RMW becomes less supergradient. The reduction

of USR eyewall supergradient wind may be due to local downdrafts or inhibition of convection in the eyewall there, or a reduction of  $M_a$  import by surface inflow below due to changes in the  $M_a$ - or  $u$ -field.

The azimuthal structure of Hurricane Irma's primary circulation outside the RMW tended to have minimal asymmetry—especially outside of its WE period on 05 September. Some asymmetry developed during and in the hours prior to weakening on 05 September, with stronger and more-supergradient  $v$  left of shear. An anomalously weak, less-supergradient BL jet was seen USR during WE, which may be due to reduced radial and/or vertical advection of  $M_a$  upwind from the BL. Irma resumed intensification on 06 September after the USR quadrant developed anomalously strong tangential flow inside the RMW, which was highly supergradient. This shift in anomalous  $v$  on 06 September was coincident with a change in Irma's motion relative to the deep-layer shear, where its motion became oriented USR. To investigate potential causes for evolutions of Irma's primary circulation on 05 and 06 September, we will next examine the properties of Irma's secondary circulation. Therein, we will look at the 3-D structure of radial and vertical flow, uncovering details of  $M_a$  advection and convection.

## 4.4 Secondary Circulation

### 4.4.1 Axisymmetric Structure

The central aspects of the BL secondary circulation to examine include radial wind  $u$  and its associated divergence, as well as vertical wind  $w$ . The azimuthal averages of these fields in Hurricane Irma are shown in Figure 4.16 using snapshots from the IN period (1200 UTC 05 September) and WE period (2100 UTC 05 September) highlighted in the previous section. In agreement with prior hurricane BL analyses using observations (including that of Chapter 3), the strongest azimuthally averaged inflow is situated adjacent to the surface and collocated with the RMW. The inflow extends inward beyond the RMW, with  $u$  approaching zero rapidly with decreasing  $r$  inside the RMW (due to high  $I^2$ , shown in Figure 4.6). Strong outflow is present near the RMW above the inflow layer; while outflow above the BL was found in the composite analysis regardless of stratification by intensity change, the composite outflow was of much weaker magnitude (possibly

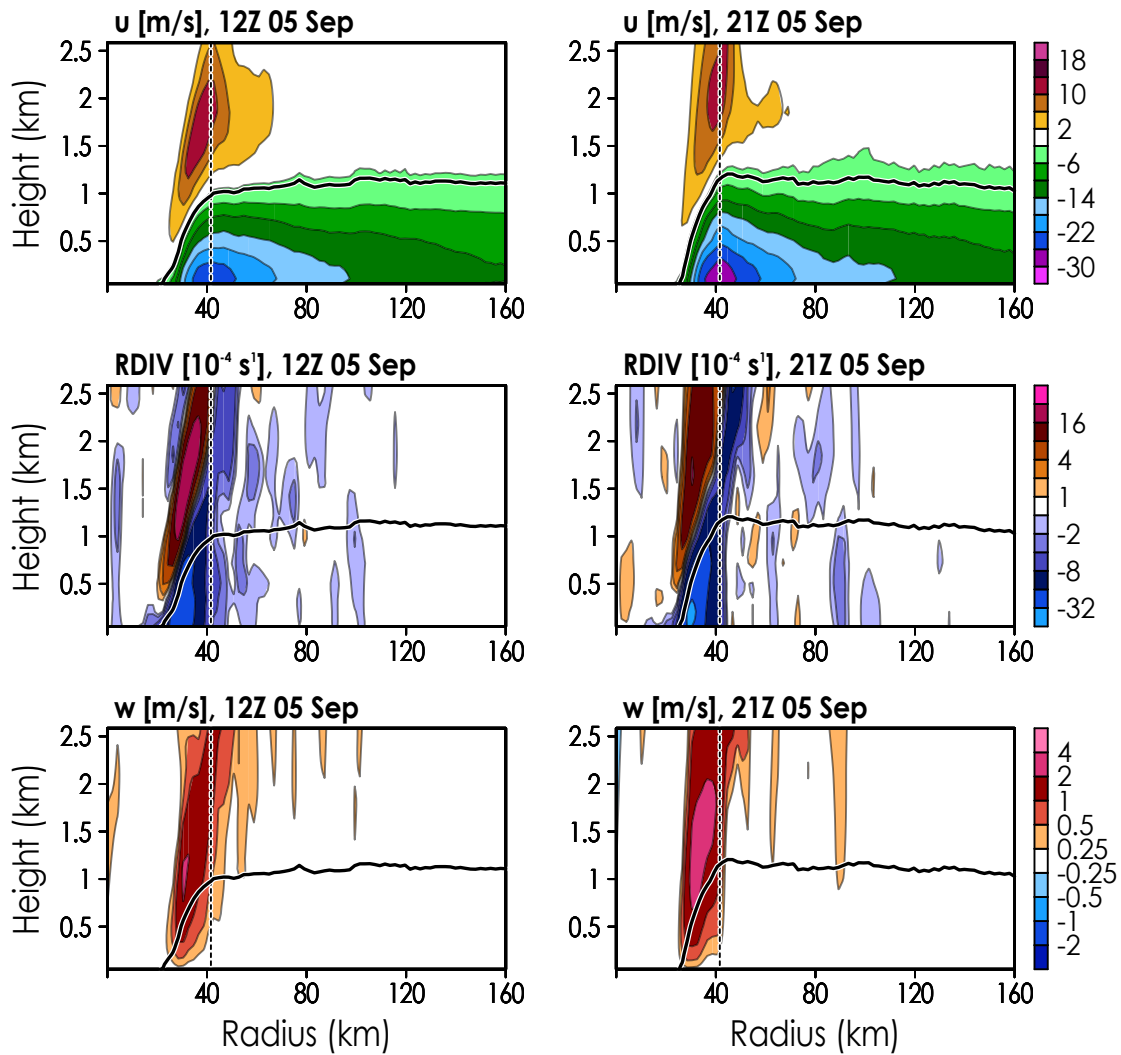


Figure 4.16: Cross sections ( $r$ - $z$ ) of Hurricane Irma’s azimuthally averaged secondary circulation using storm-relative radial wind  $u$ , radial divergence  $\nabla \cdot (\hat{r} \cdot \vec{U})\hat{r}$  (labeled “RDIV” in the plot), and vertical wind  $w$  on 1200 UTC 05 September (left, during IN) and 2100 UTC 05 September (right, during WE). Negative (positive) values in  $u$  indicate inflow (outflow). Each row of figures uses the color bar to its right, and each field has its units listed above its panel. The dashed and solid black lines indicate the RMW and azimuthally averaged inflow layer, respectively. The scales used for radial divergence and vertical velocity are geometric about zero (... -4, -2, -1, 0, 1, 2, 4, ... for radial divergence).

due to the averaging of observations required by the composite). The stronger outflow near the RMW is likely due to a combination of high inertial stability and supergradient wind there: Inflowing BL air is forced to ascend as it converges inward of the RMW, and then returns to an outer radius above the BL as effects of frictional drag (i.e., a gradient forcing) disappear. During Irma's intensification period on 05 September, near-surface inflow of  $\sim 22 \text{ m s}^{-1}$  persists near the RMW. Between the IN and WE phases on 05 September, strong near-surface inflow in excess of  $14 \text{ m s}^{-1}$  extends radially outward from  $r \approx 90 \text{ km}$  to  $r \approx 110 \text{ km}$ .

In the top panel of Figure 4.17 depicting a Hovmöller of near-surface  $u$ , Irma's inflow is shown to strengthen at most radii near and outside the RMW as Irma's intensity climbs. This is likely due to increasing tangential flow at those radii, which would be associated with an increase in gradient wind above the BL. The increased  $M_a$  above the BL results in more frictional dissipation of momentum near the surface, and thus more a gradient forcing. During the 05 September weakening phase, azimuthally averaged near-surface inflow weakens at most radii. The deep-layer shear magnitude increases to  $\sim 20 \text{ kt}$  prior to the 05 September weakening period, and then weakens to  $\sim 15 \text{ kt}$  near the end of the WE period (shown earlier in Figure 4.11). As the shear is expected to induce BL inflow asymmetries (stronger/weaker inflow downshear/upshear), the changes in shear magnitude between near 1200 UTC 05 September and 0000 UTC 06 September may affect the azimuthal mean inflow. The IN period on 06 September following the WE period is coincident with the storm motion and shear turning (toward the north-northwest and south-southeast, respectively), becoming less orthogonal and more antiparallel (Figure 4.11). As BL inflow is expected to be asymmetrically strong downstream *and* downshear (Barnes and Dolling 2013), the reorientation of motion and shear during the IN period suggests that the BL inflow may become more axisymmetric during this IN (examined further in the next subsection on asymmetric structure of the secondary circulation).

The middle and bottom panels of Figure 4.16 depict radius-height snapshots of radial divergence (RDIV) and vertical motion  $w$ , respectively. Radial convergence is maximized along the inner periphery of the BL inflow in both snapshots (inward of the RMW), as would be expected given the strong radial gradient of  $u$  there. Above the maximum radial convergence is a maximum in radial divergence, associated with the outflow there. Relatively weak and transient regions of

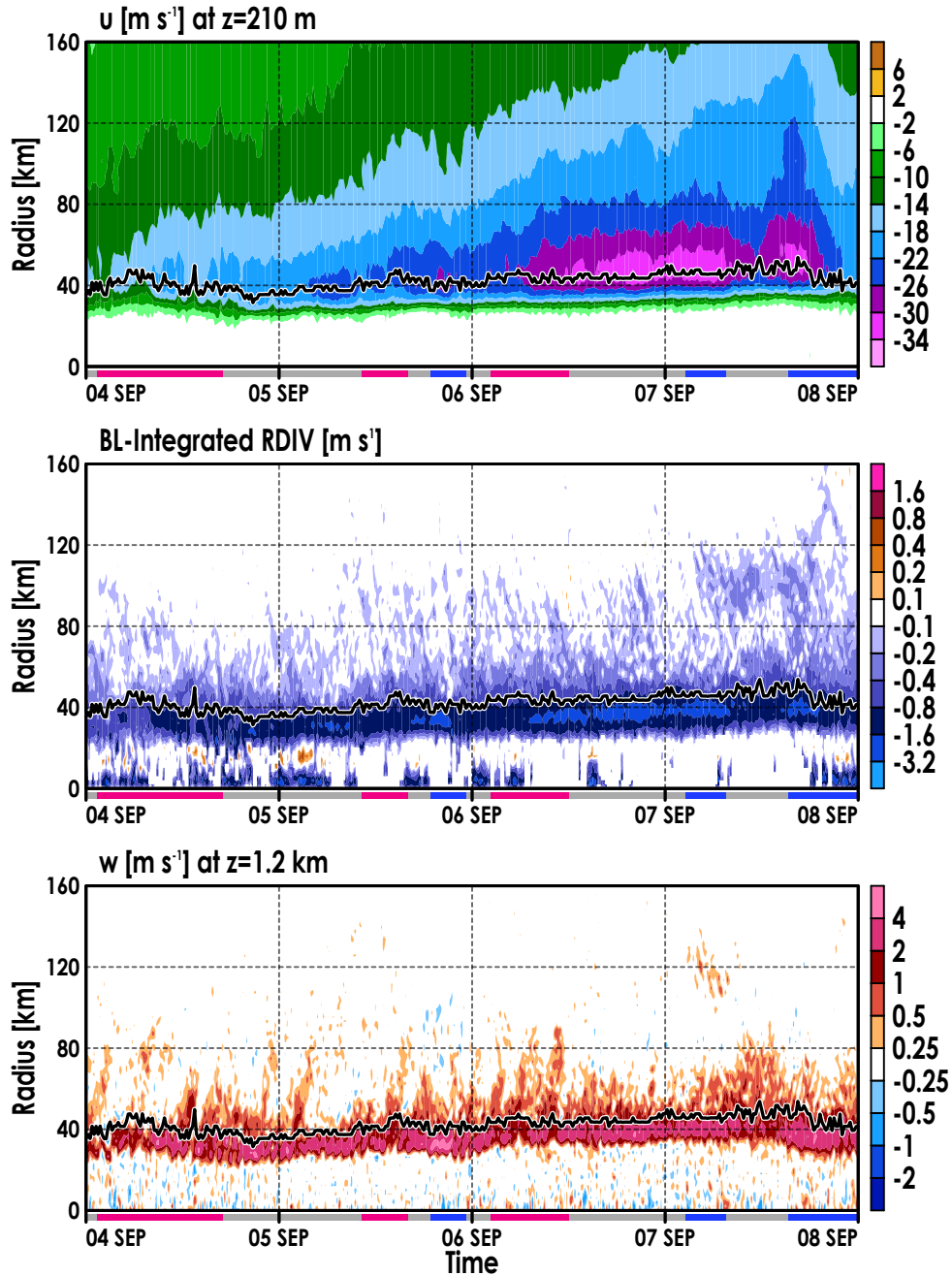


Figure 4.17: Time-radius Hovmöller plots of Hurricane Irma’s near-surface radial velocity  $u$  (at  $z \approx 210$  m, top), vertically integrated radial divergence through the *asymmetric* inflow layer (middle), and vertical motion near the top of the BL inflow  $w$  (at  $z \approx 1.2$  km, bottom). Each plot uses the color bar to its right, and all fields are expressed in  $\text{m s}^{-1}$ . A timeline shaded by intensity change (red for IN, gray for SS, blue for WE) is drawn at the bottom of each panel. The bold, black line represents the RMW.

low-level convergence appear outside the RMW (e.g., at  $r$  between 60 km and 80 km), alongside sporadic occurrences of radial divergence. In the azimuthal mean, the IN and WE periods on 05 September are associated with mostly similar profiles of BL radial divergence, although the convergence immediately inward of the RMW appears to be stronger during Irma's WE period. As stronger BL convergence near the RMW is typically associated with intensification via the expectation of high- $M_a$  and high- $\theta_e$  air ascending rapidly from the near-surface inflow layer, the stronger radial convergence near the RMW during Irma's WE should be examined further.

To investigate the cumulative effect of radial divergence through depth in the BL, we determine the radial divergence integrated vertically through the inflow layer (based on Equation 3.3):

$$-\int_0^{Z_{inf}} \nabla \cdot (\hat{r} \cdot \vec{U}) \hat{r} dz = -\int_0^{Z_{inf}} \left( \frac{u}{r} + \frac{\partial u}{\partial r} \right) dz, \quad (4.1)$$

where  $Z_{inf}$  is the height of the frictional inflow layer. Through the continuity equation, the vertically integrated radial divergence in the BL should roughly represent the vertical motion near the top of the BL (Kepert 2013). Negative BL-integrated radial divergence indicates ascent at the top of the BL. We use this term as an analog for vertical motion at the top of the frictional inflow layer, which has variable depth across radius and azimuth (i.e., assessing vertical motion not on one model level, but at the top of the kinematic BL). To calculate this term, we first vertically integrate the radial divergence through the depth of each grid cell. For each point in  $(r, \psi_s, t)$  space, we sum the integrated radial divergence from each cell in the vertical below  $z = 1.5$  km where  $u/|u_{min}| < -0.1$ . The middle Hovmöller in Figure 4.17 shows the azimuthal mean of this term, which we will refer to henceforth as BL-integrated radial divergence (RDIV). Convergence is consistently maximized inward of the RMW throughout Irma's analysis period, with changes in maximum convergence occurring alongside changes in BL jet intensity (Figure 4.7). The BL-integrated RDIV inside the RMW should be strongly dependent on  $V_{max}$ , as the strength of near-surface radial inflow at the RMW is dependent on the loss of momentum between the winds above the BL (reflected by  $V_{max}$ ) and the surface. High  $I^2$  inside the RMW prevents inflow directly beneath the BL jet from being stronger than the inflow at the RMW. Outside the RMW, BL-integrated RDIV generally approaches zero and becomes more sporadic with increasing  $r$ , and nearly vanishes at  $r > 100$  km for most output times prior to land interactions on 07 September.

Low-level vertical motion  $w$  is plotted in the bottom row of Figure 4.16 at 1200 UTC 05 September (IN) and 2100 UTC 05 September (WE). Ascent is maximized along and inward of the RMW, with the ascent sloping outward with height for both periods shown. The strength of the low-level  $w$  along the inner eyewall is linked to the BL convergence below, which is dependent on frictional inflow at the RMW. As discussed in the composite analysis, the vertical transport of air into and out of the BL may affect dynamical (e.g.,  $M_a$ ) and thermodynamical (e.g.,  $\theta_e$ ) fields in the free atmosphere immediately aloft and in the BL inflow. To examine the time evolution of azimuthal-mean vertical motion near the top of the BL, the Hovmöller of azimuthally averaged  $w$  at  $z \approx 1.2$  km (chosen based on frictional inflow layer depth) is shown in Figure 4.17. In Irma, strong ascent is nearly always situated along the inner edge of the RMW regardless of Irma's changes in intensity. Ascent of about  $1 \text{ m s}^{-1}$  or weaker appears frequently outside the RMW out to radii of about 60 km, and less so at  $r > 60$  km. At  $r > 90$  km, the magnitude of azimuthal mean  $w$  near the top of the BL is often weaker than  $0.25 \text{ m s}^{-1}$  (an exception appears during a WE phase on 07 September, associated with land interaction). During the 05 September WE period, descent is seen between  $r \approx 70$  km and  $r \approx 100$  km, which may be associated with downward transport of low- $\theta_e$  air from the free atmosphere into the BL.

Based on the Hovmöllers of azimuthally averaged BL-integrated RDIV and  $w$ , ascent of air out of (or descent of air into) Hurricane Irma's BL is minimized at  $r > 90$  km, and so inflowing BL air may be considered well-insulated from the free atmosphere aloft. Inward of  $r = 90$  km, ascent out of the BL becomes increasingly frequent with decreasing  $r$  until reaching maximum  $w$  just inward of the RMW. Within that radial band, properties of Irma's BL (e.g.,  $M_a$ , greater moist entropy relative to the free atmosphere) are more likely to translate upward into the free atmosphere, potentially affecting local dynamics and thermodynamics. A possible example of this is seen in the previous section's azimuthal-mean agradient wind at  $z \approx 1.2$  km (Figure 4.8), which showed weakly supergradient flow at that height (presumably from positive advection of  $M_a$  originating in the BL below) between the inner eyewall and  $r < 90$  km that persists for most of the analysis period after 05 September.

Prior research has found that the BL secondary circulation can have substantial azimuthal structure (Zhang et al. 2013), which may be connected to the azimuthal distribution of convection (De-

Hart et al. 2014; Hazelton et al. 2017a). If BL inflow and  $w$  are asymmetric, then BL momentum and enthalpy will be distributed asymmetrically about the storm, affecting the primary circulation and thermodynamic structure. For example, asymmetric distributions of  $M_a$  advection could explain asymmetries in the low-level  $v$ -field, as was seen in Irma during its WE phase on 05 September (Figures 4.10 and 4.10). Furthermore, the azimuthal-mean secondary circulation smooths out signals in the  $w$ -field, which may have asymmetrically distributed updrafts and downdrafts [as suggested in DeHart et al. (2014)]. This smoothing can obfuscate local convective signals, such as downdrafts extending into the inner-core BL (which could be washed out by relatively strong updrafts at other azimuth). We will next investigate the azimuthal structure of Irma’s secondary circulation, including the structure’s potential impacts on Irma’s kinematic and thermodynamic properties in the BL and beyond.

#### 4.4.2 Asymmetric Structure

The azimuthal structure of a hurricane’s radial inflow layer is influenced by its encapsulating environment (e.g., through the effects of deep-layer vertical shear and nearby land) and storm motion (which is primarily a function of steering flow—an environmental influence). Specifically, the frictional inflow layer downshear and downstream of a hurricane is expected to be deeper and more intense, while the inflow is expected to be shallower and weaker upshear and in a hurricane’s wake (Barnes and Dolling 2013). The shear-relative structure of Hurricane Irma’s low-level radial wind during IN (1200 UTC 05 September) and WE (2100 UTC 05 September) is depicted in Figure 4.18. In the hours leading up to and including 1200 UTC 05 September, Irma’s motion is mostly westward at  $\sim 13$  kt—pointing almost orthogonal and to the right of southward shear ( $\sim 15$ – $20$  kt). Based on Barnes and Dolling (2013), the BL inflow should be deepest and/or strongest downshear and to the right of shear. The downshear-right quadrant is associated with the strongest near-surface inflow, with  $u < -14$  m s $^{-1}$  extending radially outward to  $r \approx 150$  km. In the DSL quadrant, moderate inflow of at least  $6$  m s $^{-1}$  is about as thick as seen DSR (roughly 1 km), and the near-surface inflow at most radii is  $\sim 4$  m s $^{-1}$  weaker than DSR. Upshear BL inflow is generally shallower than downshear during this IN period, with the weakest inflow situated USL. The USR

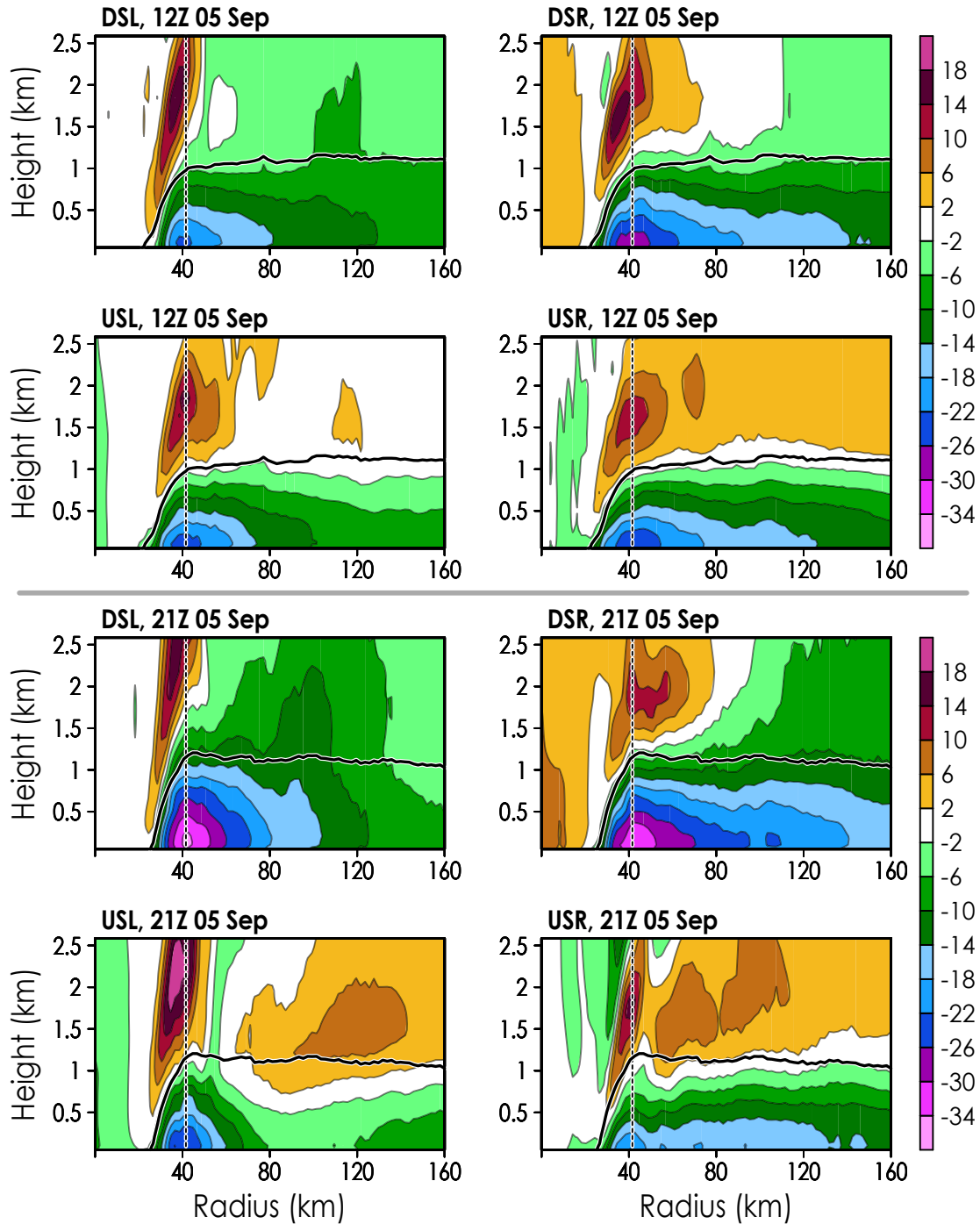


Figure 4.18: Radius-height cross sections of  $u$  ( $\text{m s}^{-1}$ ) in each shear-relative quadrant of Hurricane Irma on 1200 UTC 05 September (top two rows, during IN) and 2100 UTC 05 September (bottom two rows, during WE). Panels are labeled by the quadrant they represent. The dashed, black line marks the RMW. The bold, black line indicates the axisymmetrized radial inflow layer (as in Figure 4.16).

quadrant has stronger near-surface inflow than the DSL quadrant, but outflow is present just above the BL inflow at all radii outside the RMW.

By 2100 UTC 05 September, with Irma weakening and still moving westward at  $\sim 13$  kt, Irma's BL secondary circulation is definitively asymmetric as deep-layer shear continues out of the north at  $\sim 20$  kt. The downshear half of Irma's BL inflow is deeper and more intense, the USR inflow layer is weaker (but with roughly the same thickness), and the USL quadrant's inflow is much shallower and weaker between  $r \approx 70$  km and  $r \approx 120$  km. The near-surface inflow of at least  $14 \text{ m s}^{-1}$  seen USR extends outward to  $r \approx 150$  km, covering a larger radial range than the DSL quadrant despite being associated with weaker  $v$  aloft (Figures 4.9 and 4.10). This difference in the expanse of strong near-surface inflow suggests that the processes by which deep-layer shear and storm motion affect inflow structure are different (at least in this case). Note that between 1200 UTC and 2100 UTC 05 September, Irma's most-intense tangential winds propagated from DSR to left of shear, as the BL's strongest inflow (and thus, advection of  $M_a$  and associated spin-up tendency) rotated from right of shear to downshear. The inflow asymmetry seemingly induced by the persistent northerly shear leading up to 2100 UTC 05 September resulted in the downshear area being where BL spin-up tendency by  $M_a$  advection is greatest, and the upshear area being where BL spin-down tendency by friction and outflow is more dominant in the local  $M_a$  budget. Thus, by 2100 UTC 05 September, the maximum low-level tangential wind associated with Irma's secondary circulatory asymmetry should be oriented somewhere between the DSL and USL quadrants (in agreement with Figure 4.9).

Figure 4.19 provides shear-relative Hovmöllers of  $u$  at  $z \approx 210$  m, illustrating the evolution of BL inflow azimuthal structure in Hurricane Irma. The full horizontal structure of near-surface radial flow during Irma's IN and WE phases on 05 and 06 September is depicted in Figure 4.20. During IN on 05 September, near-surface inflow in the inner core is mostly axisymmetric. After shear increases from  $\sim 15$  kt to  $\sim 20$  kt during the 05 September IN phase, BL inflow becomes more asymmetric over time (with weaker inflow upshear and stronger inflow downshear), continuing until the IN phase ends. During the WE phase that follows hours after, inner-core near-surface inflow becomes maximized DSL and directly left of shear (Figure 4.20). The strong BL inflow DSL and left of shear during WE may more effectively converge  $M_a$  downwind, possibly explain-

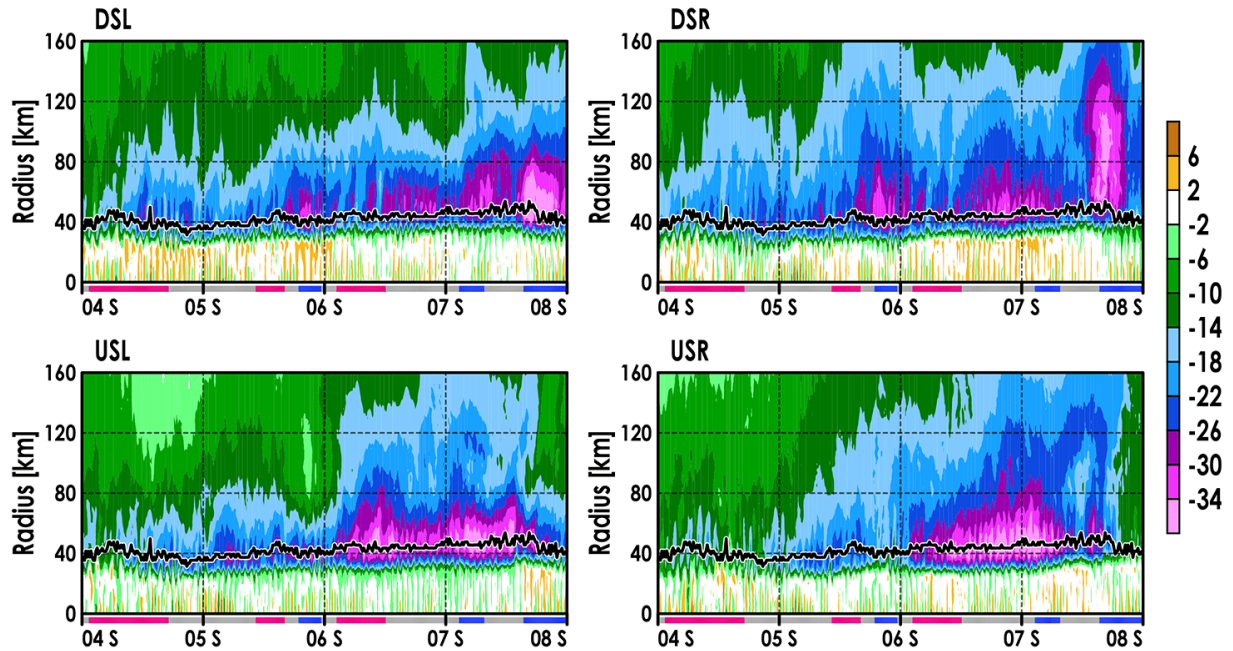


Figure 4.19: Time-radius Hovmöllers of radial velocity  $u$  ( $\text{m s}^{-1}$ ) at  $z \approx 210$  m in each quadrant of Hurricane Irma. The  $x$ -axis represents time, which is labeled by each day at 0000 UTC with the abbreviated month. A timeline shaded by intensity change (red for IN, gray for SS, blue for WE) is drawn at the bottom of each panel. The bold, black line represents the RMW. Panels are labeled by their quadrant abbreviation.

ing the anomalously strong BL tangential winds DSL at outer radii and upshear in the inner core (comparing Figures 4.11 and 4.20). After the WE period late on 05 September, the shear weakens to  $\sim 15$  kt and turns slightly toward the southeast. Irma moves more northwestward at an increased speed of  $\sim 15$  kt (moving toward USR) as it enters the 06 September IN phase. Early on 06 September, the upshear, inner-core BL inflow intensifies to over  $26 \text{ m s}^{-1}$  near the surface, while similarly positioned inflow downshear fluctuates in magnitude (between about  $14$  and  $30 \text{ m s}^{-1}$ ).

The asymmetric structures of RDIV at 1200 UTC and 2100 UTC 05 September are shown in Figure 4.21. During IN, the USL quadrant's BL appears to be associated with more divergence (and less convergence) outside the RMW. Radial divergence is also more apparent USR above the inflow layer, while radial convergence is mostly found within the inflow. The downshear quadrants are associated with more radial convergence, although small pockets of divergence also appear outside the RMW. As Irma weakens at 2100 UTC 05 September, radial convergence is present through

most of the DSR quadrant between the RMW and  $r = 100$  km. Weak RDIV is seen at  $r > 100$  km in the DSL quadrant, possibly indicative of shallow subsidence there. Strong RDIV appears upshear just radially outward from the convergent region near the RMW; this radial divergence in the USL quadrant spreads over 40 to 50 km radially, sloping outward with height. Shear-relative Hovmöllers of BL-integrated RDIV in Figure 4.22 suggest that Irma's WE period on 05 September is associated with BL divergence left of shear (particularly strong USL just outside the RMW) and weaker BL convergence USR inside the RMW. Irma's IN periods before and after the WE phase are linked to more axisymmetric BL convergence inside the RMW and weaker BL divergence outside the

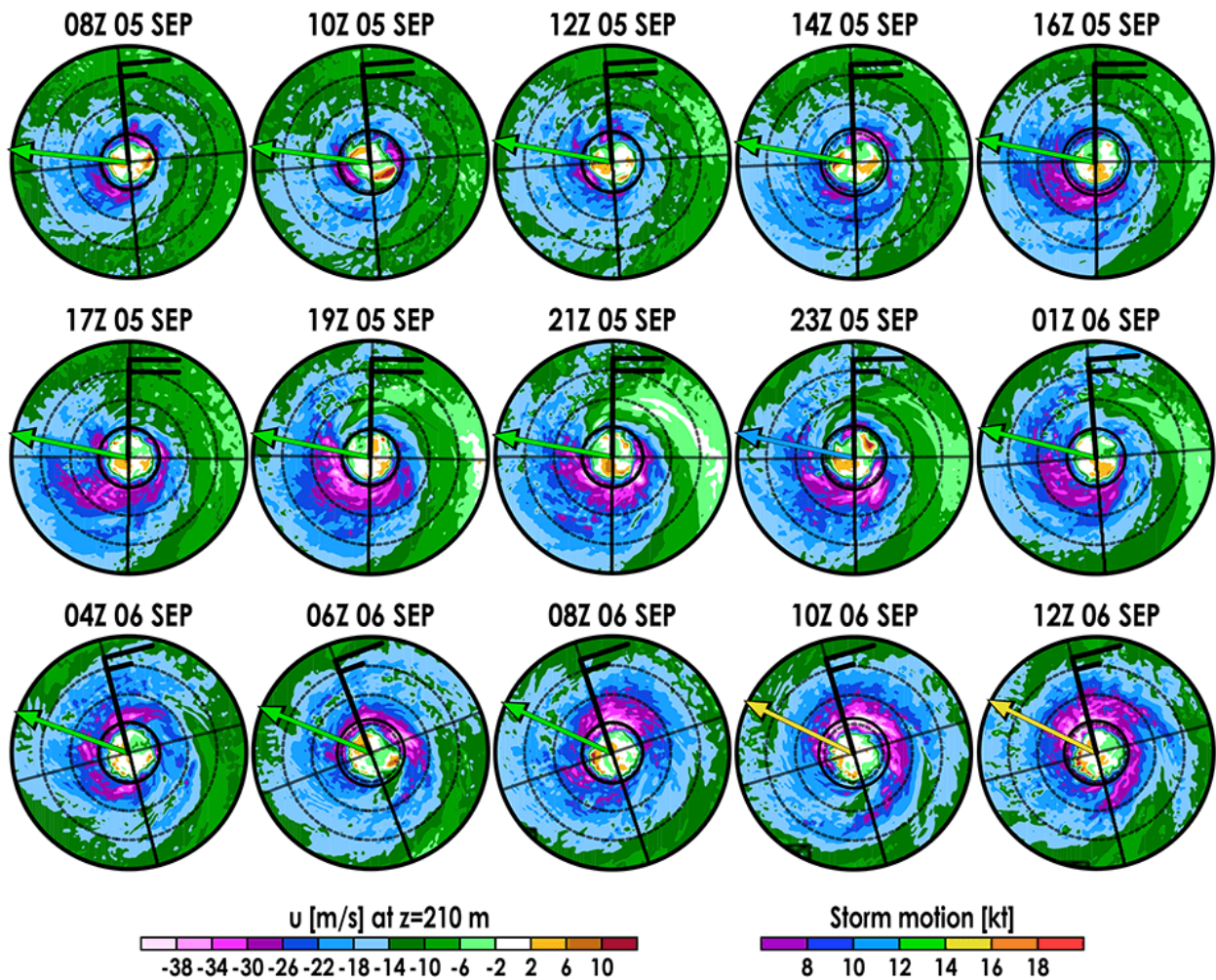


Figure 4.20: Similar to Figure 4.11, but using radial wind  $u$  ( $\text{m s}^{-1}$ ) at  $z \approx 210$  m.

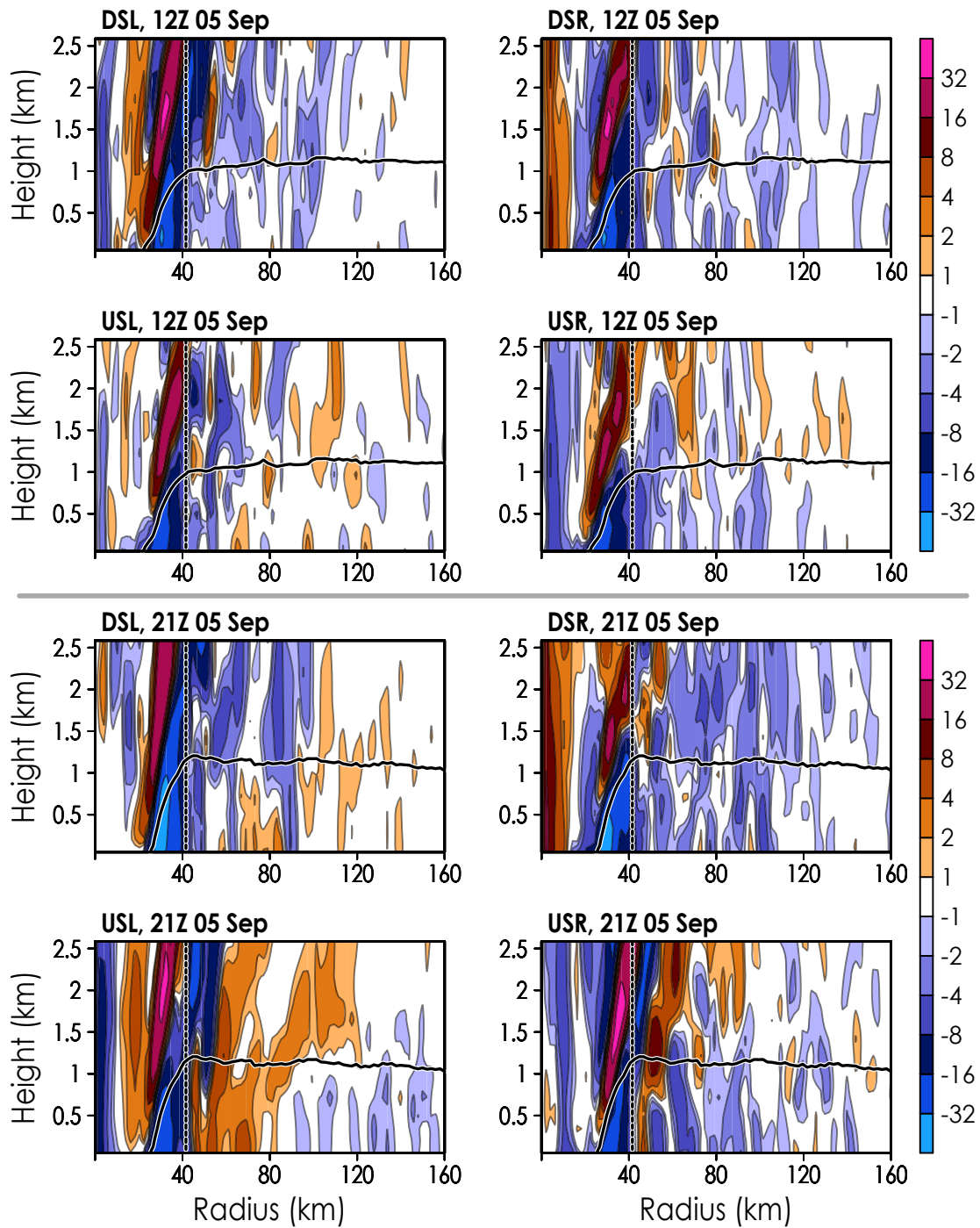


Figure 4.21: Similar to Figure 4.18, but plotted using radial divergence ( $10^{-4} \text{ s}^{-1}$ ).

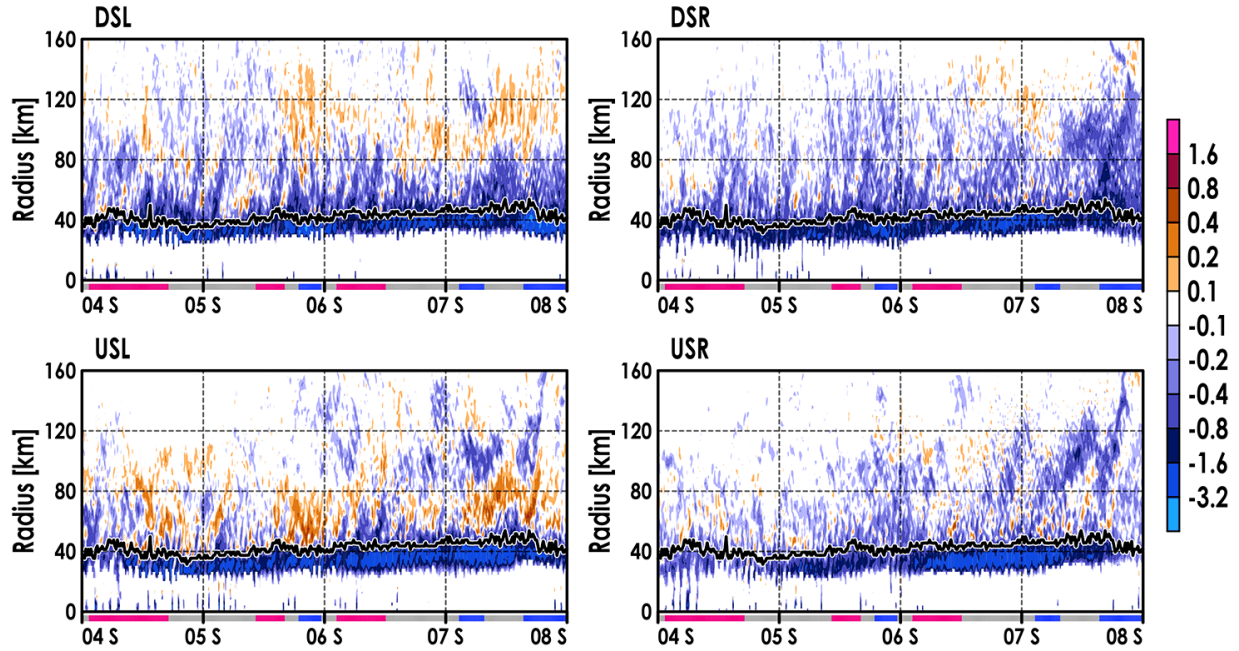


Figure 4.22: Similar to Figure 4.19, but shaded using vertically integrated radial divergence in the asymmetric radial inflow layer ( $\text{m s}^{-1}$ ).

RMW.

Similarly, cross sections depicting the azimuthal structure of vertical motion  $w$  (Figure 4.23) suggest that Irma weakens on late 05 September while descent is present at the BL top upshear and outside the RMW (particularly USL between 40 and 80 km radius). Hovmöllers of  $w$  near the top of the azimuthally averaged BL inflow shown in Figure 4.24 also show that Irma weakens on 05 September while descent occurs outside the RMW left of shear (mostly USL), and Irma's IN periods are often associated with strong, persistent ascent near and inside the RMW in all quadrants. Figure 4.25 shows a time series of vertical mass flux in the USL quadrant at  $z \approx 1.2$  km between  $r = 40$  km and  $r = 80$  km, which illustrates the downward transport of air into the BL leading up to and during Irma's WE phase on 05 September. When compared with data points from either of the neighboring IN phases using an unequal two-sample  $t$ -test, the vertical mass flux in the domain of Figure 4.25 is significantly different during Irma's WE phase to 99.9% confidence. The asymmetric, inner-core structure of  $w$  may have thermodynamic consequences—for example, the descent near the RMW in the USL quadrant may transport relatively low- $\theta_e$  air into the BL

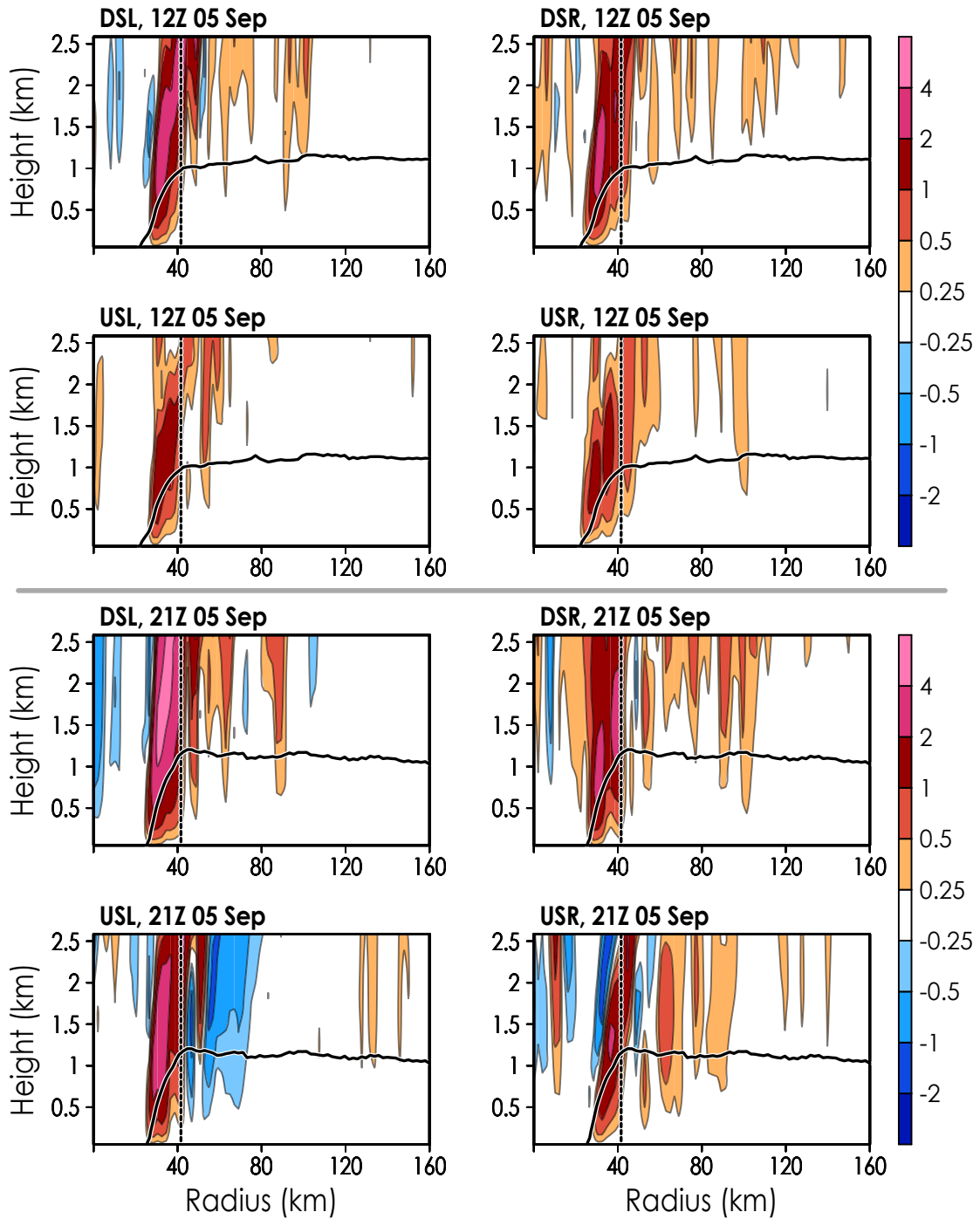


Figure 4.23: Similar to Figure 4.18, but shaded using vertical velocity  $w$  (m s<sup>-1</sup>).

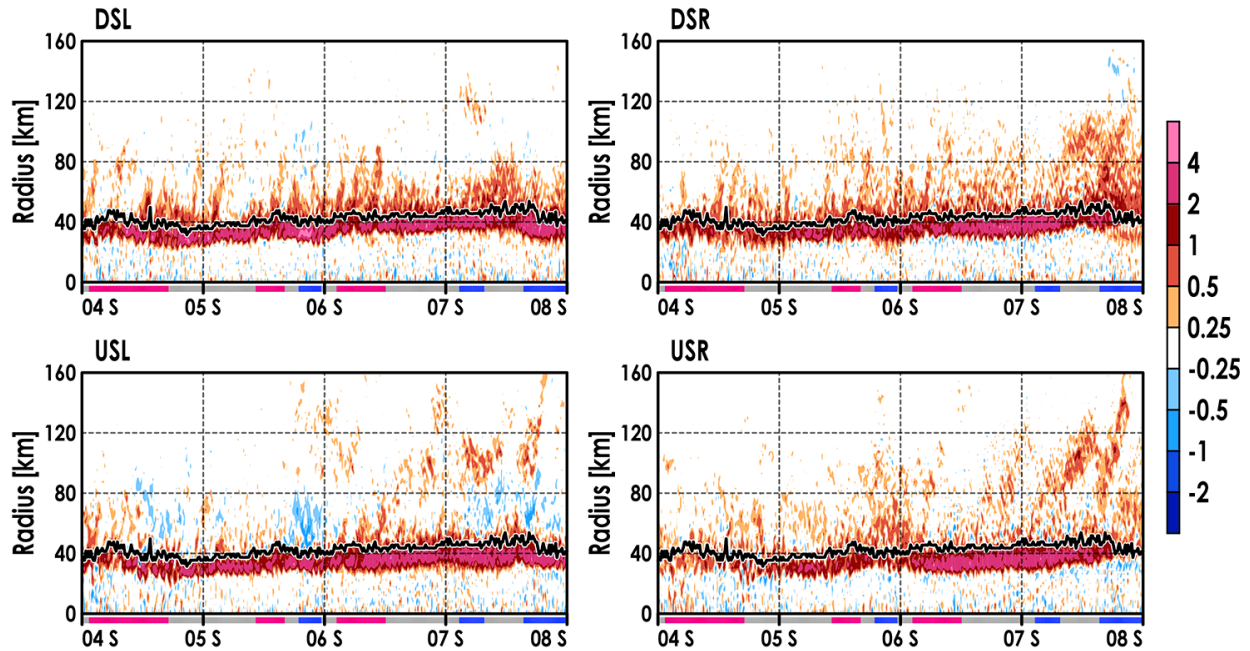


Figure 4.24: Similar to Figure 4.19, but shaded using vertical velocity  $w$  at  $z \approx 1.2$  km ( $\text{m s}^{-1}$ ).

inflow, affecting the moist entropy of parcels about to move inward through the RMW (and thus, possibly increasing low-level moist static stability by increasing  $\partial\theta_e/\partial z$ ).

The azimuthal structure of Hurricane Irma’s secondary circulation possessed some asymmetry, with stronger BL inflow located downshear and downstream. However, leading up to (and during) Irma’s weakening period on 05 September, the secondary circulation’s asymmetry amplified, with anomalously weak inner-core BL inflow upshear. The weak inflow upshear was associated with BL divergence and descent at the BL top, particularly in the USL quadrant and localized between 40 and 80 km radius. The downward motions at the BL top should export relatively low-entropy air from the free atmosphere into the BL inflow just outside the RMW. The reduced-entropy inflow would arrive at the RMW downwind (likely upshear); if air-sea fluxes do not replenish the local inflow’s moist static energy before that time, that relatively low-entropy air could affect ongoing eyewall ascent negatively. We will investigate this speculation in the following section on Irma’s thermodynamic structure.

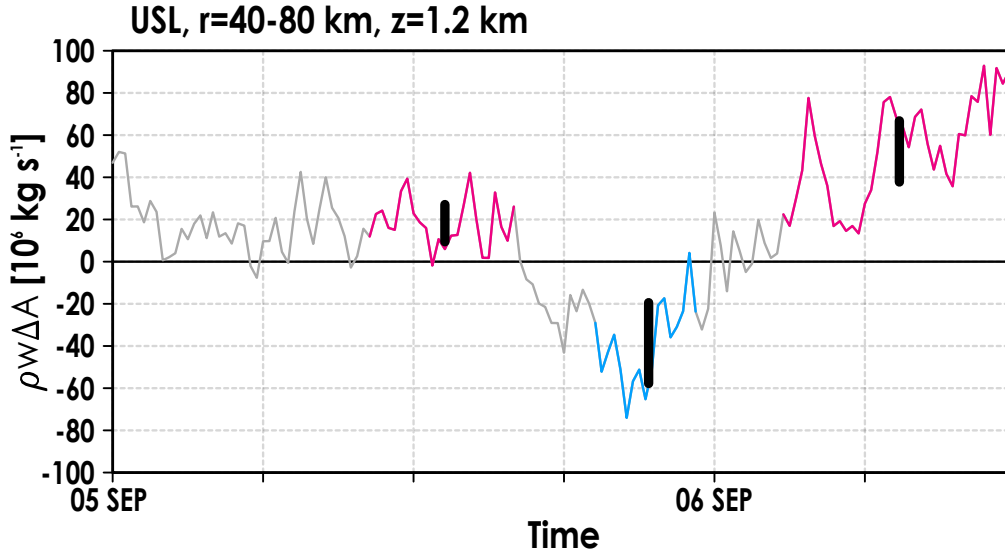


Figure 4.25: Time series of upward vertical mass flux ( $10^6 \text{ kg s}^{-1}$ ) in the upshear-left quadrant of Hurricane Irma from 0000 UTC 05 September to 1200 UTC 06 September. The flux is calculated at  $z \approx 1.2 \text{ km}$  and averaged between radii of 40 and 80 km. The time series is shaded by intensity change (red for IN, gray for SS, blue for WE). Unequal size, two-sample  $t$ -tests comparing the WE phase with each of the IN phases shown found statistically different mean vertical mass fluxes to 99.9% confidence (bold, black lines denote confidence intervals for each IN and WE phase). Statistical significance was also found using  $w$ ; it is not shown due to the fact that surface area of cylindrical data cells increases with  $r$ , which is not considered in  $w$  but is necessary to calculate the mass flux.

## 4.5 Thermodynamics

### 4.5.1 Axisymmetric Structure

Azimuthally averaged, low-level thermodynamic properties from Hurricane Irma's IN and WE phases on 05 September are shown in Figure 4.26. Virtual temperature  $T_v$  and virtual potential temperature  $\theta_v$  are quite similar between the 05 September IN and WE phases, indicating that Irma's low-level dry thermodynamics are somewhat steady across the time period shown. A radial maximum in  $T_v$  and  $\theta_v$  is situated inward of the RMW, associated with a minimum in relative humidity ( $RH$ ; also in Figure 4.26) in the hurricane's eye above the BL. The strong radial divergence along the inner edge of Irma's eyewall above  $z \approx 500 \text{ m}$  may be linked to subsidence advecting air downward from aloft. The air above that radial divergence would be dry and warm, as it would

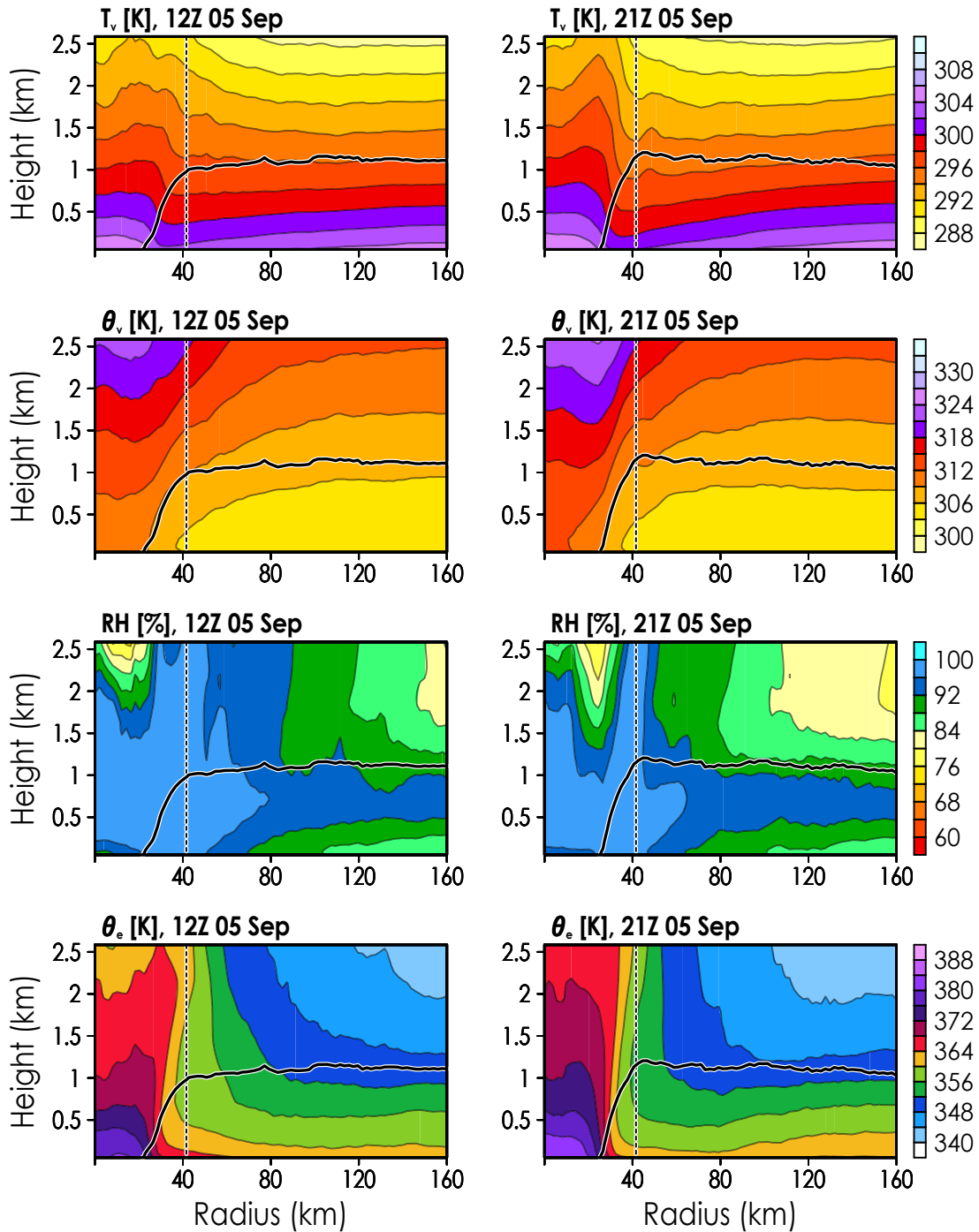


Figure 4.26: Radius-height cross sections of Hurricane Irma’s azimuthally averaged virtual temperature  $T_v$ , potential virtual temperature  $\theta_v$ , relative humidity  $RH$ , and equivalent potential temperature  $\theta_e$  on 1200 UTC 05 September (left, IN phase) and 2100 UTC 05 September (right, WE phase). Rows of figures use the color bar to their right, and each plot has its units listed above. The dashed and solid black lines indicate the RMW and azimuthally averaged inflow layer, respectively.

be near the bottom of the hurricane eye's indirect secondary circulation (where air from the upper troposphere is forced to descend dry adiabatically toward the lower troposphere).

The radial and vertical structure of relative humidity also maintains a general form over time. The BL inflow is usually moist throughout, with  $RH$  decreasing gradually over radius outside the RMW. The vertical gradient of  $RH$  is stronger than the radial gradient of  $RH$  outside the RMW, with relatively dry air in the near-surface inflow (below  $\sim 500$  m AGL), drier air above the azimuthally averaged inflow layer (above  $\sim 1.2$  km AGL), and the most-moist air between these two regions of drier air ( $z \approx 750$  m). Near the RMW, the vertical gradient of  $RH$  is minimized as the air is approximately saturated near eyewall ascent. Between Irma's IN and WE periods on 05 September, the vertical slot of dry air inward of the RMW extends downward, the air above the BL becomes somewhat drier, and the radial width of the approximately saturated air at the RMW shrinks. The time evolution of Irma's  $RH$  in the near-surface inflow and above the BL is displayed in Figure 4.27. Between Irma's IN periods on 05 September and 06 September, near-surface  $RH$  dries subtly between the RMW and  $r \approx 80$  km (with the driest near-surface  $RH$  in the middle of the 05 September WE period). Over the same time, air near the inner periphery of Irma's eyewall ( $r \approx 25$  km) dries above the BL. The drying of near surface inflow and air near the low-level inner eyewall prior to and during Irma's WE may affect eyewall buoyancy (and thus convection).

To examine properties of BL moist entropy, Figures 4.26 and 4.27 show respectively the azimuthal-mean spatial and temporal structures of Hurricane Irma's low-level  $\theta_e$ . In Figure 4.26 between the RMW and  $r = 80$  km, the BL inflow during IN on 05 September has relatively high- $\theta_e$  air compared to during the WE phase that followed on the same day. In Figure 4.27, the near-surface  $\theta_e$  is shown to decrease over time between the RMW and  $r \approx 100$  km prior to and during Irma's WE on 05 September. At  $z \approx 1.85$  km,  $\theta_e$  is shown to decrease over the same time period outside the RMW (and to a lesser degree, inside the RMW), as well. As with the profiles of azimuthal-mean relative humidity, it appears that Hurricane Irma's WE period on 05 September is associated with a reduction in BL moist entropy immediately outside the RMW, possibly due to asymmetric near-surface inflow and consequent BL divergence and descent. The reduction in moist entropy between 1200 UTC and 2100 UTC in that radial band may be associated with the asymmetric descent that developed left of shear (as discussed in subsection 4.4.2 and shown in

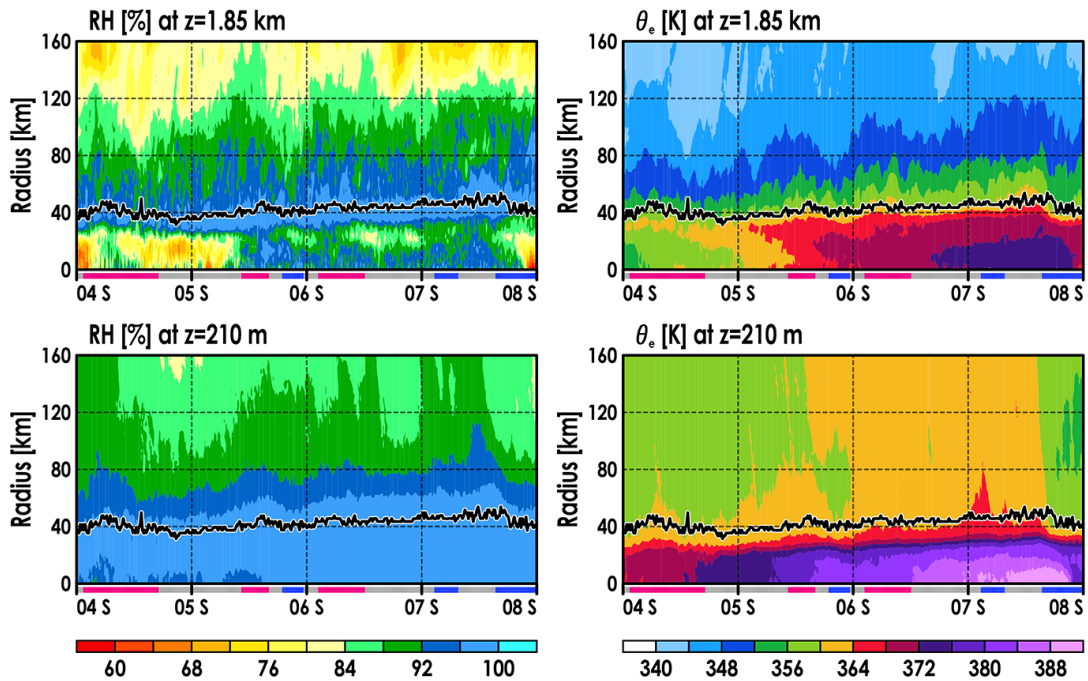


Figure 4.27: Time-radius Hovmöller plots of Hurricane Irma’s near-surface relative humidity  $RH$  (in %, left) and equivalent potential temperature  $\theta_e$  (in K, right). The top row of plots depict fields taken at  $z \approx 1.85$  km, and the bottom row of plots show fields at  $z \approx 210$  m. A timeline shaded by intensity change is drawn at the bottom of each panel. The bold, black line represents the RMW. Each column of plots uses the color bar below the column.

Figures 4.23 and 4.24), which would advect drier/colder air from the free atmosphere downward into the moist BL just outside the RMW.

The azimuthal-mean BL thermodynamics suggests that, as hypothesized in the asymmetric analysis of the secondary circulation in subsection 4.4.2, free atmospheric air with relatively low latent and internal energy entered the BL inflow just outside the RMW prior to a WE phase on 05 September. Irma’s azimuthal-mean thermodynamic structure did not appear to undergo other evident evolutions aside from a gradual increase in  $\theta_e$  in Irma’s eye (associated with decreasing central pressure). Examining the azimuthal structure of Irma’s BL thermodynamics will highlight local variations of  $RH$  and  $\theta_e$ , such as the localized reduction in moist static energy upshear where descent into the inner-core BL occurred during the 05 September WE phase.

## 4.5.2 Asymmetric Structure

Snapshots of shear-relative, low-level moisture structure in Hurricane Irma on 05 September are given in Figure 4.28. During IN at 1200 UTC, all quadrants have high moisture below 2.5 km AGL and at  $r < 100$  km. Columns of relatively high or low  $RH$  outside the RMW may be associated with locally sporadic vertical motions (as shown in Figure 4.23). Before and during Irma's WE period, drier air appears above the BL in the DSL and USL quadrants, likely due to downdrafts at or dry air intrusion from outer radii—this air is advected inward by the deep inflow DSL as it rotates into the USL quadrant (Figure 4.18), where downdrafts are occurring between the RMW and  $r \approx 80$  km (Figure 4.23). In the USR quadrant, moisture seems to be replenished, probably due to air-sea turbulent fluxes, persistent inflow, and shallow ascent associated with radial convergence outside the RMW.

Radius-height cross sections of  $\theta_e$  in each quadrant are shown in Figure 4.29, with similar properties to those implied by the  $RH$ -field. During IN at 1200 UTC 05 September, Irma's  $\theta_e$  structure is mostly axisymmetric. As shear- and motion-induced asymmetries amplify with time leading up to 2100 UTC 05 September (shown previously in Figures 4.11 and 4.20), BL  $\theta_e$  in the USL quadrant just outside the RMW becomes anomalously low. Figure 4.30, which shows horizontal snapshots of  $\theta_e$  near the end of 05 September, suggests that low- $\theta_e$  air above the BL swirls toward Irma's center left of shear, and then descends or mixes downward into the BL at  $r < 100$  km. Thus, upshear  $\theta_e$  near the RMW is lowest due to the import of drier, lower- $\theta_e$  air originating DSL. In the DSR quadrant, relatively high- $\theta_e$  air is found between the RMW and  $r = 80$  km, likely a result of radial outflow aloft and associated advection of high- $\theta_e$  air from the eyewall, or ascent of high-enthalpy air out of the BL.

The Hovmöllers in Figure 4.31 illustrate the horizontal structure of  $\theta_e$  over time at  $z \approx 1.85$  km. In the DSR quadrant,  $\theta_e$  between the RMW and  $r \approx 120$  km decreases over time between the IN and WE periods on 05 September, in tandem with enhanced inflow in that quadrant. The DSL quadrant also sees a decrease in  $\theta_e$  over the same span of time, with  $\theta_e < 348$  K at  $r > 100$  km in association with drier air being advected inward from outer radii. Moist entropy above the BL in the USL sector is also reduced in the 80 to 120 km radial band due to the inflow of drier air (which rotated into the USL quadrant from DSL) prior to and during the WE period on 05 September. These

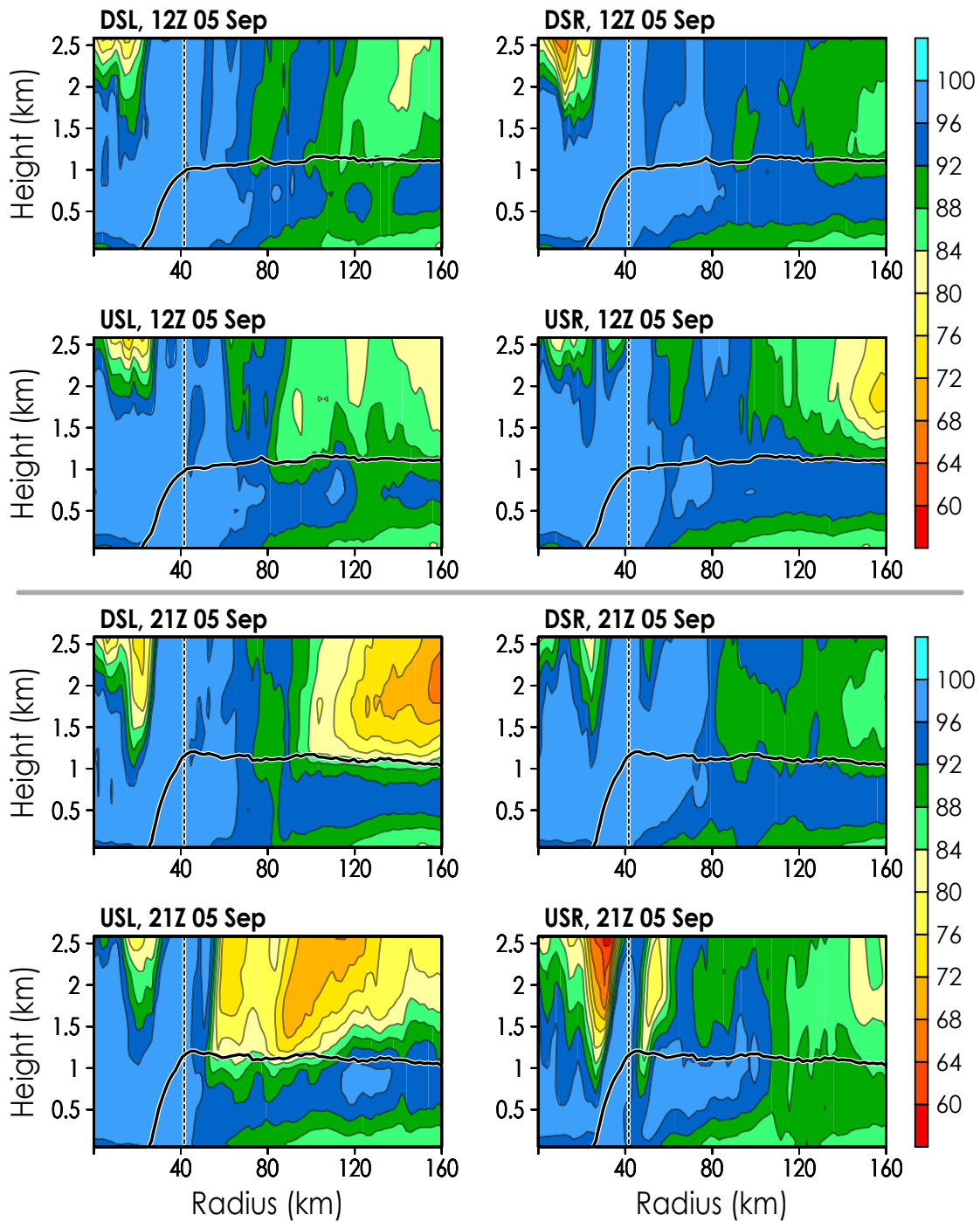


Figure 4.28: Quadrant-specific,  $r$ - $z$  cross sections of Hurricane Irma's relative humidity  $RH$  (%) on 1200 UTC 05 September (top two rows, during IN) and 2100 UTC 05 September (bottom two rows, during WE). Panels are labeled by the representative quadrant. The dashed, black line marks the RMW. The bold, black line indicates the axisymmetrized radial inflow layer.

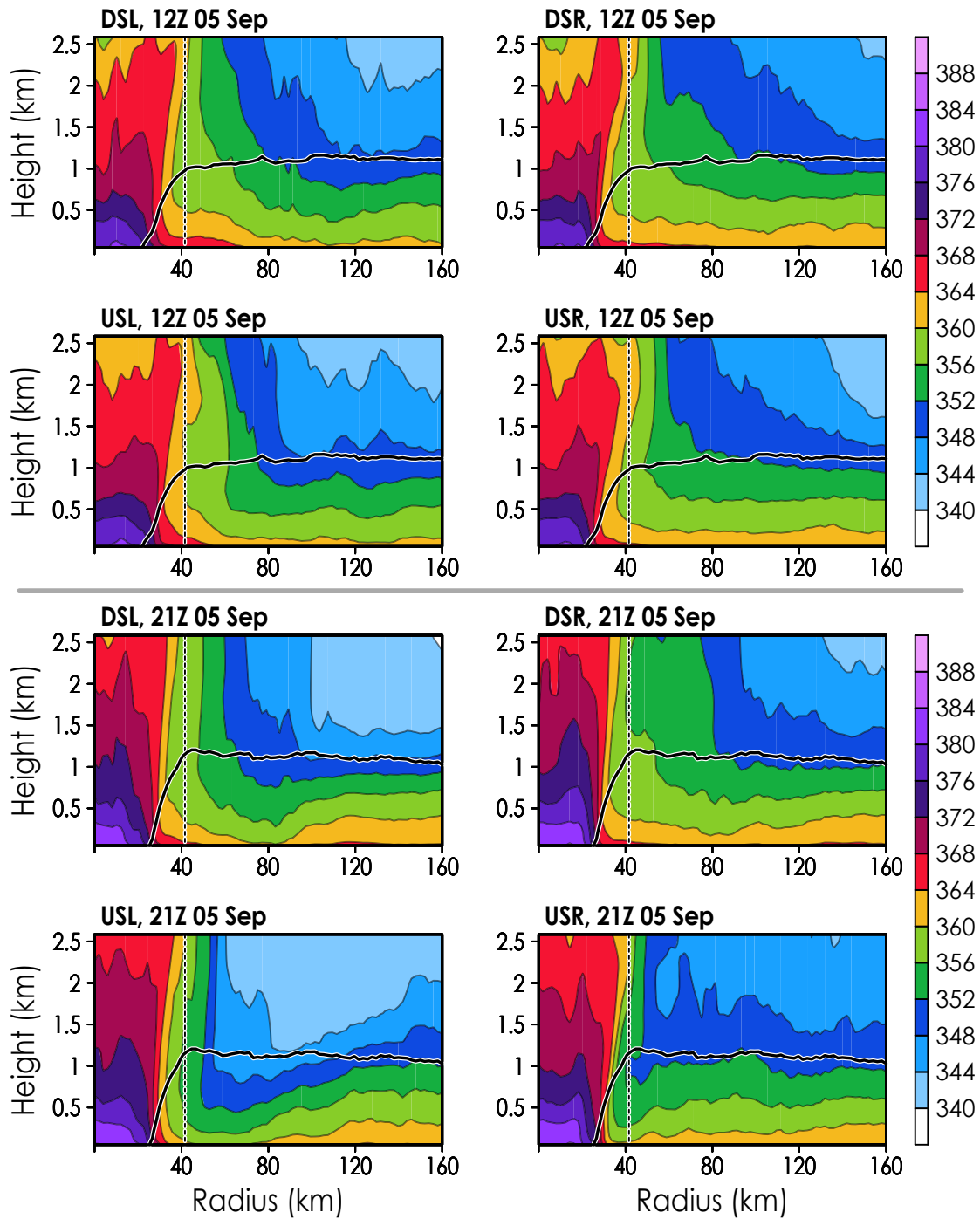


Figure 4.29: Similar to Figure 4.28, but shaded using equivalent potential temperature  $\theta_e$  (in K).

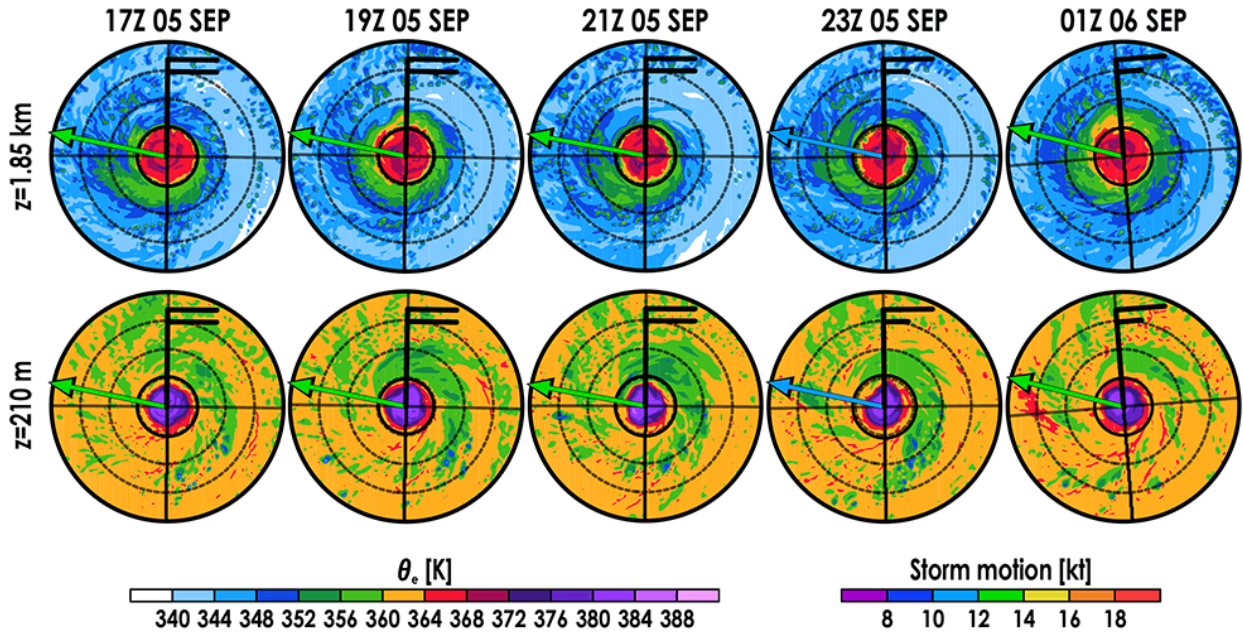


Figure 4.30: Similar to Figure 4.11, but using  $\theta_e$  (K) at  $z \approx 1.85$  km (top) and  $z \approx 210$  m (bottom) from times associated with the WE phase on 05 September.

asymmetries in  $\theta_e$  above the BL diminish after the WE period, as the BL secondary circulation reduces its asymmetry (i.e., downshear inflow becomes shallower and weaker while upshear inflow becomes stronger) in conjunction with the storm motion and deep-layer shear turning such that the motion is oriented USR (as shown in Figure 4.20).

Similar to Figure 4.31, Figure 4.32 shows the shear-relative structure of  $\theta_e$  over time near the surface ( $z \approx 210$  m). When drier air above the BL was moving radially inward left of shear in the latter half of 05 September, lower- $\theta_e$  also appeared between the RMW and  $r \approx 100$  km near the surface left of shear. Based on Irma's azimuthal distribution of  $w$  and BL-integrated RDIV, the relatively low- $\theta_e$  air at  $z \approx 210$  m in the aforementioned radial band originates from above the BL, which is brought down toward the surface via BL radial divergence and associated subsidence. This near-surface, relatively low-enthalpy air should eventually arrive at (and move inward beyond) the RMW, entering pre-existing eyewall ascent and potentially reducing slantwise (i.e., nearly parallel to a sloped  $M_a$  surface) buoyancy there. A weakening of convection in the eyewall via import of relatively low- $\theta_e$  air from the BL could negatively impact intensity by reducing the amount of

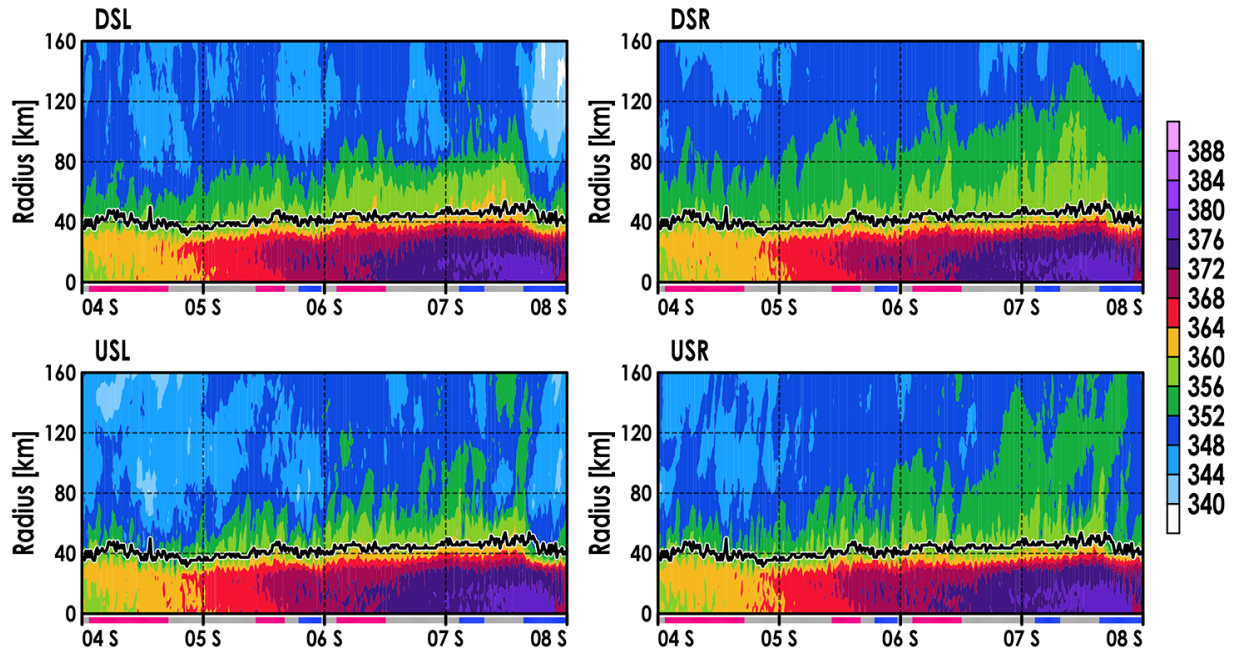


Figure 4.31: Time-radius Hovmöllers of  $\theta_e$  (K) at  $z \approx 1.85$  km in Hurricane Irma's shear-relative quadrants. The  $x$ -axis represents time, labeled by each day at 0000 UTC. A timeline shaded by intensity change is drawn at the bottom of each panel. The bold, black line represents the RMW. Panels are labeled by their quadrant abbreviation.

diabatic heating inside the RMW, thereby weakening Irma's inner-core temperature anomaly and surface pressure gradient. The low- $\theta_e$  air near the surface left of shear during Irma's WE period vanished after 0000 UTC 06 September, also likely due to Irma's secondary circulation in the BL becoming less asymmetric.

The azimuthal structure of low-level  $RH$  and  $\theta_e$  in Irma was mostly symmetric throughout the analysis period, with the exception of asymmetries that formed prior to the WE phase on 05 September. These asymmetries persisted through the WE period, and then quickly diminished during the SS phase immediately following WE. Specifically, the asymmetry consisted of drier air above the BL that swirled toward Irma's inner core in low-level inflow from downshear. The drier air was likely advected downward by subsidence into the BL left of shear, particularly in the USL quadrant (Figures 4.23 and 4.24). The reduced entropy in the inner-core BL in that quadrant would affect local eyewall convection and associated diabatic heating therefrom, possibly

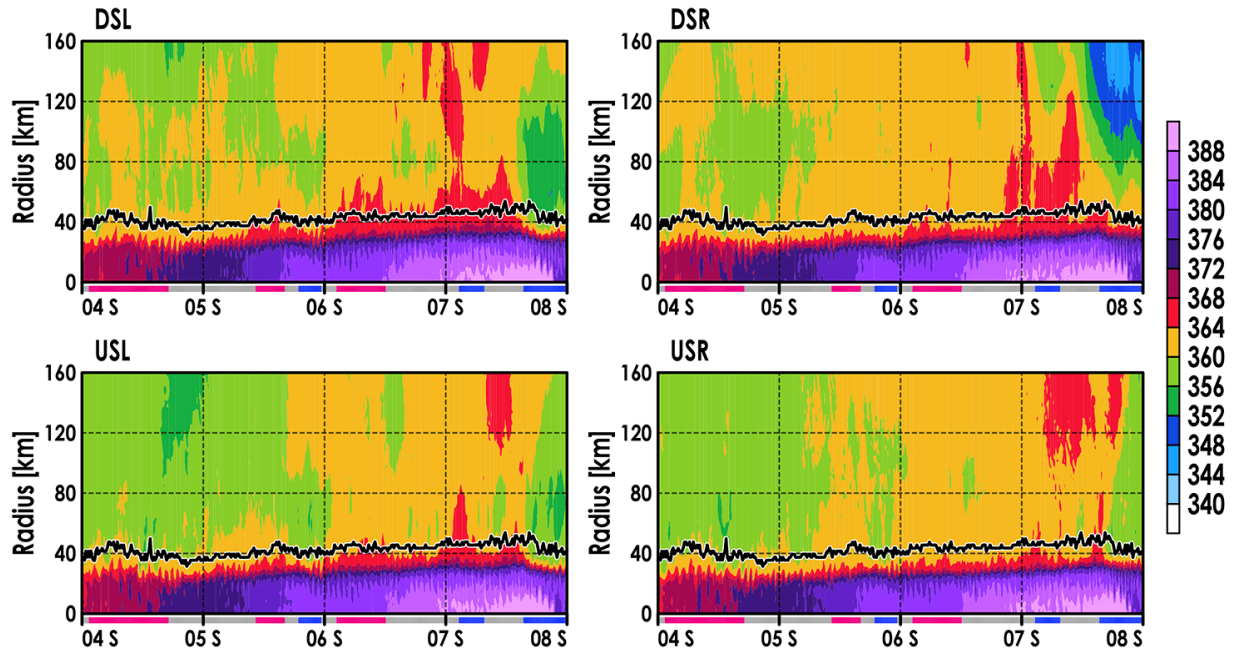


Figure 4.32: Similar to Figure 4.31, but using  $\theta_e$  (K) at  $z \approx 210$  m.

weakening Irma’s warm-core anomaly (and thus, Irma’s intensity).

## 4.6 Summary

To address the questions and uncertainties remaining after our observational composite analysis, a high-resolution, full-physics simulation of Hurricane Irma in 2017 was completed using WRF-ARW. Three-dimensional hurricane BL structure was examined from the results of the simulation, with a focus on mechanisms and structural evolutions in coincidence with intensity change. Hurricane Irma represents the first half of our numerical analysis that intended to investigate BL structure in the absence of apparently strong environmental forcing (specifically, the effects of deep-layer environmental wind shear). The numerical experiment covered Hurricane Irma’s early development and subsequent progression, spanning from 0000 UTC 03 September to 0000 UTC 11 September. The simulated hurricane moved to within a few hundred kilometers of Puerto Rico and Hispaniola, and then made landfall in Cuba—these times when Irma’s inner-core dynamics would be influenced by land began between 07 September and 08 September, affecting the sim-

ulation results thereafter. We limited our analysis of Hurricane Irma to between 05 September and 07 September prior to land interaction, allowing the simulated hurricane time to organize after initialization and avoiding complex interference from nearby land.

The analysis of Hurricane Irma's boundary layer revealed that, at least in the lowest 1.25 km of the atmosphere, Irma's simulated inner-core structure often had little asymmetry. Between 04 September and 06 September, Irma moved westward toward Puerto Rico at 8 to 14 kt, as deep-layer shear prevailed out of the north (with magnitude ranging between roughly 10 and 20 kt). Hurricane Irma organized and intensified through much of 04 September, and then intensified again following a steady-state intensity period on 05 September. Shortly after the IN period on 05 September, Irma began to weaken. Between the IN and WE phases on 05 September, Irma's BL structure developed more-pronounced kinematic and thermodynamic asymmetries (shown schematically in Figure 4.33). Irma persistently moved westward as weak-to-moderate northerly shear impinged on the system over two days leading up to the WE phase on 05 September.

In prior observational research, anomalously deep and strong BL inflow has been seen downshear, while weak and shallow BL inflow has been found upshear (Zhang et al. 2013). Storm motion has also been shown to be associated with similar BL inflow asymmetry (Barnes and Dolling 2013), where BL inflow is strongest downstream of a moving hurricane (and weakest upstream). The kinematic and thermodynamic BL asymmetries that appeared in Irma on 05 September may be representative of the time-aggregate effect of asymmetric forcing on BL structure by storm motion and environmental vertical shear. As storm motion was nearly orthogonal and to the right of shear up until 06 September, one might expect the downshear-right quadrant to develop anomalously intense and deep BL inflow (which is represented by near-surface vectors and inward movement of drier air above the BL in Figure 4.33). By the same logic, the upshear-left quadrant would be expected to have the weakest, most shallow BL inflow (also reflected in Figure 4.33). Early on 06 September, Irma began to move more northward as the shear turned more eastward (making the storm motion vector point upshear-right), and in conjunction with these changes in motion and shear was a reduction in asymmetric BL inflow. Hurricane Irma intensified once more after the near-surface inflow became stronger upshear at that time, as the storm's presentation in outgoing longwave radiation and upper-level vertical motion suggested a nearly axisymmetric inner core.

The inflow asymmetries associated with Hurricane Irma’s WE phase on 05 September likely led to changes in Irma’s primary circulation and thermodynamic structure, which may have played a role in the storm’s decay. As BL inflow deepened and intensified downshear—including at radii well outside the RMW—drier air at large radius above the BL began to move inward towards Irma’s inner core (illustrated by the yellow region at 1.5 km in Figure 4.33). The low- $\theta_e$  air was likely advected into the downshear sector by the deep inflow, which then rotated inward and into the USL quadrant. In the USL quadrant, the low- $\theta_e$  air immediately above the BL was a few kilometers away from Irma’s RMW. Because the shear and storm motion were such that BL inflow became minimized outside the RMW in the USL quadrant, substantial BL radial divergence (via strong speed divergence of inflow shown in Figure 4.33) was occurring outside the RMW, which promoted descent across the BL top. The drier, low- $\theta_e$  air above the BL was advected downward into the near-surface inflow by the subsidence in the USL quadrant, which was then fed to Irma’s eyewall by the inflow (shown by the yellow region near the surface in Figure 4.33). The drier air would presumably affect local eyewall ascent and thus vortex intensity, perhaps explaining Irma’s decay. If not for the asymmetrically deep inflow downshear, low- $\theta_e$  air from outer radii may not have been as easily moved towards Irma’s inner core. If not also for the asymmetrically weak inflow upshear-left, that low-entropy air may not have been pulled downward into the near-surface inflow by BL divergence. The lower-entropy air in the BL outside the RMW that persisted through Irma’s WE phase corroborates findings from our earlier composite analysis (subsection 3.3.3), which found that WE storms were associated with relatively low- $\theta_e$  air in the BL outside the RMW.

Aside from these thermodynamic consequences linked with the asymmetric secondary circulation, the inner-core primary circulation also developed asymmetry possibly in direct relation with the BL inflow structure. The deeper, stronger inflow downshear during (and leading up to) Irma’s weakening on 05 September is associated with the most-efficient import of high- $M_a$  air from outer radii (for a given radial gradient of  $M_a$ ). Thus, the downshear BL at that time represents the azimuthal sector where tangential wind spin-up via positive  $M_a$  advection is maximized—due to both stronger radial *and* vertical advection, the latter being linked to stronger BL convergence. Inversely, the upshear BL at the same time represents where spin-down is maximized via relatively

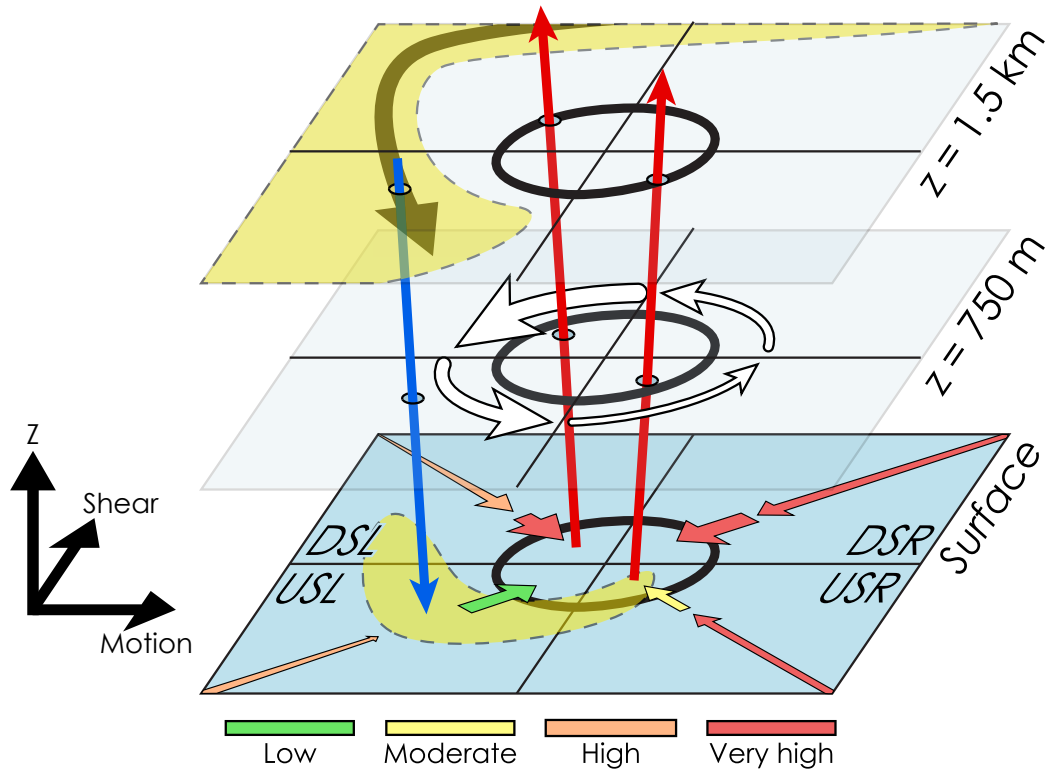


Figure 4.33: Volumetric conceptual diagram of Hurricane Irma's low-tropospheric structure during its weakening phase on 05 September. Vertical, shear, and motion directions are indicated on the left side. Each horizontal plane is labeled by its approximate vertical level on the right side of the figure. Horizontal planes are divided into shear-relative quadrants by thin black lines, and each quadrant is labeled on the surface plane. Bold black ovals represent the RMW as detected at  $z \approx 1.8$  km. Tangential vectors (white) and radial vectors (shaded) have magnitudes proportional to their thickness. Radial vectors are shaded by  $\theta_e$  using the scale at the bottom. Ascent and descent vectors are colored red and blue, respectively. The yellow shaded region on the horizontal planes represents dry, low- $\theta_e$  air.

dominant frictional dissipation (due to minimized positive  $M_a$  advection). Possibly as a result of the aforementioned dipole of spin-up/spin-down tendency along azimuth, Hurricane Irma's strongest BL tangential wind rotated from downshear to left of shear between its intensification and decay on 05 September. This evolution is explained as a result of BL air increasing its tangential velocity as it rotates through the downshear quadrants where spin-up is maximized, and upon exiting into the upshear-left quadrant enters a region of relatively dominant spin-down (and thus, the tangential

wind becomes maximized left of shear, between the regions of relatively high and low spin-up via  $M_a$  advection).

To summarize, Hurricane Irma's vortex tended to steadily intensify, with the exception of a brief WE period on 05 September. Outside of the RMW, Irma's storm-relative tangential wind decreased rapidly with increasing radius (i.e., Irma's  $v$ -field was peaked across  $r$ ). Irma's inner core was highly inertially stable, with  $I^2$  asymptoting toward zero with increasing radius. Associated with this vortex was strong radial inflow confined to the RMW, with maximized BL convergence inward of the RMW and weak BL convergence outside the RMW. Ascent near the BL top was concentrated inward of the RMW. Considering that Irma steadily intensified for much of the analysis period, the kinematic structure of Irma's simulated BL appears to be in agreement with the composite analysis in section 3.3, which found that IN storms had relatively peaked  $v$ -fields, weaker  $I^2$  outside the RMW, and BL convergence confined to the RMW.

However, Irma did undergo a WE phase on 05 September in this simulation, and Irma's azimuthally averaged kinematic structure during that time was hardly distinguishable from the mean structure seen during IN on 05 and 06 September. The azimuthal structure of Irma's BL developed some asymmetry leading up to its WE phase, likely in relation to persistent, moderate, and northerly environmental shear. Asymmetric BL inflow was associated with BL divergence (subsidence into the BL) localized left of shear. Drier, free atmospheric air downshear was advected inward by inflow toward Irma's inner core, arriving in the USL quadrant just outside the eyewall. Localized subsidence into the BL in the USL quadrant (linked with the asymmetric BL inflow) advected the low-entropy air into the BL inflow below, which was then fed to the eyewall convection downwind. We suspect that this negatively affected diabatic heating associated with eyewall convection and/or the upward acceleration of high- $M_a$  air from the BL, thus impacting Irma's intensity. Irma's azimuthal-mean structure did show a decrease in BL  $\theta_e$  just outside the RMW (relative to both time and radius), which is similar to the  $\theta_e$ -field seen in the WE composite in subsection 3.3.3 (i.e., relatively low- $\theta_e$  outside the RMW).

The simulated WE phase of Hurricane Irma on 05 September highlights the importance of azimuthal structure of the hurricane BL in relation to intensity. Based on the kinematics alone, Irma's azimuthal-mean structure did not convey any obvious structural evolution when alternating

between IN and WE phases between 05 and 06 September. The analysis of azimuthal structure gave us a clearer evolution, where asymmetries were ultimately linked to a localized import of drier air into the inner-core BL. In the forthcoming analysis of Hurricane Earl (2010) in Chapter 5, the asymmetric structure in relation to stronger shear and more northward storm motion is more pronounced and persistent. Therein, we will examine the effects of azimuthal BL structure on storm intensity further.

# CHAPTER 5

## MODERATE-SHEAR NUMERICAL ANALYSIS: HURRICANE EARL (2010)

The simulation of Hurricane Irma (2017) in Chapter 4 represented a case where a hurricane is influenced by an environment of weak-to-moderate deep-layer vertical shear. Here, we simulate Hurricane Earl in 2010, which was amongst an environment of moderate-to-strong vertical shear. A loose hypothesis regarding the environmental difference is that the increased magnitude of vertical shear will induce more BL asymmetry (note that, in our simulation of Irma, the storm conveyed weak BL asymmetry with a few exceptions). As was done in Chapter 4, we compare azimuthal-mean BL structure to our observational composite in Chapter 3 to determine if individual hurricanes possess similar BL structures during intensity change. By adding dimensionality in the form of differing environmental shear, this chapter also extends our investigation of BL azimuthal structure from Chapter 4.

### 5.1 Methodology

Similar to our study of Hurricane Irma (2017) in Chapter 4, we will use the vortex-following WRF-ARW version 3.9 to simulate Hurricane Earl in 2010, starting the model run days before its observed recurvature off the eastern U. S. seaboard. Model specifications for our simulation of Hurricane Earl are identical to those described in section 4.1 and summarized in Table 4.1, except for the simulated range of time and spatial coverage of the four domains. The simulation runs from 1200 UTC 28 August to 1200 UTC 04 September, and the initial domain setup is shown in Figure 5.1. Post-processing and determining diagnostics from the model results (e.g., storm motion, deep-layer shear, intensity) are also handled as described in section 4.1. We will not examine the first day of model output in detail, and we will also avoid analyzing the period in which Hurricane Earl appears to be undergoing extratropical transition following recurvature.

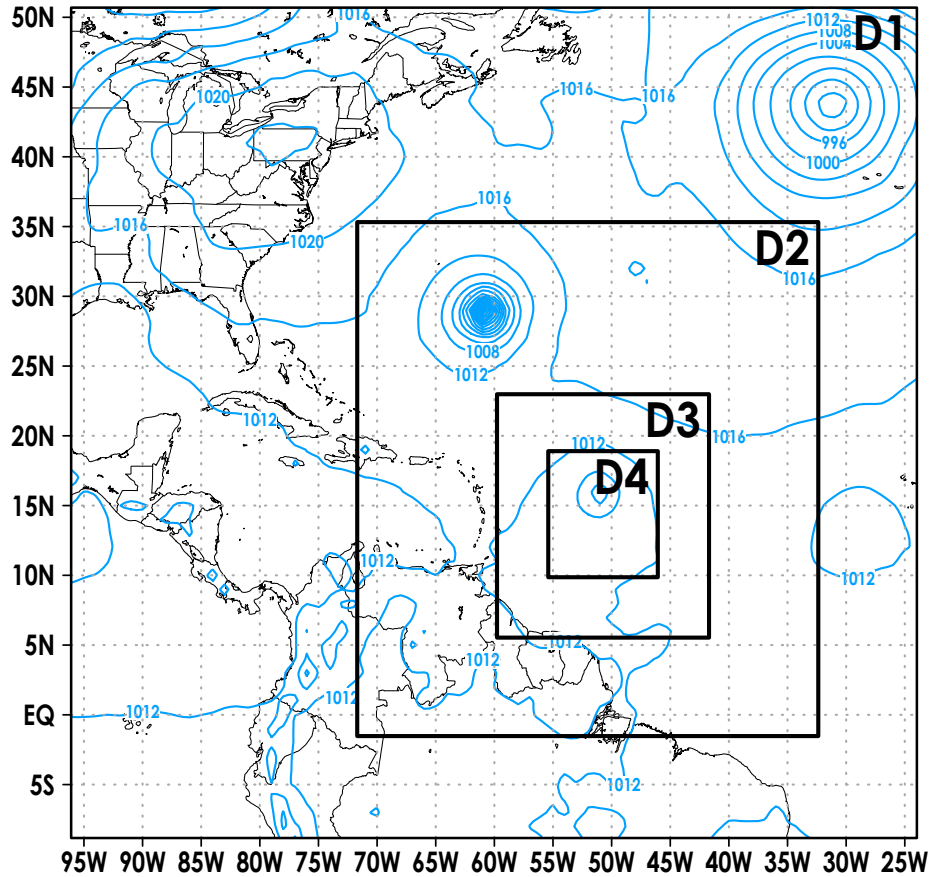


Figure 5.1: Map illustration of the four domains set at initialization (1200 UTC 28 August 2010) for the WRF-ARW simulation of Hurricane Earl. Contours of mean sea-level pressure (from eta reduction) at initialization time from NCEP FNL Operational Global Analysis data (NCEP 2000) are drawn in blue (hPa, 4 hPa interval). The outermost domain (region containing “D1”) is static with a horizontal resolution of 36 km. Domains labeled “D2,” “D3,” and “D4” are vortex-following with horizontal resolutions of 12 km, 4 km, and 1.333 km, respectively.

## 5.2 General Overview

As in section 4.2, we first analyze the general results of the simulation to provide background for our BL structure analysis. Snapshots of the high-resolution OLR field (analogous to infrared satellite imagery) from Hurricane Earl’s simulation are shown in Figure 5.2. Prior to 01 September, Hurricane Earl moves west-northwestward at 10–14 kt, due north of Puerto Rico and Hispaniola. Deep-layer shear of at least 15 kt turns counter-clockwise from north on 29 August to west at

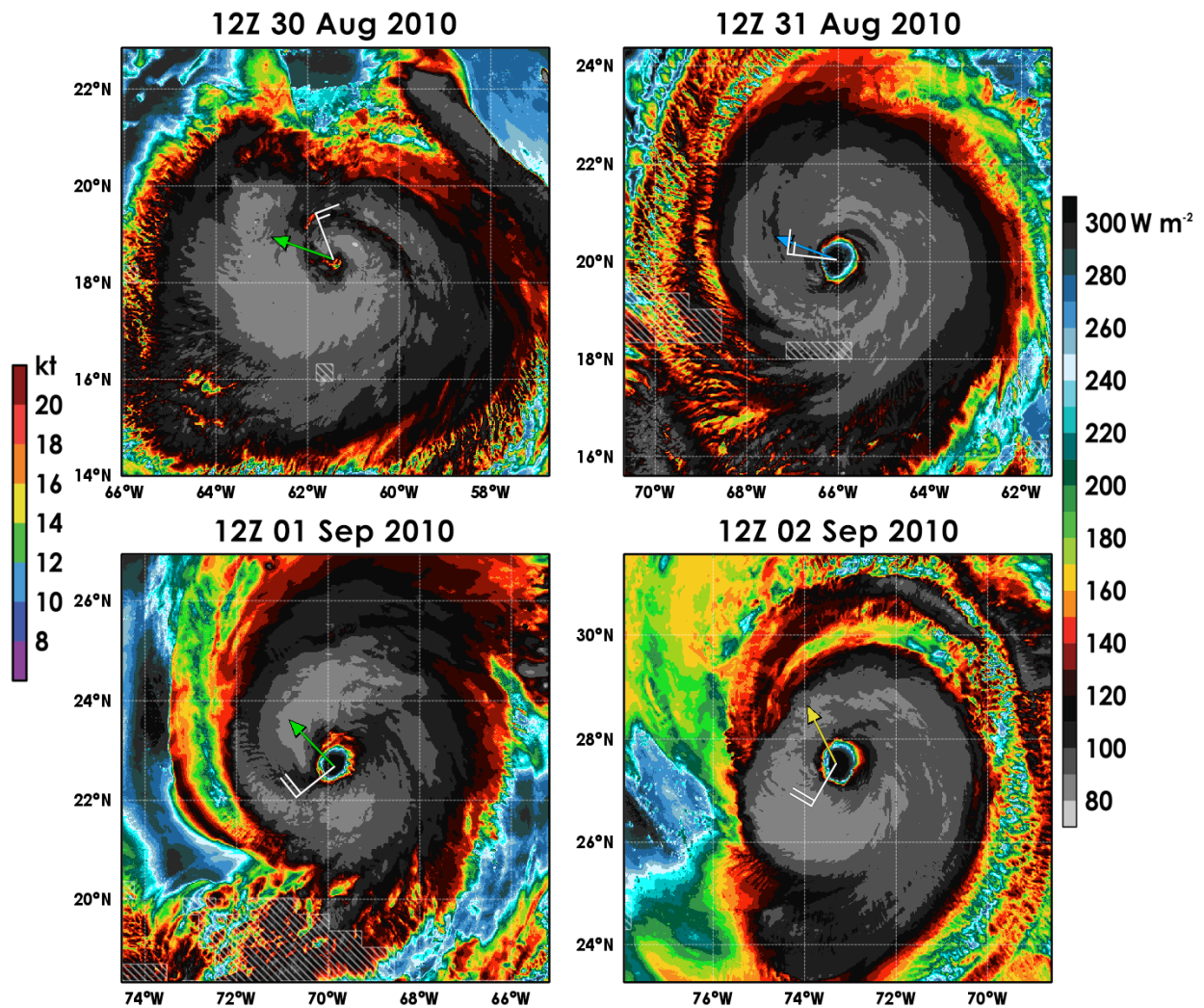


Figure 5.2: Hurricane Earl’s simulated outgoing longwave radiation at the top of the atmosphere (shaded using the right-side color bar,  $\text{W m}^{-2}$ ) at various times (labeled at the top of each panel). A storm-motion vector is drawn at Earl’s diagnosed center (shaded by magnitude in knots using the left-side color bar), along with a wind barb denoting the deep-layer shear. Gray hatched areas represent land used in the model.

1200 UTC 31 August, gradually opposing the storm motion. Between 1200 UTC 30 August and 1200 UTC 31 August, Earl's structure as seen in OLR assumes a more axisymmetric appearance, perhaps due to the azimuthal distribution of inner-core convection. Earl begins to head northwestward by 1200 UTC 01 September and north-northwestward at  $\sim 15$  kt by 1200 UTC 02 September. As Earl begins to recurve over this period, the shear intensifies to at least 20 kt and becomes north-eastward by 1200 UTC 01 September, oriented essentially orthogonal and to the right of storm motion. At that time, we see minima in OLR south and north-northwest of Earl (upstream-left with respect to storm motion and upshear-left, respectively), with "ridges" of OLR to the east and west that separate them. The OLR dipole may indicate that two deep convective avenues exist concurrently at that time (perhaps owing to BL asymmetries as a result of storm motion and shear)—one originating in the lower troposphere downstream and terminating upstream-left, and the other originating downshear and terminating upshear-left. By 1200 UTC 02 September, the shear is out of the south-southwest and continues to rotate counter-clockwise, becoming more parallel with the storm motion. By that time, the lowest OLR is generally situated upstream and upshear as Earl begins to develop obvious structural asymmetries. Earl's structure deteriorates considerably by 1200 UTC 03 September (not shown) as its principal eyewall collapses, is replaced, and then collapses again.

As in Hurricane Irma's simulation, we can examine deep convection seen in simulated IR using the vertical motion field, shown in Figure 5.3. As the shear and storm motion become nearly antiparallel at 1200 UTC 31 August, Hurricane Earl's low-level inner-core convection is wrapped around its center except in the downshear-right quadrant. At the same time, the upper-level vertical motion field is mostly axisymmetric, in agreement with the interpretation of OLR. At 1200 UTC 01 September, low-level inner-core convection is asymmetric, situated downstream of Earl and upshear with the strongest  $w$  in the upshear-left quadrant. At  $\sim 200$  hPa, the convection is maximized over a swath in the upshear-left quadrant in coincidence with an OLR minimum. Inner-core convective tops are also distributed sporadically upstream-left, near the second OLR minimum.

Hurricane Earl's simulated appearance on 01 September is starkly different from Hurricane Irma's simulated IR imagery on 06 September 2017, despite them both having storm motion and

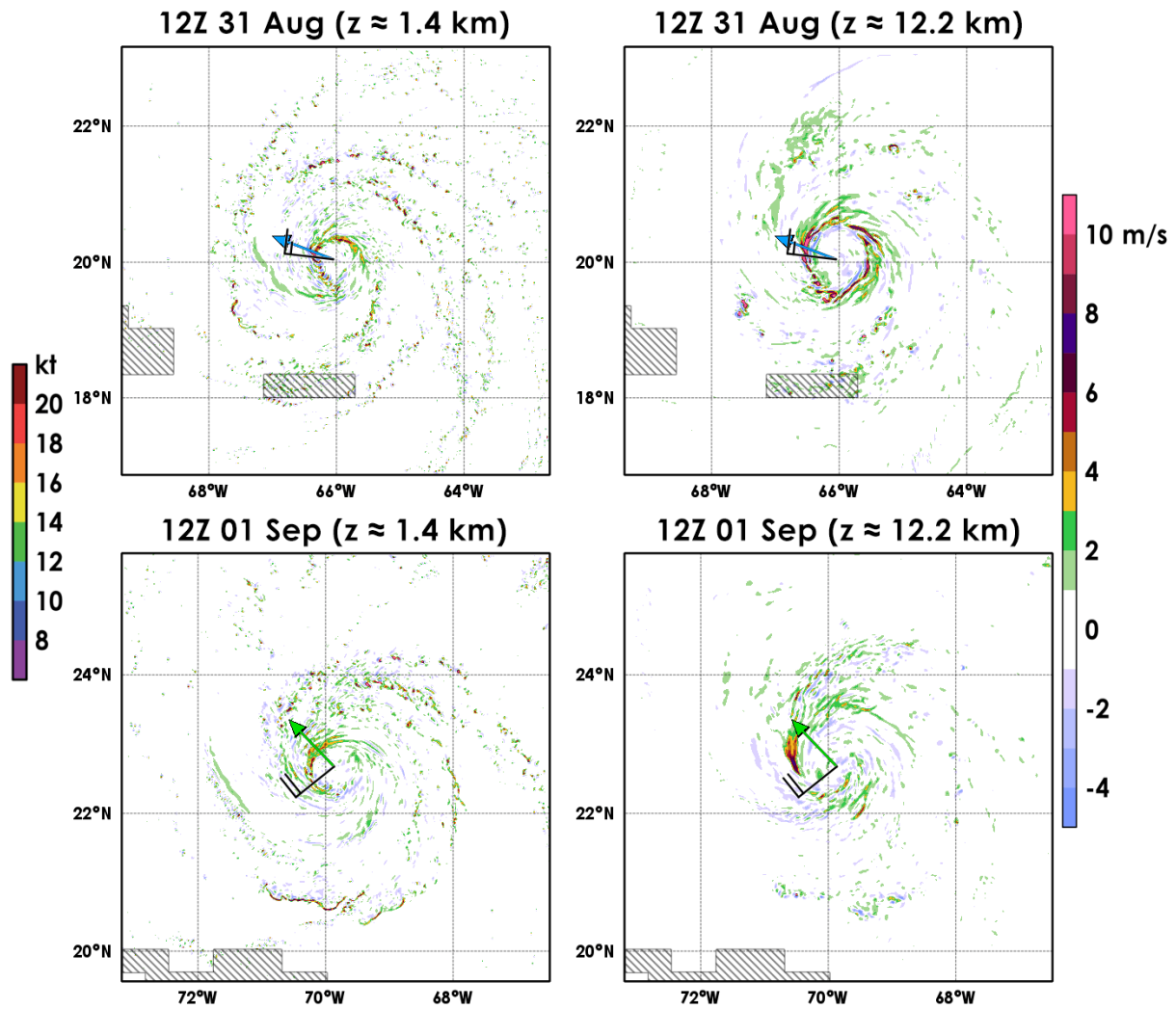


Figure 5.3: Vertical velocity ( $\text{m s}^{-1}$ ) in Hurricane Earl, similar to Figure 4.3. Snapshots shown are taken from 1200 UTC 31 August (top panels) and 01 September (bottom panels).

deep-layer shear of comparable magnitudes that are nearly orthogonal with one another. Why is there an upper-level dipole of inner-core convection apparent in Earl with such a configuration of motion and shear, but not Irma? The deep-layer shear heading might suggest where upper-level anticyclonic outflow is least resisted (by virtue of its inclusion of 200-hPa winds at large radii), while storm motion is mainly representative of low-level mass structure. In Hurricane Irma on 06 September 2017, the inner-core convective terminus associated with *motion alone* would be east of Irma, and the southward shear would provide a convenient channel for anticyclonic outflow from that convection. Convection related to Hurricane Earl's storm motion on 01 September 2010 would supposedly terminate to the south or southeast, but the northeastward shear may not provide outflow suitable for that convection: Air at the convective terminus would have to rotate roughly  $270^\circ$  around Earl's center to flow anticyclonically outward via the avenue implied by the deep-layer shear. Otherwise, air from that convection would need to flow *cyclonically* toward the northeast, anticyclonically outward through some other outflow channel, or subside downward in recirculation with the hurricane. In Earl's case, it may be that the convective branch associated with storm motion assumes outflow separate from the outflow available to convection associated with shear.

Figure 5.4 shows Hurricane Earl's simulated track, as well as the HURDAT2 best track for most of the simulated period. Similar to Hurricane Irma's simulation, Earl's simulated track follows the observed path reasonably, but the simulation lags behind the observed track by about 6 to 12 hours prior to 03 September. Hurricane Earl begins to recurve on 01 September, and then achieves recurvature toward the east on 03 September within  $\sim 300$  km of North Carolina.

Hurricane Earl's modeled intensity shown in Figure 5.5 mimics the best-track intensity remarkably well for most of the simulation period, often with  $< 5 \text{ m s}^{-1}$  and rarely with  $> 10 \text{ m s}^{-1}$  separating the time series. Earl's intensity climbs at a regular pace from  $\sim 20 \text{ m s}^{-1}$  at 0000 UTC 29 August to almost  $60 \text{ m s}^{-1}$  at 1800 UTC 30 August. Earl reaches a simulated peak intensity of  $\sim 67 \text{ m s}^{-1}$  just after 1200 UTC 31 August, and then generally weakens for the remainder of the simulation (with a brief intensification period near 1800 UTC 02 September, associated with a primary eyewall collapse and coincident secondary eyewall amplification).

The low-level structure of Hurricane Earl will be analyzed primarily with reference to its two prolonged periods of intensification and non-intensification (separated at the time of its simulated

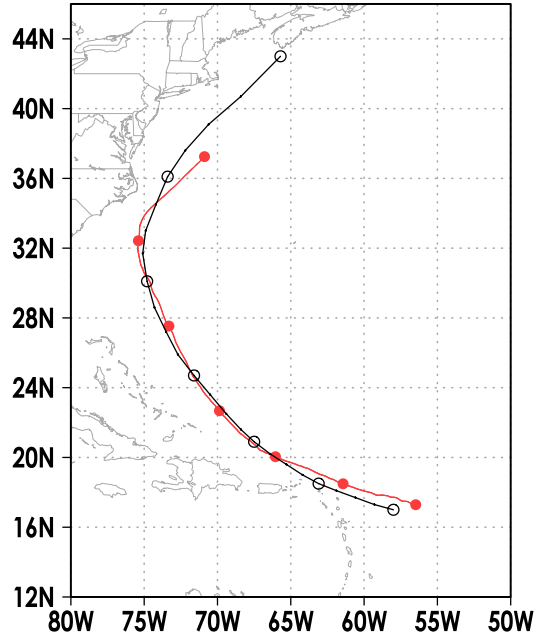


Figure 5.4: Hurricane Earl’s simulated center track (red) and HURDAT2 best-track center (black) between 1200 UTC 29 August and 04 September. Circles mark Hurricane Earl’s position at 1200 UTC for a given day.

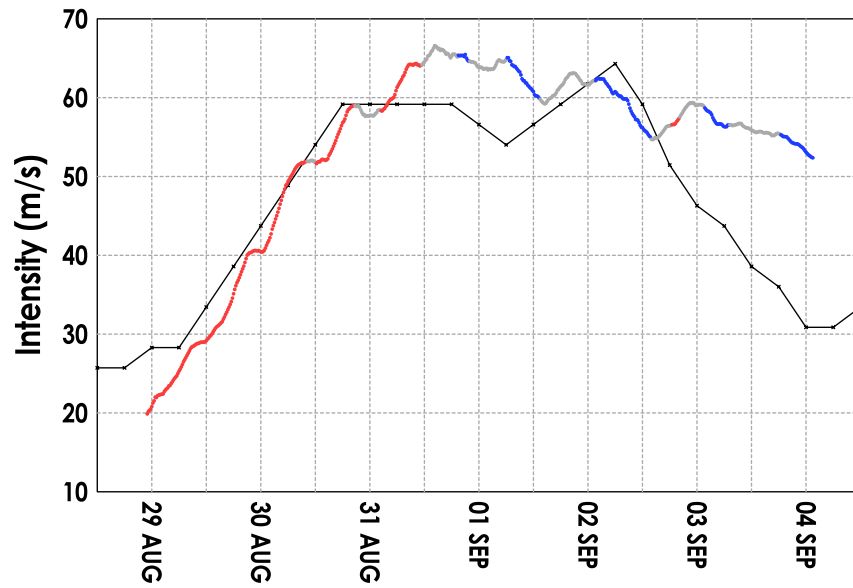


Figure 5.5: Time series of Hurricane Earl’s modeled intensity ( $\text{m s}^{-1}$ ) throughout the simulation, shaded by intensity change identifiers (red, intensifying; gray, steady-state; blue, weakening). The 6-hourly HURDAT2 best-track intensity is plotted in black.

peak intensity on 31 August). Earl’s BL characteristics during intensity change is contrasted with those simulated in Hurricane Irma, highlighting BL variability between cases regardless of similarities in intensity tendency. In the forthcoming BL analysis of Hurricane Earl (as simulated), we will not detail results after its recurvature on 1200 UTC 03 September.

## 5.3 Primary Circulation

### 5.3.1 Axisymmetric Structure

At times of Hurricane Earl’s intensification (0600 UTC 31 August) and weakening (0900 UTC 01 September), several properties of the storm’s azimuthally averaged primary circulation are shown in Figure 5.6. Similar to Hurricane Irma’s simulation, Earl’s tangential wind jet is located at about  $\sim 700$  m AGL. The wind jet’s radial position fluctuates between  $r \approx 35$  km and  $r \approx 50$  km between 30 August and 02 September. Similar to Hurricane Irma, Earl’s strongest tangential wind at a given radius outside the RMW is often near the top of the inflow layer. However, unlike Irma, Earl’s tangential wind above the BL inflow tends to weaken considerably with height, and this is especially noticeable near Earl’s peak intensity and weakening that followed. The “nose” of absolute angular momentum  $M_a$  along the top of BL inflow is more distinct in Earl compared with Irma in general, and Earl’s inertial stability during a WE phase after reaching peak intensity (which is weaker than Irma’s peak intensity) is greater at large radii. Aside from the tangential wind maximum near the RMW, Earl’s inner- and outer-core tangential winds become generally stronger than Irma’s at all radii, with a weaker radial gradient of  $v$ . In tandem with this radial profile of  $v$  (and  $M_a$ ), Earl after 30 August is often more inertially stable than Irma at radii outside the RMW regardless of Irma’s (greater) intensity. Given the prolonged non-intensification period seen in Earl, the radial profile of  $I^2$  corroborates the finding in our composite analysis that non-intensifying storms tend to have greater  $I^2$  outside the RMW in comparison to IN storms.

The azimuthally averaged agradient wind structure of Hurricane Earl also differs considerably from Hurricane Irma (shown in Figure 5.6). Earl’s tangential wind jet is supergradient, but less supergradient than Hurricane Irma’s BL jet. During Earl’s weakening at 0900 UTC 01 September, the most-supergradient wind near the RMW spreads over a greater radial range compared to Irma.

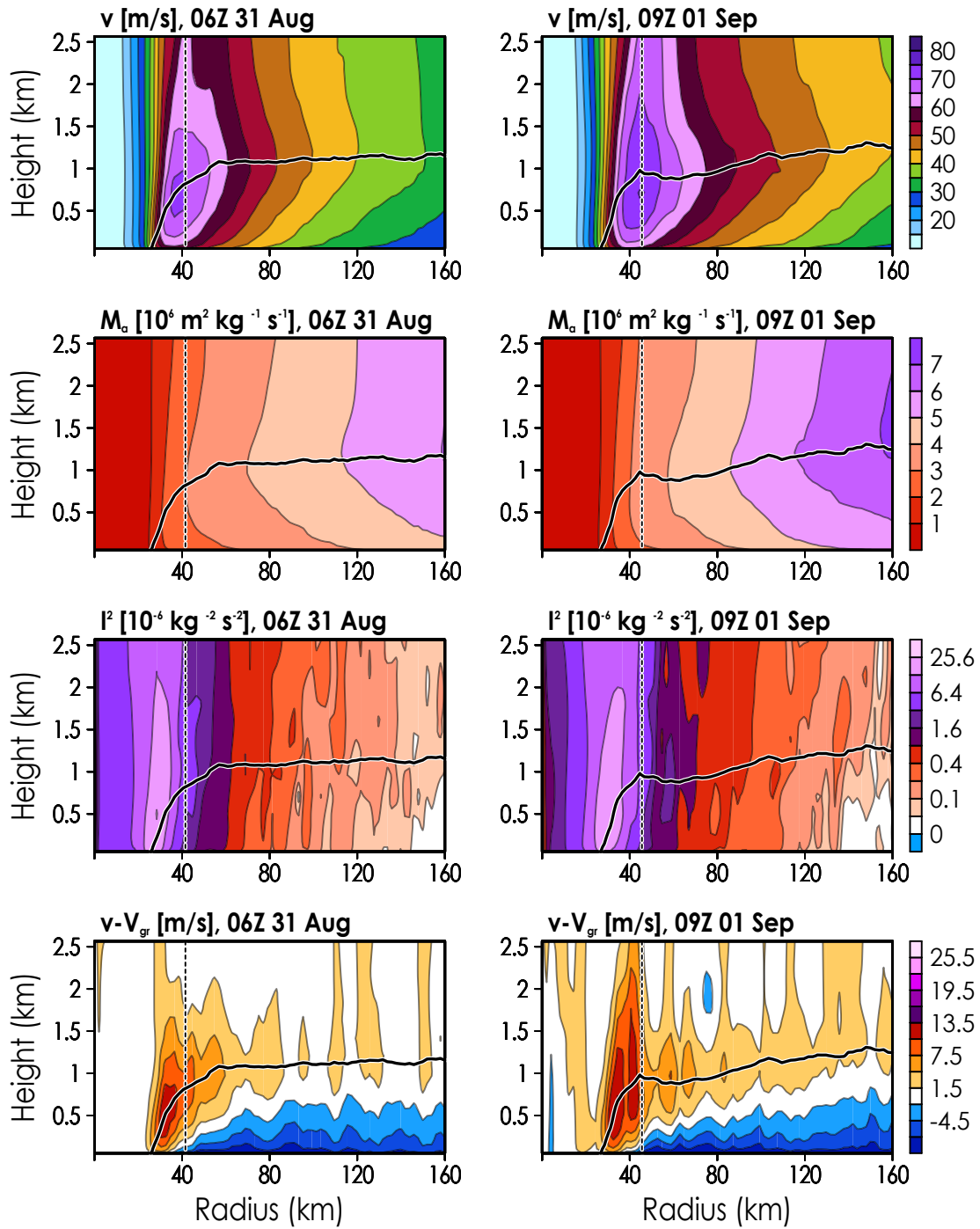


Figure 5.6: Radius-height cross sections of Hurricane Earl's azimuthally averaged primary circulation using tangential wind  $v$ , absolute angular momentum  $M_a$ , inertial stability  $I^2$ , and gradient wind  $v_{gr}$  on 0600 UTC 31 August (left, during intensification) and 0900 UTC 01 September (right, during weakening after peak intensity). Each row of figures uses the color bar to its right, and units are listed above each plot. The bold, black line indicates the radial inflow layer (10% of the maximum inflow). The scale used for  $I^2$  is geometric.

This difference may be due to less radial advection of  $M_a$  near Earl's RMW, or perhaps high- $M_a$  air being pulled inward by radial inflow escapes the surface inflow via ascent near the RMW over a larger range of  $r$ . The latter presumption would likely be associated with less localized BL convergence near the RMW compared to Irma, which will be shown in the forthcoming analysis on Earl's secondary circulation (section 5.4). Earl's BL jet becomes more supergradient between 30 August and 0900 UTC 01 September, which appears to be correlated with intensity. As with Irma's azimuthally averaged primary circulation, supergradient flow is also found along most of the top of the radial inflow layer through most of Earl's analysis period. The subgradient wind in the radial inflow layer is an expected result of frictional dissipation.

Hovmöller diagrams depicting the temporal evolution of the azimuthally averaged primary circulation at the height of the BL jet are provided in Figure 5.7. In comparison with Hurricane Irma, Hurricane Earl's BL has a weaker radial gradient of tangential wind in the axisymmetric sense throughout the analyses. This is coincident with stronger positive radial gradients of  $M_a$  in Earl's BL, as well as stronger inertial stability outside the RMW. Between 02 September and 03 September, Earl's RMW shifts abruptly from  $\sim 45$  km to  $\sim 80$  km as its principal eyewall collapses. In advance of this eyewall collapse and in tandem with Earl's weakening on 02 September, the tangential winds at radii well outside the RMW strengthen, indicating a possible secondary eyewall formation. On 02 September, Earl turns more northward and begins to move at a faster rate, which may play a role in the decay and eventual collapse of Earl's eyewall near  $r \approx 50$  km. During Earl's IN periods prior to 01 September,  $M_a$  surfaces in the BL moved inward toward the RMW, perhaps reflective of  $M_a$  advection by radial inflow and/or spin-up above the BL. After Earl's first WE period late on 31 August, however,  $M_a$  surfaces remain relatively stationary until 02 September (prior to the eyewall collapse). Figure 5.8 shows the evolution of  $I^2$  near the BL top in the vicinity of Earl's replacement eyewall on 02 September. The time series indicates that  $I^2$  outside of the RMW is minimized prior to peak intensity (1400 UTC 31 August), and then begins to increase gradually after reaching peak intensity. The gradual increase in  $I^2$  should be associated with an increase in resistance to radial displacements, thus affecting the BL inflow. Inertial stability outside the RMW increases rapidly as Earl's secondary eyewall develops and amplifies on 02 September.

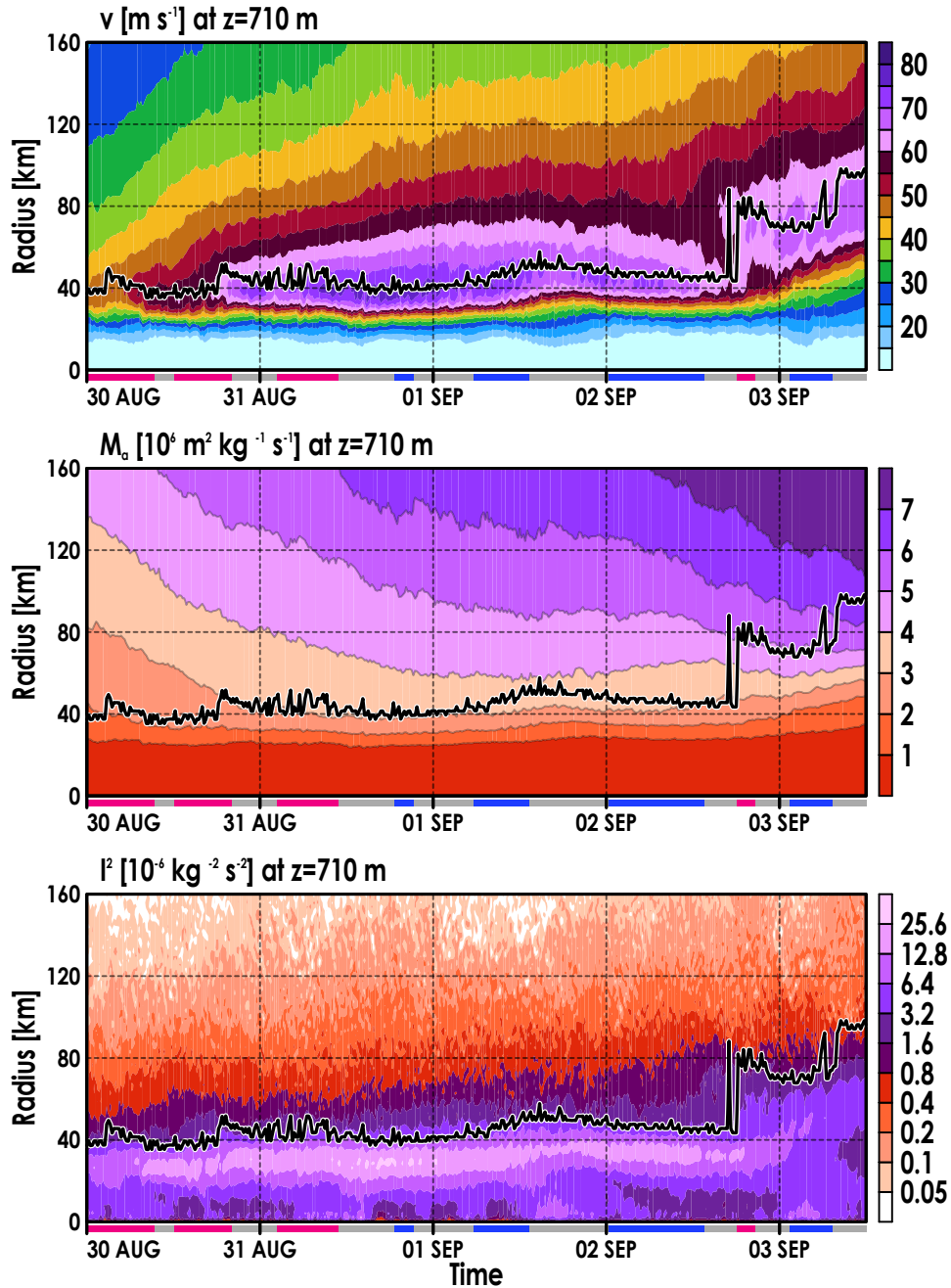


Figure 5.7: Time-radius Hovmöllers of Hurricane Earl’s tangential flow  $v$  (top), absolute angular momentum  $M_a$  (middle), and inertial stability  $I^2$  (bottom) from 0000 UTC 30 August to 1200 UTC 03 September. All fields are taken at the approximate height where the tangential wind jet occurs ( $z \approx 710$  m). A timeline shaded by intensity change (red for IN, gray for SS, blue for WE) is drawn at the bottom of each panel. The bold, black line represents the RMW. Each plot uses the color bar to its right, and units are displayed above each plot.

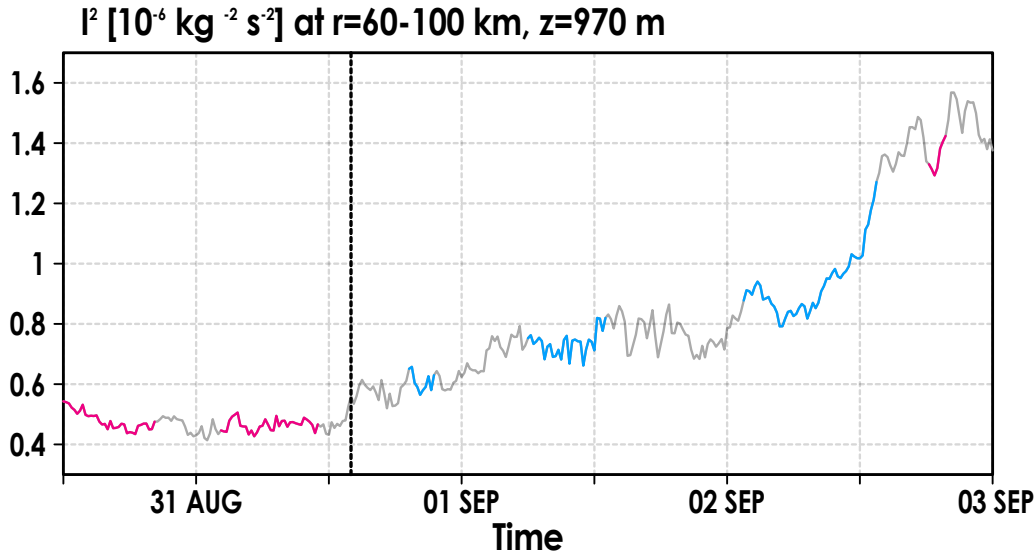


Figure 5.8: Time series of inertial stability  $I^2$  ( $10^{-6} \text{ kg}^{-2} \text{ s}^{-2}$ ) outside the RMW in Hurricane Earl between 1200 UTC 30 August and 0000 UTC 03 September. The inertial stability shown here is calculated at  $z \approx 970 \text{ m}$  and averaged between radii of 60 and 100 km. The time series is shaded by intensity change (red for IN, gray for SS, blue for WE). A black, dashed line denotes the time of peak intensity (1400 UTC 31 August).

Similar to Figure 5.7, Figure 5.9 reveals the time evolution of Earl's agradient flow above and within the azimuthally averaged BL. As noted earlier, Earl's wind jets near the RMW are generally less supergradient compared to Irma, in part related to differences in storm intensity. Outside the RMW near the top of the BL ( $z \approx 1.2 \text{ km}$ ), supergradient winds are diagnosed more often and at larger radii than in Irma. After Earl's IN phase on 31 August, a secondary maximum of supergradient wind appears outside and separate from the primary maximum inward of the RMW. This secondary maximum of supergradient flow persists clearly until a WE phase on 01 September, during which the flow becomes less supergradient and more radially widespread. In the BL, it is apparent that weak-to-moderate supergradient flow develops at progressively larger radii starting near the end of the IN phase on 31 August, below the secondary maximum of supergradient wind aloft. Near 1200 UTC 02 September, the secondary maximum of supergradient flow within and near the top of the BL becomes distinctly more supergradient, until eventually becoming more supergradient than the flow near Earl's inner eyewall jet at  $r \approx 40 \text{ km}$ . About 4 hours later, the RMW shifts outward as Earl's innermost eyewall falls apart. We note that following Earl's in-

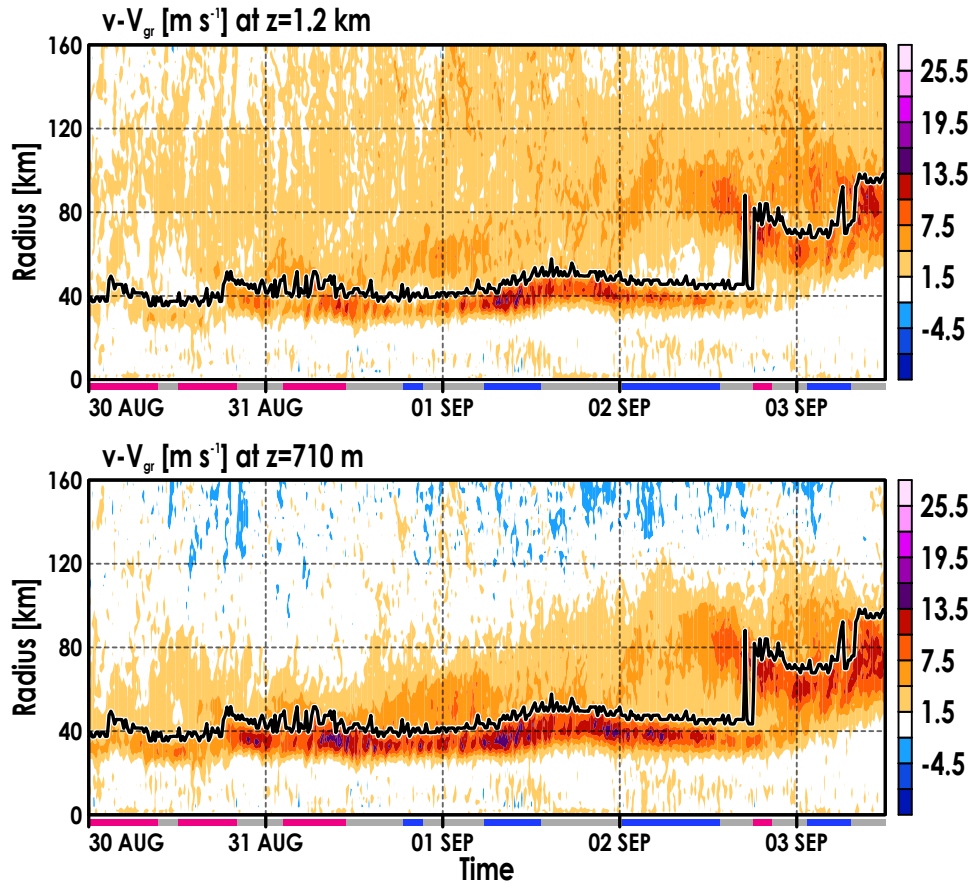


Figure 5.9: As in Figure 5.7, except using a gradient wind  $v_{ag}$  near the top of the inflow layer (top panel,  $z \approx 1.2$  km) and at the height of the tangential wind jet (bottom panel,  $z \approx 710$  m). Positive values represent supergradient winds ( $v > V_{gr}$ ), and negative values represent subgradient winds ( $v < V_{gr}$ ).

tensification on 31 August, Earl enters a prolonged state of non-intensification (a mix of SS and WE periods) until a short IN period after the eyewall collapse on 02 September. Perhaps due to the nature of Earl’s primary circulation [i.e., its relatively “flat” radial profile of  $v$ , as discussed in Kepert (2006a,b)], supergradient flow resulting from  $M_a$  advection in and immediately above the BL inflow tends to occur more often and to a stronger degree at radii outside the RMW (in comparison to Irma, at least).

In Hurricane Earl’s BL, the azimuthal mean swirling wind is notably different from Hurricane Irma’s BL. Time-radius profiles suggest that maxima of supergradient flow within and at the top of

the BL begin to persist outside of the RMW after Earl reaches peak intensity. The outer maxima propagate radially outward over time, and then amplify hours prior to the destruction of Earl's original inner eyewall on 02 September. All the while, Earl's intensity gradually weakens. Examining the primary circulation's azimuthal structure will elucidate the nature of the maxima of supergradient flow during Earl's lengthy non-intensification period. For instance, whether the formation of an azimuthal-mean, secondary wind maximum on 02 September is the result of the superposition of azimuthally local amplifications in  $v$  or just amplification of a concentric ring of maximum  $v$  is investigated.

### 5.3.2 Asymmetric Structure

Snapshots of Hurricane Earl's  $v$ -field in each shear-relative quadrant during IN and WE phases are shown in Figure 5.10. Outside the RMW, stronger low-level  $v$  is seen left of shear. The BL jet tends to be strongest upshear and weakest downshear. In the downshear quadrants at 0600 UTC 31 August (during IN), the strongest tangential winds are found along the inner periphery of the azimuthally averaged BL inflow. The weakest BL jet winds at that time are located DSR, and this attribute tends to persist through the analysis period. Additionally, two regions of distinctively strong tangential wind appear in the inner core downshear; one is associated with the BL jet, and the other is aloft at  $z \approx 2$  km and displaced radially inward of the BL jet's center. While the separate maxima of DSR tangential wind is apparent during Earl's intensification on 30 August (not shown) and 31 August, these maxima are more evident during Earl's weakening (after Earl reached peak intensity).

During Earl's WE phase shown on 0900 UTC 01 September, one could claim there are *two* low-level tangential wind jets in the DSR quadrant, with the jet *aloft* being stronger than the one in the BL. Earl's DSR quadrant is associated with pronounced vertical structure of  $v$  immediately above the azimuthally averaged inflow layer at radii outside the RMW, especially during WE. In the DSR quadrant for the period shown, tangential wind increases with  $z$  within the azimuthally averaged inflow layer (as expected given the effect of friction), decreases with height above a vertically local  $v$ -maximum near the azimuthally averaged BL top, and then increases with height once again near  $z \approx 2$  km. In the other quadrants (particularly those upshear), the maximum of  $v$  outside the

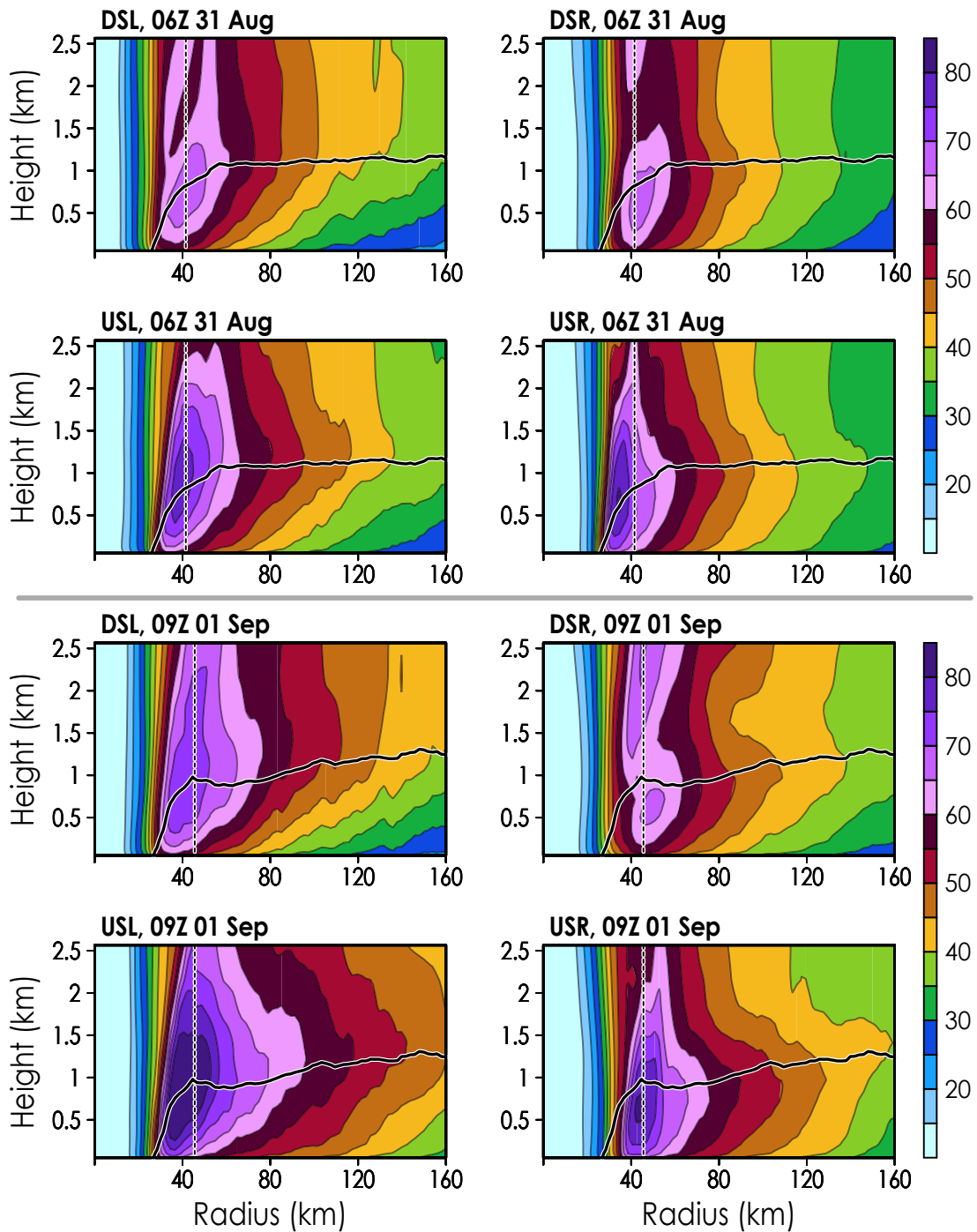


Figure 5.10: Shear-relative quadrants of  $r$ - $z$  cross sections of  $v$  ( $\text{m s}^{-1}$ ) in Hurricane Earl on 0600 UTC 31 August (top two rows, during IN toward peak intensity) and 0900 UTC 01 September (bottom two rows, during WE after peak intensity). Panels are labeled by shear-relative quadrant. The bold, black line indicates the axisymmetrized radial inflow layer (as in Figure 5.6).

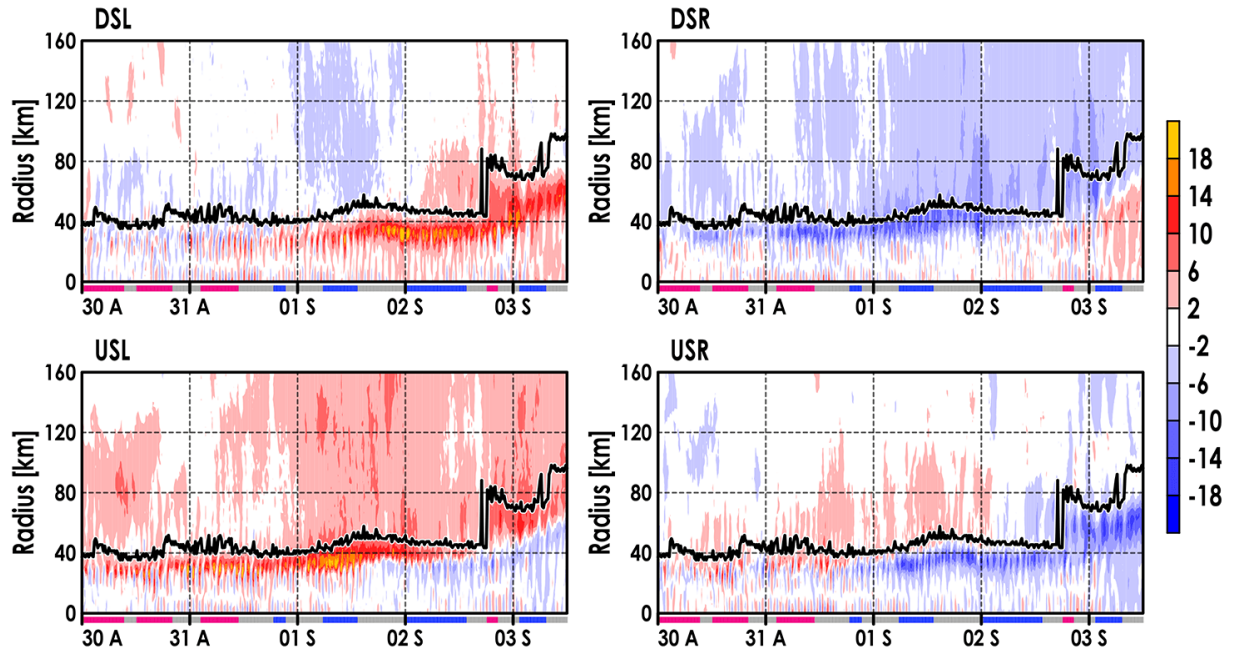


Figure 5.11: Time-radius Hovmöller diagrams of azimuthal tangential wind anomaly ( $\text{m s}^{-1}$ ) at  $z \approx 710$  m in each shear-relative quadrant from Hurricane Earl. The  $x$ -axis represents time, which is labeled by each day at 0000 UTC with the abbreviated month. A timeline shaded by intensity change (red for IN, gray for SS, blue for WE) is drawn at the bottom of each panel. The bold, black line represents the RMW. Panels are labeled by their shear-relative quadrant abbreviation.

RMW is oriented near the top of azimuthally averaged BL inflow (similar to Irma, though more pronounced). As it is expected that BL inflow and outflow aloft will not be nearly axisymmetric (based on this analysis of  $v$ ), we suspect that the azimuthal structure of the secondary circulation is tied to this arrangement of  $v$  (e.g., through arguments related to  $M_a$  advection and/or convection).

Temporal evolution of asymmetry in BL jet-level  $v$  is shown in Figure 5.11 using azimuthal  $v$  anomaly. Throughout most of the analysis, Earl's inner-core primary circulation in the BL is stronger USL and weaker DSR. Prior to and during the IN period on 31 August, Earl's BL primary circulation outside the inner eyewall is more axisymmetric. Asymmetries in the USL and DSR quadrants reappear intermittently near the end of that IN period (and near peak intensity), and then those asymmetries become persistent across all radii after Earl begins to weaken near 0000 UTC 01 September. Prior to reaching peak intensity near the end of 31 August, Earl's DSL and USR quadrants appear minimally asymmetric, and then those quadrants'  $v$ -fields become more asym-

metric as Earl begins to weaken. Those asymmetries that develop DSL and USR have a distinct radial structure—DSL,  $v$  is often anomalously strong inside the RMW and anomalously weak outside the RMW; while in the USR quadrant, anomalies on either side of the RMW have the opposite signs of DSL  $v$  anomalies.

A spatially detailed evolution of Hurricane Earl’s BL primary circulation is illustrated in Figure 5.12. We note that Earl’s storm motion and deep-layer shear vectors become nearly antiparallel during its intensification on 31 August (top row in Figure 5.12), after its progressive improvement of eye/eyewall presentation in OLR throughout 30 August (Earl’s eye cleared out dramatically and appeared circular on 31 August, during IN toward peak intensity). Shortly after Earl reaches peak intensity on 31 August, Earl’s motion slows and turns northwestward (oriented through the USL quadrant’s azimuthal center), likely leading to BL asymmetries primarily USL and DSR (as evidenced in Figure 5.11). Deep-layer shear strengthens to  $\sim 20\text{--}25$  kt after 0000 UTC 01 September, and Earl’s motion increases gradually from 10 to  $14\text{ m s}^{-1}$ . Motion becomes oriented left of shear by 1200 UTC 01 September and DSL by 0000 UTC 02 September. The azimuthal structure of Earl’s BL tangential wind evolves with the orientation of shear and motion on 01 and 02 September, with stronger tangential winds generally to the left of motion and weaker  $v$  to the right of motion (Figure 5.12). These changes in storm motion and shear may lead to secondary circulation and thermodynamic BL asymmetries that would potentially have a role in storm intensity, which will be discussed further in forthcoming sections.

Figure 5.13 plots Hurricane Earl’s shear-relative profiles of inertial stability during IN and WE periods. As implied by the Earl’s tangential wind profiles in Figure 5.10,  $I^2$  in Earl outside the RMW is generally greater than Irma despite Irma’s greater intensity. Near the RMW, Earl is generally less inertially stable than Irma regardless of azimuthal position. As Earl weakens at 0900 UTC 01 September, the maximum  $I^2$  in the DSR quadrant is located above  $I^2$  maxima in the other three quadrants, and  $I^2$  between  $r = 40$  km and  $r = 80$  km is strongest left of shear. Low-level inertial instabilities appear sporadically as they did in Irma’s simulation, though with noticeably lesser frequency in Earl. These instabilities are minimized in occurrence USL and DSR as Earl’s storm motion becomes more oriented left of shear (from USL) on 0900 UTC 01 September. At that time, inertial instabilities at outer radii are most frequent DSL, which are likely linked to

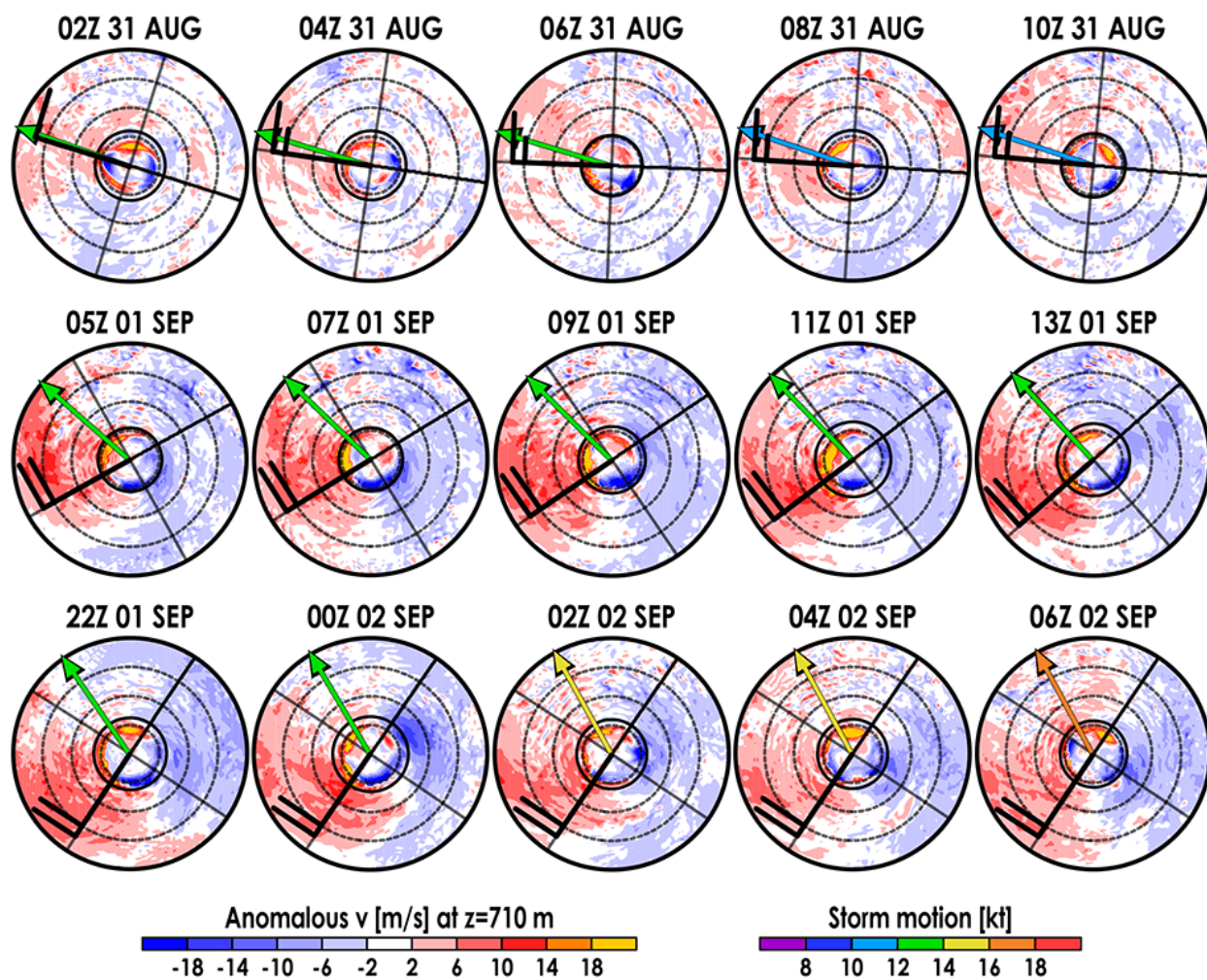


Figure 5.12: Radius-azimuth polar plots depicting the evolution of Hurricane Earl’s  $v$  anomaly ( $v$  minus the azimuthally averaged  $v$  in  $\text{m s}^{-1}$ ) at  $z \approx 710$  m. Each row of plots represents a period of intensity change: IN on 31 August (top), WE on 01 September (middle), and WE on 02 September (bottom). Time increases toward the right at a 2-hour interval. Radius is contoured (gray dashed) every 40 km out to 160 km, and the RMW is contoured in black (solid) near  $r = 40$  km. Gray contours of azimuth separate shear-relative quadrants. North points to the top of the figure. Deep-layer shear (barb) and storm motion (vector) are superimposed on Earl’s center, similar to Figure 5.3.

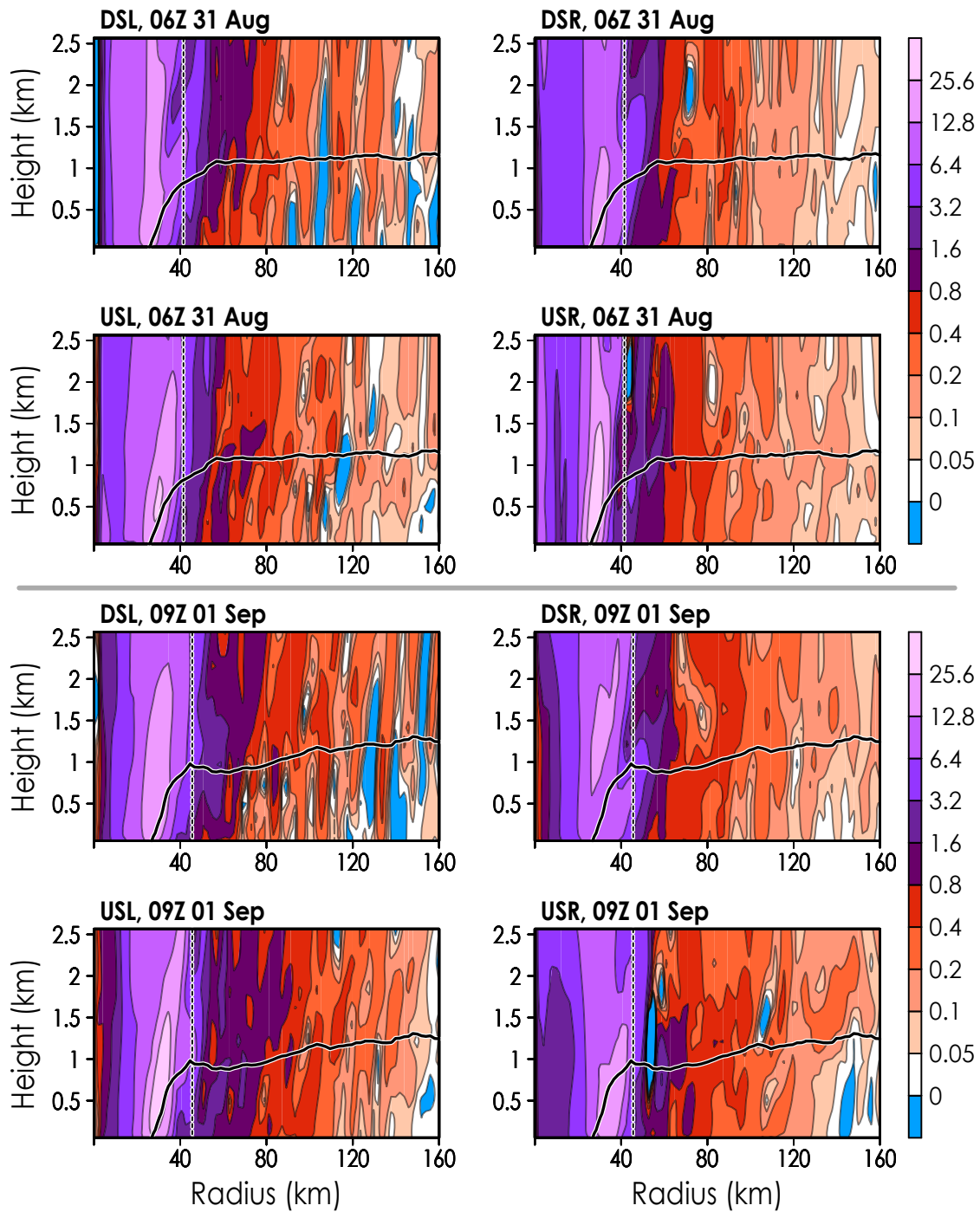


Figure 5.13: Similar to Figure 5.10, but shaded using inertial stability  $I^2$  (units  $10^{-6} \text{ kg}^{-2} \text{ s}^{-2}$ ).

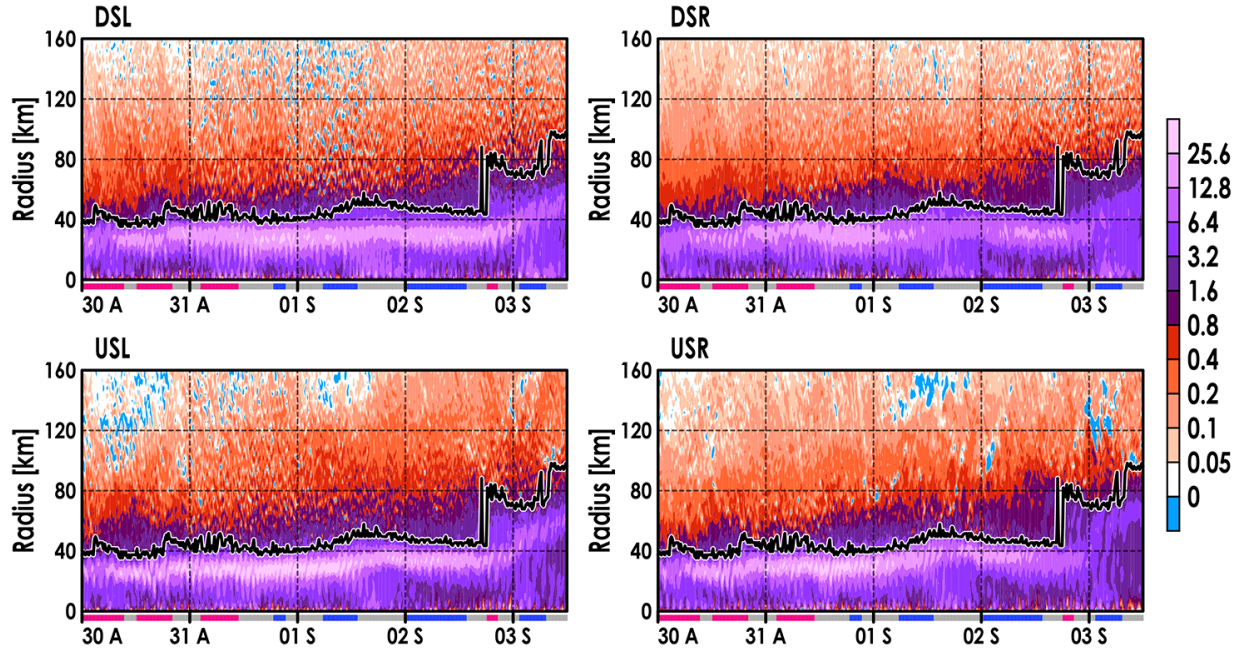


Figure 5.14: Similar to Figure 5.11, but shaded using inertial stability  $I^2$  at  $z \approx 510$  m (units  $10^{-6} \text{ kg}^{-2} \text{ s}^{-2}$ ).

vertical motion and associated  $M_a$  advection (as will be shown in analysis of asymmetric  $w$  in subsection 5.4.2). Hovmöllers of asymmetric  $I^2$  at  $z \approx 510$  m are shown in Figure 5.14. During the non-intensification period leading up to 02 September, sporadic and intermittent instances of inertial instability appear DSL, while larger-scale regions of weak or negative  $I^2$  appear upshear at  $r > 120$  km. Inner-eyewall  $I^2$  lessens through 01 September in all quadrants as Earl gradually weakens, while  $I^2$  just outside the RMW increases—this may be related to radial flow and BL convergence outside the RMW.

The agradient wind of each shear-relative quadrant during Hurricane Earl’s intensification at 0600 UTC 31 August is plotted in Figure 5.15. Unlike Irma’s intensification, Earl’s most-supergradient BL jet is in the USL quadrant during the IN period shown, and the least-supergradient jet is in the DSR and DSL quadrants. In the USL quadrant, supergradient flow near the top of the azimuthally averaged inflow layer has a distinctive wave-like radial structure, with peaks in supergradient flow every 20 km or so outside the RMW. Generally, flow above the azimuthal-mean inflow layer in the USL quadrant is most supergradient. Right of shear, subgradient flow is seen

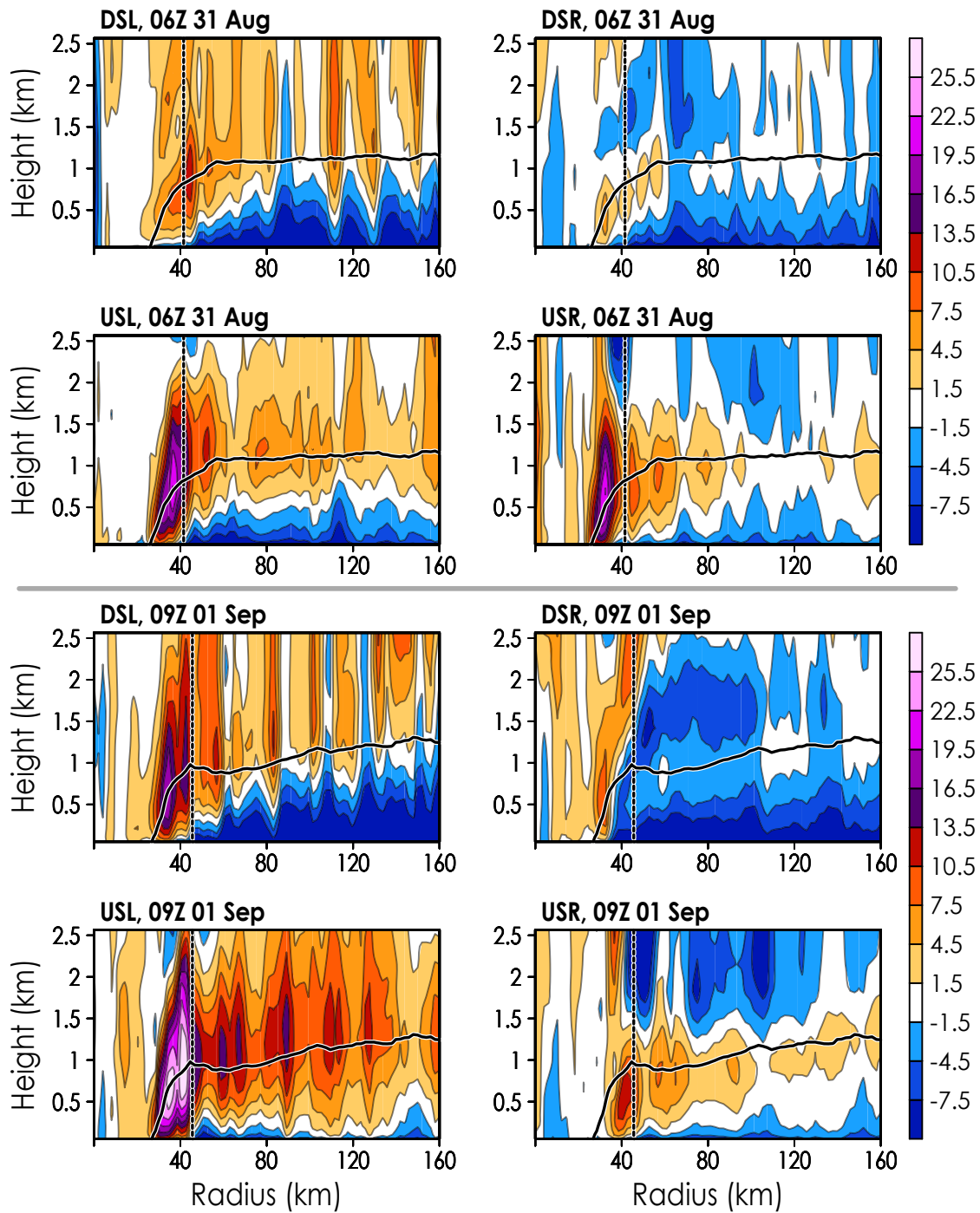


Figure 5.15: Similar to Figure 5.10, but shaded using gradient wind  $v_{ag}$  (m s<sup>-1</sup>).

above the BL near the RMW, which is of greater (DSR) or nearly equal (USR) magnitude compared with the supergradient flow immediately below.

At 0900 UTC 01 September during a WE phase (also in Figure 5.15), Earl's BL jet becomes strongly supergradient DSL and intensely supergradient USL. Multiple radii outside the RMW in the DSL and USL quadrants are associated with strongly supergradient wind at  $z \geq 1.5$  km—Hurricane Irma did not appear to develop such strongly supergradient flow at these radii in any quadrant at any time prior to land interactions (see Figures 4.14 and 4.15 in subsection 4.3.2). Eye-wall winds in the DSR quadrant become somewhat more supergradient relative to IN on 31 August; but subgradient flow dominates most of the analysis region outside of  $r = 40$  km, with two distinct peaks of subgradient flow in the vertical (one at the surface, and one at  $z \approx 1.5$  km). Subgradient flow above  $z = 1.5$  km is also seen at most radii outside the RMW in the USR quadrant.

Figure 5.16 provides the temporal evolution of agradient wind at  $z \approx 1.2$  km in Earl's quadrants. Earl's most-supergradient winds are always concentrated left of shear just above the BL. After Earl's intensification on 31 August, subgradient flow develops close to the RMW in the DSR quadrant, which persists, amplifies, and spreads radially outward until Earl's eyewall collapse on 02 September. In the USL quadrant, winds become more supergradient at  $r \approx 60$  km near 0000 UTC 01 September, and these more-supergradient winds seem to slowly translate outward over time until early on 02 September. At that time, winds outside the RMW in the USL quadrant become less supergradient. After 0000 UTC 02 September (during a WE phase associated with an impending eyewall collapse), Earl's motion increases and becomes oriented DSR, in coincidence with the appearance of supergradient flow DSR at  $r > 80$  km and subgradient flow USR between the RMW and  $r < 80$  km. Based on our analyses of  $v$ ,  $I^2$ , and  $v_{ag}$ , the evolution of shear and storm motion seems to coincide with changes in the azimuthal structure of the BL's primary circulation (Figure 5.12), as well as shifts in Earl's intensity tendency.

Hurricane Earl's simulated primary circulation is notably different from that simulated in Hurricane Irma. Earl's low-level tangential wind field is flatter across radius outside of the RMW, leading to strong inertial stability relative to Irma outward from the inner eyewall. In the azimuthal mean, a wider radial range of supergradient flow is found within and at the top of the BL, which may be linked to a similarly wide radial range of BL convergence outside the RMW (discussed

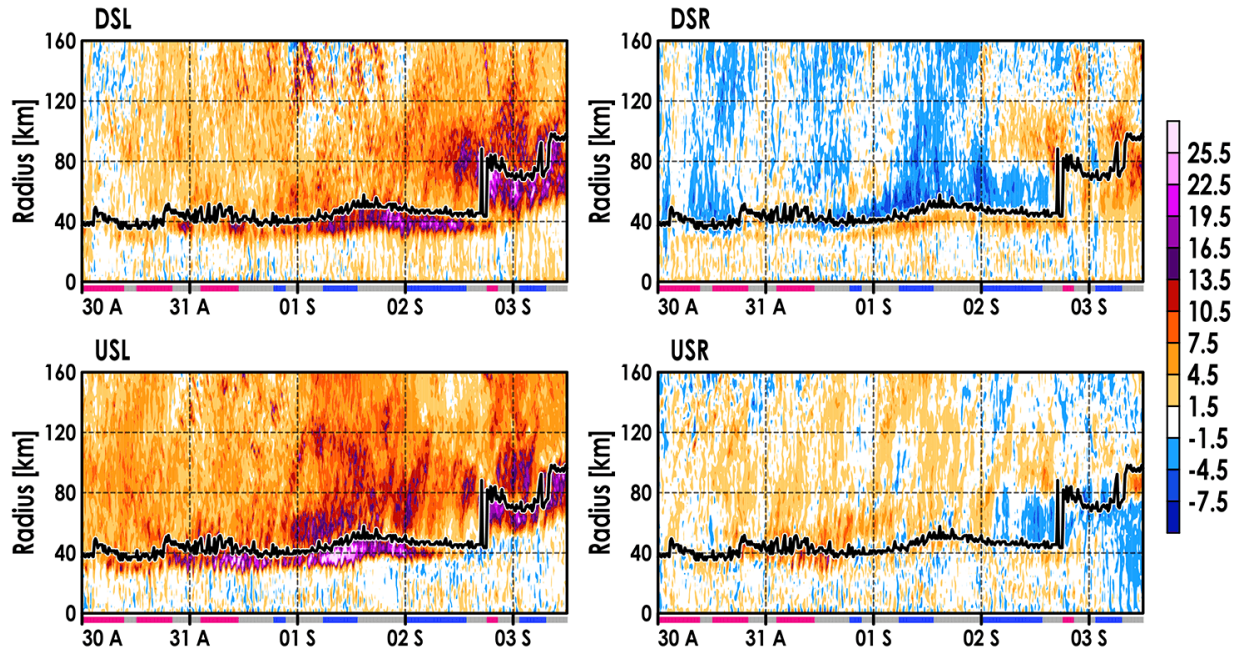


Figure 5.16: Similar to Figure 5.11, but shaded using a gradient wind  $v_{ag}$  at  $z \approx 1.2$  km ( $\text{m s}^{-1}$ ).

further in the next section). Earl’s BL primary circulation is also more asymmetric than Irma, with left-of-shear flow being highly supergradient at the BL top, spanning from the inner eye-wall outward. Throughout most of the analysis and across  $r$ , the USL quadrant has anomalously strong BL  $v$ , and the DSR quadrant has anomalously weak BL  $v$ . These asymmetries are likely related to shear- and motion-induced BL inflow asymmetry, which is presented in our analysis of the secondary circulation’s azimuthal structure.

## 5.4 Secondary Circulation

### 5.4.1 Axisymmetric Structure

Figure 5.17 shows the azimuthally averaged radial flow in the lower troposphere for instances when Hurricane Earl was intensifying and weakening on 31 August and 01 September, respectively. The inflow layers at each snapshot shown look quite similar, with strong near-surface inflow of at least  $14 \text{ m s}^{-1}$  between the RMW and  $r \approx 120$  km. The depth of inner-core inflow varies subtly between the IN and WE periods. During IN, the inflow generally deepens with radius before

tapering off just outside the RMW. During WE, the BL inflow depth inward of the RMW increases with radius to a peak value at the RMW, but the depth of inflow decreases with radius just outside the RMW before increasing with radius at  $r > 65$  km. The radial profile of inflow depth during WE implies that there may be a radial band immediately outside the RMW of enhanced vertically integrated radial divergence in the BL. Deeper weak inflow is seen at  $r > 120$  km during WE. Above the inflow layer, weak to moderate outflow is seen near the RMW during both periods. During WE, this outflow is stronger through depth near the RMW, and a secondary region of outflow outside the RMW spreads between  $r \approx 60$  km and  $r \approx 100$  km. The outer sector of outflow during Earl's WE period may be a reflection of radial divergence at the BL top immediately outward of the RMW (also shown in Figure 5.17).

The azimuthal-mean radial divergence field (RDIV) shows a maximum of radial convergence inward of the RMW, associated with the expected rapid deceleration of inflow at the highly inertially stable eyewall. Low-level outflow above the BL inflow near the RMW is associated with high RDIV inside the RMW. Because of the radial structure of inner-core outflow overlaying the BL, regions of positive RDIV also appear outside and adjacent to the RMW, at times just outward from a vertical column of strong radial convergence. Compared to Hurricane Irma, more regions of positive azimuthal-mean RDIV appear outside Earl's RMW in general, with more radial convergence in the BL inflow and more radial divergence just above the BL (comparing Figures 4.16 and 5.17). In cylindrical coordinates, the radial divergence is given by (used as the vertically integrated term in Equation 4.1):

$$RDIV \equiv \frac{u}{r} + \frac{\partial u}{\partial r}, \quad (5.1)$$

which is comprised of a curvature dependent term  $u/r$  and a speed divergence term  $\partial u/\partial r$ . Note that, in the BL inflow outside the RMW, the two terms that sum to RDIV tend to oppose one another in sign, with  $u/r < 0$  and  $\partial u/\partial r > 0$ . The speed divergence of radial flow differs between Hurricanes Earl and Irma, which is due to the differing radial profiles of  $v$  and associated  $I^2$ . Because of Hurricane Earl's broader  $v$ -field, the radial differential of a gradient forcing in the BL is weaker, resulting in weaker radial gradients of near-surface  $u$ . With a weaker magnitude of  $\partial u/\partial r$ , the curvature-dependent term of RDIV becomes increasingly dominant with decreasing  $r$ , which

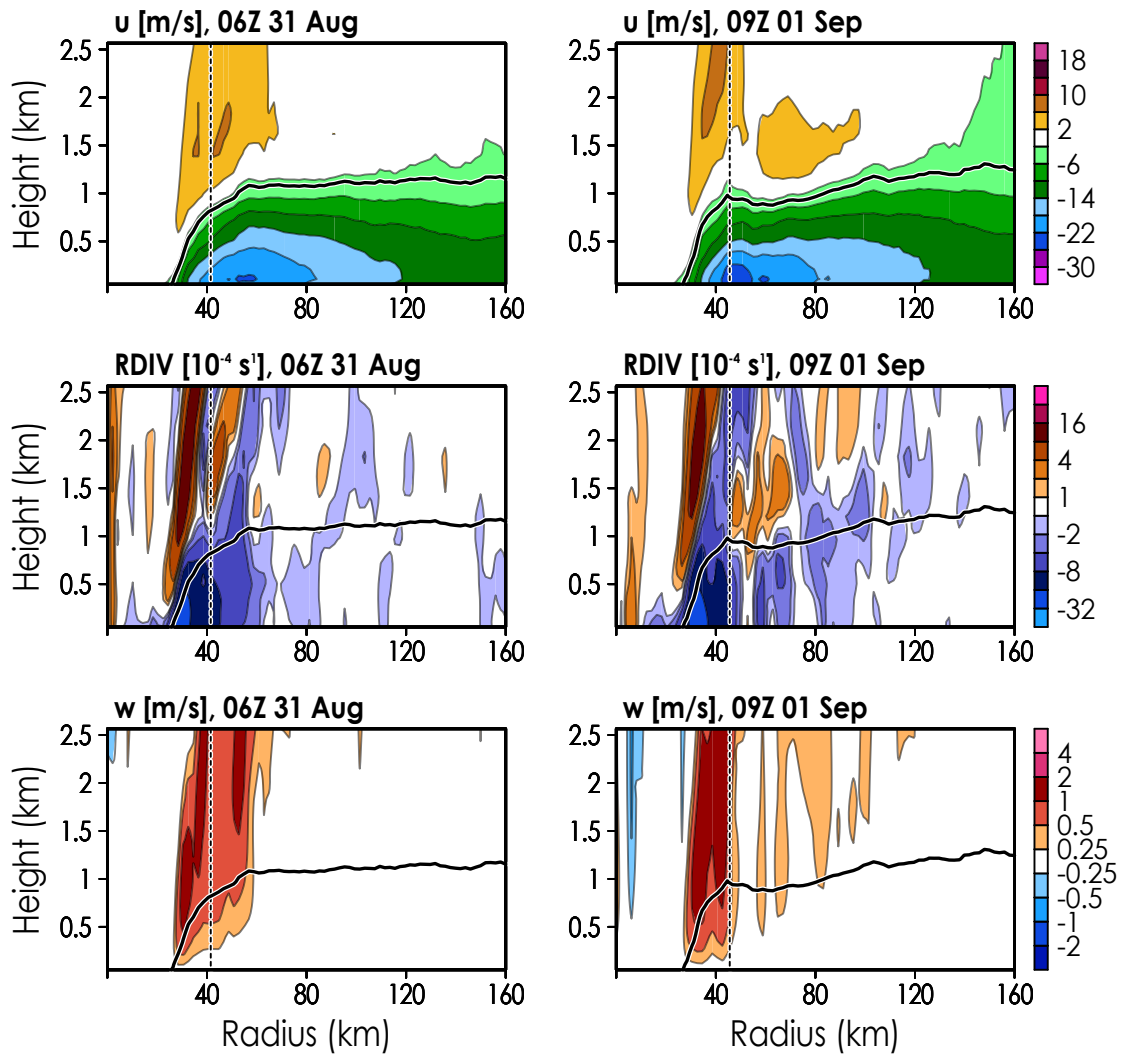


Figure 5.17: Cross sections ( $r$ - $z$ ) of Hurricane Earl's azimuthally averaged secondary circulation seen via radial wind  $u$ , radial divergence (RDIV), and vertical velocity  $w$  on 0600 UTC 31 August (left, during IN) and 0900 UTC 01 September (right, during WE). Each row of figures uses the color bar to its right, with each field's units listed above its panel. The dashed and solid black lines indicate the RMW and azimuthally averaged inflow layer, respectively. The scales used for radial divergence and vertical velocity are geometric about zero.

has sign dependent only on that of  $u$  (convergent for inflow, divergent for outflow). The suppression of BL speed divergence in Earl relative to Irma appears to explain the increased frequency of BL convergence at most radii outside the RMW.

Figure 5.17 also shows the field of vertical velocity associated with the  $u$ -field and its divergence. Both periods have pronounced vertical ascent about the RMW, although the snapshot from Earl's IN on 31 August also includes a local maximum of eyewall ascent a few kilometers outside the RMW. The differences in the radial profiles of eyewall convection appear linked to RDIV, with a sector of radial divergence just outside the RMW separating radial maxima of ascent above the BL. The radial extent of positive RDIV just outside the RMW at 0900 UTC 01 September (during WE) would likely suppress ascent out of the BL in that area. Shallow ascent of air out of the BL top appears outside the RMW in the 0900 UTC 01 September snapshot, indicating enhanced vertical exchange of air between the BL and free atmosphere at these radii.

Time-radius plots of azimuthal-mean near-surface inflow and its associated BL divergence and low-level ascent are given in Figure 5.18. Hurricane Earl's intensification prior to the end of 31 August is loosely coincident with strengthening BL inflow at all radii outside Earl's eye. Prior to Earl's first WE phase on 31 August, BL inflow between the RMW and  $r \approx 60$  km weakens, which should reduce near-surface radial convergence inward of the RMW. A brief maximum of inflow appears at  $r \approx 65$  km just before 0000 UTC 01 September, several kilometers outside the RMW during an SS phase between WE phases. Near-surface inflow between the RMW and  $r \approx 90$  km gradually weakens after 0000 UTC 01 September (at least until Earl's eyewall collapse on 02 September). The reduction of BL inflow in the aforementioned radial range has two evident consequences: a reduction of radial speed convergence in the inner eyewall, and a reduction of radial speed divergence outside the eyewall (leading to enhanced BL convergence there). In other words, the BL inflow evolves such that BL convergence becomes more radially widespread, which the observational composite analysis in Chapter 3 concluded was associated with SS and WE hurricanes. During the rapid decay of Earl's primary eyewall starting near 1200 UTC 02 September, a new maximum of near-surface inflow develops in association with a secondary tangential wind maximum at  $r \approx 90$  km, well outside the RMW.

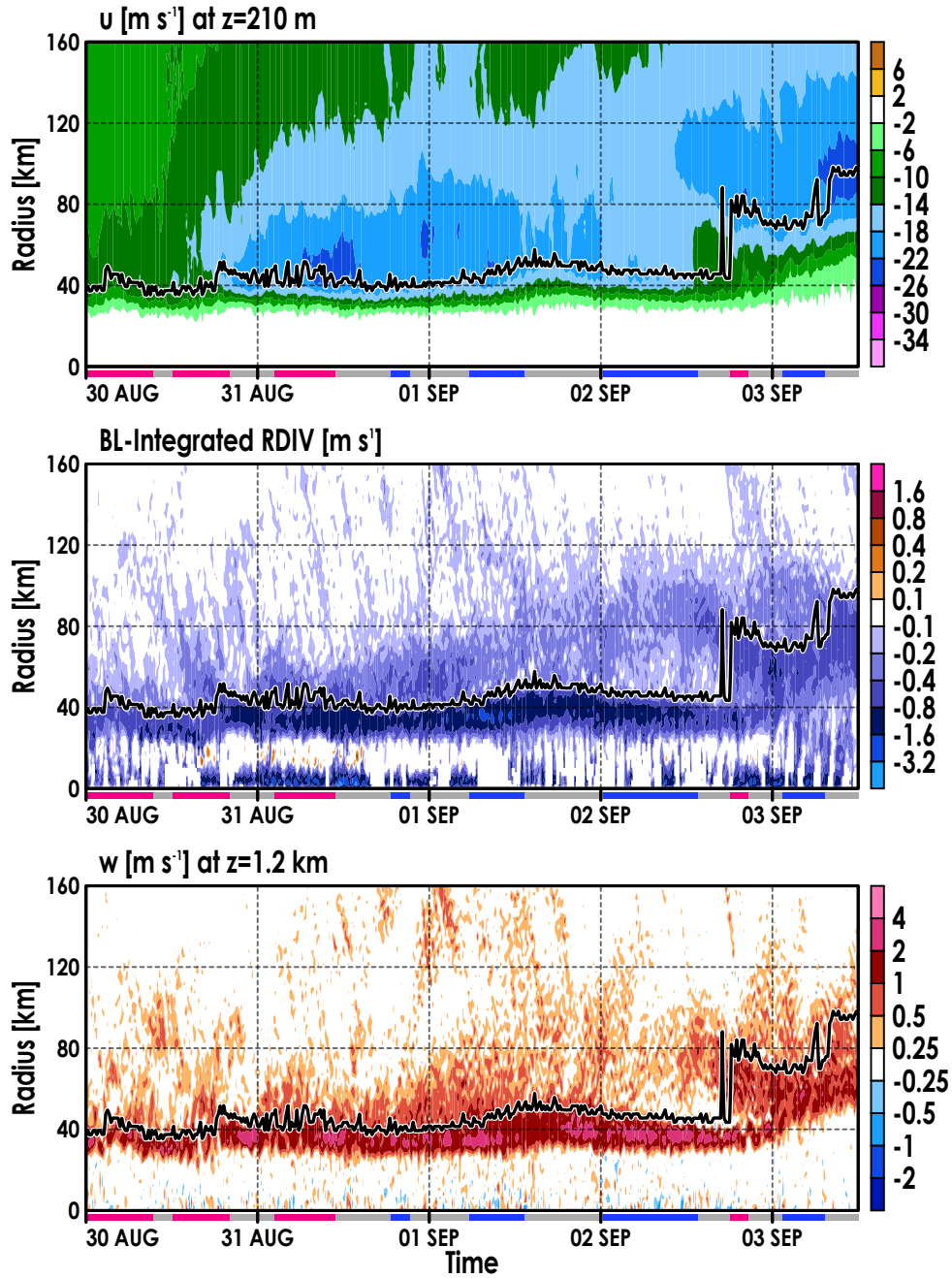


Figure 5.18: Time-radius Hovmöllers of Hurricane Earl’s radial velocity  $u$  at  $z \approx 210$  m (top), vertically integrated radial divergence through the asymmetric inflow layer (middle), and vertical motion near the top of the BL inflow  $w$  ( $z \approx 1.2$  km, bottom) from 0000 UTC 30 August to 1200 UTC 03 September. A timeline shaded by intensity change is drawn at the bottom of each panel. The bold, black line represents the RMW. Each plot uses the color bar to its right, and all fields are in  $\text{m s}^{-1}$ .

Hovmöllers of BL-integrated RDIV and vertical motion near the top of the BL shown in Figure 5.18 reflect communication between the BL and free atmosphere linked to the BL  $u$ -field. Unlike Hurricane Irma, Earl’s azimuthal mean BL-integrated radial convergence and vertical ascent at  $z \approx 1.2$  km are more radially widespread through most of the analysis period, as implied by differences in  $u$  (comparing Figures 4.17 and 5.18). Between Earl’s IN and WE phases on 31 August, BL-integrated RDIV tends to decrease (more radial convergence) between the RMW and  $r \approx 80$  km. This trend continues into Earl’s first WE period, after which BL-integrated RDIV appears to *increase* between minima at  $r < RMW$  and  $r \approx 60$  km. A “ridge” in BL-integrated RDIV builds just outside the RMW between areas of persistent radial convergence, which appears to separate two radial regions where forced ascent out of the BL is most preferred (one inside the RMW, and one well outside the RMW). The secondary minimum of BL-integrated RDIV outside the RMW gradually propagates outward to  $r \approx 80$  km by the middle of 02 September (all during SS and WE phases), hours before Earl’s principal eyewall fell apart.

The time evolution of the  $w$ -field at  $\sim 1.2$  km AGL is similar to that implied by BL radial divergence. Ascent begins to spread radially outward from the RMW between IN and WE periods on 31 August, and an area where the frequency of ascent is relatively minimized develops between the positive  $w$  inward of the RMW and a broad region of weak-to-moderate ascent centered near  $r = 80$  km on 01 September. The aforementioned radial band of relatively weak vertical motion is most apparent on 02 September, hours prior to Earl’s eyewall collapse. Note that vertical motion inside the RMW becomes less intense and more widespread during WE on 01 September, which may have an effect on eyewall convection aloft. We will point out that, starting from outer radii, regions of weak and intermittent BL RDIV seem to propagate inward over time, in coincidence with ascent at  $z \approx 1.2$  km (most evident between 31 August and 02 September). However, the mechanisms associated with these transient, radially propagating waves in the BL are unclear.

Hurricane Earl’s development of two regimes of BL ascent—one inside the RMW and the other tens of kilometers outside the RMW—should have an impact on the primary circulation above the BL, as well as on BL thermodynamics. Ascent out of the BL should transport properties of momentum and entropy into the free atmosphere above, and the air that exits the BL via this avenue would be replaced presumably via subsidence. The time-radius plot of azimuthally averaged gradient

flow from the analysis of Hurricane Earl's primary circulation (Figure 5.9) revealed that supergradient flow at  $z \approx 710$  m from the end of Earl's 31 August IN phase spread radially outward over time, with the outermost extent of supergradient wind moving from  $r \approx 60$  km at 1200 UTC 31 August to  $r \approx 120$  km at 0600 UTC 02 September. The spread of supergradient flow at that height is coincident with the spread of BL radial convergence, implying ascent of relatively high- $M_a$  air from the near-surface inflow. The widening area of ascent outside the RMW also suggests that high-enthalpy air from the BL is more likely to escape the inflow and enter the free atmosphere aloft before arriving at the RMW. By conservation of mass, the BL ascent should be compensated for via forced subsidence or expansion of air in the volume. Assuming forced subsidence is the dominant response, the ridge of BL-integrated RDIV that develops during Earl's period of non-intensification after 1200 UTC 31 August may represent the area where free atmospheric air descends into the BL to replace the air that ascends inward of the RMW. The ascending air at outer radii can be compensated for via subsidence at even greater radii (and over a far larger area). If air is forced to descend from the free atmosphere into the BL just outside the RMW, then relatively low- $\theta_e$  air may be injected to the near-surface inflow, affecting inner-core thermodynamics.

Hurricane Earl's azimuthal-mean secondary circulation during its persistent intensification to peak intensity consisted of strong BL inflow near the RMW, BL convergence concentrated inward of the RMW, and low-level ascent isolated to the inner eyewall. All of these properties are consistent with the analysis of composited intensifying hurricanes in Chapter 3. After reaching peak intensity, BL inflow near the RMW began to slow, and BL convergence began to spread radially outward from the RMW in tandem as Earl entered a long non-intensification period. Earl's intensity gradually decreased over this roughly two-day period, as BL inflow became more convergent at progressively greater radii—and at the same radii, ascent at the BL top became more frequent. The radially widespread BL convergence associated with strong BL inflow (relative to the inflow maximum) covering a large radial range outside the RMW is in agreement with the analyses for SS and WE storms in the observational composite. We will next breakdown the azimuthal structure of Earl's BL secondary circulation, highlighting the asymmetries linked to the development and persistence of the two distinct BL convergence maxima (one inside the RMW, and one outside).

## 5.4.2 Asymmetric Structure

Hurricane Earl's shear-relative quadrants of low-level radial wind  $u$  are drawn for 0600 UTC 31 August (IN period) and 0900 UTC 01 September (WE period) in Figure 5.19. Both periods exhibit two radii where inflow is maximized, depending on the quadrant examined (one at the RMW, and the other about 20 km outward at  $r \approx 60$  km), indicating two regions where BL convergence and low-level ascent may be maximized in Earl's inner-core.

During Earl's IN period on 31 August, inflow below the BL jet is maximized upshear-left, with anomalously strong inner-core inflow also seen in the DSL quadrant. Near-surface inflow left of shear is relatively vigorous at all radii outside the RMW, and the DSL quadrant has the strongest BL inflow at  $r > 100$  km. BL inflow depth and strength are minimized upshear-right, while inflow depth is greatest downshear. The deep inflow downshear would be able to advect high- $M_a$  air inward *above* substantial frictional dissipation, resulting in relatively unimpeded spin-up of tangential wind above the BL downshear across all radii outside of the RMW (more so at higher radius, possibly increasing  $I^2$  outside the RMW and explaining the strongly supergradient flow left of shear). Widespread outflow outside the RMW is situated above the BL inflow upshear, and upshear outflow near the RMW is anomalously intense relative to downshear (maximized USR). The broad outflow above the BL would be associated with advection of relatively low- $M_a$  air, inducing spin-down tendency above the BL upshear. As shown in Figure 5.20, the storm motion and shear are nearly antiparallel during the 31 August IN phase, with storm motion slightly left of shear (pointing slightly USL). Earl's movement speed at that time was  $\sim 11$  kt, with deep-layer shear of 15–20 kt. While the depth and radial extent of moderate-to-strong inflow greater than  $6 \text{ m s}^{-1}$  is mostly axisymmetric as the nearly antiparallel motion and shear vectors would suggest, Earl's inflow still possesses evident azimuthal asymmetries. The detailed influences of motion and shear on low-level inflow appear to differ, at least in this case.

Near 0000 UTC 01 September, Hurricane Earl's motion and deep-layer shear vectors become less antiparallel and more orthogonal (with motion to the left of shear in Figure 5.20), and the deep-layer shear strengthens from  $\sim 15$  kt to 20–25 kt. The azimuthal structure of  $u$  becomes far more asymmetric by 0900 UTC 01 September (during WE), as motion is nearly  $90^\circ$  counterclockwise from the shear vector. The most-intense low-level inflow is located left of shear (downstream

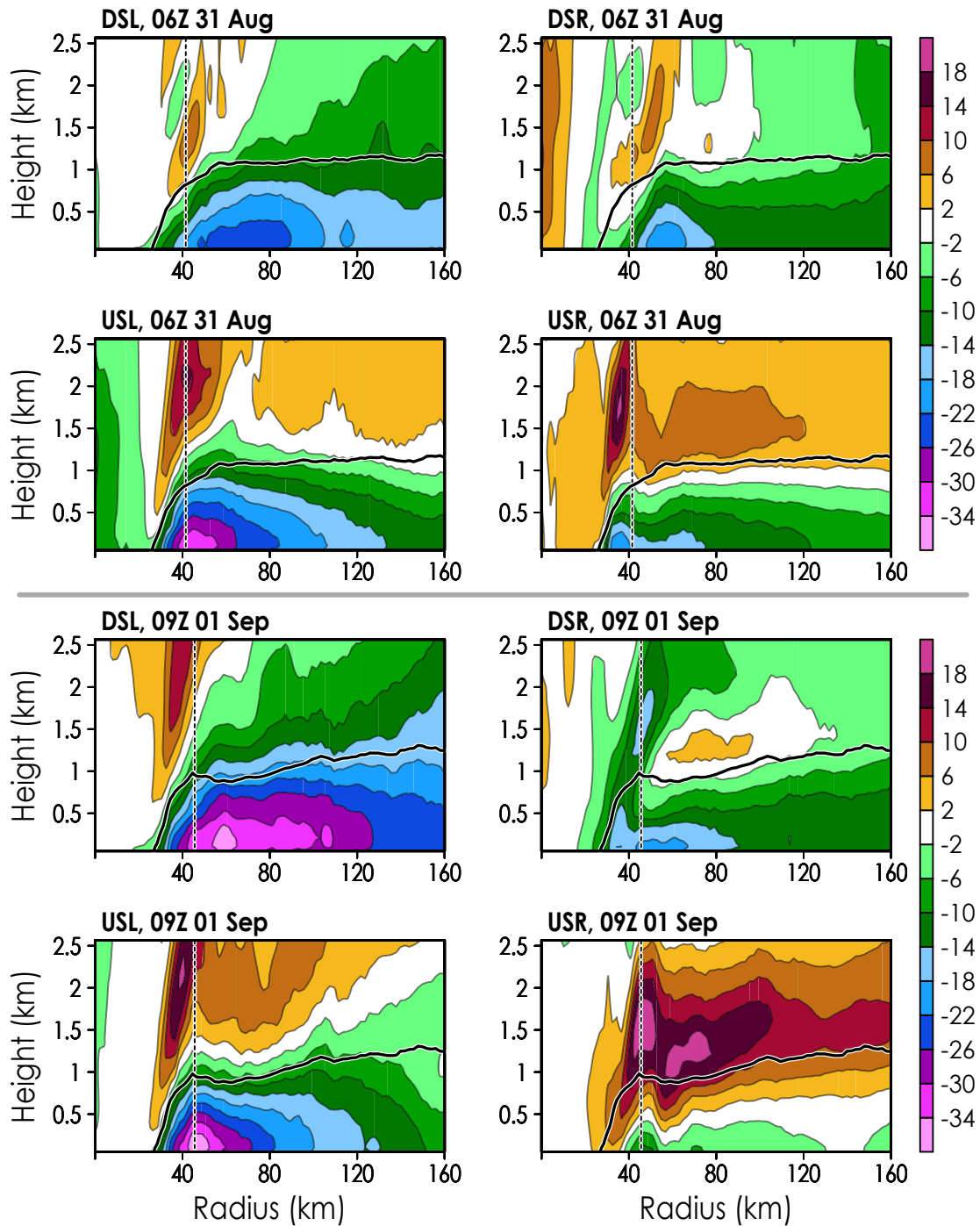


Figure 5.19: Radius-height cross sections of radial wind  $u$  ( $\text{m s}^{-1}$ ) in Hurricane Earl's shear-relative quadrants on 0600 UTC 31 August (top two rows, during IN) and 0900 UTC 01 September (bottom two rows, during WE). Panels are labeled by the quadrant they represent. The dashed, black line marks the RMW. The bold, black line indicates the axisymmetrized radial inflow layer (see Figure 5.17).

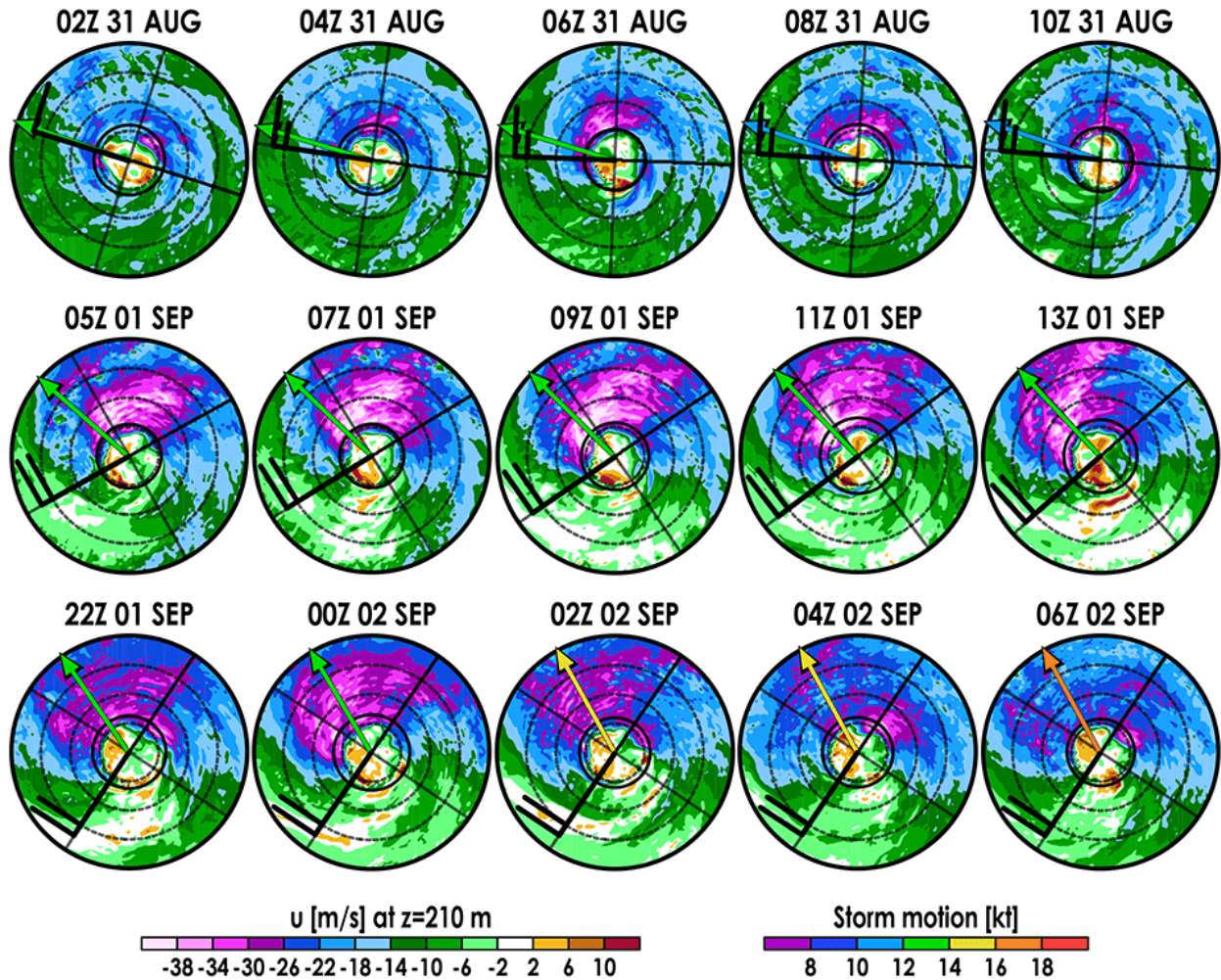


Figure 5.20: Similar to Figure 5.12, but using radial wind  $u$  ( $\text{m s}^{-1}$ ) at  $z \approx 210$  m.

of motion), with  $u < -26 \text{ m s}^{-1}$  spanning between the RMW and  $r \approx 120$  km in the DSL quadrant. While the DSL quadrant conveys deep and strong low-level inflow at all radii between the RMW and  $r = 160$  km, the USL quadrant's inflow layer is shallower, with its most-intense inflow relatively isolated to the RMW. The USL quadrant also contains outflow of at least  $6 \text{ m s}^{-1}$  between  $r \approx 30$  km and  $r \approx 100$  km above  $z \approx 1.2$  km, where local advection of relatively low- $M_d$  air should lead to a tendency for tangential wind spin-down. Near-surface inflow in the USR quadrant is anomalously weak and isolated below  $z \approx 500$  m, with strong-to-intense outflow at all analyzed radii above the shallow inflow layer. The strong outflow USR has two distinct maxima over  $r$ , in

coincidence with Earl's two near-surface inflow maxima at the RMW and  $r \approx 60$  km. The dominant low-level outflow in the USR quadrant would promote spin-down by outward transport of relatively low- $M_a$  air from inner radii. The spin-down tendency would be maximized just outside the RMW, where  $u$  and  $\partial M_a / \partial r$  are most positive (thus, implying that  $I^2$  would have a tendency to decrease over time near the RMW).

The secondary circulatory structure in the DSR quadrant at 0900 UTC 01 September is complicated. Near-surface inflow stronger than  $6 \text{ m s}^{-1}$  is present at most radii (deepening with radius outside the RMW). A vertical column of inflow is centered about the RMW, sloping outward with height. Aside from a pocket of weak  $u$  and weak outflow above the BL between the RMW and  $r \approx 120$  km, weak inflow is found throughout the analysis domain outside the RMW. The complex structure in the DSR quadrant is a reflection of the response to highly unbalanced flow upwind in the USR quadrant.

Time evolution of Hurricane Earl's asymmetric near-surface inflow is shown in Figure 5.21. Prior to Earl's persistent non-intensification, the near-surface inflow has relatively less asymmetry, with the strongest inflow located at the RMW in every quadrant and weaker inflow right of shear. As Earl's motion begins to turn clockwise on 31 August (becoming more left of shear until being roughly perpendicular near 1200 UTC 01 September), near-surface inflow in the USR quadrant deteriorates at all radii, and DSL inflow adjacent to and outside the RMW intensifies. Inflow maxima near  $r \approx 70$  km appear in the DSR quadrant between 1200 UTC 31 August and 1200 UTC 01 September, perhaps associated with a combination of high  $I^2$  at radii outside the RMW and strong outward flow USR. About 6 hours prior to the radial shift of Earl's RMW to  $r \approx 80$  km, inflow maxima appear in all quadrants at  $r \approx 100$  km, indicating strong BL convergence near the eventual RMW.

Plots of low-level radial divergence and vertical motion  $w$  are shown for each quadrant in Figures 5.22 and 5.23, respectively. During Earl's IN on 31 August, all quadrants have strong BL convergence near or inward of the RMW, although the DSR near-surface convergence maximum is displaced somewhat outward of the RMW. The DSL quadrant contains a wide band of BL convergence outside the RMW, extending out to  $r \approx 85$  km and hinting at the width of inner-core ascent in that quadrant (as shown in Figure 5.23). Boundary layer divergence near the RMW is

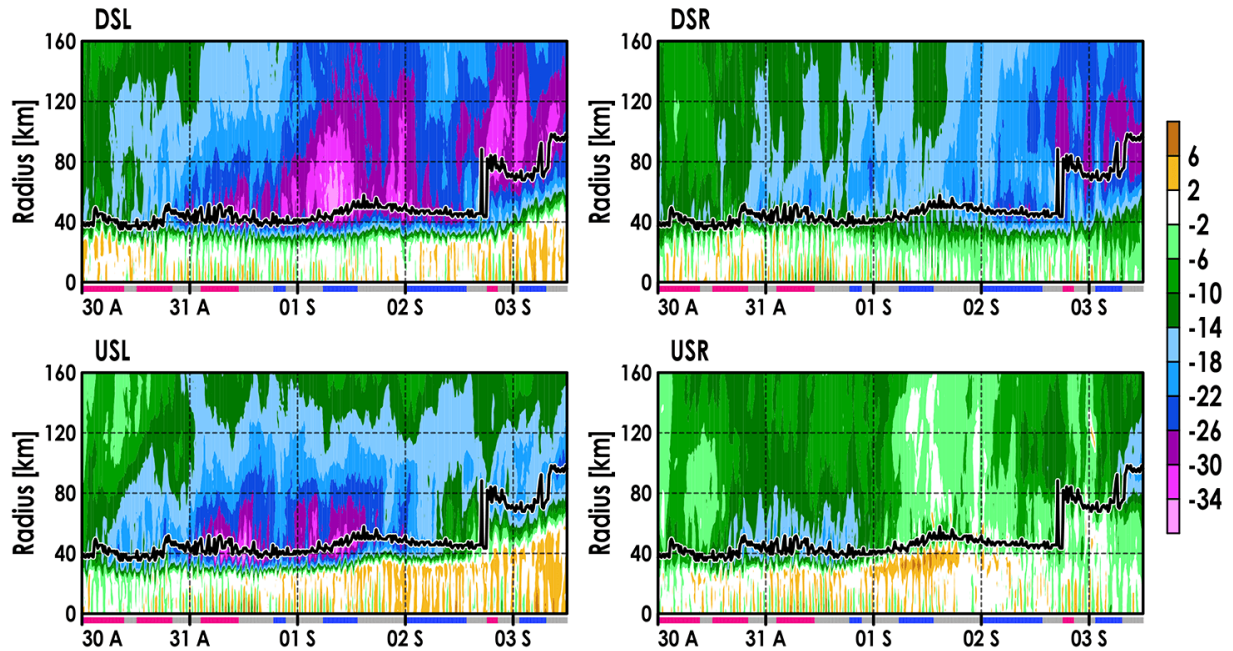


Figure 5.21: Hovmöllers ( $t$ - $r$ ) of radial wind  $u$  at  $z \approx 210$  m in Hurricane Earl’s shear-relative quadrants. The  $x$ -axis represents time, which is labeled by each day at 0000 UTC with the abbreviated month. A timeline shaded by intensity change is drawn beneath each panel, similar to Figure 5.18. The bold, black line represents the RMW. Panels are labeled by their quadrant abbreviation.

apparent in the USR quadrant, indicating some asymmetry of vertical motion in the eyewall. The vertical motion at 0600 UTC 31 August suggests that ascent at the RMW in the USR quadrant was minimized.

By the WE period at 0900 UTC 01 September, low-level convergence in the DSL quadrant has spread across nearly all analyzed radii outside of the RMW, suggesting even more widespread ascent (which is confirmed in Figure 5.23). The USL quadrant’s RDIV-field contains a prominent vertical dipole inside the RMW, indicating strong and relatively localized ascent. The upshear-right sector has a quadrupole of low-level RDIV roughly fixated on the intersection between the RMW and azimuthal-mean BL inflow (the orientation implying descent outside the RMW, and ascent inside the RMW—as reflected in the  $w$ -field). In the DSR quadrant, an outward-slanted column of convergence runs from the inner edge of the inflow layer at the surface to the RMW near  $z \approx 2.5$  km. Outward of the column of convergence, a region of strong divergence overlaps

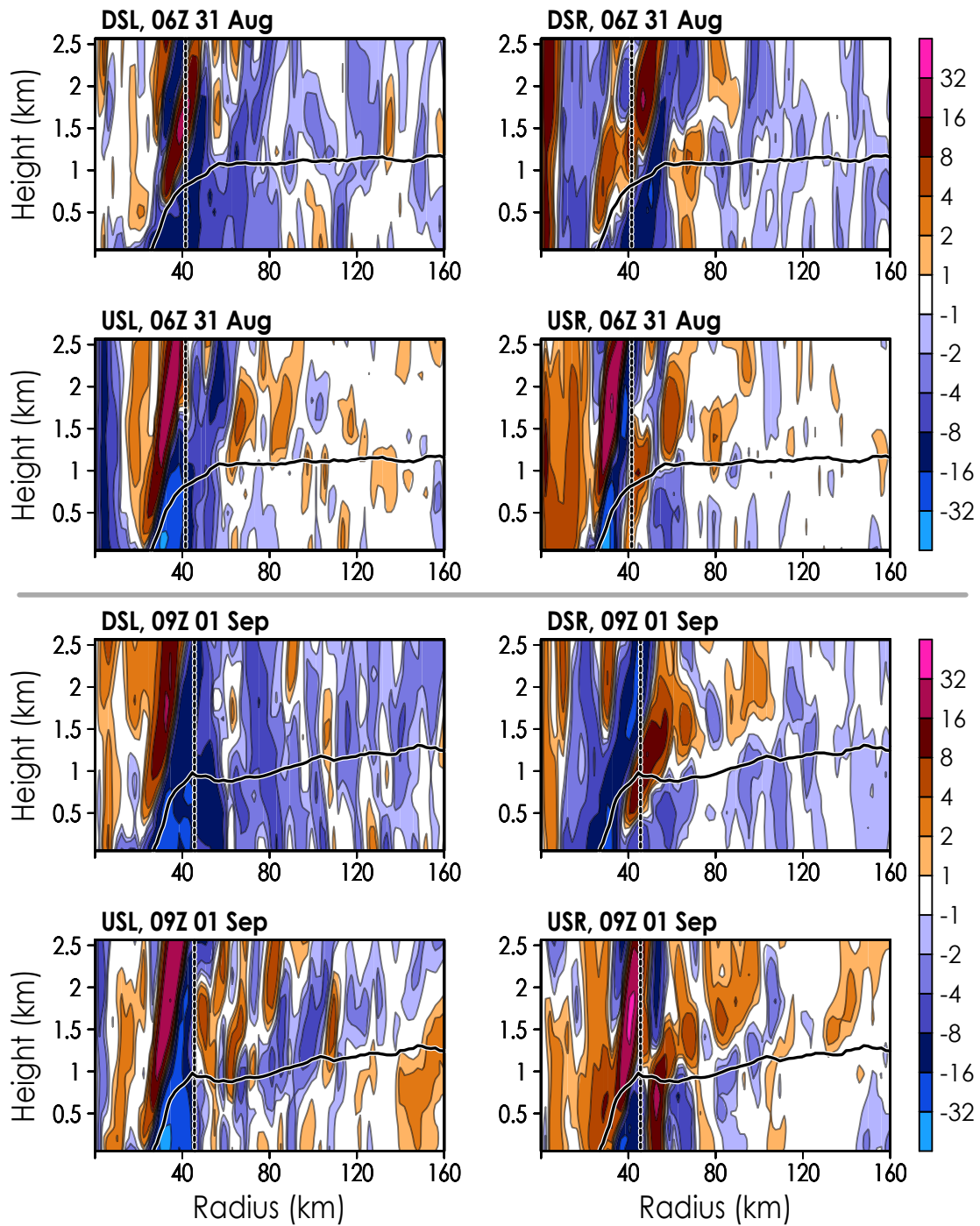


Figure 5.22: Similar to Figure 5.19, but shaded using radial divergence ( $10^{-4} \text{ s}^{-1}$ ).

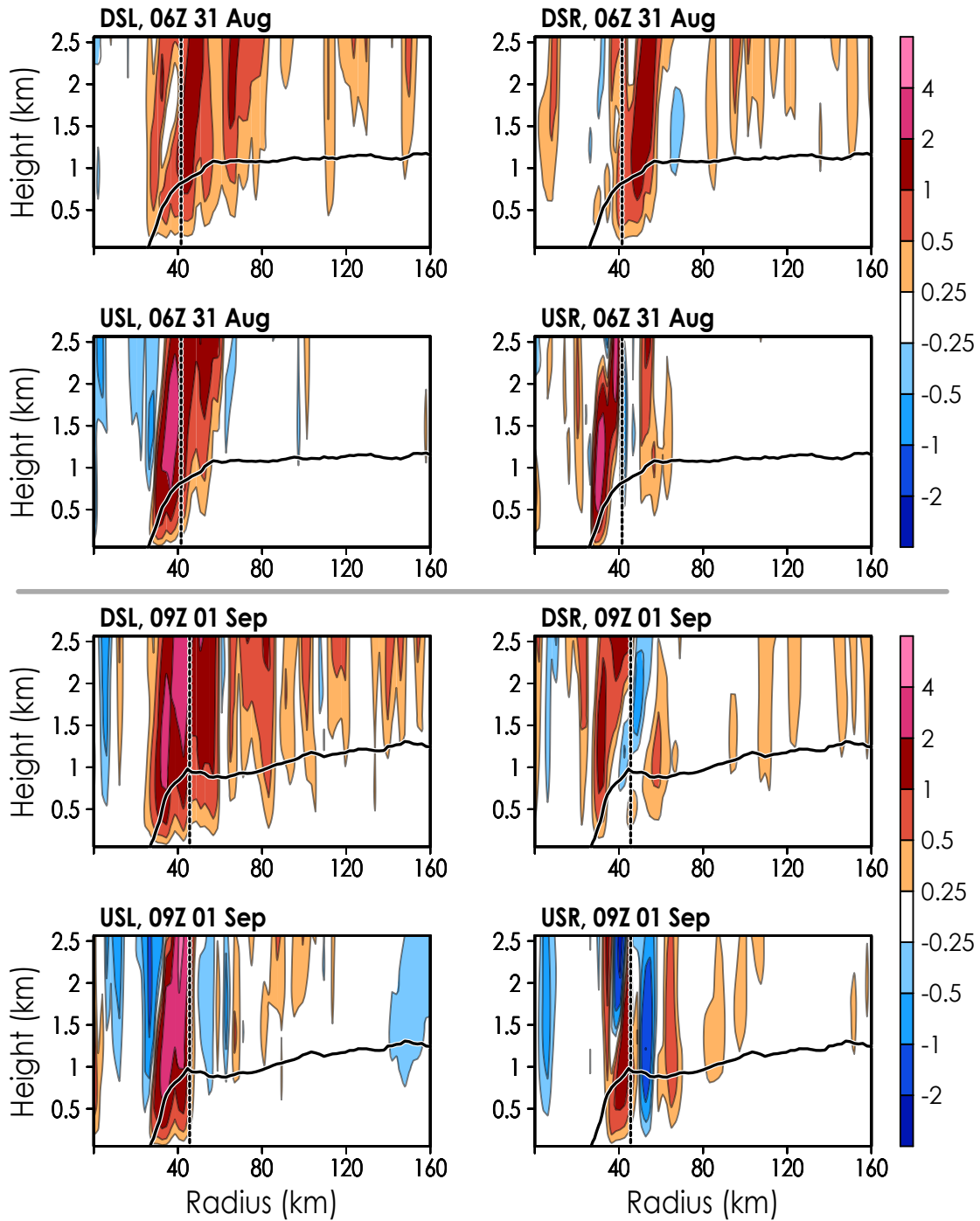


Figure 5.23: Similar to Figure 4.18, but shaded using vertical velocity  $w$  (m s<sup>-1</sup>).

the RMW, in line with the appearance of descent separating two branches of ascent on either side of the RMW in Figure 5.23. The inner- and outer-core divergence and vertical motion suggest that Earl's low-level ascent occurs more frequently in the DSL quadrant, and that the width over which that ascent occurs increases during Earl's weakening. Earl's eyewall also contains more branches of modest descent during decay.

Hovmöllers of Hurricane Earl's quadrant-specific, BL-integrated radial divergence are shown in Figure 5.24. During Earl's intensification prior to 01 September, radially widespread BL convergence is seen downshear, and the upshear quadrants are associated with strong BL convergence inward of the RMW. As Earl's motion and environmental shear begin to favor more asymmetric secondary circulatory structure after 1200 UTC 31 August, BL convergence near the RMW wanes in the USR quadrant. On 01 September, radial bands of enhanced BL divergence form along and immediately outside of the RMW in all quadrants except DSL, and those bands of divergence persist for over a day into 02 September. The BL divergence that develops near the RMW during Earl's non-intensification separates two regions where BL convergence is favored in the azimuthal mean: one just inward of the RMW, and one well outside the RMW (see Figure 5.18). By 02 September, Earl's motion becomes aligned DSL (previously from USL), and regions of BL convergence begin to take form in all quadrants at  $r \approx 80$  km in the roughly 18 hours prior to Earl's eyewall collapse. Shear-relative Hovmöllers of vertical motion at  $z \approx 1.2$  km in Figure 5.25 show a similar evolution, with two distinct regions of ascent forming on either side of the RMW in all quadrants after Earl's IN phase on 31 August. Areas of subsidence appear along the RMW between the two regions of ascent in all but the DSL quadrant.

The pronounced asymmetry in Hurricane Earl's low-level primary and secondary circulations on 01 September might explain the storm's broadening wind field (and associated increase in  $I^2$  outside the RMW as shown in Figure 5.8), progressive development of BL convergence and low-level ascent outside the RMW, and gradual decay of intensity prior to the 02 September eyewall collapse. We will conclude this section on Hurricane Earl's secondary circulation by elaborating further on the aforementioned asymmetric evolution—including the two-way interactions between the asymmetric primary and secondary circulations—and its potential consequences on structure and intensity.

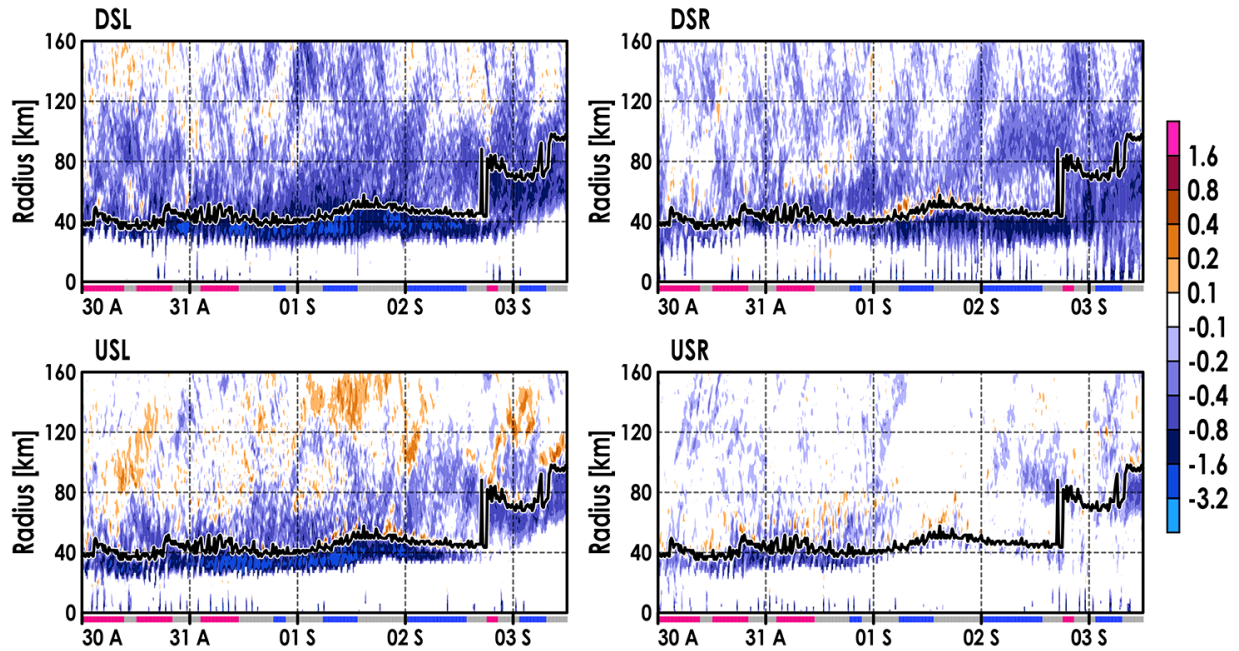


Figure 5.24: Similar to Figure 5.21, but shaded using vertically integrated radial divergence in the asymmetric radial inflow layer ( $\text{m s}^{-1}$ ).

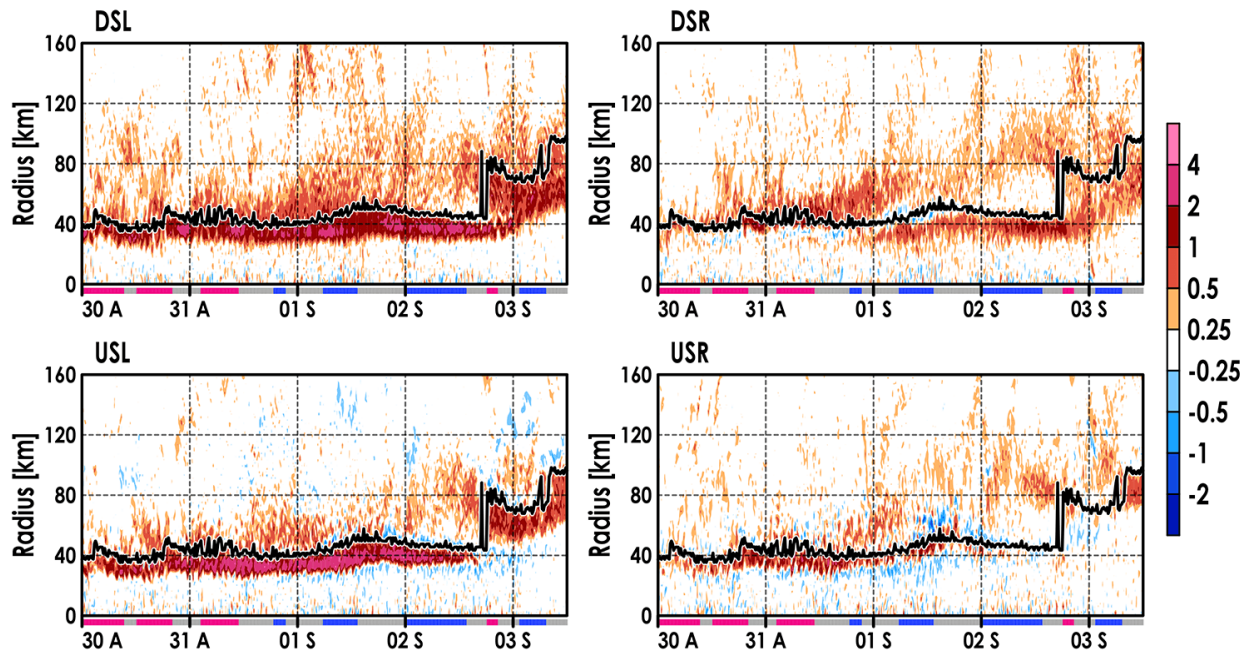


Figure 5.25: Similar to Figure 4.19, but shaded using vertical velocity  $w$  at  $z \approx 1.2 \text{ km}$  ( $\text{m s}^{-1}$ ).

**Breakdown of Asymmetric Evolution on 01 September.** With the storm motion oriented left of shear, the DSL quadrant would be expected (e.g., Zhang et al. 2013; Barnes and Dolling 2013) to have the strongest, deepest low-level inflow; and the USR quadrant should have the weakest, most-shallow low-level inflow (which are both seen in Figure 5.19). However, the intensity of near-surface inflow is offset from the azimuthal structure of inflow *depth*—while the deepest inflow is found downshear, the most-intense inflow is found *downstream* of Earl (left of shear). Just above the BL, spin-up tendency associated with inward advection of  $M_a$  is maximized downshear, while spin-down tendency due to outward advection of  $M_a$  is located upshear. Within the BL, spin-up by  $M_a$  advection is maximized left of shear and present DSR, and spin-down occurs USR. When air rotates from the USL quadrant to USR and then DSR, the BL  $v$ -field becomes stronger than  $v$  in the free atmosphere immediately above the BL (see Figure 5.10). This is because, despite frictional dissipation near the surface, the spin-down tendency induced above the BL by upshear outflow (and associated  $M_a$  advection) is apparently more effective in reducing tangential wind at most heights within the BL. This is especially the case in the USR quadrant, where the most-intense low-level outflow is seen as a result of highly supergradient wind exiting the USL quadrant. In this particular scenario, the fact that neither shear nor storm motion are expected to promote low-level inflow USR allows unbalanced flow to escape radially outward—even near the surface—in an attempt to restore gradient wind balance.

The USR outflow is strongest just outside the RMW and weakens with radius. The associated advection of low- $M_a$  air across  $r$  should reduce  $M_a$  at outer radii less while reducing  $M_a$  at inner radii more. Outside the RMW, this evolution of  $M_a$  across radius would result in stronger  $\partial M_a / \partial r$ , “flattening” of the tangential wind field near the BL top, and increased  $I^2$  relative to the inner core. The DSR quadrant inherits the air exiting the USR quadrant, with two low-level minima in  $v$ : one at the surface; and the other just above the BL ( $z \approx 1.5$  km), spatially coincident with intense outflow USR (Figure 5.10). The low-level radial inflow DSR likely results from frictional forcing, a balancing response above the BL to subgradient flow (i.e., inflow—see Figure 5.15), and the asymmetric forcing associated with shear.

It is paramount to emphasize here that a gradient forcing (due to friction or otherwise) is—as self-described—a *forcing term*, which originates from the radial momentum equation (see also

Equations 2.1 and 2.6):

$$\frac{Du}{Dt} = \left(f + \frac{v}{r}\right)v - \frac{1}{\rho} \frac{\partial p}{\partial r} + \frac{\partial \overline{u'w'}}{\partial z} = AGF + \frac{\partial \overline{u'w'}}{\partial z}. \quad (5.2)$$

A gradient forcing induced by friction in the BL will promote a Lagrangian *acceleration* of inflow ( $Du/Dt < 0$ ). However, the flow in the DSR quadrant originated from USR, which was associated with strong outflow through depth (including within the BL) and across radius. Thus, BL air rotating through the downshear quadrants will become more inwardly oriented via AGF and shear-related asymmetric forcing *over time*, but the resultant BL inflow will be asymmetrically weak at first (i.e., DSR) *because the flow was originally oriented outward* ( $u > 0$ ).

At the same time, the USR outflow should promote a broadening of the  $v$ -field downwind at the BL top, leading to enhanced  $I^2$  outside the RMW relative to  $I^2$  at the RMW. As BL inflow is regenerated downshear, BL air parcels moving inward are resisted by that enhanced  $I^2$ . The BL outside the RMW may be too inertially stable for weaker, frictionally forced inflow DSR (and even stronger inflow DSL) to reach the RMW before decelerating. The development of inflow maxima several kilometers outside the RMW in the DSR and DSL quadrants supports this interpretation (Figures 5.19 and 5.21), as does the broad radial band of ascent at the BL top (Figures 5.23 and 5.25). The fact that the outflow USR promotes broadening the  $v$ -field near the top of the BL also means that, as time passes, the inflow DSR will likely have to overcome progressively stronger resistance in the form of increasing  $I^2$  (as is shown in Figure 5.8) to reach the RMW before decelerating. Given the outward propagation of BL radial convergence downshear-right between 01 September and 03 September (Figure 5.24), it appears that the response may have been for the outer inflow maxima to propagate outward as resistance increased over time.

The inflow maxima situated outside the RMW led to forced ascent initiated downshear and outside the RMW (Figure 5.25). Should the ascent form the root for deeper convection aloft, then diabatic heating associated with the deep convection may reduce Hurricane Earl's warm-core temperature anomaly, thereby eliciting a thermal wind response in the lower troposphere that would culminate in a reduced surface pressure gradient and tangential wind at the RMW. Alternatively, the convergence may promote low- $M_a$  surfaces from radii inward of the RMW to be pulled outward by the deep ascent, resulting in dynamic spin-down aloft.

The combination of deep-layer shear, storm motion, and vortex structure (i.e., a broad  $v$ -field) are linked to asymmetric responses in Hurricane Earl’s low-level kinematic structure. We conclude these asymmetric responses were detrimental to Earl’s intensity. Outflow in the USR quadrant promoted progressive broadening of the  $v$ -field on 01 and 02 September. Boundary layer inflow in the DSR quadrant was progressively regenerated by a gradient forcing, as well as forcing associated with shear; however, due to high- $I^2$  and asymmetrically weak inflow, air parcels in the BL may have been unable to reach the RMW before decelerating and converging. This led to two regions of BL convergence and low-level ascent, with the outer region of ascent associated with Earl’s replacement eyewall on 03 September. In the next section, we will examine the evolution of Earl’s thermodynamic structure. In the forthcoming analysis of thermodynamic azimuthal structure, we will highlight evolutions that are related to Earl’s asymmetric kinematics, and their potential impact on structure and intensity.

## 5.5 Thermodynamics

### 5.5.1 Axisymmetric Structure

Cross sections of  $T_v$  and  $\theta_v$  in Figure 5.26 reveal Earl’s low-level warm-core structure, with relatively warm  $T_v$  located just inside the RMW associated with increased moisture via BL ascent and/or increased temperature through subsidence and adiabatic warming. At  $\sim 50$ – $60$  km radius, a local  $T_v$  maximum appears in and just above the BL during Earl’s WE phase on 01 September. The maximum in  $T_v$  outside the RMW suggests that either warming (e.g., through subsidence) or moistening (e.g., through moisture advection) occurred there locally. The increase in  $T_v$  implies an increase in  $\theta_v$ , which would affect dry static stability  $N^2$ . At a given height, the  $\theta_v$  field typically decreases with  $r$  in Figure 5.26; however, the radial gradient weakens where  $T_v$  increases outside the RMW, implying weaker dry static stability.

Air saturation and moisture in Hurricane Earl are also shown using relative humidity in Figure 5.26. In the BL,  $RH$  tends to decrease with radial distance, with maximum  $RH$  above the strong near-surface inflow. During Earl’s 31 August intensification,  $RH$  in the low-level eyewall is roughly 90% or greater. In the inner eyewall during WE on 01 September,  $RH$  is relatively reduced

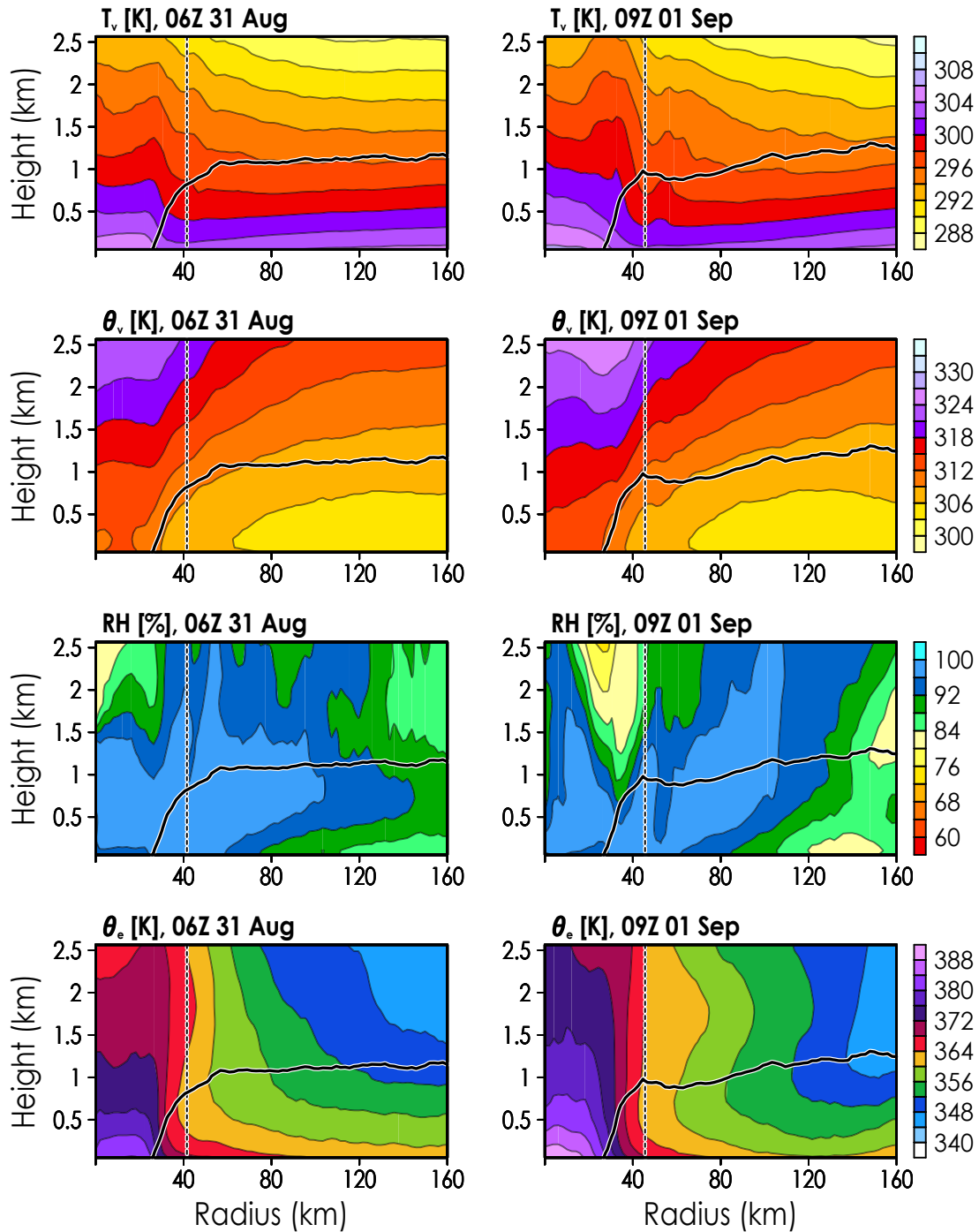


Figure 5.26: Radius-height cross sections of Hurricane Earl's azimuthally averaged virtual temperature  $T_v$ , potential virtual temperature  $\theta_v$ , relative humidity  $RH$ , and equivalent potential temperature  $\theta_e$  on 0600 UTC 31 August (left, IN phase) and 0900 UTC 01 September (right, WE phase). Rows of figures use the color bar to their right, and each plot has its units listed above. The dashed and solid black lines indicate the RMW and azimuthally averaged inflow layer, respectively.

above the BL, suggesting that more air aloft from Earl's eye may be descending there and possibly mixing with the eyewall convection. Lateral mixing of drier air into the inner eyewall may also contribute to the relatively dry air at the RMW during WE. In addition, Earl's  $RH$  just above the BL is greatest between  $r \approx 60$  km and  $r \approx 110$  km at 0900 UTC 01 September, implying that moist BL air may be effectively ascending into the free atmosphere there (which is supported by Figure 5.17).

Hurricane Earl's azimuthal mean structure of low-level moist enthalpy is illustrated through  $\theta_e$  profiles at the bottom of Figure 5.26. The BL is conditionally unstable outside the RMW, with relatively high- $\theta_e$  air near the surface due to air-sea turbulent fluxes of heat and moisture. Both IN and WE phases have their highest- $\theta_e$  air in Hurricane Earl's near-surface eye, with  $\theta_e$  being greater during WE (likely reflecting a difference in central pressure). While the  $\theta_e$  contours outside Earl's RMW during intensification tend to become more vertically aligned with decreasing radius (due to vertical motion and associated advection of high-enthalpy BL air), some contours during the WE phase become outwardly sloped with height between  $z \approx 500$  m and  $z \approx 1.5$  km, resulting in positive  $\partial\theta_e/\partial z$  that implies more slantwise eyewall ascent. The outward sloping of  $\theta_e$  surfaces may be caused by a combination of inner-core ascent of high- $\theta_e$  BL air into the free atmosphere, radial mixing, and outflow above the BL that would advect  $\theta_e$  surfaces outward.

Hovmöller plots of  $RH$  and  $\theta_e$  near the surface and above the BL are shown in Figure 5.27. Near-surface  $RH$  appears to undergo few changes prior to 1200 UTC 01 September, with nearly saturated air between the center and beyond the RMW (extending outward gradually over time from  $\sim 50$  km to  $\sim 70$  km by 1200 UTC 01 September). After 1200 UTC 01 September,  $RH$  at  $z \approx 210$  m seems to increase generally over time at all radii that are not already associated with saturated air. Equivalent potential temperature near the surface evolves similarly, with  $\theta_e$  in the inner core generally increasing before 01 September.

Prior to and during WE on 01 September, near-surface  $\theta_e$  at most radii near and outside the RMW decreases, perhaps in line with a decrease in  $RH$  (seen at outer radii in the near-surface  $RH$  Hovmöller). The relatively low- $\theta_e$  BL air outside the RMW during Earl's WE corroborates a similar finding in the composite analysis of Chapter 3, which found WE storms had significantly lower- $\theta_e$  air in the BL outside the RMW when compared against IN storms. Near-surface  $\theta_e$  begins

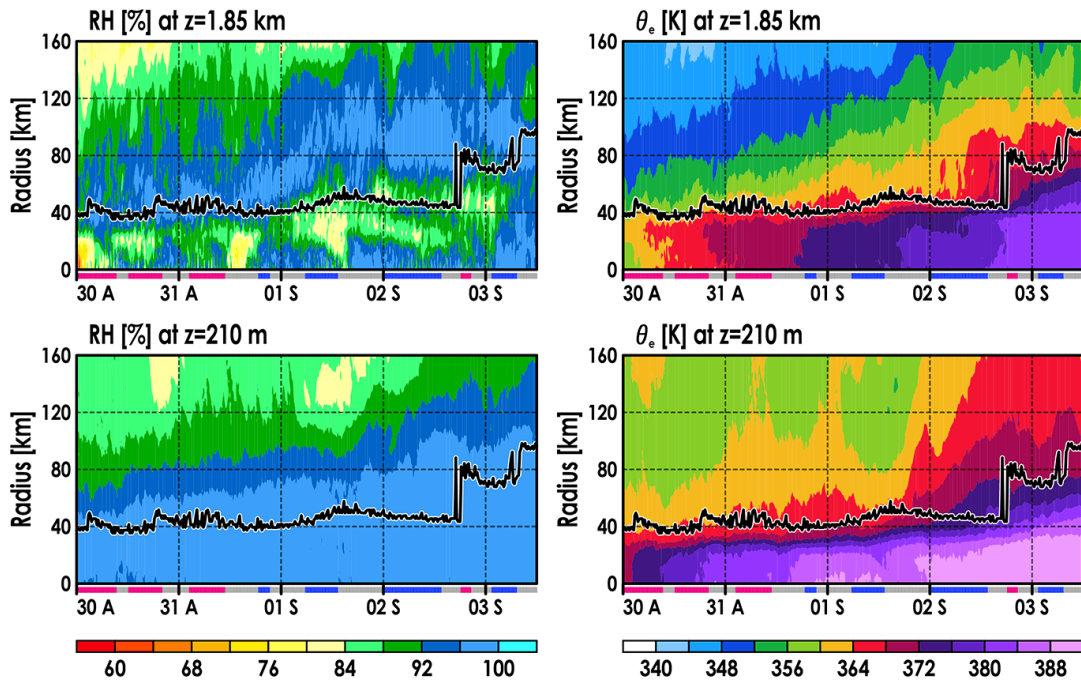


Figure 5.27: Time-radius Hovmöller plots of Hurricane Earl’s near-surface relative humidity  $RH$  (in %, left) and equivalent potential temperature  $\theta_e$  (in K, right). The top row of plots depict fields taken at  $z \approx 1.85$  km, and the bottom row of plots show fields at  $z \approx 210$  m. A timeline shaded by intensity change is drawn at the bottom of each panel. The bold, black line represents the RMW. Each column of plots uses the color bar below the column.

to increase rapidly over time at nearly all radii a few hours after 1200 UTC 01 September, similar to the  $RH$ -field. We note that the outer radii see the relatively high rate of  $\theta_e$  increase (as well as  $RH$ ) before inner radii, so the process of rapid  $\theta_e$  increase at all radii seems to originate outside the inner core. The pressure tendency near the surface (not shown) does not appear to explain the sudden increase of  $\theta_e$  at outer radii. The asymmetry of Earl’s low-level secondary circulation after 1200 UTC 01 September includes strong outflow in the USR quadrant above surface-layer inflow, which may advect high- $\theta_e$  air outward from the inner core. This would lead to a positive tendency of  $\theta_e$  at outer radii above the near-surface inflow DSR, which could then be recirculated inward from outer radii by deeper BL inflow downshear (thus, possibly explaining the increasing near-surface  $RH$  and  $\theta_e$  at outer radii prior to similar changes at inner radii).

Above the BL, the  $RH$ -field is maximized along the RMW during IN prior to Hurricane Earl’s prolonged period of non-intensification. The maximum  $RH$  moves radially outward toward  $r \approx 90$  km between around 1200 UTC 31 August (after Earl’s IN) and 1200 UTC 01 September. The

movement of the  $RH$  maximum at  $z \approx 1.85$  km is linked with the outward propagation of BL convergence and ascent over the same time period, highlighting that the radius of maximum  $RH$  is largely determined by where BL ascent is occurring. During most of Earl's WE phases,  $RH$  at the RMW is not maximized and relatively low compared to  $RH$  at the RMW during Earl's IN phases. Pockets of drier air that appear periodically in the eye are indicative of subsidence or decreased horizontal mixing with the eyewall. Equivalent potential temperature at  $z \approx 1.85$  km (also in Figure 5.27) increases over time at most radii outside the RMW, in tandem with the increasing  $RH$  and outward sloping of  $\theta_e$  surfaces. An abrupt increase of  $\theta_e$  on 02 September between the RMW and  $r \approx 90$  km is likely due to the formation of ascent associated with an outer secondary eyewall.

The low-level structure of  $RH$  and  $\theta_e$  during Hurricane Earl's evolution should be influenced by kinematics. Given the asymmetric evolution of Earl's primary and secondary circulations seen in subsections 5.3.2 and 5.4.2, it follows that Earl's thermodynamic structure should also undergo substantial asymmetric evolution. For example, the positive azimuthal-mean  $\partial\theta_e/\partial z$  above the BL during WE on 01 September may be a reflection of asymmetrically strong outflow and associated  $\theta_e$  advection. The next subsection will examine Earl's thermodynamic asymmetries and their ties to the kinematic asymmetries discussed earlier.

### 5.5.2 Asymmetric Structure

Shear-relative  $RH$  during Hurricane Earl's IN and WE phases respectively on 31 August and 01 September are provided in Figure 5.28. During the IN period shown, most of the low-level inner core is moist or nearly saturated, regardless of azimuth. Near the RMW, the  $RH$  right of shear is less saturated, with pockets of drier air amongst the otherwise moist eyewall. The azimuthal structure of  $RH$  develops much drier regions during Earl's WE phase on 01 September, with relatively low- $RH$  air surrounding or overlapping the RMW right of shear. In all but the DSL quadrant,  $RH$  above the BL is maximized and separated from  $RH$  at the RMW during the WE phase. Low-level dry air at  $r > 120$  km is seen in the USL quadrant, some of which would probably be moved inward by BL inflow there. The portion of the dry air in the outflow above the BL would be advected away. The USR quadrant at 0900 UTC 01 September has strong low-level outflow even near the surface, so

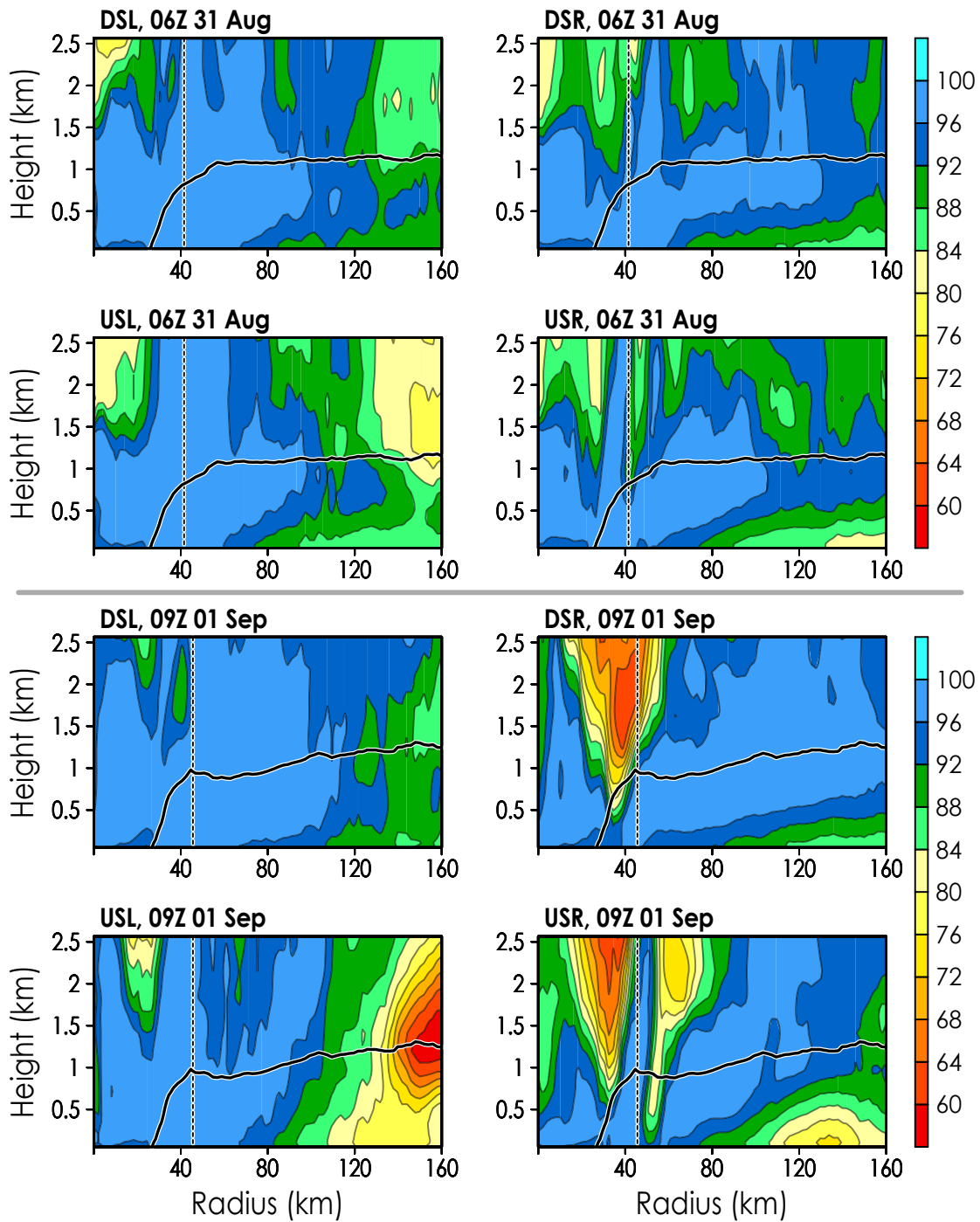


Figure 5.28: Radius-height cross sections of Hurricane Earl's relative humidity  $RH$  (%) in shear-relative quadrants on 0600 UTC 31 August (top two rows, during IN) and 0900 UTC 01 September (bottom two rows, during WE). Panels are labeled by quadrant shown. The dashed, black line marks the RMW. The bold, black line indicates the axisymmetrized radial inflow layer.

the drier BL air rotating into the USR quadrant from USL may be advected away before reaching Earl's eyewall.

Hurricane Earl's low-level moist entropy is examined in shear-relative cross sections of  $\theta_e$  in Figure 5.29. During IN on 31 August, the azimuthal structure of moist entropy appears loosely symmetric. Equivalent potential temperatures above the BL and outside the RMW are somewhat greater downshear, perhaps due to more radially widespread ascent of high- $\theta_e$  air from the BL into the free atmosphere. As Hurricane Earl's primary and secondary circulations become more asymmetric leading up to 0900 UTC 01 September, the low-level thermal structure evolves in kind. In the DSL quadrant, the radial gradient of  $\theta_e$  just outside the RMW is weak due to the ascent of high- $\theta_e$  BL air across nearly all radii between the RMW and  $r \approx 120$  km (as shown in section 5.4). Between 120 and 160 km radius in the DSL quadrant, outside of the region of BL convergence and ascent, the BL has relatively low- $\theta_e$ , possibly due to weak forced subsidence. The USL quadrant contains a minimum of BL  $\theta_e$  near  $r \approx 90$  km, which is also likely a result of BL divergence and forced subsidence pulling down low- $\theta_e$  air from above (in this case, potentially associated with the low- $\theta_e$  air at  $r > 120$  km). The widespread outflow above the BL in the USL quadrant advects  $\theta_e$  surfaces outward, leading to their outward slant outside the RMW.

Due to the strong low-level outflow in the USR quadrant, the thermodynamic structure becomes more distorted. Outflow pushes high-enthalpy air outward from Earl's USR inner core, resulting in a maximum of  $\theta_e$  above the BL and increased  $\theta_e$  above the near-surface inflow at all radii outside the RMW. Above  $z \approx 1.5$  km, Earl's very high- $\theta_e$  core is asymmetrically weak USR just inward of the RMW, suggesting that the USR outflow may be exhausting moist entropy from the low-level  $\theta_e$  core toward outer radii. As air rotates and exits the USR quadrant, it enters the DSR quadrant, where deep inflow is reestablished and far less low-level outflow exists. Relative to the other quadrants, the moist entropy of air DSR is maximized through the lowest 2.5 km at nearly all radii outside the RMW, which indirectly points to the efficiency of outward transport of high- $\theta_e$  air in the USR quadrant. The relative surplus of moist entropy in the DSR quadrant hints at the possibility that the high- $\theta_e$  air advected outward from the inner core USR begins to recirculate toward the inner core downshear. If the downshear BL inflow's moist entropy is enhanced at outer radii by the USR quadrant's outflow, then ascent out of the BL outside of the RMW (as is seen in

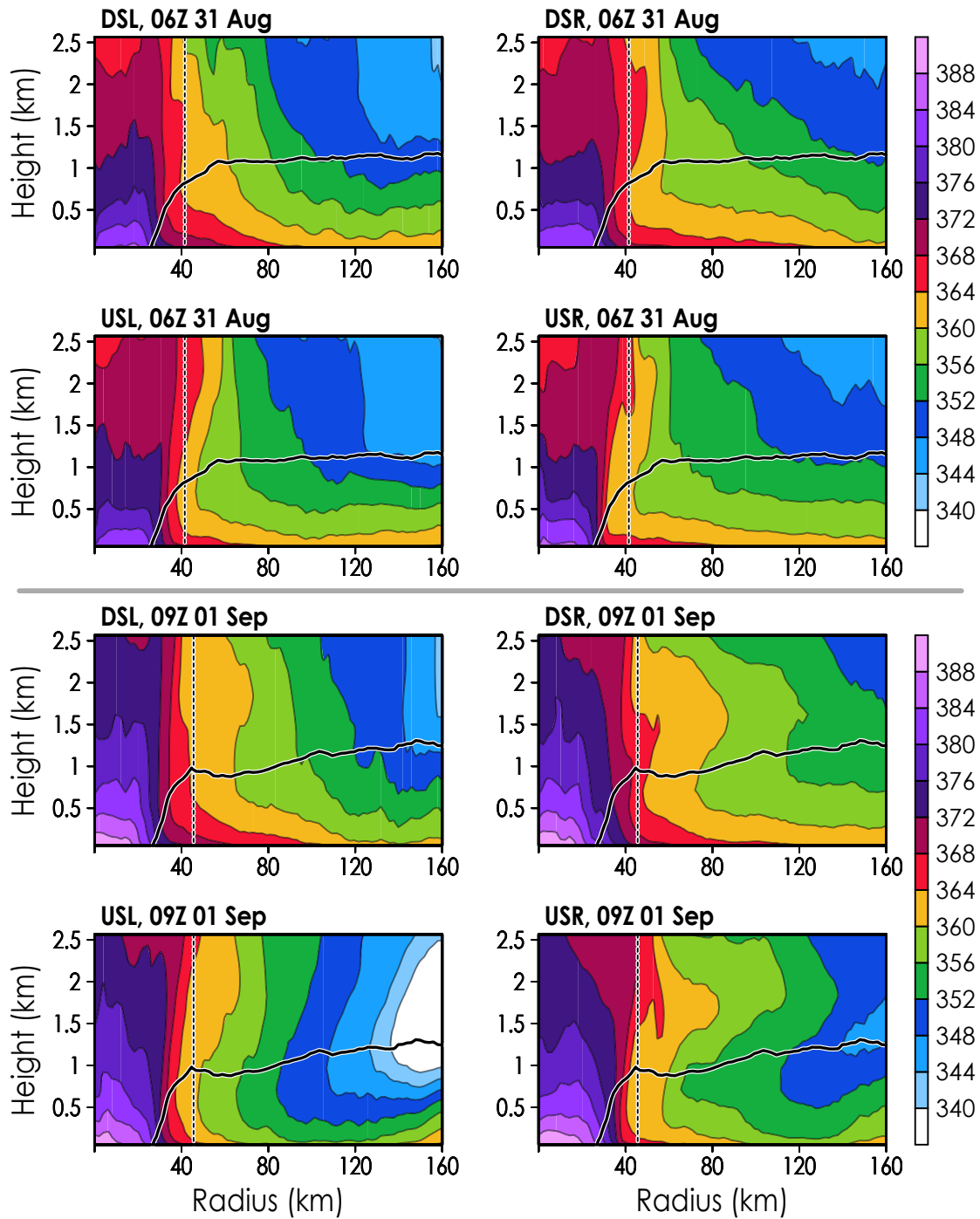


Figure 5.29: Similar to Figure 5.28, but shaded using equivalent potential temperature  $\theta_e$  (in K).

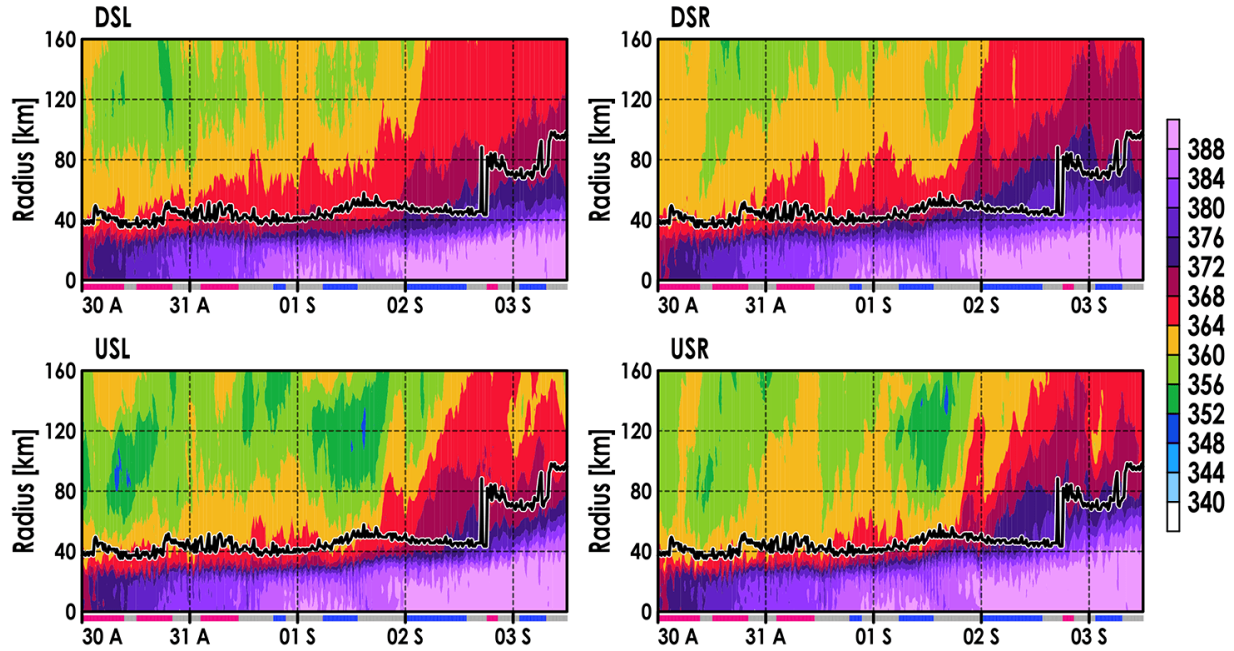


Figure 5.30: Time-radius Hovmöllers of  $\theta_e$  (K) at  $z \approx 210$  m in Hurricane Earl’s shear-relative quadrants. The  $x$ -axis represents time, labeled by each day at 0000 UTC. A timeline shaded by intensity change is drawn at the bottom of each panel. The bold, black line represents the RMW. Panels are labeled by their quadrant abbreviation.

this case) might be more likely to initiate deeper convection and promote a secondary tangential wind maximum.

To assess the effects of Hurricane Earl’s asymmetry on moist thermodynamic structure over time, we first examine  $\theta_e$  as a function of time and radius at  $z \approx 210$  m in Figure 5.30. Prior to 02 September, near-surface  $\theta_e$  is generally greatest downshear. As discussed in section 5.4, Hurricane Earl’s low-level ascent is most frequent and widespread DSL, implying that high- $\theta_e$  BL air tends to escape upward into the free atmosphere more often there. This corroborates prior analyses focused on the shear-relative distribution of convection (e.g., DeHart et al. 2014), which has suggested that convection is primarily initiated downshear-left, and downdrafts (advecting low- $\theta_e$  air downward from aloft) are most frequent downwind in the USL and USR quadrants. As the storm motion becomes more oriented to the left of shear before Earl’s first analyzed WE period on 31 August, low-level ascent DSL becomes more frequent at  $r > 120$  km, perhaps leading to

downdrafts upshear-left (and leading to the reduction of near-surface  $\theta_e$  at  $r > 80$  km upshear after 1200 UTC 31 August). The relatively low- $\theta_e$  air in the USL quadrant may then be ingested by the eyewall updraft via BL inflow, possibly affecting local convection negatively. If that is true, then the azimuthal mean heating in the eyewall may be reduced, thereby affecting Earl's intensity (note that the drier, lower- $\theta_e$  air centered at  $r \approx 100$  km upshear on 01 September is coincident with Earl's WE/SS phases). Horizontal plots of near-surface  $\theta_e$  during Earl's WE phase on 01 September (Figure 5.31) also show that BL moist entropy is reduced at outer radii upshear.

After 1200 UTC 01 September, the near-surface  $\theta_e$  begins to amplify rapidly over time at all radii outward of the RMW, with the amplification starting at outer radii and then propagating inward. We hypothesize that the strong low-level outflow in the USR quadrant transports high- $\theta_e$  air from Hurricane Earl's inner core to outer radii near the top of the BL (above the  $z \approx 210$  m level shown in Figure 5.30), which then rotates into the relatively deep low-level inflow in the DSR quadrant. The high- $\theta_e$  air at outer radii DSR can then mix downward or subside into the near-surface inflow, essentially allowing the outwardly exhausted air to return toward Earl's core downwind of the USR quadrant. This is partially illustrated in Figure 5.31, which shows anomalously high- $\theta_e$  air at outer radii in the USR quadrant that appears to spread outward and rotate into quadrants downwind. If the anomalously high-enthalpy BL air manages to ascend outside the RMW (as is seen downshear) and form deep convection aloft, then more diabatic heating may occur outside the RMW, leading to a thermal wind adjustment that involves tangential wind at the RMW to spin down, and the tangential wind near the region of heating to spin up (Shapiro and Willoughby 1982). Hours prior to Earl's eyewall collapse on 02 September, low-level tangential wind at the RMW spins down as  $v$  spins up at  $r \approx 90$  km, all in coincidence with increased ascent at the top of the BL at  $r \approx 80$  km.

To track the asymmetric evolution of Hurricane Earl's inner-core  $\theta_e$  near the top of the BL, a similar time-radius Hovmöller of  $\theta_e$  at  $z \approx 1.2$  km is examined in Figure 5.32. Before 01 September, Hurricane Earl's  $\theta_e$  near the BL top is somewhat maximized right of shear, with inner-core  $\theta_e$  increasing gradually over time. When substantial radial flow asymmetries develop in tandem with Earl's motion orienting more cross-shear after the 31 August IN phase, air near the BL top at  $r > 100$  km becomes drier USL. In the USL quadrant on 01 September, radial flow near the BL

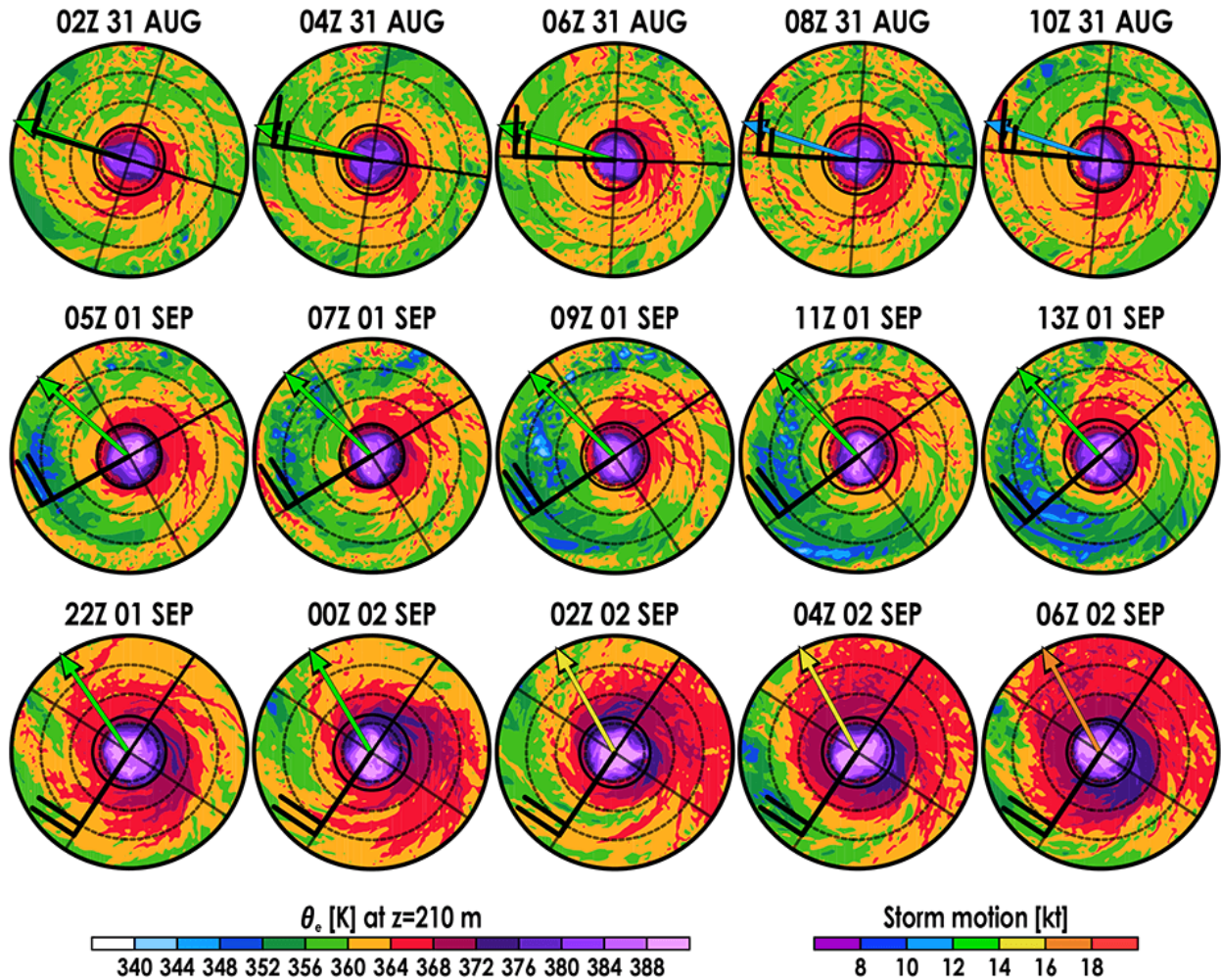


Figure 5.31: Similar to Figure 5.12, but using  $\theta_e$  (K) at  $z \approx 210$  m.

top is inward at  $2\text{--}10 \text{ m s}^{-1}$ , so the dry air may rotate into the USR quadrant before moving far in the radial sense (thus, explaining the relatively dry air at  $r > 90$  km USR). In the USR quadrant, widespread low-level outflow strengthens as part of the asymmetric response to the changes in motion and shear. The outflow advects the inner core's high- $\theta_e$  air outward early on 01 September. However, the dry air entering USR from the USL quadrant may counteract the positive tendency of  $\theta_e$  by advection, such that USR  $\theta_e$  actually *decreases* with time through the first 12 hours of 01 September outside the inner core. As air exits the USR quadrant and enters the DSR quadrant,  $\theta_e$  at the BL top is maximized outside the RMW as outflow and its associated  $\theta_e$  advection

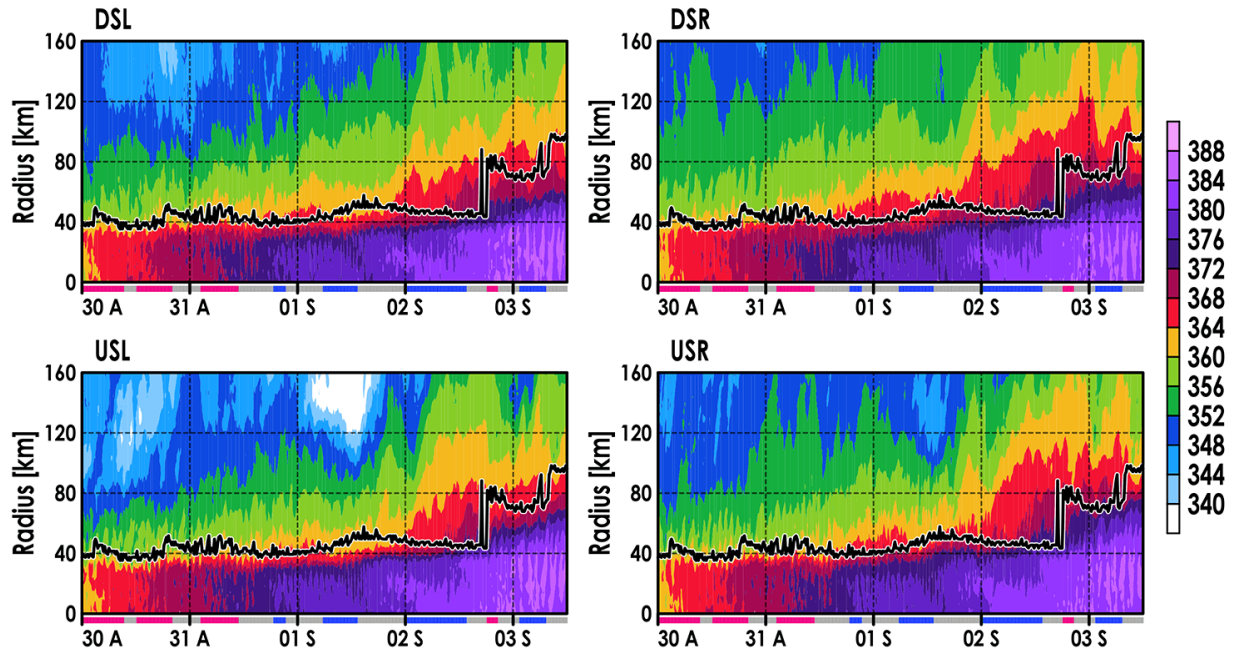


Figure 5.32: Similar to Figure 5.30, but using  $\theta_e$  (K) at  $z \approx 1.2$  km.

becomes replaced by inflow. The dry air at outer radii in the USL quadrant begins to moisten near 1200 UTC 01 September, and then  $\theta_e$  begins to increase at all radii outside the RMW with relative haste, with the  $\theta_e$  increase propagating outward over time (unlike near-surface  $\theta_e$ ). The rapid increase of low-level  $\theta_e$  outside the RMW appears to occur at the top of the BL prior to the similar  $\theta_e$  increase near the surface, supporting the hypothesis that the outflow and associated  $\theta_e$  advection leads to a near-surface response via recirculation of high-enthalpy air toward Hurricane Earl's center.

## 5.6 Summary

For the second part of our numerical analysis using the WRF-ARW model, Hurricane Earl in 2010 was chosen to study BL structure under moderate-to-strong deep-layer shear. While the environmental shear enveloping Hurricane Earl was sometimes stronger in magnitude compared to shear in our study of Hurricane Irma (2017), the primary systematic differences between Hurricanes Earl and Irma were the breadth of strong tangential winds (a more broad  $v$ -field seen in

Earl), and the orientation of storm motion with respect to shear. Hurricane Earl was simulated from 1200 UTC 28 August to 1200 UTC 04 September, with our analysis limited between 1200 UTC 30 August and 1200 UTC 03 September. Our analysis became chiefly concerned with a prolonged non-intensification period between 31 August and 02 September, after Hurricane Earl reached peak intensity.

Due to Hurricane Earl's relatively flat radial profile of low-level tangential wind outside the RMW, inertial stability outside the RMW was generally greater in Earl than in Irma throughout the analysis period. BL convergence and low-level ascent were more radially widespread in Earl than in Irma (particularly during non-intensification), which reflects the differing profiles of  $I^2$  between the cases and corroborates the conclusions drawn from our composite analysis (i.e., that more BL convergence and low-level ascent outside the RMW may occur during SS and WE phases). During a WE phase on 01 September, azimuthally averaged moist entropy in the BL at outer radii was reduced by an influx of relatively dry air, which may have been drawn into eyewall convection by BL inflow. As discussed in Chapter 3, this may inhibit eyewall convection to some degree, thereby impacting Earl's intensity negatively.

For most of 31 August, Hurricane Earl moved toward the west-northwest at  $\sim 11$  kt, while deep-layer shear of  $\sim 15$  kt pointed eastward. While Earl's motion and environmental shear were nearly antiparallel, the low-level inner core maintained a somewhat asymmetric structure, with deeper inflow downshear, weak and widespread low-level outflow upshear, slightly stronger tangential wind in the USL quadrant, and weaker  $v$  in the DSR quadrant. The stronger  $v$  in the USL quadrant may have been the result of aggregate  $M_a$  spin-up from deeper inflow downshear, which would allow relatively unimpeded spin-up of air above the BL and its associated frictional dissipation.

A gradient forcing within deep inflow downshear promoted stronger *frictionally driven* inflow, leading to the asymmetrically intense near-surface inflow left of shear. The  $M_a$  advection associated with the asymmetric inflow would be maximized left of shear, before dynamical imbalances in the USL quadrant (i.e., supergradient flow) added a tendency for outward acceleration that outweighed tendencies for inflow by storm motion and frictional dissipation. This could cause  $Du/Dt$  to be positive (Lagrangian outward acceleration of radial flow), decelerating the inflow of air as it rotates through the upshear quadrants. Thus, the USR quadrant would contain the weakest in-

flow (as shown in Figures 5.19 and 5.21). The weaker inflow would rotate into the DSR quadrant, where asymmetric forcing due to shear and a gradient forcing in the absence of strongly supergradient flow (Figure 5.15) would again accelerate low-level inflow, completing a cyclical process (see Figure 5.33). Perhaps owing to a combination of Earl's high  $I^2$  outside the RMW and weak BL inflow translating into the DSR quadrant from USR, the downshear quadrants tended to have their inflow maxima positioned outward from the RMW.

After Hurricane Earl's intensification on 31 August, the storm motion and shear reoriented such that the motion vector became more perpendicular and to the left of shear. Following the turning of motion and shear vectors on 31 August, Hurricane Earl failed to intensify for the next two days, instead undergoing WE and SS phases that appeared to be linked to asymmetric features in the low-level troposphere. This contrasts with the simulation of Hurricane Irma, which had its storm motion vector nearly orthogonal and to the *right* of shear for the first half of the analysis period (during which Irma had periods of IN and WE between short periods of steady-state intensity). We note that the magnitudes of shear and storm motion were nearly identical between Irma and Earl whilst those vectors were near-orthogonal, with translational speed of  $\sim 13$  kt and deep-layer shear of  $\sim 20$  kt.

In coincidence with the adjustment of shear and motion on 31 August, azimuthally averaged radial convergence in Hurricane Earl's BL began to amplify just outside the RMW, distinct from the strong BL convergence inward of the RMW. Over time, the outer locus of BL convergence propagated outward from Earl's center, moving from a few kilometers outward of the RMW ( $r \approx 45$  km) on 31 August to roughly 50 km outside the RMW ( $r \approx 90$  km) on 02 September. Low-level ascent followed a similar pattern, with more radially widespread upward motion near the BL top appearing over the same period. Near 1200 UTC 02 September, a secondary tangential wind maximum strengthened near the outer region of BL convergence and low-level ascent, eventually growing more intense than the tangential winds at  $r \approx 45$  km and becoming the new RMW.

Hurricane Earl's BL structure developed substantial kinematic and thermodynamic asymmetries after the reorientation of storm motion and shear that began on 31 August (illustrated conceptually in Figure 5.33). Near-surface inflow became most intense near the RMW downstream of Earl's motion (shown in Figure 5.33 left of shear), and the deepest inflow remained downs-

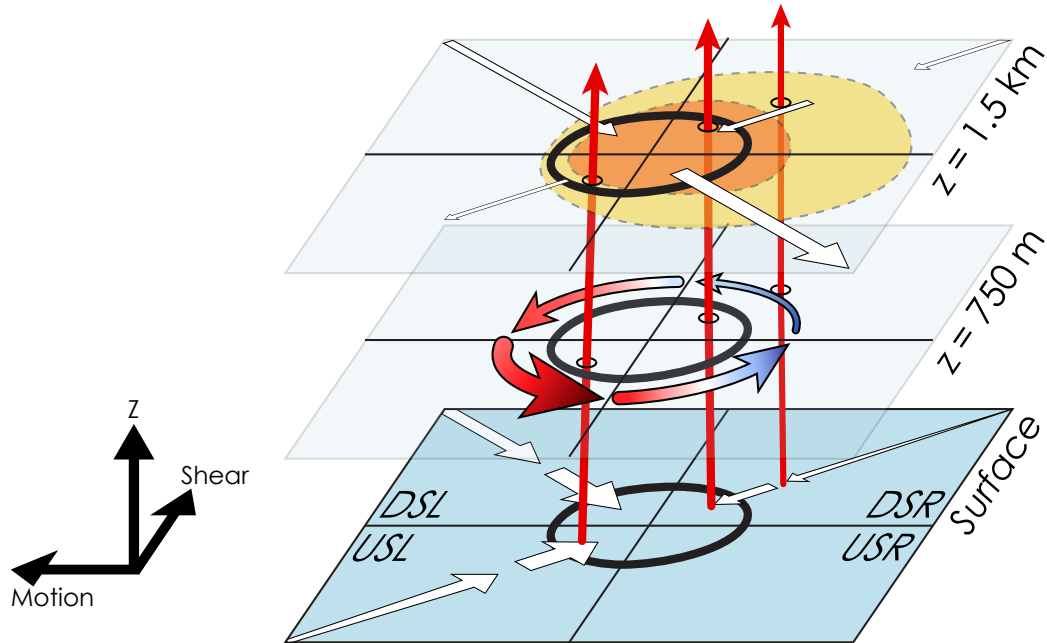


Figure 5.33: Volumetric schematic of Hurricane Earl’s low-level tropospheric structure during its gradual weakening following peak intensity on 31 August. The schematic’s frame is identical to Figure 4.33. Tangential vectors (shaded) and radial vectors (white) have magnitudes proportional to their thickness. Tangential vectors are shaded by their degree of gradient imbalance, with deeper shades of red or blue indicating strongly supergradient or subgradient flow, respectively. Ascent vectors are solid red without an outline, with two regions of ascent shown in the DSR quadrant. The orange and yellow shaded regions indicate areas of very high- and high- $\theta_e$  air, respectively.

hear. In the upshear-right quadrant, the BL inflow was replaced by outflow in most areas except at the lowest vertical levels outside the RMW (shown in Figure 5.33 as an absence of substantial radial flow near the surface). Above the surface, strong outflow dominated the USR quadrant’s low-level atmosphere outside Earl’s eye. Low-level inflow can be influenced by storm motion and shear, such that the inflow is expected to be amplified both downstream of storm motion as well as downshear (Barnes and Dolling 2013; Zhang et al. 2013). Thus, the low-level inflow’s asymmetric structure appears sensible in this case. However, the expectation for weaker inflow (in the integral sense) USR based on the orientation of storm motion relative to shear does not consider why *strong outflow* occurs USR (instead of, for instance, an absence of strong radial flow altogether). The prominent outflow and lack of BL inflow USR may have serious dynamic and thermodynamic

consequences (e.g., broadening of  $v$  at the BL top downwind, outward advection of  $\theta_e$ ), so making sense of how Hurricane Earl came to develop such an asymmetric low-level secondary circulation seems critical.

Within the deep low-level inflow downshear, there generally exists the tendency for spin-up of tangential wind via inward transport of relatively high- $M_a$  air from outer radii. In the BL, frictional torque should largely counter spin-up tendency by  $M_a$  advection. However, if rapidly inflowing, high- $M_a$  air manages to ascend out of the frictional BL inflow and into the free atmosphere before dissipation can nullify the influx of  $M_a$ , then a net spin-up tendency should be induced near and above the BL top (Montgomery et al. 2018). Assuming the hurricane's  $v$ -field is roughly gradient-balanced in the free atmosphere, the upward turbulent flux of  $M_a$  out of the BL should result in locally supergradient flow. In Hurricane Earl, supergradient flow was found at most radii near and immediately above the BL top in the DSL quadrant, as the radially widespread BL convergence in that quadrant may have facilitated the upward flux of  $M_a$  from the BL inflow. Furthermore, the depth of inflow downshear allows inward transport of high- $M_a$  air *above* the frictional BL, possibly leading to uninhibited spin-up there. However, the inflow above the BL is far weaker than the inflow near the surface, and supergradient flows seen in Hurricane Earl's simulation appear to collocate closely with BL radial convergence and ascent, so the direct effect of inflow above the BL on unbalanced flow may be relatively insignificant.

With the storm motion to the left of shear, Hurricane Earl's near-surface inflow was most intense DSL and USL. After supergradient winds develop near the BL top in the DSL quadrant (represented by a change of shading of tangential vectors in Figure 5.33) due to the inward and upward translation of high- $M_a$  air within the BL, the air rotates into the USL quadrant. The low-level inflow asymmetry induced by Earl's motion to the left of shear leads to more inward transport of high- $M_a$  air from outer radii in the BL. This results in further departure of the flow along the BL top from gradient wind balance, culminating in the USL quadrant possessing the most-intense supergradient flow in the inner and outer core (indicated by dark red tangential vectors in Figure 5.33). Restoration of gradient balance outside the BL in this case could be achieved through outflow and resultant spin-down via advection of relatively low- $M_a$  outward from inner radii. However, when supergradient wind moves into the USL quadrant from DSL, the inflow asymmetry asso-

ciated with Earl's motion may prevent efficient outflow from forming USL, inhibiting restorative forcing and promoting further imbalance. Neither shear nor Earl's motion would be expected to asymmetrically amplify low-level inflow in the USR quadrant, so when highly unbalanced flow moves from USL to USR, sufficiently strong outflow can finally form to attempt restoring gradient wind balance.

The outflow region in the USR quadrant during Earl's prolonged non-intensification period had several consequences: low-level divergence and downward motion linked with the outflow, rapid spin-down of air along the top of the BL (where outflow was generally maximized), and outward exhaust of high-entropy air from Earl's core to large radius near the top of the BL (shown by the shaded regions in Figure 5.33). The downward motions associated with radial divergence were strongest near the RMW. Asymmetrically weak BL inflow in the DSR quadrant is likely due to the  $u$ -field that it inherits from the USR quadrant; a gradient forcing from friction accelerates the BL inflow over distance and time, but inflow in the DSR quadrant will be relatively weak as it regenerates from the strong outflow upwind in the USR quadrant.

Hurricane Earl's broad  $v$ -field is associated with greater inertial stability outside the RMW, so air parcels within the weaker inflow DSR may have been forced to decelerate and deflect upward prior to arriving at the RMW. The USR outflow was strongest above the BL at inner radii, so spin-down via  $M_a$  advection was most effective at inner radii and least effective at outer radii. This would lead to a progressive broadening of the  $v$ -field downwind, thereby increasing  $I^2$  at outer radii. If low-level  $I^2$  increased over time in the DSR quadrant, then the inflow maximum in the DSR quadrant would gradually propagate radially outward as resistance to radial flow increases outside the RMW. The DSR quadrant was found to have a region of BL convergence and ascent propagate radially outward from outside the RMW over roughly two days following the secondary circulation's asymmetric evolution on 31 August, in tandem with gradual broadening of  $v$  over radius outside the RMW.

The exhaust of high- $\theta_e$  air from Earl's inner core (yellow and orange shaded areas in Figure 5.33) by the USR outflow became most evident near 1200 UTC 01 September, after relatively dry air originating from outer radii in the USL quadrant became replaced by more moist air. Because the outflow USR was generally above the strong near-surface inflow, the high- $\theta_e$  air from

Earl's core first spread outward at altitudes near and above the BL top. Afterward, we hypothesize that the high-entropy air originally advected outward above the BL is then recirculated into the near-surface inflow downwind, resulting in a rapid increase of near-surface  $\theta_e$  that begins at *outer* radii. This thermodynamic evolution not only weakens Earl's high- $\theta_e$  core—and, potentially, diminishing eyewall convection by affecting moist static stability—but it also adds enthalpy to the BL that can be utilized by shallow ascent well outside the RMW. The upward motions outside the RMW may continue upward through moist convection, wherein diabatic heating aloft would lead to a thermal wind response that strengthens low-level  $v$  near the heating outside the RMW, and also weakens low-level  $v$  near the RMW.

In summary, Hurricane Earl's asymmetric BL response after its IN periods in August seems linked to storm motion and deep-layer shear—and perhaps more specifically, their orientation with respect to each other. The BL asymmetry that developed after the shear and motion became less antiparallel was associated with a prolonged non-intensification period, which may have been influenced or instigated by the BL's asymmetric response. The asymmetric response may have also been affected by Hurricane Earl's broad wind field and high- $I^2$  outside the eyewall. The asymmetric BL structure associated with Earl's two-day period of SS and WE phases may have promoted ascent out of the BL downshear and outside the RMW, which may explain Earl's steady decline in intensity.

# CHAPTER 6

## CONCLUSION

This project used a combination of observational and numerical analyses to investigate boundary layer structure in Atlantic basin hurricanes, with a focus on BL structure relative to modes of intensity change [intensifying (IN), weakening (WE), and steady-state (SS)]. The endeavors herein intended to improve our understanding of the hurricane BL—in particular, its role in the two-way interaction between itself and the free atmosphere that can influence storm growth and decay. Our observational analysis identified general, robust features of the hurricane BL associated with some or all phases of intensity change; while our numerical analyses addressed some uncertainties and unanswered questions from the observational analysis.

Thousands of soundings from GPS dropwindsondes released during flight reconnaissance in Atlantic hurricanes were collected, quality controlled and filtered, and then composited based on diagnosed rates of intensity change. For analysis, a total of 3,091 soundings were categorized and blended to comprise three composites, each representative of a different mode of intensity change (IN, SS, WE).

All dropsonde composites rendered a low-level tangential wind jet that extends through the BL at the RMW, in general agreement with prior observational studies (Franklin et al. 2003; Powell et al. 2003; Zhang et al. 2011, 2013). The inner-core primary circulation in the WE composite was generally stronger than found in the composite for IN storms, as well as for SS storms (though to a lesser degree). However, this difference in composites stems from a sampling bias in storm intensity: Weakening hurricanes are often sampled at greater intensity than steady-state or intensifying hurricanes. To account for the intensity bias, we then normalized the  $v$ -field by intensity. Using the normalized tangential velocity, we found that the IN composite possessed the deepest low-level jet in the eyewall, perhaps reflecting more vigorous vertical motions/mixing there in comparison to SS and WE hurricanes of a given intensity. The normalized  $v$  was also used to infer properties of inertial stability, which suggested that the eyewall region was most inertially stable in the IN com-

posite, and least inertially stable in the WE composite. At radii outside and away from the RMW, the normalized  $v$ -field implied that the WE composite was associated with the highest  $I^2$ , while the IN group had the lowest  $I^2$  at outer radii. The differences in inferred inertial stability may be linked with differences in BL radial convergence, low-level ascent, and possibly convection (Rogers et al. 2013a). Specifically, more BL convergence and ascent may be expected outside the RMW in non-intensifying storms, while intensifying hurricanes could be associated with ascent and convection that are mostly isolated near the RMW.

Radial velocities in every composite presented a strong near-surface inflow layer, with the most-intense inflow located adjacent to the RMW and below the tangential wind jet [as seen in prior studies (Zhang et al. 2011, 2013)]. The SS and WE groups had a wider radial extent of strong inflow compared to IN, which was interpreted as an increased potential for BL convergence and associated ascent outside of the RMW. If more ascent out of the BL were to occur outside the RMW, then perhaps there would be an increased likelihood of convection outside the RMW (Kepert 2013; Hazelton et al. 2017b,a), owing to the export of high-enthalpy air from the BL into the low-level free atmosphere.

Properties of BL dry and moist thermodynamics were also examined in the dropsonde composites. Regardless of stratification by intensity change, the inflow layer was associated with minimized dry static stability  $N^2$ , and more statically stable air was found to overlay the inflow layer [corroborating works by Zhang et al. (2011) and Kepert et al. (2016)]. The non-intensifying storms' composites had relatively low  $N^2$  near the top of the inflow layer well outside the RMW. This weaker static stability may reflect a greater prevalence of vertical exchange between the inflow layer and free atmospheric air aloft, possibly resulting in the reduction of moist static energy in the BL inflow (and also increasing moist static stability in the free atmosphere directly above the BL).

Similarities and differences in  $\theta_e$  between composite groups were also examined. All composites had high- $\theta_e$  center (eye) regions, with an oft-negative vertical gradient of  $\theta_e$  inside the RMW. The central  $\partial\theta_e/\partial z$  was generally most negative in the IN group, implying greater conditional instability in the eye relative to SS and WE storms. Lateral mixing between the eye and eyewall (e.g., through shear instability) could mix relatively high-entropy air from the eye into the

low-level eyewall, possibly adding buoyancy and affecting eyewall convection (Montgomery et al. 2006b). As the strongest central  $\partial\theta_e/\partial z$  was found in the IN group, conditional instability (or buoyancy) may be more effectively introduced to the inner eyewall during intensification if lateral mixing were to occur through depth in the lower troposphere. Outside the eyewall region in all composites, relatively low- $\theta_e$  air is seen through much of the lower troposphere, extending into the near-surface inflow. In the WE composite, the low- $\theta_e$  air at outer radii appeared to extend deeper into the BL inflow from the free atmosphere aloft to a statistically significant degree compared to IN. Lower-entropy air may originate from outside the hurricane BL and entrain into the frictional inflow at outer radii more often in WE storms, which could affect the air that eventually arrives at the eyewall. This difference in BL  $\theta_e$  at outer radii may be due to differences in air-sea fluxes of heat (e.g., due to lower ocean heat content), vertical motions near the BL top (including convective downdrafts), and increased vertical diffusion from vertical shear.

The observation-based composite analysis revealed several distinctive BL structures. In general, the BL structures seen corroborate prior research, and the kinematic and thermodynamic differences between intensifying and non-intensifying composites are new to the existing literature (Ahern et al. 2019). While the composite analysis provides insight regarding the hurricane BL and its ties to intensity change, the analysis only considered the azimuthally averaged BL structure—we did not consider the asymmetric structure of the BL due to data limitations. The composites necessitated data from multiple hurricanes, each with their own characteristics (e.g., location, size, intensity, translational speed, shear magnitude) and sampling frequency. Although mature hurricanes are more often sampled because of their time spent in the Atlantic basin and their potential to become a threat to land, the fact that each composite is a meld of many different storms (both mature and otherwise) undermines confidence that the composite structure is representative of actual hurricanes.

To ascertain to some degree the veracity of the composite analysis with regard to its representation of individual hurricanes, and to probe the azimuthal structure of the hurricane BL during changes in intensity, we turned to numerical case studies. Two spatiotemporally high-resolution simulations were completed and analyzed: the first for Hurricane Irma in 2017, and the second for Hurricane Earl in 2010. The two hurricanes differed in their shear magnitude and direction,

intensity evolution, and track. Specifically, these two cases were chosen for their differing environmental shear profiles, their comparable intensity, and sustainment of high intensity over a prolonged period (i.e., several days). The Weather Research and Forecasting Model for Advanced Research (WRF-ARW) was employed for these full-physics simulations. Despite environmental differences between the two cases, both exhibited several azimuthally averaged BL structures consistent with those found in the composite analysis.

Prior to substantial land interaction, Hurricane Irma was associated with a low-level primary circulation that was highly inertially stable near/inside the RMW, but less inertially stable outside the RMW. Irma's BL was such that the most-intense inflow was isolated to the RMW, linked with radial convergence that promoted forced ascent of high-enthalpy, high- $M_a$  air from the BL almost exclusively at and inward of the RMW. During the analysis period, Irma steadily intensified prior to interacting with land (in line with the composite analysis that suggested such a profile of  $I^2$  and BL inflow is linked with IN), but Irma did undergo a brief weakening phase away from land.

In an analysis of the azimuthal structure of Irma's BL, we found an increase in BL asymmetry leading up to and during the aforementioned decay, possibly instigated by persistent weak-to-moderate northerly shear and westward storm motion. The asymmetry promoted inward advection of relatively low-enthalpy air downshear, which primarily reduced  $\theta_e$  immediately above the BL downwind (left of shear). Inflow asymmetry in the upshear-left quadrant was associated with BL divergence and descent of air into the BL from aloft, which allowed the low-enthalpy air to enter the near-surface inflow a few kilometers outside Irma's RMW. We conclude that this injection of low- $\theta_e$  air into the near-surface inflow in Irma's inner core may have negatively affected eyewall convection and thus reduced diabatic heating aloft (or advection of  $M_a$  surfaces by reducing convergence along the inner eyewall aloft), thereby explaining Irma's brief WE phase on 05 September. Irma's WE phase linked with the downward entrainment of low- $\theta_e$  air into the BL inflow is consistent with the composite analysis, which suggested descent of low- $\theta_e$  air into the inner-core BL inflow may occur during storm weakening. Irma's WE phase ended and promptly returned to intensification with a reduction in BL asymmetry, coincident with changes in storm motion and shear that may have discouraged asymmetry (Barnes and Dolling 2013).

Numerical analysis of Hurricane Earl was less obfuscated by interactions with land, but the later portion of the simulation following recurvature was largely ignored. In the simulations, Earl was similar to Irma in its eye size, RMW, and peak intensity. Unique from Irma, Hurricane Earl underwent a prolonged period of non-intensification with weakening following peak intensity, unrelated to interactions with land. Hurricane Earl's low-level primary circulation was more inertially stable outside the RMW (even when Earl was of weaker intensity), and  $I^2$  was somewhat lessened relative to Irma near and inside the RMW. Compared to Irma, Earl's azimuthally averaged BL inflow was weaker in the inner core, with the radial inflow maxima near/outside the RMW (apparently regardless of intensity change). Outside the RMW, the near-surface inflow was strong relative to Earl's inflow maximum over a larger radial band, indicating more widespread BL convergence.

After Earl reached peak intensity and entered a roughly two-day period of SS and WE phases, BL convergence and low-level ascent began to gradually spread across radius outside the RMW, eventually forming two distinct regions of BL convergence: one adjacent to the RMW, and the other tens of kilometers outside the RMW. During a WE period on 01 September,  $RH$  and  $\theta_e$  in Hurricane Earl's near-surface inflow was reduced at most radii outside the RMW, possibly due to descent or a radial influx of relatively dry air from outer radii. These properties of Earl's BL (e.g., high  $I^2$  outside the RMW, more BL convergence outside the RMW due to a wider radial band of strong inflow, relatively low BL  $\theta_e$ ) during its alternating SS and WE phases corroborate the findings of the composite analysis. However, near the end of 01 September (during an SS phase and prior to a long WE phase), near-surface  $\theta_e$  began to *increase* rapidly at all radii outside the RMW, about one day prior to a collapse of Earl's primary eyewall.

The azimuthal profile of Hurricane Earl's BL was notably distinguished from Hurricane Irma, the former often possessing pronounced asymmetry. After reaching peak intensity, evident asymmetries in Earl's primary and secondary circulations developed; these asymmetries appeared in tandem with storm motion becoming less antiparallel with deep-layer shear, and more oriented left of shear. We note that the shear and motion for Earl were of comparable magnitude to Irma's when those vectors were nearly orthogonal in each case; and while Irma *did* become more asymmetric when its motion and shear were perpendicular, the asymmetric response was not as drastic as seen in Hurricane Earl.

After Hurricane Earl's intensification early in the simulation, storm motion became oriented to the left of shear, which contrasts with Hurricane Irma where motion was generally *right* of shear. Low-level radial inflow has been observed to be amplified downshear and downstream of storm motion (Barnes and Dolling 2013; Zhang et al. 2013), and this property was seen in simulations of both Earl and Irma. With storm motion to the left of shear in Hurricane Earl, the downshear-right, downshear-left, and upshear-left quadrants exhibited substantial low-level inflow. The downshear quadrants housed the deepest inflow, while the downstream quadrants had the most-intense near-surface inflow (thus, the DSL quadrant had the strongest inflow, in the integral sense). However, the upshear-right quadrant—which would be expected to have anomalously weak inflow—evolved to have nearly *no* substantial BL inflow; instead, the quadrant developed strong outflow a few hundred meters above the ground, which extended outwards from the inner core. The outflow in the USR quadrant appeared to exhaust low- $M_a$ , high- $\theta_e$  air from the core to radii as far as 160 km away from Earl's center in the lower troposphere.

The spin-down tendency induced by Earl's strong outflow seemed to cause a broadening of the wind field along the top of the BL in the DSR quadrant, as well as a vertical minimum of tangential wind near the BL top in the DSR quadrant. Compounded with the fact that the BL air moving from USR to DSR was associated with minimal inflow, the local increase in  $I^2$  due to the progressive broadening of the DSR  $v$ -field may have led to near-surface inflow becoming radially maximized outside the RMW in the downshear quadrants. In tandem with the change in the downshear  $v$ -field over time, the BL convergence downshear would become relatively strong farther outside the RMW, as was seen in Hurricane Earl's simulation over the course of two days prior to its inner-eyewall collapse. Furthermore, the USR outflow of high- $\theta_e$  air from Earl's core may have recirculated into the BL inflow downwind (i.e., at larger radii downshear), increasing the moist entropy of near-surface inflow well outside Earl's RMW. Along with enhanced BL convergence and ascent outside the RMW in the downshear sector, the increase in BL moist entropy on 02 September may have promoted convection and consequent diabatic heating tens of kilometers outside Earl's RMW, leading to a thermal wind response that would weaken winds at the RMW and increase winds near the radius of outer convection (Shapiro and Willoughby 1982). Thus, the shear- and motion-induced low-level asymmetries in Hurricane Earl may have led to progres-

sive broadening of the wind field, outward radial propagation of BL convergence and ascent, and rapid increase in BL moist entropy outside the RMW that culminated in the demise of Earl's inner eyewall on 02 September.

While the strong outflow in the USR quadrant of Hurricane Earl appeared to lead to major dynamic and thermodynamic consequences that may explain its weakening over time, it is not yet entirely clear why that outflow formed at all; or why the dominant outflow appeared in Earl's USR quadrant but not, for instance, in Hurricane Irma's USL quadrant when its motion was orthogonal and to the right of shear. Although links between storm motion, shear, and low-level inflow have been examined (e.g., Kepert 2006a; Barnes and Dolling 2013; Zhang et al. 2013), the detailed nature of the effects of motion and shear on the *structure* of low-level inflow is less understood. For example, does shear have a greater influence on low-level inflow depth than storm motion? Does storm motion have a more direct effect on near-surface inflow intensity than shear?

At least in our two simulations of Hurricanes Irma and Earl, it would appear that the deep-layer shear has a stronger influence on the *depth* of low-level inflow, with deeper inflow downshear. As air rotates through the downshear quadrants, the inflow induces spin-up tendency via  $M_a$  advection in the BL *and immediately above* the BL, because of the greater depth of inflow. The combination of relatively high- $M_a$  air expelled from near-surface inflow by forced ascent and undeterred spin-up above the frictional BL by deep inflow allows supergradient winds to develop along the BL top downshear. This reasoning is supported by the fact that, in both simulations, the most supergradient winds along the BL top were generally found left of shear.

If the air that rotates into the USL quadrant from DSL is highly supergradient near the BL top, then a restorative response (e.g., outflow) may occur USL or USR to reinstate gradient wind balance above the BL. When the motion was oriented directly right of shear in Hurricane Irma, the USL quadrant had the weakest inflow—in alignment with the idea that upshear and upstream quadrants have weaker low-level inflow. Moderate outflow existed USL outside the RMW above the shallow and weak BL inflow, presumably in response to unbalanced flow entering from DSL. The inflow USR is stronger at outer radii possibly due to storm motion, but the moderate outflow layer still exists above the BL inflow, which may be an immediate response to supergradient flow being generated in the USR quadrant itself. In Hurricane Earl, when highly supergradient flow

enters the USL quadrant from DSL, the inflow asymmetry induced by storm motion may prevent effective outflow from forming to restore gradient wind balance, and promote further dynamical imbalance via BL  $M_a$  advection despite the outflow just above the BL. The restorative outflow that occurred in Irma USL in response to the dynamical imbalance that developed downshear *may not occur* in Earl due to the storm motion. In Earl, sufficient restorative outflow may be postponed until air rotates through the USL quadrant (where the flow may become more unbalanced due to strong BL inflow) and into the USR quadrant, where neither shear nor storm motion promote low-level inflow. Thus, the USR quadrant of Earl develops powerful low-level outflow in response to highly unbalanced low-level flow. The greater inertial stability outside the RMW in Earl may have also enhanced the supergradient flow leaving the DSL quadrant (and the eventual dynamic response upshear) due to the wider radial range of BL convergence (and thus, evacuation of high- $M_a$  air from the near-surface inflow into the free atmosphere).

The corroborative results of the composite and numerical analyses instill confidence that the BL structures highlighted in relation to intensity change are physically relevant. In the future, observational analysis of the azimuthal BL structure should be pursued, perhaps using similar methods employed here. In our simulation of Hurricane Earl, we found a gradual evolution of dynamic and thermodynamic structure supposedly linked to shear- and motion-induced asymmetries, which could benefit from trajectory modeling (e.g., to track the movement of high-enthalpy air from Earl's USR quadrant during weakening). Our simulations only entail the structures of two Atlantic hurricanes; it is possible that these two cases are anomalous, and they are likely not representative of every mature hurricane to appear in the Atlantic basin. More simulations could be completed and investigated to further test and build upon the results of this analysis. The findings of the numerical analyses encourage a detailed, idealized analysis of hurricane BL structure under varying arrangements of shear, storm motion, and vortex inertial stability. Such simulations could broach the topic of how asymmetric responses in the BL by shear and storm motion may interact constructively or destructively, and whether certain orientations of shear and motion—and thus, resulting azimuthal structures of the hurricane BL—are conducive for storm growth, decay, or maintenance.

# APPENDIX A

## DATA CONVERSION FROM EARTH-RELATIVE TO VORTEX-RELATIVE SPACE

All original fields of data used in this project are geospatial, gridded in terms of longitude, latitude, and height above the surface. The nature of our analyses requires these data to be regridded to storm-relative cylindrical space, with radial, azimuthal, and height coordinates. Radius  $r$  can be normalized by various measures [such as radius of maximum winds (RMW)] after its calculation, and the azimuthal coordinate is often defined relative to the storm motion or deep-layer shear vector. In prior research, the methods assumed to calculate  $r$  and the angular coordinate (which we will generalize as  $\psi$ ) may be prone to significant error (Ahern and Cowan 2018). By consequence, derived fields that require  $r$  or  $\psi$  are also subject to substantial error. Here we outline the sources of error when calculating  $r$  and  $\psi$  (and the variables dependent on them) and provide solutions that minimize error. These solutions are utilized throughout this project.

### A.1 Explanation of the Problem

When tasked with conforming geospatial data to a polar grid centered at some point on the Earth's surface, it can help to envision and understand the desired solution first. Let us imagine a polar grid with concentric circles about the origin, and straight rays extending outward from the origin (see Figure A.1). The concentric circles of our polar grid represent radial distance from the center (these circles can basically be looked at as radial distance *contours*). Each radial ray drawn from the origin is a geodesic (i.e., the shortest path between two points on the surface of a sphere), and the radial unit vector  $\hat{r}$  everywhere points away from the origin and parallel to these paths. These rays are perpendicular to the concentric circles of the grid, and thus, geodesics from the origin are perpendicular to contours of radius. By definition, the tangential unit vector  $\hat{t}$  is perpendicular to  $\hat{r}$ , so  $\hat{t}$  will point parallel to contours of radius and to the left of  $\hat{r}$  everywhere. At

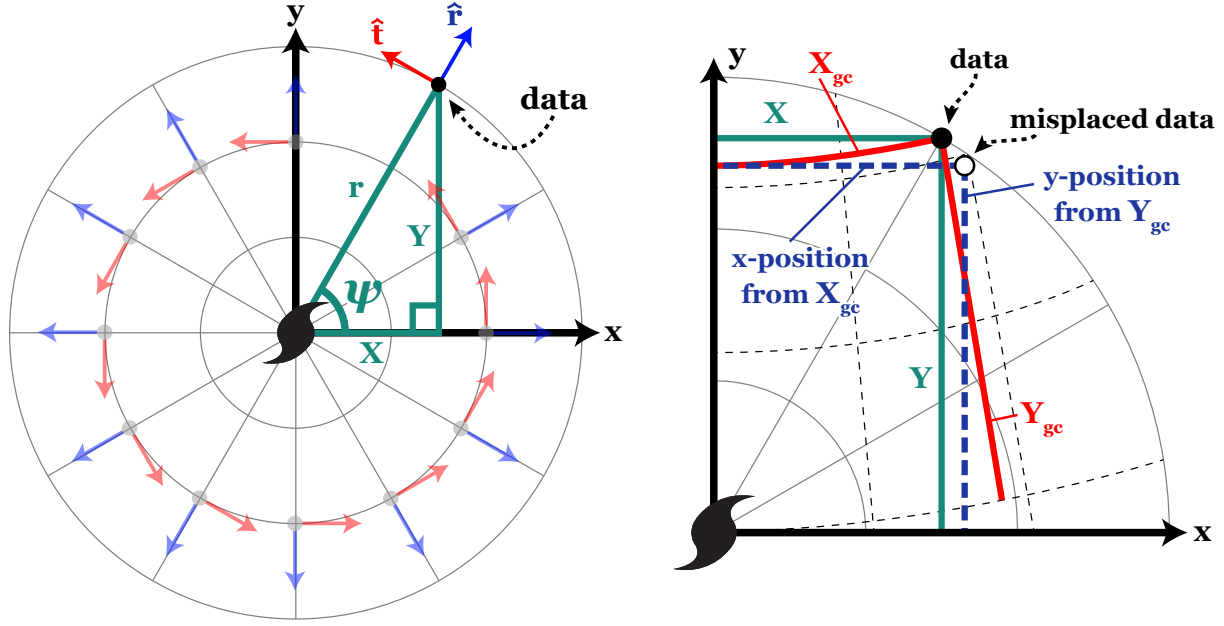


Figure A.1: (left) Schematic of a vortex-centered polar grid, with Cartesian axes  $(x, y)$  drawn over the grid as black vectors; contours of radius  $r$  (concentric circles) and azimuth  $\psi$  (radial rays extending from the center) in gray. Red and blue vectors represent tangential and radial unit vectors, respectively. The green triangle with sides  $X$ ,  $Y$ , and  $r$  (radius) depicts a conceptual example of calculating  $\psi$  at a position (the black point marked “data”) using trigonometry. (right) Illustration of position error due to assuming  $X = X_{gc}$  and  $Y = Y_{gc}$ , where the solid black dot represents the actual data position and the hollow dot represents the erroneous position calculated. The paths in red represent  $X_{gc}$  and  $Y_{gc}$ , which are computed along lines of latitude and longitude (dashed lines) respectively. The lengths of  $X_{gc}$  and  $Y_{gc}$  are used to approximate  $r$  and  $\psi$  (illustrated by blue dashed lines), resulting in position error.

a given point on the grid, the angular coordinate  $\psi$  is simply the angle between the grid’s positive  $x$ -axis and the geodesic drawn between the point and the origin. In that sense, the radial rays of our grid can be likened to contours of *azimuth*  $\psi$ . In regridding geospatial data to an  $(r, \psi)$  polar grid originating at a TC’s central axis, we want the grid to have all the aforementioned properties.

Many TC analyses that require the kind of grid described above use the method that follows. Radial position on the TC-centered grid is made equal to the great-circle distance from the origin

$$r(\lambda, \phi) = \sigma(a + h), \quad (\text{A.1})$$

where  $r(\lambda, \phi)$  is the radius at longitude  $\lambda$  and latitude  $\phi$ ,  $a$  is Earth’s radius,  $h$  is vertical distance

from the Earth's surface (which is usually set to zero due to its relatively small magnitude compared to  $a$ ), and  $\sigma$  is the central angle from the origin

$$\sigma(\lambda, \phi) = \cos^{-1}[\sin \phi_c \sin \phi + \cos \phi_c \cos \phi \cos(\lambda - \lambda_c)]. \quad (\text{A.2})$$

The longitude and latitude of the TC center are  $\lambda_c$  and  $\phi_c$ , respectively. The azimuthal position is often approximated using purely zonal and meridional great-circle distances ( $X_{gc}$  and  $Y_{gc}$ , respectively) from the vortex center

$$\begin{aligned} X_{gc} &= (a+h)(\lambda - \lambda_c) \cos \phi_c \\ Y_{gc} &= (a+h)(\phi - \phi_c); \end{aligned} \quad (\text{A.3})$$

and these distances are assumed to form the legs of a right triangle (shown in Figure A.1), which allows for the use of simple trigonometry to solve for  $\psi$ :

$$\tan \psi(\lambda, \phi) \approx Y_{gc}/X_{gc}. \quad (\text{A.4})$$

The approximated  $\psi$  is then used to derive the unit vector fields  $\hat{r}$  and  $\hat{t}$

$$\begin{aligned} \hat{r}(\lambda, \phi) &= \hat{i} \cos \psi + \hat{j} \sin \psi \\ \hat{t}(\lambda, \phi) &= -\hat{i} \sin \psi + \hat{j} \cos \psi, \end{aligned} \quad (\text{A.5})$$

where  $\hat{i}$  and  $\hat{j}$  are the eastward and northward unit vectors, respectively. Because  $\hat{r}$  and  $\hat{t}$  are functions of Earth-relative unit vectors in this method, the radial and tangential components of an arbitrary vector field defined in Earth-relative coordinates are easily found using dot products.

The method above has been used in TC analysis presumably under the assumption that errors resulting from its approximations are either negligible or non-existent. Since  $X_{gc}$  and  $Y_{gc}$  are distances along curved lines of longitude and latitude (Figure A.1), there will be errors when assuming that  $X_{gc}$  and  $Y_{gc}$  have lengths equal to the lengths of the triangle's legs in Figure A.1. As a result, the calculation of  $\psi$  will be wrong to some degree, so regridded data will be positioned incorrectly. (Similarly,  $r$  will be erroneous if, instead of equating  $r$  to great-circle distance from the origin, it is solved for in the Pythagorean theorem using  $X_{gc}$  and  $Y_{gc}$ .) Data that are positioned in  $(r, \psi)$  space—as well as any derivative fields necessitating  $r$  or  $\psi$ —using this method will suffer

errors related to incorrect positioning (which we will call “position error”). The assumption that  $\hat{i}$  and  $\hat{j}$  are everywhere parallel to the  $(x,y)$  axes of the polar grid will lead to additional errors due to neglecting vector rotation on the grid (this “rotation error” is independent of the position error, and discussed in section A.3).

The (potentially non-negligible) implications of projecting data to TC-centered space in the manner described above was described in Ahern and Cowan (2018). To limit the scope of this appendix, we will not detail the potential for significant errors here. The recommended methods for projecting geospatial data to vortex-centered polar coordinates, which were found accidentally while trying to conform the data in this research to a TC-centered grid, are described in the remainder of this appendix.

## A.2 Solution to Position Error

The ideal projection upon which to remap our geospatial data (described in the first paragraph of the previous section) should, in summary, have two specific map qualities: conservation of angles and distances relative to the origin at all points. The azimuthal equidistant map (AE) possesses these traits (Snyder 1987), so we will use this projection to remap our geospatial data to cylindrical grids originating on TC centers.

For any AE grid originating at  $(\lambda_c, \phi_c)$ , the positions of data at given longitudes and latitudes are transposed onto the  $xy$ -plane of the AE grid via

$$\begin{aligned} x(\lambda, \phi) &= \sigma(a+h)(\sin \sigma)^{-1} \cos \phi \sin(\lambda - \lambda_c) \\ y(\lambda, \phi) &= \sigma(a+h)(\sin \sigma)^{-1} [\cos \phi_c \sin \phi - \sin \phi_c \cos \phi \cos(\lambda - \lambda_c)], \end{aligned} \quad (\text{A.6})$$

where  $\sigma$  is the central angle as defined in Equation A.2. Because the  $x$  and  $y$  positions calculated above correctly represent the Cartesian location of data as projected on the AE map (our polar grid), we can calculate the azimuthal position  $\psi$  as normally intended:

$$\tan \psi(\lambda, \phi) = y/x. \quad (\text{A.7})$$

The radial position  $r$  of data on the AE projection is just the great-circle distance given in Equation A.1.

With  $r$  and  $\psi$  found as functions of longitude and latitude, all data can be mapped to the appropriate TC-centered polar space. Using the above method to remap data eliminates position error, which is all that is necessary to remove map distortion errors in scalar fields like temperature. However, further work is required to remove “rotation error,” which applies to Earth-relative vector fields like wind or temperature gradient.

### A.3 Solution to Rotation Error

With azimuth  $\psi$  known, the radial and tangential unit vector fields are

$$\begin{aligned}\hat{r}(\lambda, \phi) &= \hat{x} \cos \psi + \hat{y} \sin \psi \\ \hat{t}(\lambda, \phi) &= -\hat{x} \sin \psi + \hat{y} \cos \psi,\end{aligned}\tag{A.8}$$

where  $\hat{x}$  and  $\hat{y}$  are the unit vectors pointing in the direction of the AE map’s positive  $x$  and  $y$  axes, respectively. Note that  $\hat{x}$  is not equivalent to the eastward unit vector  $\hat{i}$ , nor is  $\hat{y}$  the same as the northward unit vector  $\hat{j}$  (comparing Equation A.5 with Equation A.8, and examining Figure A.2). This is because the basis set of vectors for the polar space are functions of  $x$  and  $y$  *on the map projection* when using the simple formulae for Cartesian-to-polar vector conversion—not  $\lambda$  and  $\phi$ . Except at specific points like the polar grid’s origin, the direction of an Earth-relative vector  $\vec{V}$  (i.e., azimuth relative to *east* in mathematical convention) is generally not equal to the direction of  $\vec{V}$  relative to  $\hat{x}$ . Thus, using a scalar product of  $\vec{V}$  and  $\hat{r}$  or  $\hat{t}$  to calculate polar components of  $\vec{V}$  leads to errors *if* the rotation of  $\hat{i}$  and  $\hat{j}$  as a function of position on the AE projection is neglected.

To derive the radial and tangential components of  $\vec{V}$ , we will redefine  $\vec{V}$  such that its horizontal components are aligned in the  $x$  and  $y$  directions:

$$\vec{V}_* = \|\vec{V}\|(\hat{x} \cos \alpha + \hat{y} \sin \alpha),\tag{A.9}$$

where  $\alpha$  is the angle between  $\hat{x}$  and  $\vec{V}$  *as it appears on the AE projection*, which we will call the projected direction (see Figure A.2). Finding  $\alpha$  would allow us to use simple vector multiplication to solve for the radial and tangential components of  $\vec{V}$ .

The process of learning a vector’s projected direction  $\alpha$  can be envisioned by imagining the amount of rotation in  $(\hat{i}, \hat{j})$  on the polar grid relative to  $(\hat{x}, \hat{y})$ , and then using that angle of rotation

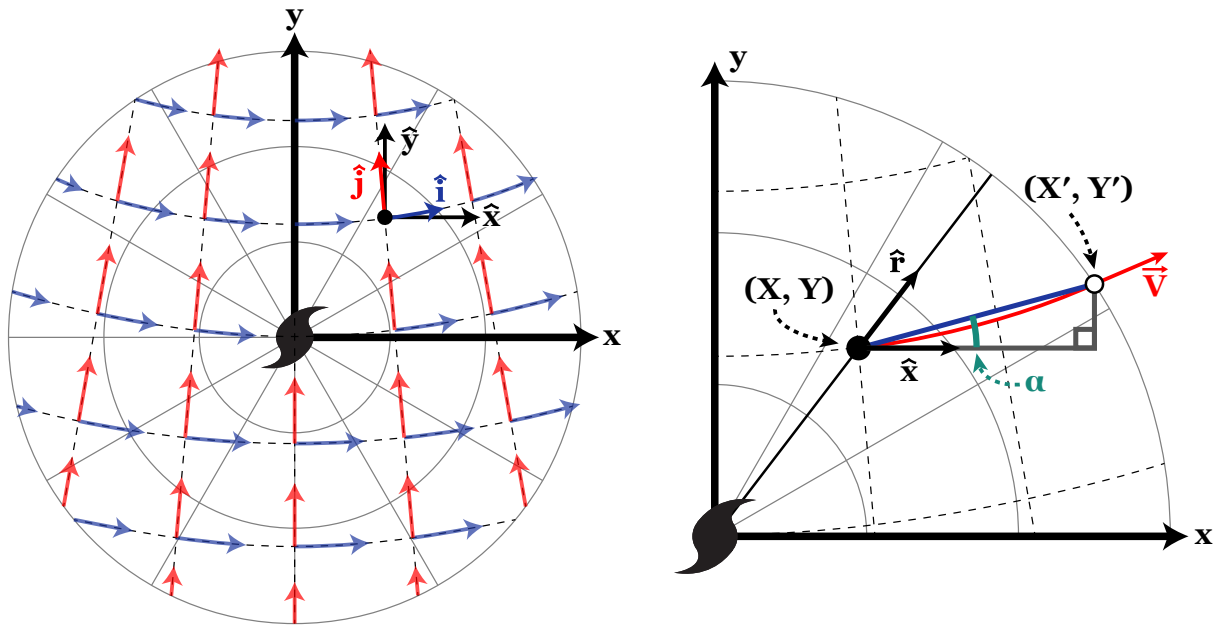


Figure A.2: (left) Eastward and northward unit vectors  $\hat{i}$  (blue) and  $\hat{j}$  (red) superimposed on a vortex-centered polar grid, illustrating deviations of  $\hat{i}$  and  $\hat{j}$  from the Cartesian axes  $(x, y)$ . (right) Example schematic of approximating the projected direction  $\alpha$  (green) of an eastward vector  $\vec{V}$  (red) at some location of data (black dot). Radial and  $x$  unit vectors for the example data are drawn in black. The position of data  $(X, Y)$  is perturbed downstream with the flow, yielding a perturbed position at  $(X', Y')$  (hollow dot). The  $x$  unit vector and a line (in blue) drawn on the projection between  $(X, Y)$  and  $(X', Y')$  are used to form a right triangle, which is used to solve for  $\alpha$ . Note that in this case,  $\alpha$  is not zero—the mathematical direction of an eastward vector on a latitude-longitude grid.

to turn the vector in kind. The projected direction of  $\vec{V}$  resulting from the aforementioned process can be closely estimated by drawing an infinitesimal forward trajectory along the Earth-relative direction of  $\vec{V}$ , and then transforming that trajectory's endpoints to AE space. (A backward trajectory would also suffice, but the mathematics below would be slightly altered.) A line is drawn between the transformed endpoints on the AE grid, and that line is used to approximate the vector's orientation relative to  $\hat{x}$  using trigonometry (Figure A.2). The downstream endpoint of the trajectory is given by perturbing the vector's original longitude and latitude along the vector's Earth-relative direction:

$$\begin{aligned}\lambda'(\lambda, \phi) &= \lambda + \frac{\varepsilon \hat{i} \cdot \vec{V}}{\|\vec{V}\| \cos \phi} \\ \phi'(\lambda, \phi) &= \phi + \frac{\varepsilon \hat{j} \cdot \vec{V}}{\|\vec{V}\|} \\ 0 < \varepsilon &\ll 1,\end{aligned}\tag{A.10}$$

where  $\varepsilon$  is a central angle perturbation. In the case where  $\|\vec{V}\| = 0$ , the radial and tangential components of  $\vec{V}$  are zero, so the above equations would not be used. Equation A.10 also becomes problematic at Earth's poles, which is no concern for this research.

The perturbed position field is transferred to the AE grid using Equation A.6:

$$\begin{aligned}x'(\lambda, \phi) &= x(\lambda', \phi') \\ y'(\lambda, \phi) &= y(\lambda', \phi').\end{aligned}\tag{A.11}$$

A line is drawn between  $(x, y)$  and  $(x', y')$  on the projection itself (blue line in Figure A.2). A right triangle is formed with this line as the hypotenuse. The angle between  $\hat{x}$  and the drawn line approaches  $\alpha$  as  $\varepsilon$  approaches zero:

$$\tan \alpha(\lambda, \phi) = \lim_{\varepsilon \rightarrow 0} \left( \frac{y' - y}{x' - x} \right).\tag{A.12}$$

With  $\alpha$  found as functions of longitude and latitude, the projected vector field  $\vec{V}_*$  is known. Using Equations A.8 and A.9, we are free to deduce polar components of  $\vec{V}$

$$\begin{aligned}
 V_r(\lambda, \phi) &= \vec{V}_* \cdot (\hat{x} \cos \psi + \hat{y} \sin \psi) \\
 &= \|\vec{V}\| (\cos \alpha \cos \psi + \sin \alpha \sin \psi) \\
 &= \|\vec{V}\| \cos(\alpha - \psi),
 \end{aligned} \tag{A.13}$$

$$\begin{aligned}
 V_t(\lambda, \phi) &= \vec{V}_* \cdot (-\hat{x} \sin \psi + \hat{y} \cos \psi) \\
 &= \|\vec{V}\| (\sin \alpha \cos \psi - \cos \alpha \sin \psi) \\
 &= \|\vec{V}\| \sin(\alpha - \psi),
 \end{aligned} \tag{A.14}$$

where  $V_r$  and  $V_t$  are the radial and tangential components of  $\vec{V}$ , respectively.

# REFERENCES

- Ahern, K., M. A. Bourassa, R. E. Hart, J. A. Zhang, and R. F. Rogers, 2019: Observed kinematic and thermodynamic structure in the hurricane boundary layer during intensity change. *Mon. Wea. Rev.*, **147** (8), 2765–2785.
- Ahern, K., and L. Cowan, 2018: Minimizing common errors when projecting geospatial data onto a vortex-centered space. *Geophys. Res. Lett.*, **45**, doi:10.1029/2018GL079953.
- Barnes, G. M., 2008: Atypical thermodynamic profiles in hurricanes. *Mon. Wea. Rev.*, **136** (2), 631–643.
- Barnes, G. M., and K. P. Dolling, 2013: The inflow to Tropical Cyclone Humberto (2001) as viewed with azimuth-height surfaces over three days. *Mon. Wea. Rev.*, **141** (4), 1324–1336.
- Bell, M. M., and M. T. Montgomery, 2008: Observed structure, evolution, and potential intensity of category 5 Hurricane Isabel (2003) from 12 to 14 September. *Mon. Wea. Rev.*, **136** (6), 2023–2046.
- Black, M., J. Gamache, F. Marks, C. Samsury, and H. Willoughby, 2002: Eastern Pacific Hurricanes Jimena of 1991 and Olivia of 1994: The effect of vertical shear on structure and intensity. *Mon. Wea. Rev.*, **130** (9), 2291–2312.
- Black, M. L., R. W. Burpee, and F. D. J. Marks, 1996: Vertical motion characteristics of tropical cyclones determined with airborne Doppler radial velocities. *J. Atmos. Sci.*, **53** (13), 1887–1909.
- Black, P. G., and Coauthors, 2007: Air-sea exchange in hurricanes: Synthesis of observations from the Coupled Boundary Layer Air-Sea Transfer experiment. *Bull. Amer. Meteor. Soc.*, **88** (3), 357–374.
- Braun, S. A., and W.-K. Tao, 2000: Sensitivity of high-resolution simulations of Hurricane Bob (1991) to planetary boundary layer parameterizations. *Mon. Wea. Rev.*, **128** (12), 3941–3961.
- Bryan, G. H., 2012: Effects of surface exchange coefficients and turbulence length scales on the intensity and structure of numerically simulated hurricanes. *Mon. Wea. Rev.*, **140** (4), 1125–1143.
- Bryan, G. H., and M. J. Fritsch, 2000: Moist absolute instability: The sixth static stability state. *Bull. Amer. Meteor. Soc.*, **81** (6), 1207–1230.

- Bryan, G. H., and R. Rotunno, 2009: The maximum intensity of tropical cyclones in axisymmetric numerical model simulations. *Mon. Wea. Rev.*, **137** (6), 1770–1789.
- Chan, J. C., and J. D. Kepert, 2010: *Global Perspectives on Tropical Cyclones: From Science to Mitigation*, Vol. 4. World Scientific, 436 pp.
- Chen, S. S., J. A. Knaff, and F. D. J. Marks, 2006: Effects of vertical wind shear and storm motion on tropical cyclone rainfall asymmetries deduced from TRMM. *Mon. Wea. Rev.*, **134** (11), 3190–3208.
- Chen, S. S., W. Zhao, M. A. Donelan, J. F. Price, and E. J. Walsh, 2007: The CBLAST-Hurricane Program and the next-generation fully coupled atmosphere-wave-ocean models for hurricane research and prediction. *Bull. Amer. Meteor. Soc.*, **88** (3), 311–317.
- Corbosiero, K. L., and J. Molinari, 2002: The effects of vertical wind shear on the distribution of convection in tropical cyclones. *Mon. Wea. Rev.*, **130** (8), 2110–2123.
- Corbosiero, K. L., and J. Molinari, 2003: The relationship between storm motion, vertical wind shear, and convective asymmetries in tropical cyclones. *J. Atmos. Sci.*, **60** (2), 366–376.
- Cram, T. A., J. Persing, M. T. Montgomery, and S. A. Braun, 2007: A Lagrangian trajectory view on transport and mixing processes between the eye, eyewall, and environment using a high-resolution simulation of Hurricane Bonnie (1998). *J. Atmos. Sci.*, **64** (6), 1835–1856.
- Dee, D. P., and Coauthors, 2011: The ERA-Interim reanalysis: Configuration and performance of the data assimilation system. *Quart. J. Roy. Meteor. Soc.*, **137** (656), 553–597.
- DeHart, J. C., R. A. J. Houze, and R. F. Rogers, 2014: Quadrant distribution of tropical cyclone inner-core kinematics in relation to environmental shear. *J. Atmos. Sci.*, **71** (7), 2713–2732.
- DeMaria, M., 1996: The effect of vertical shear on tropical cyclone intensity change. *J. Atmos. Sci.*, **53** (14), 2076–2088.
- DeMaria, M., M. Mainelli, L. K. Shay, J. A. Knaff, and J. Kaplan, 2005: Further improvements to the statistical hurricane intensity prediction scheme (SHIPS). *Wea. Forecasting*, **20** (4), 531–543.
- Donelan, M. A., B. K. Haus, N. Reul, W. J. Plant, M. Stiassnie, H. C. Graber, O. B. Brown, and E. S. Saltzman, 2004: On the limiting aerodynamic roughness of the ocean in very strong winds. *Geophys. Res. Lett.*, **31** (18).
- Emanuel, K. A., 1986: An air-sea interaction theory for tropical cyclones. Part I: Steady-state maintenance. *J. Atmos. Sci.*, **43** (6), 585–605.

- Emanuel, K. A., 1988: The maximum intensity of hurricanes. *J. Atmos. Sci.*, **45** (7), 1143–1155.
- Emanuel, K. A., 1995: Sensitivity of tropical cyclones to surface exchange coefficients and a revised steady-state model incorporating eye dynamics. *J. Atmos. Sci.*, **52** (22), 3969–3976.
- Emanuel, K. A., 1997: Some aspects of hurricane inner-core dynamics and energetics. *J. Atmos. Sci.*, **54** (8), 1014–1026.
- Foster, R. C., 2009: Boundary-layer similarity under an axisymmetric, gradient wind vortex. *Bound.-Layer Meteor.*, **131** (3), 321–344.
- Franklin, J. L., M. L. Black, and K. Valde, 2003: GPS dropwindsonde wind profiles in hurricanes and their operational implications. *Wea. Forecasting*, **18** (1), 32–44.
- Gallina, G. M., and C. S. Velden, 2002: Environmental vertical wind shear and tropical cyclone intensity change utilizing enhanced satellite derived wind information. *Extended Abstracts, 25th Conf. on Hurricanes and Tropical Meteorology*, San Diego, CA, Amer. Meteor. Soc., 172–173.
- Guimond, S. R., G. M. Heymsfield, P. D. Reasor, and A. C. Didlake Jr, 2016: The rapid intensification of Hurricane Karl (2010): New remote sensing observations of convective bursts from the Global Hawk platform. *J. Atmos. Sci.*, **73** (9), 3617–3639.
- Guimond, S. R., G. M. Heymsfield, and F. J. Turk, 2010: Multiscale observations of Hurricane Dennis (2005): The effects of hot towers on rapid intensification. *J. Atmos. Sci.*, **67** (3), 633–654.
- Hazelton, A. T., R. E. Hart, and R. F. Rogers, 2017a: Analyzing simulated convective bursts in two Atlantic hurricanes. Part II: Intensity change due to bursts. *Mon. Wea. Rev.*, **145** (8), 3095–3117.
- Hazelton, A. T., R. F. Rogers, and R. E. Hart, 2017b: Analyzing simulated convective bursts in two Atlantic hurricanes. Part I: Burst formation and development. *Mon. Wea. Rev.*, **145** (8), 3073–3094.
- Hence, D. A., and R. A. J. Houze, 2011: Vertical structure of hurricane eyewalls as seen by the TRMM Precipitation Radar. *J. Atmos. Sci.*, **68** (8), 1637–1652.
- Hendricks, E. A., M. T. Montgomery, and C. A. Davis, 2004: The role of “vortical” hot towers in the formation of tropical cyclone Diana (1984). *J. Atmos. Sci.*, **61** (11), 1209–1232.
- Heng, J., Y. Wang, and W. Zhou, 2017: Revisiting the balanced and unbalanced aspects of tropical cyclone intensification. *J. Atmos. Sci.*, **74** (8), 2575–2591.

- Hock, T. F., and J. L. Franklin, 1999: The NCAR GPS dropwindsonde. *Bull. Amer. Meteor. Soc.*, **80** (3), 407–420.
- Holland, G., and R. T. Merrill, 1984: On the dynamics of tropical cyclone structural changes. *Quart. J. Roy. Meteor. Soc.*, **110** (465), 723–745.
- Holton, J. R., 2004: *An Introduction to Dynamic Meteorology*. 4th ed., Elsevier Academic Press, 535 pp.
- Hong, S.-Y., Y. Noh, and J. Dudhia, 2006: A new vertical diffusion package with an explicit treatment of entrainment processes. *Mon. Wea. Rev.*, **134** (9), 2318–2341.
- Houze, R. A. J., W.-C. Lee, and M. M. Bell, 2009: Convective contribution to the genesis of Hurricane Ophelia (2005). *Mon. Wea. Rev.*, **137** (9), 2778–2800.
- Iacono, M. J., J. S. Delamere, E. J. Mlawer, M. W. Shephard, S. A. Clough, and W. D. Collins, 2008: Radiative forcing by long-lived greenhouse gases: Calculations with the AER radiative transfer models. *J. Geophys. Res.*, **113** (D13103).
- Jiménez, P. A., J. Dudhia, J. F. González-Rouco, J. Navarro, J. P. Montávez, and E. García-Bustamante, 2012: A revised scheme for the WRF surface layer formulation. *Mon. Wea. Rev.*, **140** (3), 898–918.
- Kaimal, J. C., and J. J. Finnigan, 1994: *Atmospheric Boundary Layer Flows: Their Structure and Measurement*. Oxford University Press, 289 pp.
- Kain, J. S., 2004: The Kain-Fritsch convective parameterization: an update. *J. Appl. Meteor.*, **43** (1), 170–181.
- Kepert, J., 2001: The dynamics of boundary layer jets within the tropical cyclone core. Part I: Linear theory. *J. Atmos. Sci.*, **58** (17), 2469–2484.
- Kepert, J., and Y. Wang, 2001: The dynamics of boundary layer jets within the tropical cyclone core. Part II: Nonlinear enhancement. *J. Atmos. Sci.*, **58** (17), 2485–2501.
- Kepert, J. D., 2006a: Observed boundary layer wind structure and balance in the hurricane core. Part I: Hurricane Georges. *J. Atmos. Sci.*, **63** (9), 2169–2193.
- Kepert, J. D., 2006b: Observed boundary layer wind structure and balance in the hurricane core. Part II: Hurricane Mitch. *J. Atmos. Sci.*, **63** (9), 2194–2211.
- Kepert, J. D., 2010: Slab- and height-resolving models of the tropical cyclone boundary layer. Part I: Comparing the simulations. *Quart. J. Roy. Meteor. Soc.*, **136** (652), 1686–1699.

- Kepert, J. D., 2013: How does the boundary layer contribute to eyewall replacement cycles in axisymmetric tropical cyclones? *J. Atmos. Sci.*, **70** (9), 2808–2830.
- Kepert, J. D., 2017: Time and space scales in the tropical cyclone boundary layer, and the location of the eyewall updraft. *J. Atmos. Sci.*, **74** (10), 3305–3323.
- Kepert, J. D., J. Schwendike, and H. Ramsay, 2016: Why is the tropical cyclone boundary layer not “well mixed”? *J. Atmos. Sci.*, **73** (3), 957–973.
- Klotz, B. W., and E. W. Uhlhorn, 2014: Improved stepped frequency microwave radiometer tropical cyclone surface winds in heavy precipitation. *J. Atmos. Oceanic Technol.*, **31** (11), 2392–2408.
- Knupp, K. R., J. Walters, and M. Biggerstaff, 2006: Doppler profiler and radar observations of boundary layer variability during the landfall of Tropical Storm Gabrielle. *J. Atmos. Sci.*, **63** (1), 234–251.
- Krishnamurti, T., S. Pattnaik, L. Stefanova, T. V. Kumar, B. P. Mackey, A. O’Shay, and R. J. Pasch, 2005: The hurricane intensity issue. *Mon. Wea. Rev.*, **133** (7), 1886–1912.
- Landsea, C. W., and J. L. Franklin, 2013: Atlantic hurricane database uncertainty and presentation of a new database format. *Mon. Wea. Rev.*, **141** (10), 3576–3592.
- Leipper, D. F., and D. Volgenau, 1972: Hurricane heat potential of the Gulf of Mexico. *J. Phys. Oceanogr.*, **2** (3), 218–224.
- Marks, F. D. J., and R. A. J. Houze, 1987: Inner core structure of Hurricane Alicia from airborne Doppler radar observations. *J. Atmos. Sci.*, **44** (9), 1296–1317.
- Marks, F. D. J., R. A. J. Houze, and J. F. Gamache, 1992: Dual-aircraft investigation of the inner core of Hurricane Norbert. Part I: Kinematic structure. *J. Atmos. Sci.*, **49** (11), 919–942.
- Möller, J. D., and M. T. Montgomery, 2000: Tropical cyclone evolution via potential vorticity anomalies in a three-dimensional balance model. *J. Atmos. Sci.*, **57** (20), 3366–3387.
- Montgomery, M., M. Nicholls, T. Cram, and A. Saunders, 2006a: A vortical hot tower route to tropical cyclogenesis. *J. Atmos. Sci.*, **63** (1), 355–386.
- Montgomery, M. T., M. M. Bell, S. D. Aberson, and M. L. Black, 2006b: Hurricane Isabel (2003): New insights into the physics of intense storms. Part I: Mean vortex structure and maximum intensity estimates. *Bull. Amer. Meteor. Soc.*, **87** (10), 1335–1347.

- Montgomery, M. T., and R. J. Kallenbach, 1997: A theory for vortex rossby-waves and its application to spiral bands and intensity changes in hurricanes. *Quart. J. Roy. Meteor. Soc.*, **123 (538)**, 435–465.
- Montgomery, M. T., and R. K. Smith, 2018: Comments on “revisiting the balanced and unbalanced aspects of tropical cyclone intensification”. *J. Atmos. Sci.*, **75 (7)**, 2491–2496.
- Montgomery, M. T., R. K. Smith, and S. V. Nguyen, 2010: Sensitivity of tropical-cyclone models to the surface drag coefficient. *Quart. J. Roy. Meteor. Soc.*, **136 (653)**, 1945–1953.
- Montgomery, M. T., R. K. Smith, and J. Persing, 2018: Revisiting the boundary layer spin up mechanism in tropical cyclones. Part I: Refuting recent challenges. *33rd Conf. on Hurricanes and Tropical Meteorology*, Ponte Vedra Beach, FL, Amer. Meteor. Soc.
- Morrison, H., G. Thompson, and V. Tatarskii, 2009: Impact of cloud microphysics on the development of trailing stratiform precipitation in a simulated squall line: Comparison of one- and two-moment schemes. *Mon. Wea. Rev.*, **137 (3)**, 991–1007.
- NCEP, 2000: NCEP FNL Operational Model Global Tropospheric Analyses, continuing from July 1999. Research Data Archive at the National Center for Atmospheric Research, Computational and Information Systems Laboratory, Boulder CO, URL <https://doi.org/10.5065/D6M043C6>.
- Nguyen, L. T., J. Molinari, and D. Thomas, 2014: Evaluation of tropical cyclone center identification methods in numerical models. *Mon. Wea. Rev.*, **142 (11)**, 4326–4339.
- Nguyen, L. T., R. F. Rogers, and P. D. Reasor, 2017: Thermodynamic and kinematic influences on precipitation symmetry in sheared tropical cyclones: Bertha and Cristobal (2014). *Mon. Wea. Rev.*, **145 (11)**, 4423–4446.
- Nolan, D. S., and L. D. Grasso, 2003: Nonhydrostatic, three-dimensional perturbations to balanced, hurricane-like vortices. Part II: Symmetric response and nonlinear simulations. *J. Atmos. Sci.*, **60 (22)**, 2717–2745.
- Nolan, D. S., and M. T. Montgomery, 2002: Nonhydrostatic, three-dimensional perturbations to balanced, hurricane-like vortices. Part I: Linearized formulation, stability, and evolution. *J. Atmos. Sci.*, **59 (21)**, 2989–3020.
- Nolan, D. S., Y. Moon, and D. P. Stern, 2007: Tropical cyclone intensification from asymmetric convection: Energetics and efficiency. *J. Atmos. Sci.*, **64 (10)**, 3377–3405.

- Nolan, D. S., J. A. Zhang, and D. P. Stern, 2009a: Evaluation of planetary boundary layer parameterizations in tropical cyclones by comparison of in situ observations and high-resolution simulations of Hurricane Isabel (2003). Part I: Initialization, maximum winds, and the outer-core boundary layer. *Mon. Wea. Rev.*, **137** (11), 3651–3674.
- Nolan, D. S., J. A. Zhang, and D. P. Stern, 2009b: Evaluation of planetary boundary layer parameterizations in tropical cyclones by comparison of in situ observations and high-resolution simulations of Hurricane Isabel (2003). Part II: Inner-core boundary layer and eyewall structure. *Mon. Wea. Rev.*, **137** (11), 3675–3698.
- Ooyama, K., 1969: Numerical simulation of the life cycle of tropical cyclones. *J. Atmos. Sci.*, **26** (1), 3–40.
- Ooyama, K. V., 1982: Conceptual evolution of the theory and modeling of the tropical cyclone. *J. Meteor. Soc. Japan*, **60** (1), 369–380.
- Paterson, L. A., B. N. Hanstrum, N. E. Davidson, and H. C. Weber, 2005: Influence of environmental vertical wind shear on the intensity of hurricane-strength tropical cyclones in the Australian region. *Mon. Wea. Rev.*, **133** (12), 3644–3660.
- Pendergrass, A. G., and H. E. Willoughby, 2009: Diabatically induced secondary flows in tropical cyclones. Part I: Quasi-steady forcing. *Mon. Wea. Rev.*, **137** (3), 805–821.
- Persing, J., and M. T. Montgomery, 2003: Hurricane superintensity. *J. Atmos. Sci.*, **60** (19), 2349–2371.
- Powell, M. D., P. J. Vickery, and T. A. Reinhold, 2003: Reduced drag coefficient for high wind speeds in tropical cyclones. *Nature*, **422** (6929), 279–283.
- Reasor, P. D., M. T. Montgomery, and L. F. Bosart, 2005: Mesoscale observations of the genesis of Hurricane Dolly (1996). *J. Atmos. Sci.*, **62** (9), 3151–3171.
- Reasor, P. D., R. Rogers, and S. Lorsolo, 2013: Environmental flow impacts on tropical cyclone structure diagnosed from airborne Doppler radar composites. *Mon. Wea. Rev.*, **141** (9), 2949–2969.
- Riehl, H., 1954: *Tropical Meteorology*. McGraw-Hill, New York, 392 pp.
- Rogers, R., S. Lorsolo, P. Reasor, J. Gamache, and F. Marks, 2012: Multiscale analysis of tropical cyclone kinematic structure from airborne Doppler radar composites. *Mon. Wea. Rev.*, **140** (1), 77–99.

- Rogers, R., P. Reasor, and S. Lorsolo, 2013a: Airborne Doppler observations of the inner-core structural differences between intensifying and steady-state tropical cyclones. *Mon. Wea. Rev.*, **141** (9), 2970–2991.
- Rogers, R., and Coauthors, 2006: The intensity forecasting experiment: A NOAA multiyear field program for improving tropical cyclone intensity forecasts. *Bull. Amer. Meteor. Soc.*, **87** (11), 1523–1537.
- Rogers, R., and Coauthors, 2013b: NOAA’s hurricane intensity forecasting experiment: A progress report. *Bull. Amer. Meteor. Soc.*, **94** (6), 859–882.
- Rosenthal, S. L., 1971: The response of a tropical cyclone model to variations in boundary layer parameters, initial conditions, lateral boundary conditions, and domain size. *Mon. Wea. Rev.*, **99** (10), 767–777.
- Ryglicki, D. R., and R. E. Hart, 2015: An investigation of center-finding techniques for tropical cyclones in mesoscale models. *J. Appl. Meteor. Climatol.*, **54** (4), 825–846.
- Schubert, W. H., and J. J. Hack, 1982: Inertial stability and tropical cyclone development. *J. Atmos. Sci.*, **39** (8), 1687–1697.
- Schubert, W. H., C. M. Rozoff, J. L. Vigh, B. D. McNoldy, and J. P. Kossin, 2007: On the distribution of subsidence in the hurricane eye. *Quart. J. Roy. Meteor. Soc.*, **133** (624), 595–605.
- Schwendike, J., and J. D. Kepert, 2008: The boundary layer winds in Hurricanes Danielle (1998) and Isabel (2003). *Mon. Wea. Rev.*, **136** (8), 3168–3192.
- Shapiro, L. J., 2000: Potential vorticity asymmetries and tropical cyclone evolution in a moist three-layer model. *J. Atmos. Sci.*, **57** (21), 3645–3662.
- Shapiro, L. J., and H. E. Willoughby, 1982: The response of balanced hurricanes to local sources of heat and momentum. *J. Atmos. Sci.*, **39** (2), 378–394.
- Shi, Q., and M. A. Bourassa, 2019: Coupling ocean currents and waves with wind stress over the gulf stream. *Rem. Sens.*, **11** (12), 1476.
- Simpson, R., and L. Starrett, 1955: Further studies of hurricane structure by aircraft reconnaissance. *Bull. Amer. Meteor. Soc.*, **36** (9), 459–468.
- Sitkowski, M., and G. M. Barnes, 2009: Low-level thermodynamic, kinematic, and reflectivity fields of Hurricane Guillermo (1997) during rapid intensification. *Mon. Wea. Rev.*, **137** (2), 645–663.

- Skamarock, W. C., and Coauthors, 2008: A description of the advanced research WRF version 3. NCAR Tech. Note NCAR/TN-475+STR, NCAR, Boulder, CO, 113 pp.
- Smith, R. K., and M. T. Montgomery, 2008: Balanced boundary layers used in hurricane models. *Quart. J. Roy. Meteor. Soc.*, **134 (635)**, 1385–1395.
- Smith, R. K., and M. T. Montgomery, 2016: The efficiency of diabatic heating and tropical cyclone intensification. *Quart. J. Roy. Meteor. Soc.*, **142 (698)**, 2081–2086.
- Smith, R. K., M. T. Montgomery, and G. L. Thomsen, 2014: Sensitivity of tropical-cyclone models to the surface drag coefficient in different boundary-layer schemes. *Quart. J. Roy. Meteor. Soc.*, **140 (680)**, 792–804.
- Smith, R. K., M. T. Montgomery, and N. Van Sang, 2009: Tropical cyclone spin-up revisited. *Quart. J. Roy. Meteor. Soc.*, **135 (642)**, 1321–1335.
- Smith, R. K., M. T. Montgomery, and H. Zhu, 2005: Buoyancy in tropical cyclones and other rapidly rotating atmospheric vortices. *Dyn. Atmos. Oceans*, **40 (3)**, 189–208.
- Smith, R. K., and G. L. Thomsen, 2010: Dependence of tropical-cyclone intensification on the boundary-layer representation in a numerical model. *Quart. J. Roy. Meteor. Soc.*, **136 (652)**, 1671–1685.
- Snyder, J. P., 1987: *Map projections—A working manual*, Vol. 1395. US Government Printing Office.
- Stern, D. P., J. L. Vigh, D. S. Nolan, and F. Zhang, 2015: Revisiting the relationship between eyewall contraction and intensification. *J. Atmos. Sci.*, **72 (4)**, 1283–1306.
- Tewari, M., and Coauthors, 2004: Implementation and verification of the unified NOAA land surface model in the WRF model. *20th Conf. on Weather Analysis and Forecasting/16th Conf. on Numerical Weather Prediction*, Seattle, WA, Amer. Meteor. Soc., 11–15.
- Uhlhorn, E. W., and P. G. Black, 2003: Verification of remotely sensed sea surface winds in hurricanes. *J. Atmos. Oceanic Technol.*, **20 (1)**, 99–116.
- Uhlhorn, E. W., P. G. Black, J. L. Franklin, M. Goodberlet, J. Carswell, and A. S. Goldstein, 2007: Hurricane surface wind measurements from an operational stepped frequency microwave radiometer. *Mon. Wea. Rev.*, **135 (9)**, 3070–3085.
- Vigh, J. L., and W. H. Schubert, 2009: Rapid development of the tropical cyclone warm core. *J. Atmos. Sci.*, **66 (11)**, 3335–3350.

- Willoughby, H. E., 1988: The dynamics of the tropical cyclone core. *Aust. Meteor. Mag.*, **36** (3), 183–191.
- Willoughby, H. E., 1990: Gradient balance in tropical cyclones. *J. Atmos. Sci.*, **47** (2), 265–274.
- Willoughby, H. E., and M. B. Chelmon, 1982: Objective determination of hurricane tracks from aircraft observations. *Mon. Wea. Rev.*, **110** (9), 1298–1305.
- Yano, J.-I., and K. Emanuel, 1991: An improved model of the equatorial troposphere and its coupling with the stratosphere. *J. Atmos. Sci.*, **48** (3), 377–389.
- Zhang, F., and K. Emanuel, 2016: On the role of surface fluxes and WISHE in tropical cyclone intensification. *J. Atmos. Sci.*, **73** (5), 2011–2019.
- Zhang, J. A., P. G. Black, J. R. French, and W. M. Drennan, 2008: First direct measurements of enthalpy flux in the hurricane boundary layer: The CBLAST results. *Geophys. Res. Lett.*, **35** (14).
- Zhang, J. A., W. M. Drennan, P. G. Black, and J. R. French, 2009: Turbulence structure of the hurricane boundary layer between the outer rainbands. *J. Atmos. Sci.*, **66** (8), 2455–2467.
- Zhang, J. A., R. F. Rogers, D. S. Nolan, and F. D. J. Marks, 2011: On the characteristic height scales of the hurricane boundary layer. *Mon. Wea. Rev.*, **139** (8), 2523–2535.
- Zhang, J. A., R. F. Rogers, P. D. Reasor, E. W. Uhlhorn, and F. D. J. Marks, 2013: Asymmetric hurricane boundary layer structure from dropsonde composites in relation to the environmental vertical wind shear. *Mon. Wea. Rev.*, **141** (11), 3968–3984.
- Zhang, J. A., R. F. Rogers, and V. Tallapragada, 2017: Impact of parameterized boundary layer structure on tropical cyclone rapid intensification forecasts in HWRF. *Mon. Wea. Rev.*, **145** (4), 1413–1426.

# BIOGRAPHICAL SKETCH

Kyle enrolled at The Florida State University in 2009 to pursue a bachelor's degree in meteorology. He took undergraduate classes there, as well as at Palm Beach State College and Florida Atlantic University between 2009 and 2013. In 2012, he fulfilled an internship at the Weather Forecast Office in Anchorage, Alaska under James A. Nelson's direction. Kyle completed an undergraduate research thesis with the guidance of Dr. Henry E. Fuelberg, as well as with invaluable assistance and training from Dr. Fuelberg's then doctoral student, Dr. Nick K. Heath. The thesis, "Analysis of Convective Transport of Biomass Burning Emissions in Southeast Asia," was given the AMS Father James B. MacElwane Award in Meteorology in 2013.

Through the advisement and support of Dr. Mark A. Bourassa, Kyle continued his studies at The Florida State University graduate school in 2013. He defended a master's thesis, "Analysis of Polar Mesocyclonic Surface Turbulent Fluxes in the Arctic System Reanalysis (ASRV1) Dataset," in 2015. As part of his doctoral research, he visited scientists at the Hurricane Research Division in Miami, Florida during the 2018 Atlantic hurricane season with support from Drs. Jun A. Zhang and Robert F. Rogers. He has had two scientific articles accepted for publication related to his research: one with friend and lab colleague Levi P. Cowan; and the second with his advisers Drs. Bourassa and Hart, as well as Drs. Zhang and Rogers.